Far-infrared-to-centimeter-wave spectroscopic observations of *Planck*-selected starburst galaxies

Dissertation
zur
Erlangung des Doktorgrades (Dr. rer. nat.)
der
Mathematisch-Naturwissenschaftlichen Fakultät
der
Rheinischen Friedrich-Wilhelms-Universität Bonn

von
Kevin Corneilus Harrington
aus
Boston, Massachusetts, United States of America

Bonn, 2020

Dieser Forschungsbericht wurde als Dissertation von der Mathematisch-Naturwissenschaftlichen Fakultät der Universität Bonn angenommen und ist auf dem Hochschulschriftenserver der ULB Bonn \https://nbn-resolving.org/urn:nbn:de:hbz:5-61361.

1. Gutachter:	Prof. Dr. Frank Bertoldi
2. Gutachter:	Prof. Dr. Cristiano Porciani
Tag der Promotion:	18.02.2021
Erscheinungsjahr:	2021

I am truly grateful for Mary and Mike Gyra for bringing me into the world of astronomy. Their care, compassion, curiosity, grit, teaching and service will forever inspire me as a scientist, teacher and human being. Most importantly, this is for Annie, my late mother. She was a massive star with a short life-time, gone supernova. May she rest in peace and joy, shining and smiling amongst friends and the cosmic microwave background radiation.

Abstract

Star-formation processes in the early Universe have had a dramatic influence on the further development of galaxies. The peak era for stellar production occurred in early cosmic times, and most of the stars that could have formed in the Universe had already taken place during these times. The physical properties of the cold molecular gas are still poorly investigated, yet this gas serves as a primary fuel to sustain such on-going star-formation. This thesis presents detailed analyses of the turbulent molecular gas and dust in some of the most rare and extreme star-forming galaxies in the early Universe. These systems will likely become massive galaxies with more than 100 billion solar masses, and may reside in centers of local galaxy cluster environments. The Milky Way galaxy has been evolving for more than 10 billion years, with a current star-formation rate of about two solar masses per year. Dusty star-forming galaxies have extreme star formation rates, forming 100 to 1000 times the amount of stars, and existed primarily between two to four billion years after the initial conditions of the Universe. Studying such galaxies during these early cosmic times is an important way to better understand the star formation history of the Universe. It is well known that such star-forming galaxies have molecular gas mass to stellar mass fractions up to 50-80% or more. This is 5 - 10 times the amount of molecular gas available to form stars for most local star-forming galaxies. The largely unknown nature of the gas excitation conditions are due to observational limitations and the distant nature of these objects, yet radio/(sub)mm technology has been rapidly advancing the past twenty years. Some of these observational limitations were avoided in this thesis work by exploiting the natural magnification which occurs due to strong gravitational lensing. The galaxies examined in this thesis are along the line of sight with an intervening foreground galaxy, which results in this lensing effect. This effect amplifies the apparent flux density of the background, lensed galaxy, reducing telescope integration times. This thesis focuses on 24 lensed, dusty star-forming galaxies identified by the *Planck* satellite telescope, each with an inferred star formation rate of about 1000 times the Milky Way value.

Radio-to-millimeter spectroscopic observations and analyses of carbon and carbon monoxide (CO) emission lines were used to address the nature of the gas supply. The core of this thesis work includes the modelling of the gas excitation conditions using 162 CO, and 37 atomic carbon, emission lines in this sample of 24 galaxies. This is the largest CO and carbon line study of any sample of distant, star-forming galaxies, and contributes to roughly 15-20% of all such line detections published to-date. The modelling procedure follows a novel approach to simultaneously model all emission lines and the dust continuum radiation field. Overall, these *Planck*-selected galaxies are some of the most gas-rich, infrared luminous galaxies ever observed. The high values for the surface density of molecular gas mass and IR luminosity suggest that both mechanical feedback from stars, combined with the accretion of intergalactic gas, are involved in the total gas excitation. Our results are consistent with theoretical models of turbulent motions regulating the molecular gas conditions within star-forming galaxies. This thesis work therefore helps to better understand the average gas conditions for the most massive star-forming galaxies in the early Universe as they were rapidly forming.

List of publications

Throughout this Ph.D. thesis, I investigate the star-forming interstellar medium and average gas contents of some of the most infrared-bright galaxies in the early Universe. In Chapter 1.4, I summarize the methods used to select the sample of 24 dusty star-forming galaxies which serve as the focus of this dissertation. These galaxies had existed between 9-11 Gyr ago, during the peak epoch of cosmic star formation activity. In Chapter 3, I first explore the nature of the cool molecular gas and the total molecular gas mass in a pilot study using measurements of the CO(1-0) line emission for a sub-set of this sample. In Chapter 4, I present observations and modeling of the physical gas properties in all 24 galaxies using a wealth of CO and carbon emission line – together with the ancillary information of the dust spectral energy distribution. Thereafter in Chapter 5 I probe the ionized and molecular gas conditions of one galaxy in the sample which has been known to harbor both an active galactic nucleus and intense SF activity. Altogether, these research projects have resulted in three, lead author, peer-reviewed research publications. One of the three manuscripts is still in the referee process, yet is approved for publication after minor revisions.

- Berman, D., Yun, M.S., **Harrington K.C,**, et al. to be submitted to the Monthly Notices of the Royal Astronomical Society. *Author Contributions:* K.C.H. helped to establish the initial selection method which was later used to obtain a larger number of high-redshift strongly lensed star-forming galaxies. This manuscript outlines the updated selection method for the galaxy sample used in this dissertation. K.C.H. is responsible for writing parts of the manuscript (part of discussion section and sample description). Further details about this sample will be discussed in Chapter 1.4.

- Chapter 3: **Harrington, K. C**., Yun, M. S., Magnelli, B., Frayer, D. T., Karim, A., Weiss, A., Riechers, D., Jiménez-Andrade, E. F., Berman, D., Lowenthal, J., Bertoldi, F. (2018). Total molecular gas masses of *Planck* - *Herschel* selected strongly lensed hyper luminous infrared galaxies. *Monthly Notices of the Royal Astronomical Society*, 474, 3866. *Author Contributions:* K.C.H. performed the telescope observations and subsequent scientific analysis under the supervision of B.M, A.W. and F.B. K.C.H. wrote the manuscript with the aid of B.M. The other co-authors contributed with the interpretation of the results and commented on the manuscript.

- Chapter 4: **Harrington K.C,**, Weiss, A., Yun, M.S., Magnelli, B., Sharon, C., Leung, T.K., Vishwas, A., Jiménez-Andrade, E. F., Frayer, D., Liu, D., Garcia, P., Romano-Diaz, E., Frye, B., Jarugula, S., Bertoldi, F., et al. (2020). Turbulent Gas in Lensed *Planck*-selected Starbursts at $z \sim 1-3.5$, submitted to The Astrophysical Journal. *Author Contributions:* K.C.H. performed the telescope observations and subsequent scientific analysis using state-of-the-art models developed by A.W., under the supervision of B.M, A.W. and F.B. K.C.H. wrote the manuscript

with the aid of A.W. The other co-authors contributed with the interpretation of the results and commented on the manuscript.

- Chapter 5: **Harrington, K. C**, Vishwas, A., Weiss, A., Magnelli, B., Stacey, G., Yun, M.S., Leung, T.K.D., Grassitelli, L., Zajacek, M., Jiménez-Andrade, E. F., Frayer, D.T., Riechers, D., Bertoldi, F. (2019). The "Red Radio Ring": Ionised and Molecular Gas in a Starburst/Active Galactic Nucleus at $z \sim 2.55$. *Monthly Notices of the Royal Astronomical Society*, 488, 2, 1489. *Author Contributions:* K.C.H. performed the telescope observations and subsequent scientific analysis under the supervision of B.M, A.W. and F.B. K.C.H. wrote the manuscript with the aid of A.W., A.V. and B.M. The other co-authors contributed with the interpretation of the results and commented on the manuscript.

The conclusions presented in this work are complementary to results from related collaborative research projects, to which the author of this dissertation has contributed throughout the duration of this thesis work. The publications derived from these projects are listed below.

- **Harrington K.C,**, Frayer, D. and Dannerbauer, H. (2019). *Astro2020 Science White Paper: The Extended Cool Gas Reservoirs Within $z > 1$ (Proto-)Cluster Environments*. Astro2020 US Decadal Review White Paper Series. K.C.H. wrote the manuscript with the assitance of D.F. and H.D.

- Dannerbauer, H., **Harrington K.C,**, Diaz-Sanchez, A., Iglesias-Groth, S., Rebolo, R., Genova-Santos, R. T., Krips, M. (2019). Ultra-bright CO and [CI] emission in a lensed z=2.04 submillimeter galaxy with extreme molecular gas properties. *The Astronomical Journal*, 158, 1. *Author Contributions:* K.C.H. performed observations and analysis published in this manuscript. K.C.H. also wrote a significant portion of the results and discussion sections.

- Liu, D., Lang, P., Magnelli., B., Schinnerer, E., Leslie, S., Fudamoto, Y., Bondi, M., Groves, B., Jiménez-Andrade, E. F., **Harrington, K. C**, Karim, A., Oesch, P., Sargent, M., Vardoulaki, E. et al. (2019). Auto-mining the ALMA Archive in the COSMOS Field (A^3COSMOS): I. Robust ALMA Continuum Photometry Catalogs and Stellar Mass and Star Formation Properties for 700+ Galaxies at Redshift 0.5–6. *The Astrophysical Journal Supplement Series*, 244, 2. *Author Contributions:* K.C.H. contributed edits to improve the manuscript and had in-depth discussions of the results with the lead-author.

- Jiménez-Andrade, E. F., Magnelli, B., Karim, A., Zamorani, G., Bondi, M., Schinnerer, E., Sargent, M., Novak, M., Lang, P., Bertoldi, F., Vardoulaki, E., Romano-Díaz, E., Toft, S., Smolčić, V., **Harrington, K. C**, Leslie, S., Delhaize, J., Liu, D., Karoumpis, C., Kartaltepe, J., Koekemoer, A.M. (2019). Radio continuum size evolution of star-forming galaxies over $0.35 < z < 2.25$. *Astronomy & Astrophysics*, 625, A114. *Author Contributions:* K.C.H. contributed edits to improve the manuscript and had in-depth discussions of the results with the

lead-author.

- Jiménez-Andrade, E. F., Magnelli, B., Karim, A., Jones, G. C., Carilli, C. L., Romano-Díaz, E., Gómez-Guijarro, C., Toft, S., Bertoldi, F., Riechers, D. A., Schinnerer, E., Sargent, M., Michałowski, M. J., Fraternali, F., Staguhn, J. G., Smolčić, V., Aravena, M., **Harrington, K. C.**, Sheth, K., Capak, P. L., Koekemoer, A. M., van Kampen, E., Swinbank, M., Zirm, A., Magdis, G. E., Navarrete, F. (2018). Molecular gas in AzTEC/C159: a star-forming disk galaxy 1.3 Gyr after the Big Bang. *Astronomy & Astrophysics*, 615, A25. *Author Contributions:* K.C.H. contributed edits to improve the manuscript and had in-depth discussions of the results with the lead-author.

- Jiménez-Andrade, E. F., Zavala, J. A., Magnelli, B., Casey, C. M.,Liu, D., Romano-Díaz, E., Schinnerer, E., **Harrington, K. C.**, Aretxaga, I., Karim, A., Staguhn, J., Burnham, A. D., Montaña, A., Smolcic, V., Yun, M., Bertoldi, F., Hughes, D. (2020). The Redshift and Star Formation Mode of AzTEC2: A Pair of Massive Galaxies at z = 4.63. *The Astrophysical Journal*, 890, 2. *Author Contributions:* K.C.H. contributed edits to improve the manuscript and had in-depth discussions of the results with the lead-author.

In summary, the overall scientific production consists of ten peer-reviewed articles, including three first-authored and one second-authored manuscript.

Contents

CHAPTER 1

Understanding Galaxy Evolution and the Gas which Seeds Star Formation

Radiation from gas and dust can be thought of as a concert within the interstellar medium. Continuum radiation from infrared-emitting dust particles can be likened to the rhythm section of a band. Just as the rhythm guitar continually plays chords (multiple notes simultaneously), continuum radiation is emission across a wide range of frequencies. Spectral lines from atoms and molecules, however, are like the lead guitar playing the solo parts. Together they trace the personalities and structure of star-formation processes as they broadcast their signal and pervade the galaxy and beyond.

The central role of this thesis is to better understand the physical properties of the ingredients for star-formation in distant, star-forming galaxies: the molecular and atomic gas within the interstellar medium. A first thought may lead to the question: "Why are stars so important?" We have admired them for ages. Is it that we may value human life, and that somehow we have always known that without stars we would not be here? Previously, our ancestors knew nothing about the chemical composition of stars and the material between them, yet as before we still feel a sense of home, of a beginning, of an origin, when looking up into the sky. Now we better understand that we are looking into where we once came from, yet there is still much to unravel about our past.

I will first explore the cosmological landscape which sets the context for understanding the extragalactic observations and analyses presented in this thesis. Afterwards I will move towards describing both galaxy and large-scale structure formation. After discussing the nature of galaxies and their stellar mass assembly across cosmic time, I will briefly describe the general conditions of the turbulent, star-forming material in the interstellar medium (ISM). In the next section I will focus on the characteristics of distant, dusty star-forming galaxies – the galaxy population which defines the sample of galaxies in this thesis. Afterwards, I will then focus on the current state-of-the-art understanding of the cold gas reservoirs in the star-forming galaxies of the early Universe. I will italicize points most relevant to this work throughout this introduction.

1.1 A Universal context: the observable cosmos

1.1.1 Rewinding our expanding sky to its thermal origins

The present Universe contains information about how everything is (has been) interconnected, since the initial conditions. Everything is above absolute zero on the Kelvin scale of temperature, and thus has energy. There is also a relatively uniform background temperature of the space surrounding us. In fact, it was in 1965 when the Cosmic Microwave Background (CMB) radiation was discovered, as Penzias and Wilson could not subtract what they believed to be the antenna radiation noise they were constantly receiving (Penzias & Wilson, 1965; Gawiser & Silk, 2000; Hu & Dodelson, 2002) – leading to the 1978 Nobel Prize in Physics. Since then, many people may take for granted that we exist in this cosmic oven – the remnants of the initial conditions of the observable Universe.

A series of space-based telescopes have sequentially chipped away at decomposing this background signal into all of its physical properties (*COBE,* Boggess et al., 1992; Melchiorri et al., 1981)[1], (*WMAP,* Bennett et al., 2003; Hinshaw et al., 2009)[2] where most recently the *Planck* telescope measurements have analyzed the entire CMB radiation for minute anisotropies across the sky (i.e. small differences in global quantities such as temperature with varying spatial direction). The temperature of the CMB radiation measured by the Planck satellite is only 2.73 K above absolute zero, with $\Delta T/T \sim 10^{-5}$ (Planck Collaboration et al., 2015). These small differences in temperature that we observe currently reflect initial inhomegeneities in the early Universe, which ultimately gave rise to distribution of galaxies we see today.

It has also now been observed that we live in an *accelerated*, expanding Universe (Riess et al., 1998, 2011). Therefore, if we reverse our observational vantage point, and rewind our observed sky background temperature towards our cosmic origins, the CMB radiation temperature steadily increases. Everything also becomes physically closer. In the current-day Universe, objects recede away from one another at faster and faster rates the further the distances between them become.

Given the constraints we have on an expanding Universe, there had to have been a point in time where/when the density and temperature of the Universe experienced the most extreme initial conditions (commonly referred to as the 'Big Bang'). Actually, since no place is particularly different from one another on the largest scales of the observable cosmos, in every direction, we are forced to reconcile that the 'Big Bang' began nowhere and at no time.

Parameterizing the expanding Universe

Less than 100 years ago, in 1922, Einstein's field equations, which describe how a source of energy (or mass) curves space-time, were solved in the Friedmann and Lemaitre cosmological framework (Friedmann, 1922). This framework describes the dynamical evolution of a Universe which is homogeneous and isotropic. Thereafter, the description of the observable cosmos had a language, and theoretical predictions of a Universe with any arbitrary geometry could be empirically tested.

[1] Cosmic Background Explorer.
[2] Wilkinson Microwave Anisotropy Probe.

Meanwhile in the 1920's, Edwin Hubble (Hubble, 1926, 1929) had revolutionized the picture of what was then a static Universe. In observing stars which have known luminosity variations, corresponding to pulsation periods of days (so-called Cepheid variable stars), he was able to reliably trace the distances to well-studied objects. With increasing distance, there was a linear increase in the measured recessional velocity of the system. This relationship, now known as the Hubble's Law, relates the recessional velocity, V, and source distance, D_s, via the Hubble Constant, H_0 as:

$$V = H_0 D_s, \tag{1.1}$$

with $H_0 \approx 70$ km s^{-1} per Mpc (1 pc = 3.26 light yr $\sim 3 \times 10^{13}$ km).

The current value of the Hubble constant is, to this day, still under debate. However, there is indisputable evidence which suggests the Universe is expanding at an accelerated, non-linear, rate. Up until the 1990's it was not certain that there was anything other than the energy content from electromagnetic radiation and matter, and that the latter dominated how the Universe evolved at later cosmic times. Observations by Edwin Hubble already indicated that a constant recession velocity per space-time volume forces us to accept that, as something is farther away from us, it is moving faster away. The 1930's marked a shift towards a serious study of an expanding Universe, as opposed to the previously accepted view of a static Universe. Therefore, the constant which describes the current rate of expansion, i.e. H_0, will change depending on the location in space-time. Efforts were soon made to formalize the Friedmann equation, which simply describes the dynamics of the Universe in terms of a gravitationally bound system with density and pressure, and energy conservation. Solving Friedmann's equation for a homogenous and isotropic Universe leads to an expression of expansion involving a mathematical constant of integration. This constant of integration is related to the geometric properties of the Universe; i.e. the curvature. The mathematical metric which agrees with the assumption of the cosmological principle, which states that there is large-scale homogeneity and isotropy and we are in no unique or special place, is often called the Robertson-Walker metric (Robertson, 1929).

Light has a fixed speed, which has numerous implications when considering astronomical phenomena. The inverse of time is frequency, and the velocity V of a light-emitting object can be given by the speed of light, c, and the frequency of electromagnetic radiation, ν, and / or wavelength, λ, as:

$$\Delta V/c = \delta\lambda/\lambda = \nu/\delta\nu. \tag{1.2}$$

The Doppler effect describes the shift from a reference-frame (a.k.a rest-frame) wavelength and / or frequency, and the actual wavelength / frequency measured from a source moving with a radial velocity. The respective shift is thus termed the redshift,

$$z = (\lambda - \lambda_0)/\lambda_0, \tag{1.3}$$

where a positive redshift corresponds to a source moving away from Earth.

When using spectroscopy to study very distant objects at cosmological distances, a cosmological redshift needs to be considered. The elapsed time due to the expansion and evolution of space itself is, in some sense, the stretching of time as a photon traverses the Universe. Therefore, the redshifted

photons can be determined with respect to their emitted and observed frequencies, such that:

$$(1 + z) = \nu_{\rm emitted}/\nu_{\rm observed} = 1/a(t). \tag{1.4}$$

Using this known effect of cosmological redshift, the Hubble constant was determined explicitly in 1998 (Riess et al., 1998). When a star that is above 8 $M_\odot$, and below ~50 $M_\odot$, reaches the end of its lifetime of burning hydrogen into helium, it has enough gravitational potential to overcome radiation pressure support and effectively explode in what is called a supernova. A particular type, 'SN-Ia', have a reliable relationship between the measured width of the light intensity over time (so-called light-curve) and their peak output luminosity. They are referred to as standard candles, as they will predictably become dimmer as they are observed at greater and greater distances.

The observed flux S, from a source with a known intrinsc luminosity, L, depends on the luminosity distance, $D_{\rm L}$, as:

$$S = \frac{L}{4\pi D_{\rm L}^2}. \tag{1.5}$$

These SN-Ia were used to measure the distances to galaxies out to considerable look-back times of approximately 7 Gyr (roughly half the age of the Universe). These findings, reported only 22 years ago, led to the 2012 Nobel Prize in Physics and have since re-framed our perception of the Universe. Thereafter, it has been accepted, and further confirmed, that the Universe is not only expanding, as Hubble proclaimed in the 1920's, but currently expanding at an accelerated rate. This implies that the attractive force of gravity due to the presence of matter, which shapes how the curvature of space-time will respond, is not the only energetic content implicated in the overall expansion of our observable Universe.

Co-moving coordinates are used to reflect the fact that there was a respective co-moving position and physical scale at each stage of cosmic evolution. Co-moving coordinates are determined by a scale factor which effectively scales the coordinate system. A system evolving in co-moving coordinates grows with the expanding Universe and is said to follow the smooth distribution of velocity according to the Hubble relation. A source that is radially expanding along a trajectory because of a cosmic scale factor, $a(t)$ can be defined by 1.) the source position at a current time, 2.) the co-moving position, x, and 3.) the new radial position as:

$$r(t) = a(t)x \tag{1.6}$$

This cosmic scale factor changes with time only, and corresponds to the Hubble constant at any given epoch.

This thesis work consists of the use of spectroscopy in the observed cm-to-mm wavelengths to finely measure the exact observed frequencies of line radiation from distant cool gas reservoirs, since their electromagnetic signals have been shifted from their quantum mechanically predicted rest-frequency. This in turn gives us the redshift and the cosmic epoch at which these galaxies reside.

Main epochs of the Universe

The CMB radiation, which originated at $z \sim 1100$, is the remnant of the epoch of last scattering, i.e. when photons were no longer scattered within a baryon-photon fluid. It is the recombination of

electrons with protons, forming the first hydrogen atoms, which later became more favorable as the Universe cooled. Meanwhile, the mean free path of photons was sufficiently large to allow light to freely escape the confines of the photon-baryon fluid [3]. Radiation density dominates at early times, when 'Big Bang' nucleosynthesis took place. During this brief period of time, the other energy constituents had negligible effects. The radiation density parameter scales with $1/a(t)^4$. With such a strong inverse dependence with time, as the Universe cooled, matter began to more prominently shape in the total mass-energy density contribution and the way in which the Universe expanded and evolved. Initially, small fluctuations in temperature during recombination provided the initial instabilities of the matter distribution. Since gravity is an attractive force, these instabilities were strengthened over time to form structure on larger scales. The density of matter scales as $1/a(t)^3$, and thus lasted longer as the predominant energy constituent which determined the cosmological evolution. The vacuum energy density is constant, and therefore becomes important in determining the evolutionary state of the Universe at later epochs when the influence of the relative density of matter decreases. The Universe is essentially decelerating in its expansion when the matter energy density is dominant, however the effect of the non-zero cosmological constant becomes dominant at $z \sim 0.4$ (about 4 Gyr ago), as it influences the evolution of the Universe more strongly than the gravitational and electromagnetic effects from the cosmic density of matter and radiation, respectively.

The galaxies which form the basis of this thesis work therefore reside during a period in cosmic history when matter dominated the evolution of the Universe. These massive galaxies are likely responsible for shaping the distribution of matter in the early Universe, and are believed to seed the massive clusters of galaxies which form the junction points for the observed large-scale structure of galaxies throughout the local Universe.

1.1.2 The evolution of galaxies

The ΛCDM model is currently the accepted framework for describing the contents and evolution of the Universe. This framework considers a Universe in which galaxy evolution (e.g. Shapley, 2011; Silk & Mamon, 2012) takes place within the seeds of dark matter halos[4]. The discovery of a dark matter content within the Universe was hinted at as early as 1933 when Zwicky (Zwicky, 1933) had spectroscopically measured galaxies in the Coma cluster which exceeded the escape velocity, $V_{\rm esc}$, defined as the speed at which the galaxies have exceeded the force of gravity determined by the sum of all stellar mass, $M_\star$, in the galactic cluster for the observed effective radius, R:

$$V_{\rm esc} = \sqrt{(2GM_\star)/R}, \tag{1.7}$$

where G is the gravitational constant.

Therefore since the object is gravitationally bound, there indicates the presence of additional mass which must account for the higher than expected velocity dispersion. The existence of an extended component of dark matter was also put forth by (Bosma, 1978), using measurements of the

[3] $l = (\sigma \times n)^{-1}$; l [cm^{-2}] is the mean free path, considering n collision partners and σ the cross-sectional area for the collision.

[4] Halos can be classified as a dynamically bound system in virial equilibrium; i.e. the kinetic energy is equal to half of the potential energy of the system.

atomic hydrogen column density in spiral systems, and later when Rubin et al. (1980) made detailed observations of spiral galaxies and realized there also appeared to exist a dark matter (non-interacting with light). It appeared the dark matter component had been substantially influencing the stable circular velocities of stars out to extreme radii. The Keplerian disk rotation curve for an enclosed mass, $M(\leq R)$, at a given radius, R, is given by the rotation velocity,

$$V(R) = (GM(\leq R)/R)^{1/2}, \tag{1.8}$$

which tapers off at high radii. This dark matter is essentially a blanket around galaxies, flattening the rotation curve near its maximum stellar velocities.

Dark matter halos are believed to have evolved from the primordial dark matter density perturbations soon after the hot, dense state of the Big Bang. Therefore the distribution of dark matter heavily influences the baryonic matter[5] through gravitational forces. Once star-formation processes occur, the evolution of baryonic matter is strongly subject to hydrodynamic and radiative feedback effects (White & Rees, 1978). It is worth noting that there is a so-called *biasing effect* (BBKS; Bardeen et al., 1986), in which baryonic matter can also have a gravitational influence (although relatively small) on dark matter.

Not every galaxy is the same in its morphological nature and detailed composition. There are both spiral disks and irregular mergers with tidal tails (Poggianti et al., 2017), as well as elliptical galaxies (Sandage, 1970). The formation mechanisms of these systems are an open question as we continue to gather more and more information about the star-formation activity, physical gas/dust conditions and kinematic activity in early Universe. Local spiral galaxies exhibit bluer colors due to the presence of young blue stellar populations, whereas massive elliptical galaxies often have red colors due to the older, red stellar populations. These commonly lack any indication of ongoing star-formation, and can often be associated with a strong radio emitting active galactic nucleus (AGN) jet (Fanaroff & Riley, 1974).

Star formation (SF) takes place largely at the interface of spiral arms for spiral galaxies, and they also have increased gas masses compared to ellipticals. Stars appear to follow mostly circular orbits in spiral galaxies, compared to seemingly random motion within elliptical galaxies. Such random motion is still difficult to explain in galaxy evolution models, and may be linked to vigorous major gas-rich mergers which had random turbulent motion and massive gas reservoirs fueling the central regions of coalescence. In Fig. 1.1, Hopkins et al. (2008) describe the process of how accumulation of gas, after two merging cores of baryonic matter coaelesce, feeds the supermassive black hole accretion and further increases the AGN signature of the system, while the subsequent interplay with stellar feedback and a dearth of molecular star-forming material can later result in an elliptical galaxy from a major-gas-rich merger (Kim et al., 2009; Teyssier et al., 2010; Hayward et al., 2013) – a phenomena first proposed by (Sanders et al., 1988). Eventually, throughout various major and minor mergers and gas accretion, galaxies evolved to form the large-scale structure in the nearby Universe, with local ($z << 0.5$) galaxy clusters containing more than 50 galaxies, spanning many 10s of Mpc in linear size, with smaller groups of galaxies confined to a physical radius of about 1 Mpc.

Both simulations and observational data consistently agree upon the general process of dark matter

[5] Baryonic matter technically includes some short life-time quarks by definition, however here we will only refer to protons, neutrons and electrons. The latter is negligible in terms of mass contribution.

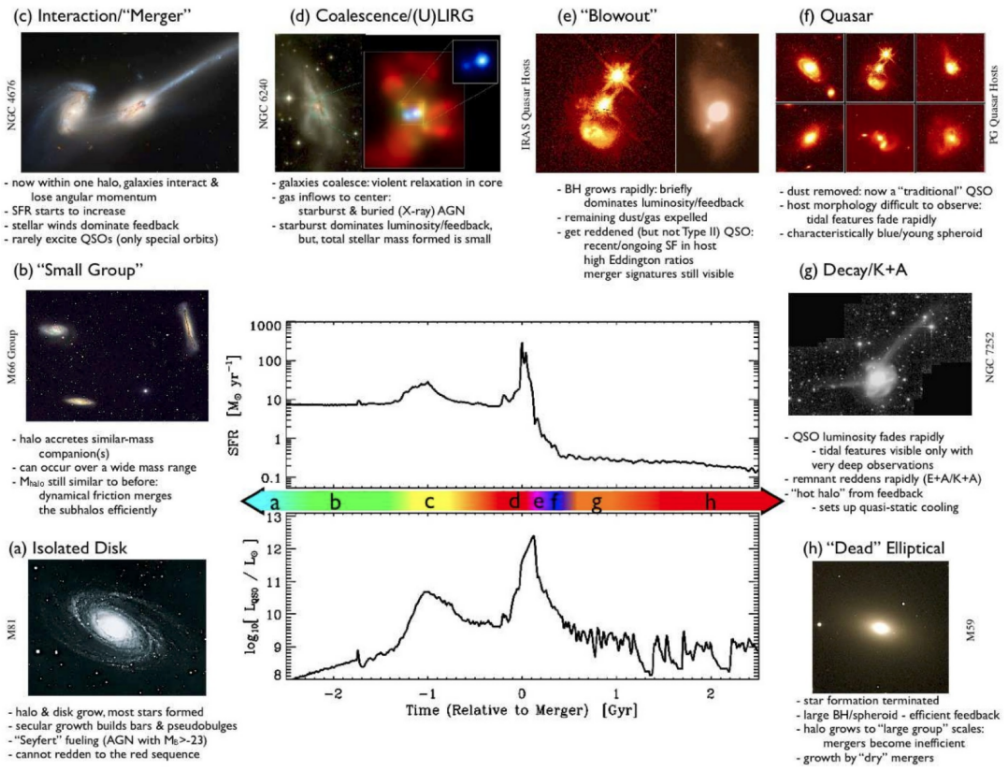

Figure 1.1: Schematic outline of the typical evolution of a galaxy as it experiences various growth phases, including merger activity and the quenching of star-formation triggered by supermassive black hole growth and feedback. This schematic was originally published by Hopkins et al. (2008), and later reproduced in Casey et al. (2014).

halos merging hierarchically as the Universe evolves in time. It is therefore a primary objective to better understand the process of assembling baryonic content and forming large associations of the galactic groups, clusters, filaments and voids seen in the local Universe. Key developments in cosmological hydrodynamic simulations are still needed, including a consistent description of the formation of stars from cold gas, and their energetic feedback into their surroundings (e.g. stellar winds from Wolf-Rayet and massive main-sequence stars) – including both SN feedback and feedback from the accretion of matter onto a supermassive black hole (Navarro & Steinmetz, 2000; Kereš et al., 2005; Governato et al., 2010; Guedes et al., 2011; Hopkins et al., 2012).

1.1.3 The production of stellar mass across cosmic time

In the Λ-CDM (Cold Dark Matter) hierarchical dark matter model, one observational goal is to measure the build-up of the baryonic content within galactic systems across cosmic time. This, therefore includes a general understanding of the life-cycle of stars and the necessary ingredients responsible for the formation of stellar mass. Key local constraints suggest that SF is, in general, inefficient, while 5% of all baryonic matter appears to reside in stellar mass (Fukugita & Peebles, 2004). In general, one can consider three major epochs in galaxy formation and evolution.

The epoch of reionization began as soon as 100-800 Myr after the Big Bang, between $z \sim 11-6$. It is the first major epoch in the build-up of stellar mass through increased star-formation activity (Fan et al., 2006; Bouwens et al., 2012; Finkelstein et al., 2012; Coe et al., 2013). As dark matter halos grew in size to about 10^{8-9} $M_{\odot}$; (Spergel et al., 2007), the relative baryonic content increased sufficiently to form the first proto-galaxies from the first stellar populations. The ionizing radiation from the first stars effectively radiates freely until absorbed into the neutral circumgalactic medium (CGM) or intergalactic medium (IGM). The *HST* satellite offered deep imaging to select a sample of early star-forming systems at $z > 6$, and now many have confirmed redshifts and tight constraints out to the epoch of reionization (McLure et al., 2015; Bradley et al., 2014; Finkelstein et al., 2015; Stark, 2016; Livermore et al., 2017), to within 1 Gyr of the Big Bang. Observations and numerical studies agree in the distribution of galaxies based on structure formation via instabilities in gravity (Spergel et al., 2007; Coe et al., 2013). The general picture is that low-mass components collapse and will merge hierarchically to form the larger extragalactic systems throughout the stages of galaxy evolution (Peebles, 1982; Blumenthal et al., 1984).

After the epoch of reionization there was a rapid development in star-formation and galaxy evolution. The IRAS and COBE-FIRAS space satellite maps first revealed the all-sky far-Infrared (IR) background, which led to our current understanding of the SF history of the Universe. This FIR background complemented what had previously been observed, i.e. the products of star-formation: the stars themselves and ionized gas, usually observed in optical and near-IR wavelengths. Most surprisingly the cosmic background of optical/near-IR light is of comparable energy density as the far-IR background (Madau & Dickinson, 2014).

The cosmic far-IR background has since been resolved into individual sources (Berta et al., 2011; Dole et al., 2004; Béthermin et al., 2010a; Kawara et al., 2004; Béthermin et al., 2010b; Rujopakarn et al., 2010; Clements et al., 2010; Scott et al., 2012a, 2010; Hatsukade et al., 2011; Austermann et al., 2010; Aretxaga et al., 2011) and has progressed our understanding of galaxy evolution in the context of the historic peak in the co-moving cosmic rate of star-formation activity. At $z = 1-3$, such galaxies were closer to one another by a factor of three. This redshift range corresponds to the second major epoch of galaxy assembly, and is perhaps the most significant in terms of the climactic formation of stars in galaxies. It is of vital importance to understand this epoch because about half the stars of the stellar populations in nearby galaxies/large-scale structure had formed (Reddy et al., 2008; Marchesini et al., 2009). Still only a handful of dusty star-forming galaxies have spectroscopically confirmed redshifts between $z = 4-6$. Worth noting, only 1% of the stellar mass density in the Universe having formed at $z > 6$, while the co-moving SFR density at $z \sim 7$ was roughly the value of today (Madau & Dickinson, 2014). These high-z galaxies, particularly at $z \sim 1-3$, are the main contributors to the co-moving cosmic SFR density during the second epoch of galaxy assembly (Magnelli et al., 2011; Murphy et al., 2011). For comparison, local star-forming galaxies with such SFR values are less than a few percent of the local IR luminosity background (Sargent et al., 2012). The first luminous IRAS selected systems in the local Universe were classified by their high IR luminosity, i.e. Luminous IR Galaxies (LIRGs) have $L_{\rm IR} > 10^{11}$ $L_{\odot}$. Ultra-LIRGs (ULIRGs) are local starburst systems with an order of magnitude higher IR luminosity by definition, with an integrated dust SED (8 - 1000 μm) equal to or greater than 10^{12} $L_{\odot}$ (Lemke et al., 1996; de Jong et al., 1984; Veilleux et al., 2002; Sanders & Mirabel, 1996). Significant gas column densities enriched with high dust contents, make ULIRGs highly efficient in obscuring the ongoing star-formation activity (Downes & Solomon, 1998),

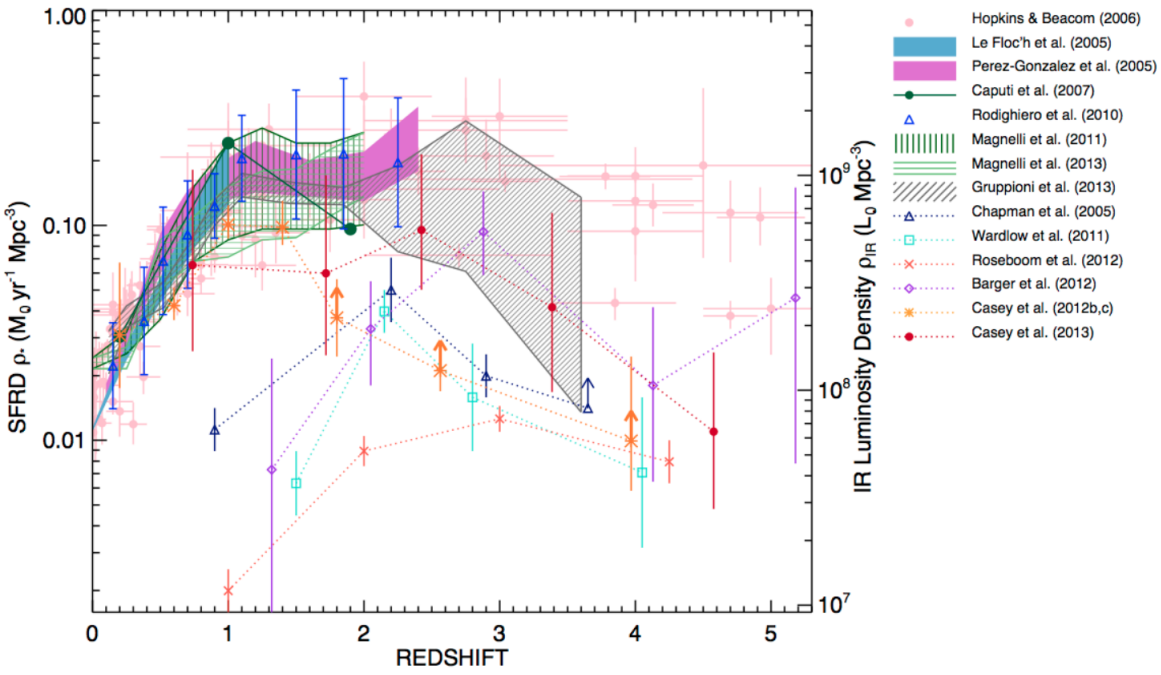

Figure 1.2: The contribution of different high redshift galaxy populations to the cosmic SFR density. This SFRD plot shows the contributions from total surveyed infrared populations, as published in Casey et al. (2014).

which may likely be true as well for the dusty star-forming galaxies in the early Universe.

Understanding the actual physical properties of dusty, gas-rich galaxies in the second major epoch of galaxy evolution is at the heart of this thesis work, as the sample of galaxies are selected to be at $z \sim 1-3$. *The typical molecular gas to stellar mass fractions of such galaxies may be up to 80% (Carilli & Walter, 2013; Casey et al., 2014; Tacconi et al., 2018).*

After the second epoch there was more than an order of magnitude decline in the inferred co-moving star-formation rate (SFR) density over the past 7 Gyr (Lilly et al., 1996; Madau et al., 1996). The third major epoch of the cosmic history of SF is characterized by less frequent star-forming episodes and more quiescent galaxy evolution, inferred by the dramatic decline in the radio, optical and IR luminosity functions from $z \sim 1$ to today. The overall star-formation history of the Universe is summarized in Fig. 1.2 (Casey et al., 2014).

Studies of these three cosmic epochs of SF have revealed an empirical linear relation between the inferred SFR in a galaxy versus the stellar mass. This is now termed the 'main-sequence of star-forming galaxies'. Studies of this low-scatter relationship (dispersion 0.3 dex) of SFR versus stellar mass, $M_\star$, reveal that the majority of galaxies across cosmic time follow this relation. For increasing redshift, the normalization increases to higher SFRs (Noeske et al., 2007; Elbaz et al., 2011; Rodighiero et al., 2011).

Recent studies (Jiménez-Andrade et al., 2019a; Elbaz et al., 2018a) indicate that the *SFR surface density*, rather than the globally averaged SFR, is a more telling indicator of the, main-sequence versus

starburst, phase of galaxy evolution. It appears most galaxies undergo some sort of starburst period (for a few 10s to 100 Myr), primarily driven by violent disk instabilities and / or galaxy mergers. Star-forming galaxies at $z \sim 1-3$ also have abundant shipments of cool molecular gas from the intergalactic medium, which likely sustains the on-going star-formation while on the main-sequence. Although it is not clear whether or not an AGN is a primary factor in preventing the ongoing production of stars, the black hole growth and star-formation processes are linked throughout cosmic time (Boyle & Terlevich, 1998; Silverman et al., 2008). In some cases a strong quasar mode may considerably disrupt the thermodynamics and evolution of matter in a star-forming disk (Hopkins & Quataert, 2010). Once the molecular gas supply has reduced, by either expelling gas in a galactic outflow (Veilleux et al., 2002), having the gas stripped via a merger and / or depleting the molecular reservoirs to build up more stellar mass, a galaxy will likely evolve into one of the locally observed red, massive, passive star-forming galaxies ($M_\star > 10^{10.5-11.5}$ $M_\odot$[6]), as shown in the schematic in Fig 1.1 (Hopkins et al., 2008).

1.2 The interstellar medium of star-forming galaxies

This thesis involves studying the emission line properties of highly supersonic turbulent gas in star-forming galaxies in the early Universe. In the following, I will outline some important considerations regarding the overall processes and time-scales of star-formation, gathered from theoretical work and conclusions based on local observations within the Milky Way and nearby star-forming galaxies.

1.2.1 Turbulent gas conditions

The role of interstellar turbulence in the process of SF has been long considered an important subject, dating back to the 1950's. A general picture of the ISM has been emerging, described as the result of hierarchical cloud structures exposed to a series of shock waves from ambient supersonic turbulence, in addition to large-scale energy input from Galactic motions (von Weizsäcker, 1951; von Hoerner, 1951; Chandrasekhar, 1951; Fleck, 1981). The Milky Way consists of many Giant molecular cloud complexes (GMCs), which are the result of fragmentary collapse into molecular structures of a few pc to 100 pc in size, typically $\sim$ 50 pc (Lada et al., 2010). For star-forming galaxies across cosmic time, it is widely accepted that although atomic hydrogen gas is needed to form H_2, it is H_2 which forms the seeds of dense clouds in the cool, neutral ISM. GMCs have therefore been the best means to study ongoing star-formation locally (Hollenbach & Tielens, 1997) within the ISM of the Milky Way and other nearby galaxies, for which telescopes can spatially resolve GMC structures.

Observations have shown that galaxies can have turbulent properties on kpc scales. The large-scale turbulent energy dissipates as the turbulent power decreases as the energy cascades down to the smaller cloud scales according to the Kolmogorov energy spectrum (Kolmogorov, 1941; Wilson et al., 1959). The compressible[7] nature of interstellar turbulence is a key aspect in the behavior of such cloud structures (Elmegreen, 1991). Additionally, it is important to study the turbulent energy of a high-z

[6] $1\ M_\odot = \sim 2 \times 10^{30}$ kg

[7] Compressible here refers to possible energy transfer between kinetic and thermal modes (Elmegreen & Scalo, 2004).

star-forming galaxy, as recent theoretical and observational work has revealed that there may be a significant role of turbulence in regulating SF and influencing the chemical enrichment of the ISM (see e.g. Elmegreen & Scalo, 2004; Scalo & Elmegreen, 2004, and references therein).

Turbulence-driven gas density probability distribution functions (PDFs) are determined by a characteristic width set by the supersonic velocity dispersion, centered at a mean gas density. It is well-described as a log-normal distribution (Krumholz et al., 2009b, 2012; Hopkins & Quataert, 2010; Hopkins et al., 2012; Ginsburg et al., 2013). The physical reasoning for such a distribution can be better understood by considering all of the random cancellations of shocks and the compressive rarefactions which multiply and divide the density by the Mach number squared, M^2, respectively (Vazquez-Semadeni et al., 1996). The Mach number is an expression of the speed of a flowing mass of particles with respect to the sound speed of the medium. The Mach number can be expressed in terms of the turbulent velocity, ΔV [km/s], and sound speed c_s,

$$M_{\rm Mach} = \Delta V / c_s \propto \frac{\Delta V}{\sqrt{(k_B T_{\rm kin})/2m_H}}, \tag{1.9}$$

where k_B is the Boltzmann constant, and $T_{\rm kin}$ is the gas kinetic temperature. The speed of sound is calculated in the form, $c_s \propto \sqrt{p/\rho}$, which can be rewritten, using the ideal gas law relation, $pV = nRT$, as $c_s \propto \sqrt{(k_B T_{\rm kin})/m_H}$. The value of $T_{\rm kin}$ is determined by the kinetic theory of gases, which states that particles of mass, m, will have a probability distribution determined by a Maxwell-Boltzmann distribution. This function, f_v, can be expressed in terms of particle speed, i.e. $v = \sqrt{v_x^2 + v_y^2 + v_z^2}$. The Maxwellian distribution expresses the particle speed probability distribution as:

$$f_v = \sqrt{2/\pi}(m/k_B T_{\rm kin})^{3/2} v^2 \times e^{-0.5 \frac{mv^2}{k_B T_{\rm kin}}}. \tag{1.10}$$

The ratio in the exponential term is that of kinetic energy per unit $k_B T_{\rm kin}$. For a given temperature bath in thermal equilibrium with the system of particles, a statistical ensemble of possible energy states in equilibrium is described as one in which each state has a probability to have a given energy proportional to $e^{\Delta E/(k_B T_{\rm kin})}$.

The physical gas properties and kinematic behavior of the gas are also linked to the initial mass function (IMF) for a star-forming environment. The IMF describes the number distribution of stars, with a certain mass, which are present at the birth of a star-forming environment. The IMF is a key indicator for describing the initial conditions and distribution of stars *before* stellar evolution occurs, and has been extensively reviewed (Bastian et al., 2010; Kroupa et al., 2013; Offner et al., 2014). In general, the IMF is responsible for shaping the ratio of the hottest, and most luminous, stars, to the fainter, less-massive stars – the latter usually represent most of the stellar mass in a galaxy (Madau & Dickinson, 2014, and references therein). Although the IMF is not directly measured in any extragalactic observation, the nature of the IMF can be better understood for high-z star-forming galaxies by comparing their turbulent gas properties to local galaxies and theoretical models. The shape of the IMF out to higher masses may vary depending on the physical conditions of the ISM, in particular the turbulent gas motions (Bastian et al., 2010; Kroupa et al., 2013; Offner et al., 2014). Many theoretical models even suggest that the IMF may be slightly different in the star-forming regions of high-z dusty galaxies (Baugh et al., 2005b). In the early Universe, it is believed that the atomic and

molecular gas of the ISM may be thoroughly mixed (co-spatial) in the active star-forming galaxies, with cloud structures on 100s of pc to kpc scales (Swinbank et al., 2015). The turbulent gas properties at the galactic scale, in the most extreme star-forming galaxies, may help explain the nature of these violent episodes of stellar mass assembly at high-z.

This thesis aims to determine the average global properties of the turbulent molecular and atomic gas in some of the most extreme dusty star-forming galaxies, in order to quantify the physical conditions on a spatially unresolved galactic scale. This pivotal step is required, as the insight gained from determining the global properties will be used in future follow-up research to measure the spatially resolved (sub)-kpc gas properties.

1.2.2 Properties of local star-forming galaxies

The spectral energy distribution (SED) of star-forming galaxies can provide a useful tool to characterize a star-forming galaxy. This requires observations across the vast range of the electromagnetic spectrum to unveil a plethora of diagnostics. In general, stars form from gas, therefore it is important to derive both the SFR and the physical gas properties of a star-forming galaxy.

Since the star formation rate (SFR) and the density of gas can be strongly related with one another, i.e. the so-called Schmidt relation (Schmidt, 1959), it is important to use a variety of tools to infer the SFR and density (and other physical gas properties). This Schmidt relation was later reviewed by Kennicutt (1998) and more recently in Kennicutt & Evans (2012), and has been at the forefront of studying the star-formation processes as stars in local star-forming regions in the Milky Way and in local star-forming galaxies. Specifically, the Schmidt-relation is characterized by a log-linear relation between SFR surface density, and reflects an average over 100s of pc: $\Sigma(SFR) \propto \Sigma_{gas}^{n}$, where the power law index, $n \sim 1.4$. The relation between the SFR and the gas density may vary within regions of extremely high (or low) molecular gas mass surface densities, of the order of $> 100 \mathrm{M}_{\odot}\ \mathrm{pc}^{-2}$ ($< 1 \mathrm{M}_{\odot}\ \mathrm{pc}^{-2}$). Local and theoretical studies have extensively explored these relations (Krumholz et al., 2007; Bigiel et al., 2008; Leroy et al., 2007; Greve et al., 2005; Bouché et al., 2007), and the value of n may increase to $n = 2$ in extreme feedback-driven, turbulent regions (Ostriker & Shetty, 2011; Faucher-Giguère et al., 2013; McKee & Ostriker, 2007).

The SFR of a star-forming galaxy can be determined from a variety of methods. Local galaxies which are not heavily dust-obscured may have detectable far-UV emission exposing the radiation from newly formed stellar associations. The SFR can be inferred from a calibration between the far-UV emission and theoretical models Kennicutt & Evans (2012). The far-UV observations offer a direct measurement of the ongoing star-formation, and together with optical data can derive SFRs corrected by dust extinction (Calzetti et al., 1994, 2000). Such short-wavelength measurements are sensitive to the lifetimes of massive stars (a few to tens of Myr). Kennicutt & Evans (2012) note the specific luminosity of the Hα line emission can also be used to infer a SFR. Since this line traces the ionized regions surrounding young massive stars, it can also trace the ongoing SFR on the time-scales of a few to tens of Myr.

*In this thesis I primarily focus on the IR based SFR, derived from the integrated 8-1000μ*m *luminosity*, which was initially determined as the integration range used to infer the SFR in Kennicutt & Evans

(2012). In particular, Kennicutt & Evans (2012) consider radiative transfer models for continuous starbursts, with a range of 10-100 Myr bursts, and a Salpeter IMF (Salpeter, 1955; Leitherer & Heckman, 1995). The resulting calibration to SFR for the derived, integrated IR luminosity is:

$$SFR = 4.5 \times 10^{-44} L_{\mathrm{IR\ [erg/s]}} = 1.7 \times 10^{-10} L_{\mathrm{IR}[L_\odot]}. \tag{1.11}$$

Note, the integrated 8-1000μm dust SED is considered here to be the total L_{IR}. Typically, only a portion of the dust SED is sampled for high-z galaxies due to observational limitations, and it is considered that the rest-frame far-IR (~40-120μm) may also be a reliable means of characterizing dusty star-formation activity (Helou et al., 1985). For reference, the Milky Way has an estimated SFR of 2 $\mathrm{M_\odot\ yr^{-1}}$ (Robitaille & Whitney, 2010; Chomiuk & Povich, 2011). Since it is also common for other quiescent star-forming galaxies ($L_{\mathrm{IR}} \sim 10^{10}$ $\mathrm{L_\odot}$), one should note that the far-IR emission of the Milky Way is *not* dominated from the reprocessing of light from young stellar populations, but instead from dust heated by older stars (Lonsdale & Hacking, 1987).

The local starburst galaxies have considerably more star-formation than 90-95% of most other local galaxies (Sargent et al., 2012). Although they provide the only local comparison to the extreme nature of star-formation in galaxies in the early Universe (Casey et al., 2014), they are not direct analogs to high-z starburst systems. For instance, local starbursts do not have SF which extends far beyond their galactic center, as seen in high-z systems. At $z > 1$, systems with $L_{\mathrm{IR}} > 10^{12-13}$ $\mathrm{L_\odot}$ may harbor molecular gas reservoirs and SF extending more than 10 kpc (Pope et al., 2006; Daddi et al., 2009; Carilli et al., 2011; Hodge et al., 2012).

The diversity of local CO SLEDs in ULIRGs (Papadopoulos et al., 2012a,b) can be attributed to violent, large-scale, supersonic turbulence in addition to stellar feedback and SN-driven shocks. High cosmic ray densities (as opposed to far-UV photons) can also sustain the excitation of a large fraction of the highly excited molecular gas. Many starburst systems may also harbor a compact component ($\leq$ 50-100 pc) traced by the highest-J CO lines (Liu et al., 2017). This hot molecular medium, likely a dust-obscured active galactic nucleus AGN, may provide strong feedback. An obscured mid-IR or X-ray luminous AGN (Greve et al., 2014; van der Werf et al., 2010) may also influence the ongoing SF. It is important to note that the *Herschel* spectral surveys from the past decade were the first surveys capable of distinguishing the various properties and excitation mechanisms associated with the molecular gas in strong starburst galaxies in the local Universe. These rest-frame far-IR spectral surveys revealed how a significant energy contribution from the diffuse and warm molecular gas should be accounted for when studying galaxies with extreme amounts of SF (Kamenetzky et al., 2014). These analyses ruled-out the presence of strong PDR/cosmic ray/x-ray heating of the molecular gas, in favor of more mechanical heating mechanisms, i.e. shocks / turbulence, for the most extreme star-forming galaxies (Rangwala et al., 2011). Contrary to low-z, little is known about the physical gas conditions during the peak epoch of SF, when the co-moving SFR density was >30x higher at $z \sim 2-3$ than it is today (Madau & Dickinson, 2014). In addition, the gas-to-stellar mass fractions were ~5x the local average (Carilli & Walter, 2013).

This thesis aims at studying the molecular gas properties in gas-rich systems at high-z via the assembly and analyses of the largest compendium of emission lines. Local studies revealed that strong mechanical energy is one of the main mechanisms required to sustain the CO line excitation in local

starbursts. I explore in this thesis whether or not the nature of the heating/cooling of the gas is similar in the ISM of dusty star-forming galaxies at high-z.

1.3 Characterizing the peak epoch in cosmic star-formation

1.3.1 Distant, dusty star-forming galaxies: background and overview

The radio Universe has been well-studied since Karl Jansky pioneered the theoretical and observational work of radio astronomy in the early 1930's. Everything shifted after he detected strong emission from the Milky Way for the first time (Jansky, 1933). Comparatively, optical techniques have been developed since Galileo invented the refractor telescope in the 1500's. Due to a variety of technical challenges, the world of the invisible Universe observed at wavelengths shorter than the radio ($\lambda_{\rm obs} \leq$1 mm), but longer than the near-infrared, was not revealed to humanity until the 1990s.

In the late 1990's and early 2000's, the study of the rest-frame far-IR-to-mm emission from distant galaxies began, forming the foundation for this thesis work. This recent discovery of these distant, dusty galaxies with high amounts of star-formation activity signifies how we are still in our early stages of understanding this unique time period in the SF history of the Universe.

The IRAS infrared maps made in the 1980's were not sensitive enough to detect the population of distant dusty star-forming galaxies, although IRAS did serendipitously discover a high-z system at z = 2.3 during a study of cool carbon stars Rowan-Robinson et al. (1991), as well as a lensed quasar host galaxy (QSO) at z = 3.9 (Irwin et al., 1998). The Max-Planck Millimetre Bolomter Array (MAMBO; Kreysa et al., 1998) and Submillimetre Common-User Bolometer Array (SCUBA; Holland et al., 1999) were the first two cameras to be installed on single-dish radio antennas, and observed the sky in the mm and sub-mm regime. As the observed wavelengths are still comparably large, a significant aperture is required to spatially resolve sources on the sky. Thus, the earliest (sub)mm maps were highly confusion-limited, such that individual sources along the line of sight could blend together and act as a single point source detection. Although the first (sub)-mm maps were limited to a few to tens of square arcmin in size, a population of distant, dusty star forming galaxies were discovered (Barger et al., 1998; Hughes et al., 1998; Barger et al., 1999; Eales et al., 1999; Lilly et al., 1999; Bertoldi et al., 2000; Borys et al., 2002; Chapman et al., 2002; Cowie et al., 2002; Dannerbauer et al., 2002; Fox et al., 2002; Scott et al., 2012b; Smail et al., 2002; Webb, 2002). Evidence in the early 2000's already indicated that the typical median redshift was around z = 2-3, however less than two or three data points were available to measure the dust SED of the candidate high-z sources (Blain et al., 2002; Casey et al., 2014, and references therein). It had been predicted that the number density of galaxies with 850μm flux density greater than 5 mJy was only 0.25 sources per square degree on the sky. However, the observed density was later realized to be many 100 deg^{-2} (Casey et al., 2014). It became immediately clear that these systems were vitally important in understanding galaxy evolution, as the co-moving density at z > 0.5 had 400 times the amount of galaxies with bolometric luminosities greater than 10^{13} L$_{\odot}$ (Casey et al., 2014) than observed locally. Results from the first statistical studies of (sub)mm bright galaxies suggested that the luminosity function is much greater than that of the IRAS selected galaxies. Wide-field surveys began studying these dusty galaxies in greater detail on statistically significant patches of the sky, often over hundreds

of square arcminutes of blank sky. Others focused on smaller, ~ 5 square arcminute fields which have strong local foreground clusters (Smail et al., 1997). Cluster environments can together amplify the background (sub)mm emission to increase the ability to detect fainter sources, and to infer intrinsic number counts of these galaxies across the sky.

1.3.2 Selecting distant, dusty star-forming galaxies

During star-formation, a rapid generation of dust can be produced, which has a multitude of influences in the interstellar medium (Draine & Li, 2007). Theoretical simulations reveal that only a thin layer of dust is required to effectively attenuate the UV/optical stellar light emission and re-radiate in the far-IR-to-mm wavelengths. Almost all of the far-IR luminosity of a star-forming galaxy arises from thermal dust continuum, however the functional shape of this emission cannot account for features of the conditions and the physical powering source as it is essentially a modified black-body emitter. In order for complex molecules to form in the first place, to further create interstellar dust grains, a cool environment must be available (Draine, 2011). It is useful to note that the temperature at which dust grains sublimates is of the order of ~2000 K – setting a physical upper limit to consider the temperatures of the dust emitting environments.

Modelling the observed dust continuum involves parameterizing the dust temperature and the function describing the emissivity of the dust grains. The emissivity function can be defined as a power-law function of frequency, with the power-law slope index denoted commonly as β, such that the emissivity is:

$$\epsilon_\nu \propto \nu^\beta \tag{1.12}$$

Typically $\beta = 1.5 - 2$, however theories and observations have set limitations on the values closer to 2 at low frequencies based on scattering theory. The SED can be expressed as the flux density,

$$f \propto \epsilon_\nu B_\nu(T) \times (1 - e^{-\tau(\nu)}), \tag{1.13}$$

in the simplest form – here taking into account the variation in opacity for a non-uniform dust temperature throughout the galaxy (Casey et al., 2014). The pioneering work in the early 1900s by Max Planck resulted in a function for black-body radiation based on the principle of quantized light packets:

$$B_\nu = \frac{2h\nu^3}{c^2(e^{h\nu/k_\mathrm{B}T} - 1)} \sim \frac{2k_\mathrm{B}\nu^2 T}{c^2}, \tag{1.14}$$

where h is Planck's constant, k_B, the Boltzmann constant and c the speed of light. In the $h\nu << kT$ limit, the flux density that is well-described by the Planck function can be approximated (i.e. $e^x \approx 1 + x$), resulting in the Rayleigh-Jeans limit, which is proportional, for first order, to ν^2 and the characteristic temperature of the source of the blackbody radiation – in this case the dust temperature.

The temperature of a perfect black-body (a system which can absorb and emit at 100% efficiency)

follows the Planck function. A host of templates and models have now been developed to approach the empirical and physical evidence explaining the dusty star forming population at high-z (Dale et al., 2001; Chary & Elbaz, 2001; Rieke et al., 2009; Kirkpatrick et al., 2015; Burgarella et al., 2005; Noll et al., 2009). Other modeling approaches utilise fitting functions, such as a χ^2 minimization procedure, to optimize the far-IR SED, as outlined above as a modified black-body distribution function. The dust properties themselves may not be well-known in external galaxies, however it is a fair assumption that the intrinsic SED of a star-forming galaxy will not vary wildly as it is a featureless modified blackbody.

The advantage of studying galaxies with strong rest-frame far-IR emission is that the SED is favorably redshifted. For a bolometric luminosity, L, at redshift, z, and luminosity distance, $D_{\rm L}$, with an intrinsic dust SED function, f_ν, the flux density at an observed frequency, ν, is defined as:

$$S_\nu = \frac{(1+z)Lf_\nu}{4\pi D_{\rm L}^2 \int f_{\nu'}\, d\nu'}. \tag{1.15}$$

For any galaxy, the observed dust emission subtends a solid angle, Ω, given the radius of the emitting region, r, and the angular diameter distance,

$$D_{\rm Ang} = D_{\rm L} \times (1+z)^{-2}, \tag{1.16}$$

with:

$$\Omega = \pi (r/D_{\rm Ang})^2. \tag{1.17}$$

Since the functional form of the flux density at the sampled dust SED points is strongly increasing as a function of frequency in the (sub)mm, then, as the flux density is redshifted, the flux density does not suffer from the natural $1/D_{\rm L}^2$ cosmological dimming that would be expected for optical or radio (Fig. 1.3). This is also known as a negative-K correction (Blain & Longair, 1993). It is important to note that this is a significant advantage when trying to detect distant galaxies which indeed have sufficient amounts of dust.

Due to the immense advantage of this negative K-correction in the (sub)mm wavelengths, it has now become one of the most widely exploited natural tools to study high-z systems. Nowadays, sensitive ALMA measurements have detected dust continuum in systems selected via optical/near-IR methods (which are not expected to have much dust content).

The negative K-correction effect theoretically extends to $z > 10$, while the optical and radio flux densities drop significantly at higher redshift (Blain & Longair, 1993; Blain et al., 2002). This assumes the intrinsic SED shape of a star-forming galaxy used as a template applies to other star-forming galaxies at high-z.

The CMB black-body temperature becomes significantly warmer than the dust temperature out to very high redshifts. Therefore, this technique of detecting dusty galaxies based on the negative K-correction loses its applicability because the required signal from the dust emission is more challenging to distinguish from the CMB radiation. At $z \geq 5$, this becomes increasingly important, and many efforts have been developed to explicitly correct for CMB radiation contributions to the observed line or continuum intensities (Combes et al., 1999; Obreschkow et al., 2009; da Cunha et al.,

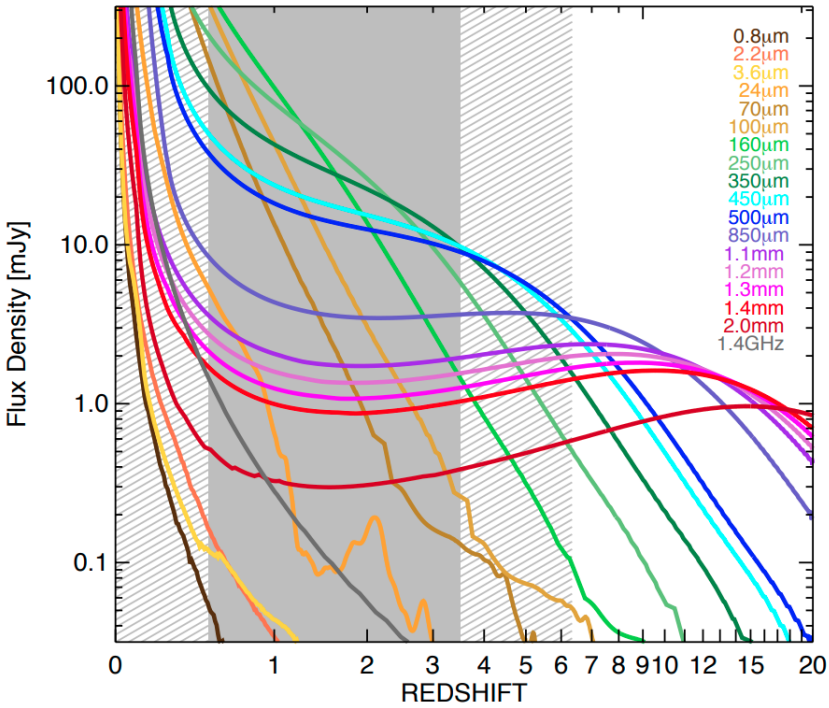

Figure 1.3: Observed flux density as a function of redshift. This plot illustrates the prominent negative K-correction in the mm for a galaxy with $L_{IR} = 10^{12.5}$ $L_{\odot}$, assuming an SED template derived for high redshift dusty galaxies – as published in Casey et al. (2014).

2013).

The local merging galaxies tend to be dust-rich, so it was believed early on that the dusty population of distant star-forming galaxies would be the natural culprit for the progenitors of local massive ellipticals with randomly distributed stellar velocity dispersions. Theoretical simulations, and now many observations have proven that the population of distant, dusty galaxies consists of a variety of major/minor mergers, and are a heterogenous population in a transient state of evolution (Finlator et al., 2006; Hayward et al., 2011, 2012, 2013; Narayanan et al., 2009). The discovery of stable spiral disk galaxies at $z > 2 - 3$ (e.g. Hodge, 2010) suggests both spirals and ellipticals formed within the first four billion years of the Universe. Galaxy mergers can trigger lots of gas to produce shock waves throughout the ISM of each system. To account for the local K-band luminosity function (Kochanek et al., 2000; Fardal et al., 2007) and the observed number counts of dusty high-z galaxies, theorists have argued that at high-z, many of the systems with observed $L_{IR} \sim 10^{12.5}$ $L_{\odot}$ or greater may have a top-heavy IMF. That is, high redshift galaxies are believed to harbor a significant amount of massive stars, and thus may have an over-estimated SFR (Baugh et al., 2005b).

The strong interplay of a coeval AGN / starburst is central to a complete understanding of galaxy evolution. Observations and theoretical work suggest that throughout the lifetime of a star forming galaxy, a combination of gas replenishment and metal enrichment, stellar and supermassive blackhole feedback, merger activity and accretion processes are all likely to play a role in shaping the ISM.

The ubiquity of dust emission associated with radio selected AGN galaxies (Archibald et al., 2001) provided one of the first clues of coeval AGN/star-formation at high-z at the time when the distant population of dusty galaxies were beginning to be discovered. Feedback from AGN / SMBHs in massive galaxies can induce broad line emission, as seen out to 10 kpc, concurrent with the ongoing SF activity, even at z = 4 (Jiang et al., 2019). The duration and physical influence of such outflows remains an open area of research for high redshift galaxies.

This thesis will explore the nature of star-forming galaxies during the topics by focusing on the peak epoch of the SF history of the Universe. The sub-mm selected galaxy sample that is used in the analyses for this thesis work have been previously identified due to their extreme IR luminosities. Both the dust and line fluxes are subject to the negative K-correction of the emission in the rest-frame IR to mm, therefore these galaxies offer a unique sample to study this most intense cosmic epoch of SF. Additionally, many open questions abound for the exact conditions present in coeval AGN/starburst systems, particularly at $z \sim 2$. Therefore, as a core chapter of this thesis (see Chapter 5), a case-study will further discuss the physical nature of a $z = 2.55$ coeval AGN/starburst galaxy with multiple CO line detections and [NII] line emission (Harrington et al., 2019).

1.3.3 Physical gas properties from high redshift emission line detections

Most of the bolometric luminosity output from a dusty star forming galaxy is in the rest-IR-mm in the form of (i.) thermal dust continuum radiation and (ii.) the spectral line emission from atomic/molecular rotational or fine-structure transitions. Here we briefly highlight the techniques used to study the observed emission lines.

Line measurements

Molecular and atomic emission lines can yield a wealth of information about galaxy evolution and the build-up of stellar mass across cosmic time. Emission lines offer direct measurements of individual galaxies with known redshifts, and have provided a set of mainstream tools calibrated in the local ISM environments to understand the evolution of star-forming material (Spitzer, 1978). The nature of the dusty, high-z systems has made observations of optical emission lines (e.g. Lyα, Hα) difficult, if not impossible. A review of galaxy evolution studied through the lens of optical/near-IR emission lines and metallicity diagnostics are recently reviewed by Kewley et al. (2019). Such lines offer critical insight into the stellar populations. Rest-frame far-IR to mm emission lines, on the other hand, offer deep insight into the cool gas content associated with star-forming galaxies. They may yield insight into the distribution and mass of the molecular reservoir, as well as the physical conditions of both the diffuse and dense molecular gas.

A spectral line emits at a specific central frequency, which corresponds to a specific line luminosity, i.e. the frequency weighted luminosity, L_ν. Following Solomon et al. (1992); Solomon & Vanden Bout (2005), this is expressed as:

$$\nu_{\rm rest} L_{\nu\ \rm rest} = 4\pi D_{\rm L}^2 \nu_{\rm obs} S_{\nu\ \rm obs}. \tag{1.18}$$

Re-writing this equation for the line luminosity (in units of $L_\odot$) in terms of the measured, velocity-integrated line flux, $S_{\rm CO}\Delta V$ (Jy km/s), yields:

$$L_{\rm line} = 1.04\times10^{-3} S_{\rm line}\Delta V \nu_{\rm rest}\frac{D_{\rm L}^2}{(1+z)}, \tag{1.19}$$

with the luminosity distance $D_{\rm L}$ in Mpc and the rest-frequency in GHz. The integrated line intensity that is observed is convolved with the beam if the source solid angle is within the observed antenna main-beam. As an antenna measures temperature directly from the power of the received electromagnetic signal, it is often the case to convert this line luminosity to a measure of the effective, areal-integrated brightness temperature integrated across the velocity axis of the line profile, i.e. the integral resultant: $T_{\rm b}\Delta V$. Thus, the line luminosity is expressed in terms of this quantity multiplied by the source solid angle,

$$L'_{\rm line} = T_{\rm b}\Delta V \Omega_{\rm source} D_{\rm ang}^2. \tag{1.20}$$

The velocity-integrated temperature can be re-written in terms of its flux density in the Rayleigh-Jeans limit, such that for any source size, the line luminosity can be expressed (in units of K km/s pc^2) with respect to the total line flux,

$$L'_{\rm line} = (c^2/2k_{\rm B}) S_{\rm line}\Delta V D_{\rm L}^2 \frac{\nu_{\rm obs}^2}{(1+z)^3}. \tag{1.21}$$

This quantity is often used in the literature as it has the advantage that, for an assumed co-spatial emitting region, the ratio of the L' value for any two line transitions probes the intrinsic brightness temperature ratio, and hence the thermodynamic conditions of the gas. If this brightness temperature ratio were unity this would lead to thermalized gas, as the relative level populations for the levels in the two transitions would be saturated.

It is crucial to derive the mass and other physical properties of the molecular and atomic gas in a star-forming galaxy as it helps to understand the nature of the total baryonic content of the Universe. The CO(1-0) and [CI](1-0) transitions have the lowest Einstein A coefficients (and are thereby the most easily excited), and are essential to constrain the cool, low-excitation gas. Measurements of higher-transitions, and other molecules such as HCN, trace denser and more energetic gas conditions. Altogether these characterize the physical conditions of the gas.

Estimates of the molecular gas mass and excitation conditions

To estimate the molecular gas mass of the ISM in a high-z galaxy, one needs to consider the locally calibrated techniques to convert from a measured line luminosity, typically CO, to the gas column density (mass) of molecular hydrogen, as reviewed by Bolatto et al. (2013). For spatially resolved clouds, the molecular hydrogen column density [cm^2] can be mapped by measuring the CO line luminosity [K km/s pc^2]. This has been calibrated extensively in the Milky Way, e.g. using CO isotopologues, which may trace the effects on determining the molecular gas mass by studying gas at various optical depths (Dickman, 1975, 1978; Dame & Thaddeus, 2011). It was also shown that ~ 300 CO emitting clouds in the Milky Way can be well-described as being in a state of virial equilibrium,

with a characteristic mean gas mass surface density of about 150 $M_\odot$ pc^{-2} (Dickman et al., 1986; Solomon et al., 1987). This allowed for a calibration of this conversion factor, guided by dynamical mass measurements and the strong relationship over four orders of magnitude in cloud mass and velocity dispersion. The latter is estimated from the width of the CO emission line profiles. Overall, Bolatto et al. (2013) synthesized all the various methods to derive the conversion factor for a galaxy with Milky Way gas-phase abundances. This value for the conversion factor, $\alpha_{CO} \sim 4.3$ $M_\odot$ per K km/s $pc^2)^{-1}$, which is systematically higher than α_{CO} ~0.8. The latter has become more commonly accepted as the standard value in local starbursts (Downes & Solomon, 1998). The local starburst value is based on dynamical mass constraints, such that the dynamical mass can be expressed in virial equilibrium as,

$$M_{\rm dyn} = R\Delta V^2/G, \tag{1.22}$$

combined with radiative transfer modeling of the lowest two CO transitions.

The situation is more complex as the gas-phase metallicity can factor into this determination, as a lower metallicity, and hence a lower CO/H_2 ratio, would require a higher value of α_{CO}, and higher-metallicity systems tend to have lower values (more CO line emission per unit molecular gas mass). For a turbulent ISM with a log-normal molecular gas density PDF in a highly active star-forming galaxy, a realistic description would have a spectrum of values. The dependence on metallicity has been used extensively to calibrate the molecular gas-to-dust mass ratio, or to use this as a means of empirically measuring α_{CO} (Draine & Li, 2007; Leroy et al., 2011), however α_{CO} depends on the local ISM conditions (Glover & Mac Low, 2011; Shetty et al., 2011a; Scoville et al., 2012; Eales et al., 2012; Magnelli et al., 2012; Leroy et al., 2013; Narayanan & Davé, 2013).

Non-LTE radiative transfer modelling

Gas masses and physical properties which are derived from radiative transfer models are derived in from a more physical basis, and may lead to robust calibrations of the line luminosity to gas mass conversion factor. Physical models solve for the partition function of the CO molecule in order to account for the observed line intensities, therefore the CO column density can then be converted directly to a molecular hydrogen gas mass. When one considers the total partition function for the CO molecule, which is the effective distribution of CO molecules in varying population levels, the largest probability is for the J = 1 state at the temperatures and densities of a cool GMC in the Milky Way (T = 10-25 K; log(n(H_2)) = 1.5 - 2.5 cm^{-3}). This has therefore been used as the standard to constrain the total molecular gas mass from other methods, although for increased temperatures, the higher-J levels can contribute more significant fractional contributions to the partition function, and thus trace more CO column density (and thus more molecular gas) – highlighting the importance of measuring multiple CO transitions and modeling the line intensities properly (Carilli & Walter, 2013).

In order to model the excitation conditions of the molecular gas one needs to consider the densities and temperatures, among other parameters such as the size of the emitting region. Following a Maxwellian distribution, the gas kinetic temperature of H_2 sets the probability distribution of molecular velocities. For the gas to be in local thermodynamic equilibrium (LTE), the gas must have a kinetic temperature equal to the excitation temperature – which is the temperature given in the Boltzmann

distribution governing the molecular level populations. Altogether the balance of spontaneous and collisional excitation processes determines the critical density at which the two mechanisms of radiative, versus collisional, processes are in equilibrium:

$$n_{\rm crit} = A/\gamma. \tag{1.23}$$

The collision rate coefficient, γ, has the units of cm^3 s^{-1}, and is proportional to the collision cross section σ and the molecule velocity (Flower & Launay, 1985):

$$\gamma \propto < \sigma \times v > . \tag{1.24}$$

In the context of the most extreme starburst environments, modeling the observed line intensities has required physical models which go beyond 1-D or 3-D PDR or X-ray dominated region (XDR Meijerink et al., 2006) conditions which are fundamentally described by an incident radiation field and a chemical network to compute the gas-phase abundances and later the line intensities. It appears that a strong mechanical input of kinetic energy into these active star-forming systems are well-characterized by shock models of dense molecular regions (Flower & Pineau des Forêts, 2003; Kristensen et al., 2008; Stacey et al., 2010; Nikola et al., 2011a).

As we provide detailed descriptions of the modeling procedures in Chapter 5 (Harrington et al. submitted), where we briefly review the LVG approximation framework (Scoville & Solomon, 1974; Kwan & Thuan, 1974; Young & Scoville, 1991; van der Tak et al., 2007). This tool accounts for the turbulent motion of gas particles with a systemic velocity gradient, dV/dr, gas-phase abundance, gas kinetic temperature and H_2 volume density (input parameters) as the observed CO lines are fit. High-z galaxies have line profiles with velocity dispersions (line-widths) driven primarily by galactic rotation and significantly greater than what would be predicted from their thermal velocities, which would be typically much less than 1 km/s for temperatures less than ∼10 K, also justifying the notion to describe the molecular gas excitation in the context of a turbulent, velocity driven framework.

For well-shielded molecular clouds, the CO line opacity is optically thick. As a part of the LVG approximation, there exists a probability for CO line photons to escape this optically thick medium. The escape probability method assumes the critical density scales inversely with the line opacity. The opacity itself is determined by the turbulent velocity of the system, which is influential in Doppler shifting CO photons out of the emitting medium. Originally the gas kinetic temperatures, column densities and number densities could be obtained based upon approximations to compute the local radiative transfer along any line of sight for an expanding atmosphere (Lucy, 1971).

As shown in Fig. 1.4, there can be strong degeneracy in the major two input parameters for solving for the line excitation: molecular gas density and kinetic temperature. A wide-range of CO excitation ladder shapes are observed for high-z systems based on the wide range of selection methods, from radio selected galaxies to Lyman-break selected galaxies and (sub)mm bright, dusty galaxies. Therefore it is crucial to provide galaxy-integrated measurements of galaxies at various levels of star-formation activity, with differing levels of ISM conditions, based on a wide-range of line/continuum diagnostics. The degeneracies indicate that a sampling of the peak, rise and turnover of the CO excitation ladder is important to constrain these modeling effects.

There has been a rapid increase in the number of emission line detections from high-z galaxies over the past 20 years. In 1992, the high-z IRAS-selected galaxy, F10214, was confirmed to have a strong presence of warm molecular gas when it was detected in CO(3-2) and CO(6-5) (Solomon et al., 1992). The initial discoveries of dusty high-z galaxies in the early 2000s were limited to sources with sparsely sampled dust SEDs, and only 36 galaxies at z >1 had been detected in CO (Solomon & Vanden Bout, 2005). In a follow-up review by Carilli & Walter (2013), there were 200 galaxies, most of which had only a single emission line – with one or two exceptionally bright QSOs having high-J CO lines detected (e.g. CO(J≥ 6) and only 11 high-z systems with [CI] lines detected.

Most importantly, today there still exists a limited number of high-z galaxies with multiple measurements of ISM lines. Open questions remain as to how much molecular gas mass there is in the most extreme systems, and what the nature of their in-situ evolution is. This requires, for instance, measurements of the faint CO(1-0) and [CI] line emission at $z = 1-3$, and also further modeling of the warmer molecular gas conditions with higher-J CO lines. To build an understanding of the processes that drive galaxy evolution across the peak epoch of cosmic star-formation, spatially resolved studies tracing the reservoirs of cold molecular gas and their dynamics and energetics are required. At high redshift, $z > 1$, such studies have been limited due to large investment of telescope time (e.g., GN20, 120 hours on the VLA (Hodge et al., 2016)). Few interferometric maps of CO(1-0) from galaxies between z∼1-3.5 exist, typically with a beam of 3-5", limited in probing emission at ∼20-30kpc scales (Ivison et al., 2011, 2013).

Here in this thesis work, I have measured and modeled the emission of a significant amount (∼ 200) CO/[CI] emission lines detected in a sample of 24 galaxies. This amounts to almost 20% of the known line detections at $z > 1$, now only 15 years later than the first review of cool interstellar gas in the early Universe. This thesis work will therefore offer a rich insight into the most luminous star-forming galaxies in the Universe, and their galaxy-wide molecular gas/dust properties.

Carbon monoxide, CO

The most popular tracer of the cool ISM has traditionally been the CO molecule. It is a stable molecule with a low dipole moment, therefore it will not easily dissociate and it is easily excited in the coolest conditions. Stars must form within cool, collapsing clouds, therefore CO is an excellent tracer of this supply for star-formation. It is the second most abundant molecule in the ISM after H_2, therefore it is a crucial molecule to study the physical properties and kinematics of the interstellar molecular gas. The most abundant molecule, H_2, is stable and has strongly forbidden ro-vibrational lines which require temperatures far exceeding the typical temperatures of molecular clouds ($T_{GMC} < 10^4$ K). The first quadropole line is about 500 K above the ground state, tracing a small percentage of the total molecular gas mass, which typically has temperatures of order 10 K. As H_2 is significantly abundant, it is the primary collisional partner with CO. Like any atom or molecule, CO has a fingerprint – most notably the CO ladder of excitation characterized by the rotational transitions. Rotational transitions of CO are due to C and O orbiting around their central mass, and the lowest energetic transitions for this diatomic molecule can effectively trace the bulk of the molecular ISM. The next higher energetic transitions are typically due to vibrational motions between C and O (vibrational transitions), followed

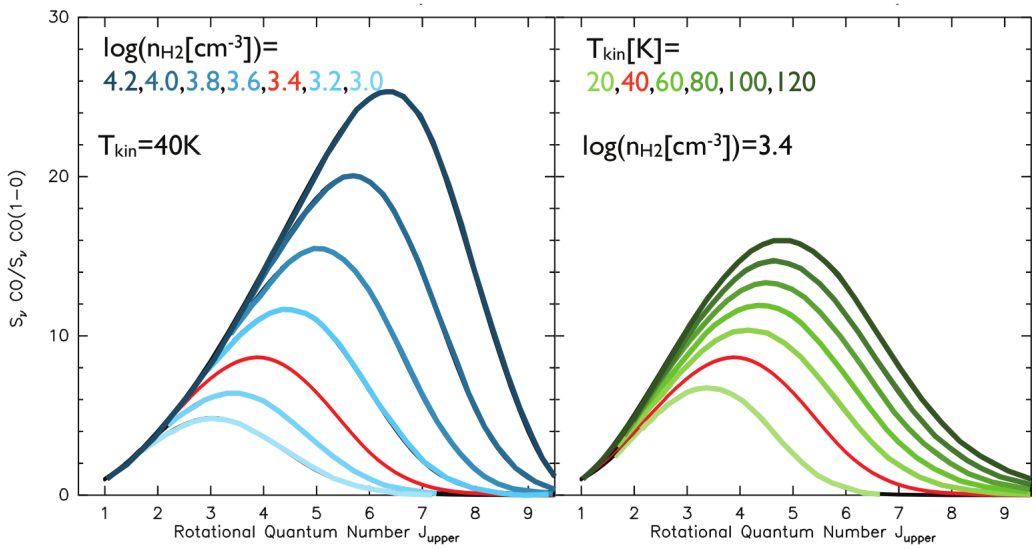

Figure 1.4: Observed velocity integrated line flux density, normalized by the CO(1-0) line flux, plotted against each respective rotational quantum number, as published in Carilli & Walter (2013). The degeneracy between the gas kinetic temperature and volume density is shown to illustrate the inherent challenges of modelling the CO line emission.

by electronic transitions (excitation of electron(s)). At only 5 K, the CO molecule can emit radiation from the ground-state rotational transition.

Through the conservation angular momentum and quantized rotational states, the orbital angular moment is: $L = nh/2\pi$, where n is an integer and h is Planck's constant (Townes & Schawlow, 1975). The rotational energy is proportional to L^2, and inversely proportional to the moment of inertia, I, of the linear polar molecule of CO:

$$E_{\rm rot} = L^2/2I = n^2({\rm h}/2\pi)^2/2I = {\rm J(J+1)}({\rm h}/2\pi)^{2/2I}.$$

For a change in energy to occur, a molecule needs to leave a higher level to a single level lower, such that $\Delta J = \pm 1$, and the change in rotational energy, as the energy state decreases from state J to J-1, results in $\Delta E = ({\rm h}/2\pi)^2 J/I = h\nu_{\rm line}$. The ground-state emission line for CO occurs at a rest-frequency of $\nu_{\rm CO(1\text{-}0)} = 115.27$ GHz, and the subsequent transitions which constitute the CO excitation ladder (CO(2-1), CO(3-2), etc) each emit energy at multiples of this ground-state rotational transition frequency. The centrifugal forces increase for higher rotational levels of J, and the mean nuclear radius between the carbon and oxygen atom of CO increases. This then results in a relative decrease for the rest-frame spectral line frequency.

CO and H_2 are the dominant colliding partners in the molecular ISM. For reference the Milky Way GMC CO/H_2 gas-phase abundance is roughly 1×10^{-4} (Blake et al., 1987). The cross-section is thus highest between these two molecules, and the increased densities largely determine the rate at which molecular interactions can occur. Collisions with H_2 inject kinetic energy into the CO molecules to increase the likelihood of entering into higher level energy states, and release this energy as the molecule de-excites to a lower energy level. The CO molecule simultaneously experiences a

spontaneous decay rate given by the Einstein A-coefficient, $A \propto \mu^2 \nu^3$ [s^{-1}], with μ the dipole moment.

Atomic carbon, [CI]

In the HI atom, when a hyper-fine structure atomic transition occurs, it emits at roughly 21cm radio wavelengths. This is due to the electron movement inducing a magnetic field, which interacts with the nuclear spin of the atom. Similarly, in atoms such as carbon and nitrogen, the spin-orbit coupling of the spin of the electron and the internal magnetic fields induces, not a hyperfine, but a fine-structure splitting of the spectral lines of the atom (Münch & Wilson, 1962). Such lines have relatively long-lived spontaneous decay rates, and are considered to be forbidden lines, yet they can be collisionally excited and / or stimulated from the ambient far-IR radiation field.

Neutral atomic carbon has a three-level structure with two fine-structure transitions: $^3P_2 \rightarrow^3 P_1$ at $\sim$ 809.34 GHz, and the $^3P_1 \rightarrow^3 P_0$ transition occurs at $\sim$ 492.16GHz for the [CI]370μm and [CI]609μm lines, respectively. Both lines have low Einstein A coefficients, lowering the threshold for a critical density for excitation. The excitation temperature of the carbon ^3P fine-structure population levels can be estimated if both lines are measured and one assumes that the emitting gas is optically thin and in local thermodynamic equilibrium (completely, thermally populated, as described below) (Stutzki et al., 1997). If both lines are measured, then the line luminosities can be used to infer the carbon gas column density (Stutzki et al., 1997; Schneider et al., 2003b; Ojha et al., 2001; Walter et al., 2011). Atomic carbon has shown a great promise to study the cool ISM of the high-z SFGs, as locally it is observed to trace a wide range of environments closely with CO and / or ^{13}CO (Gerin & Phillips, 2000; Israel & Baas, 2002; Israel, 2005). Sharing similar volumes they offer excellent probes of regions similar to the CO(1-0) and CO(2-1) transitions (which can trace the most diffuse up to the dense molecular gas log(n) >4 cm^{-3}). Only 13 high-z galaxies at the time in 2011 had [CI] line detections, however, constraints were made in those with both [CI] lines to derive the excitation temperatures of $\sim$ 30 K (Walter et al., 2011). This cool temperature, close to cold GMCs in the MW, had been a surprising result considering the extreme nature of SF in these high-z systems. A slightly lower value was recently derived for a sample of $z \sim 1$ main-sequence star-forming galaxies (Valentino), with $T_{\rm exc}$ = 25 K. For such well-shielded, cool environments in massive star-forming systems, there is likely a large portion of gas not directly associated with star-formation (Carilli & Walter, 2013). Since the [CI] lines are typically optically thin, they can be used to measure the carbon mass, and with an assumed carbon abundance, can be used to derive the bulk mass of the molecular hydrogen (Weiß et al., 2005a; Valentino et al., 2018). Recent theoretical/observational work has shown that 30-70% of the total H_2 mass can be unaccounted for by CO if the abundances and/or geometry favor CO photodissociation by ultraviolet radiation (Glover et al., 2015). Thus, the combination of CO and [CI] is vital for characterizing the total column density from the diffuse *and* dense gas.

Atomic nitrogen [NII]

Electrons in warm ionized gas (ambient or otherwise associated with HII regions surrounding young massive stars), are the main collision partners with atomic nitrogen. Far-infrared fine-structure lines with ionizaton potentials higher than 13.6 eV can trace purely ionized gas, such as in the case of nitrogen: the $^3P_1 \rightarrow^3 P_2$ fine-structure transition occurs at $\sim$ 2459.4 GHz, and the $^3P_1 \rightarrow^3 P_0$

transition occurs at ~ 1461.1GHz for the [NII]122μm and [NII]205μm lines, respectively. A map of [NII] within the Milky Way Galactic plane has shown that it can trace the warm ionized regions around HII and ambient regions with electron density $n_e \sim 0.1 - 10$ (Goldsmith et al., 2015). Locally, the [NII] line luminosity shows a linear relation to the total IR luminosity, and therefore acts as a SFR tracer. Herrera-Camus et al. (2016b) have spatially resolved the two [NII] lines in local star forming galaxies to extensively calibrate the line luminosity of nitrogen to a SFR (global or surface integrated). This calibration was based on publicly used templates. These templates are developed based on stellar population synthesis models and can provide a specific ionizing photon rate, together with an assumed IMF, which yield a value for the SFR based on the measured [NII] line flux. This SFR estimate also requires an assumed nitrogen abundance and fractional ionization state.

[NII] 205μm line is also optically thin in many systems and insensitive to gas temperature, so the line luminosity is directly proportional to the mass of low ionization gas, or the minimum ionized gas mass. Using the [NII] 122μm, Ferkinhoff et al. (2011) determined the ionized to molecular gas fraction, $M_{min}(H^+)/M(H_2)$=0.08-0.17. As the two fine-structure levels are separated by only a few 100 K and the typical temperature of the gas in the Hii region is ~8000K, level populations are often thermalized. Following Ferkinhoff et al. (2011), Decarli et al. (2014) studied the 205 μm line in a $z > 4.5$ Lyman-α emitting galaxy, an SMG and QSO and found that, overall, these high-z sources suggest that a significant (20-50% ionized gas mass to molecular gas mass) fraction of the ISM is ionized by stellar UV radiation.

The detection of singly ionized nitrogen directly measures the 14.5 - 29.6 eV luminosity, and can be compared with the FIR luminosity to estimate the UV field hardness (Stacey et al., 1991) . It takes 14.5 eV to form N^+, and 29.6 eV to ionize it to N^{++}. Hence, the HII regions created by O8 to B2 stars would dominate the [NII] emission, and harder radiation fields will push nitrogen to N^{++} state. Earlier type stars, (or emission from an active galactic nucleus) would produce more energetic ionizing radiation, creating higher ionization species like [NIII], and decrease the relative power emitted in the [NII] 205 μm line.

In this thesis, I present novel measurements for a large amount of CO and [CI] lines in star-forming galaxies at $z > 1$ (Harrington et al. submitted; Chapter 4). Since dusty star-forming galaxies exhibit intense SFRs with $L_{IR} > 10^{13}\ L_\odot \sim 1000\ M_\odot\ yr^{-1}$ (Casey et al., 2014), it has often been assumed that they should have a lower CO luminosity per unit gas mass, similar to local starbursts, with a value of $\alpha_{CO} \sim 1$. In this thesis work, I explore whether it is correct to simply apply a single value for the conversion factor to these distant star-forming galaxies. I utilize a set of recently developed, state-of-the-art models (Weiß et al., 2007b, , and Weiss et al. in prep.) which simultaneously fits the thermal dust emission and the observed CO/[CI] line fluxes. In Chapter 5, I will present the first detection of [NII]205 in a galaxy between $z = 0.4 - 3.9$ (Harrington et al., 2019). Using this line measurement, in conjunction with ancillary CO and [CI] line measurements, I explore the ionized and molecular gas contents in a case-study of a starburst/AGN galaxy in the sample of lensed Planck-selected galaxies.

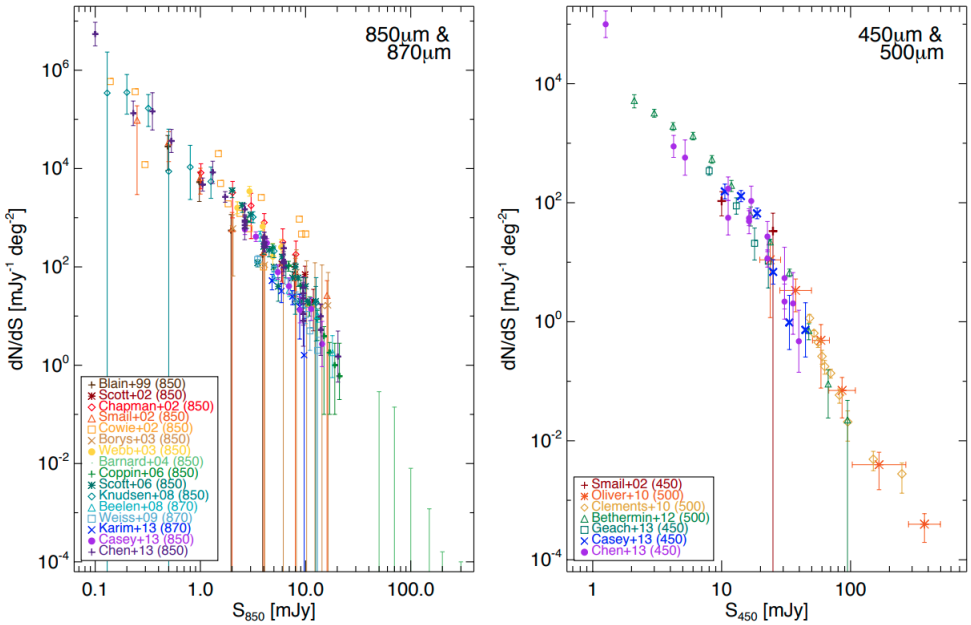

Figure 1.5: *Left Panel:* Submillimeter number counts estimated from observations at 850μm/870μm. *Left Panel:* The same plot for number counts at an observed wavelength of 450–500μm. Individual references and details about each survey can be found in the original publication (Casey et al., 2014).

1.4 Finding Luminous pearls in the cosmic ocean: strongly lensed starbursts

1.4.1 Sample Selection

This section will outline the selection method used to identify the sample of galaxies which are the focus of this thesis. Throughout this thesis work I will present a series of studies aimed at understanding the nature of the gas conditions within distant star-forming galaxies selected using data from the *Planck* satellite telescope. They have been gravitationally magnified, and are therefore useful laboratories to study how galaxies evolve. If a background source galaxy is along the line of sight it can be gravitationally imaged, only if a massive foreground galaxy(ies) are also along the line of sight to become a gravitational lens. Since these *Planck*-selected star-forming galaxies are gravitationally imaged, it becomes easier to detect their emission, even if it is faint and distant. This allows one to overcome observational barriers in sensitivity. Thanks to this powerful microscope in space, I have been able to systematically detect more than 150 emission lines from cool molecular gas in twenty-four, rare *Planck*-selected star-forming galaxies. The equivalent study would have otherwise taken up to two orders of magnitude more telescope time.

To begin, I will briefly outline some of the background topics related to strong gravitational lensing. Gravitational lensing theory describes the process by which light is deflected in a weak gravitational field, i.e. not the strong field (i.e. in the case of photons passing by a black hole). Small deflections occur as light passes by an object. This can be viewed when the line-of-sight

geometry is aligned with the foreground mass distribution, which acts as a lens that magnifies the light distribution from a distant object directly behind. As the light is distorted due to the presence of the foreground mass distribution's gravitational field, such light can therefore probe the foreground mass distribution with an accuracy that is unparalleled by other extragalactic methods. This is an example of how powerful a tool strong lens magnification can be to study galaxy evolution and cosmology.

The gravitational field of a galaxy or galaxy cluster can distort the background light by deflecting this light by an angle on the sky, proportional to the radius and surface mass distribution of the foreground lens. A paramount feature in studying high-redshift galaxies lensed by an intervening foreground is the geometrically-thin condition, which states that the mass distribution is of an extent that is negligible in size compared to the distances between the observer, the lens and the lensed source. On average, if a galaxy cluster mass distribution is strongly magnifying the light from a background image, with magnification factor $\mu > 2$, the deflection angle measured (i.e. the angular extent of the lensed background light viewed on the sky) is usually less than 25". For one galaxy (and perhaps a small satellite) in the foreground acting as a lens, the deflection angle usually encompasses an angular extent of order 1", and typically less. If there is a perfect alignment between the sources and observer a complete ring of magnified, deflected light is observed: a so-called 'Einstein Ring'. The appearance of lensed images reveals insight into the intrinsic distribution of mass and light in the background (unlensed) source plane, however detailed modeling to reconstruct this lensed light is required to derive the intrinsic properties of the magnified background object.

Of course, as the image has naturally been magnified, this creates additional caution when interpreting the results. For instance, the size of the source being lensed must be less than the projected size of the lens to ensure that the whole galaxy is in fact observed, and not just a portion. The process of lens modeling is very case-sensitive, as each unique system has a variety of factors. Here I will only briefly mention the basic notions of selecting strongly lensed galaxies and the context with which to consider the sample in this thesis.

The deflection of starlight due to the Sun's mass that was observed during the 1919 solar eclipse precisely confirmed Einstein's prediction, from his General Theory of Relativity, that mass itself can re-direct light. The advancement of new radio facilities like the Very Large Array radio interferometer and the new technologies employed on optical facilities, such as Charged Coupling Devices (a.k.a. CCDs), allowed for measurements testing the prediction of a galaxy (not the Sun) lensing the light from another distant galaxy directly behind the line-of-sight. The idea goes back to Zwicky and was confirmed with the optically selected quasar, QSOJ0957+561 (Walsh et al., 1979). This source appeared as a quadruply imaged system. Larger samples of lensed galaxies, starting with CASTLES (cfa-www.harvard.edu/castles), appeared as *HST* revolutionized our imaging of the sky with, e.g. ~ 0.1" angular resolution. Many of the brightest optical or near-IR selected QSOs were strongly lensed. Recent samples include: SLACS, Reionization Lensing Cluster Survey (RELICS) fields (Coe et al., 2019).

The brightest (sub)mm galaxies on the sky are expected to populate the sky of the order of one per hundreds to thousands of square degrees. Fig. 1.5, from the review by (Casey et al., 2014) demonstrates this. Specific attention is paid to the observed number count detections at 850μm and 500μm wavelengths. These number counts are derived from the surveyed fields shown in Fig. 1.6. Expanding the number counts to wider and wider fields allows for the possibility of detecting the low

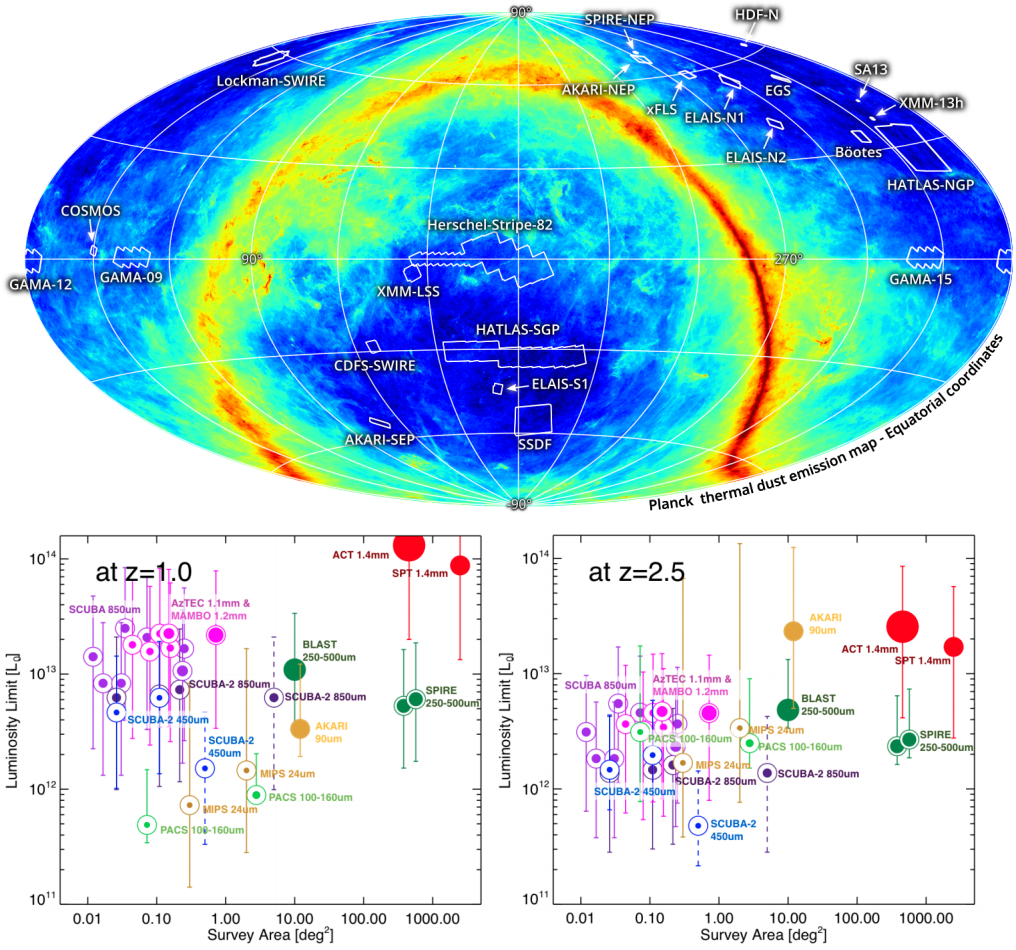

Figure 1.6: *Top:* Observed wide-field areas mapped by the *Herschel* sub-mm satellite telescope, overlaid with the all-sky (sub)-mm maps from the *Planck* satellite telescope. See HELP. *Bottom Left:* Infrared luminosity sensitivity limit for the majority of (sub)-mm surveys in the literature. Here, the sensitivity limit depth refers to galaxies at $z = 1$. *Bottom Right:* The sensitivity limit for the different surveys for a corresponding redshift, $z = 2.5$, as published in Casey et al. (2014).

statistical probability objects. In the review of dusty, star-forming galaxies, Casey et al. (2014) showed the limited coverage of the sky at (sub)mm wavelengths at the time five years ago. These (sub)mm fields were mapped at varying angular resolution and sensitivity. The Herschel Space Observatory covered roughly 1300 sq deg between 100 and 500μm, while the South Pole Telescope (SPT) in its first generation of 1.4-2.0mm-maps observed about 2500 sq deg, both of which resulted in impressive confirmations of strongly lensed, dusty source candidates at high-z, with a median redshift of z = 3.2 (Weiß et al., 2013; Strandet et al., 2016), however a broad tail out to z = 7 (De Breuck et al., 2019; Marrone et al., 2018b; Vieira et al., 2013; Hezaveh et al., 2013; Spilker et al., 2017). Later these are now being followed up with the high spatial resolution and sensivity of the (sub)mm ALMA telescope, such as the *Herschel* selected lensed galaxy in Fig. 1.8 (Tamura et al., 2015; Negrello et al., 2010).

The bright end of the luminosity function was not sufficiently sampled by the tens to hundred sq arcmin surveys until Herschel began observing the (sub)mm sky. As *Herschel* and *Planck* were launched on the same rocket, the wide-field, finer angular resolution sub-mm maps of *Herschel* could be combined with the data from the *Planck* satellite, which offered a coarse angular resolution, but still a remarkable sensitivity, at the observed sub-mm wavelengths across the entire sky.

It was predicted in Blain (1998) that the Planck survey mission would be able to detect the brightest (sub)mm sources across the entire sky. The top of Fig. 1.7 shows the probability, a(z), of a galaxy lensing another galaxy as a function of redshift, z. Blain (1998) found that the optical depth can be calculated by taking the value of scale factor, a(z)/8, based on a magnification distribution model, as a function of redshift (Peacock & Wall, 1982; Pei, 1993). They convolved this model with the estimated surface and flux densities derived from models of distant, dusty star-forming galaxies (Blain, 1996). The probability of lensing magnification is determined by the mass distribution, and in the Press-Schechter formalism this deems a hierarchical structure formation approach. It is then expected that smaller galaxies are observed at higher redshifts, and thereby Blain (1998) used this overall method predicting the evolving mass distribution (solid line). The peak of the two distributions, and therefore among the highest probabilities of lensing, both occur around $z = 1 - 3$, and thereafter diverges depending on the model used. On the bottom are predictions of the number of lensed galaxies detected at a threshold flux density for *Planck* at 550μm. At 100 mJy, there were expected to be 10 unlensed field galaxies for every square degree on the sky, compared to 0.1 or less per square degree probability for a lensed galaxy to be detected. The number count of a population of observed sources is simply a matter of counting signal against the noise, and is often denoted as the number above a given flux density limit N($> S_{\nu_{obs}}$). The number per square degree drops significantly for higher luminosity objects, which would predictably converge to zero for unphysical luminosities. In total, based on those predictions (Blain, 1998), and an integrated lens source count of 0.01 - 0.1 lensed occurences detected by *Planck* at 550μm, this equals (with 41,253 square degrees encompassing the sky) anywhere from a few hundred to a few thousand galaxies magnified by a strong magnification factor (at least $\mu > 2$).

(Negrello et al., 2007), has shown that above the expected steep–drop-off in the (sub)mm number counts (e.g. S500>80 mJy), any point source detected by Herschel (and Planck) is almost exclusively a lensed candidate. This technique was later developed by Ivison et al. (2010); Wardlow et al. (2013); Bussmann et al. (2013); Harrington et al. (2016) using a simple selection method including a simple flux-limit at S350>100 mJy and cleanly detect lensed galaxies with high efficiency. In the latter

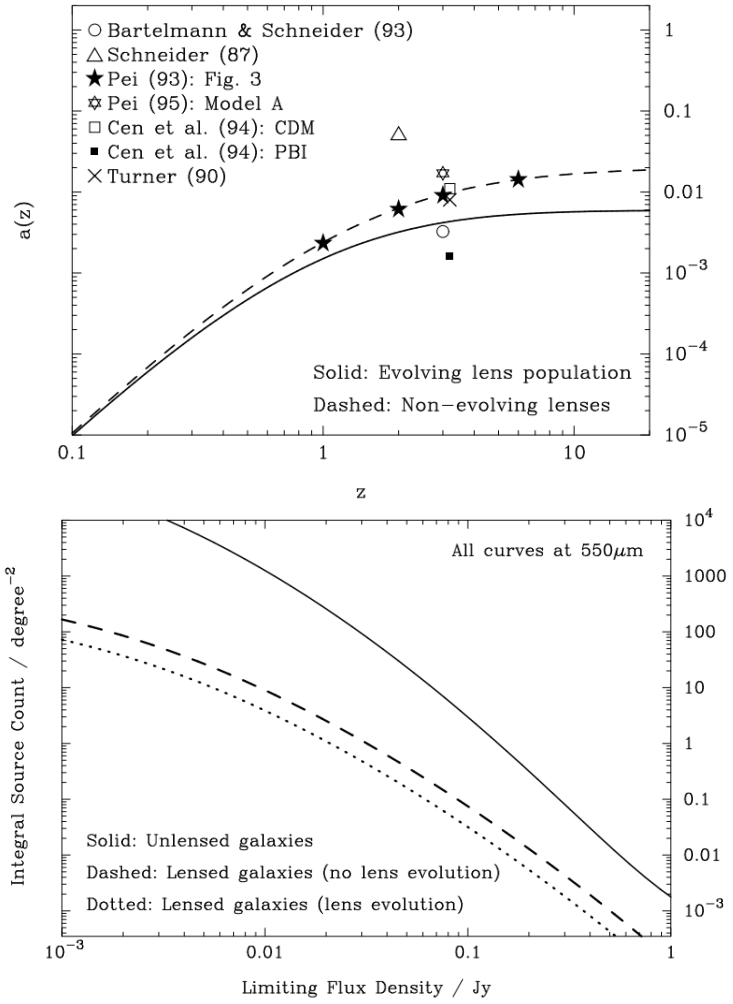

Figure 1.7: *Top Panel:* Probability for strong gravitational lensing as a function of redshift, according to the cosmological assumptions and analyses in the original publication of Blain (1998). *Bottom Panel:* The predicted differential submillimeter number counts, with and without an evolving foreground lensn population (Blain, 1998).

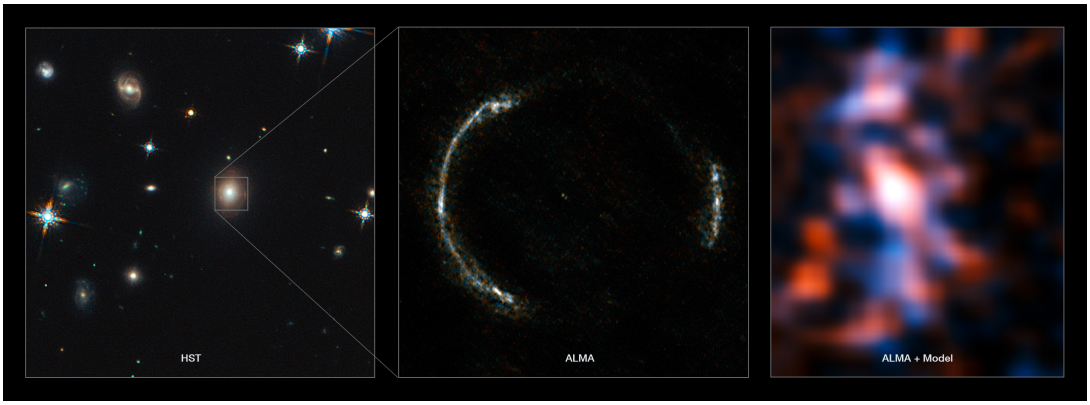

Figure 1.8: Images of a strongly lensed, dusty star-forming galaxy (Tamura et al., 2015). *Left:* The Hubble Space Telescope near-IR image of the lensing field. The box indicates the strongly lensed galaxy. *Middle:* The lensed image, observed at $\sim$ 1 mm. *Right:* The reconstructed source plane image of the lensed galaxy at $z \sim 3$. These results are from the Science Demonstration Phase period of testing the Atacama Large Millimeter Array (reaching unprecedented angular resolutions of milliarcseconds in the (sub)-mm wavelength regime. See ESO press release.

case, Harrington et al. (2016) use the all sky sensitivity of *Planck*, albeit with a coarser angular resolution than Herschel, to identify strongly lensed candidates by first cross-matching all Planck data to publicly available Herschel data at the overlapping 350μm observed wavelength. Independently other approaches have been adopted using similar Planck color criteria (Cañameras et al., 2015) and or WISE data (Díaz-Sánchez et al., 2017).

Since observation times can be expensive, many dusty high-z galaxies do not have spectroscopically confirmed redshfits. Due to the degeneracies in modeling and assumed templates of SEDs, combined with limited data available, it is often difficult to trust the redshfit based on photometry alone. As these systems are intrinsically faint, if not undetectable in the optical, mm emission lines yield strong measurements of the source distance to accurately conduct follow up observations. And if the lines are gravitationally lensed, it make the follow-up observations much more efficient. Fortunately, as the rest-wavelengths of the CO ladder are in the far-IR/mm, they also experience the same negative-K correction as the adjacent dust continuum.

In this thesis work, I have utilized this method to securely determine the redshfits of more than a dozen of the recently discovered LPs, which had otherwise a single line detection and / or limited dust photometry – thanks to the emission being strongly magnified. The latter is important to note, as a single line measurement still leaves open the possibility of the line being associated with a different transition than expected, thence corresponding to another redshift. The selection method we have used contains objects with a Planck identification, matched with a WISE color selection to identify red mid-IR sources (Yun et al., 2008). So far we have confirmed roughly 30 lensed, Planck selected starburst candidates at high-z (LPs) by measuring dust continuum and / or low-J CO line emission with the Large Millimeter Telescope in the past 6 years (Harrington et al., 2016, Berman et al. in prep).

The overall number of candidates we have compiled is of the order 200 Planck identified,

WISE/Herschel cross-matched point sources, most of which have yet to be followed up. Many may be local foreground spirals, although Casey et al. (2014) remarked that at least 250 lensed dusty star-forming galaxies could still be identified in the wide-field areas surveyed and stored in the Herschel Science Archive alone. Many have already been identified and followed-up extensively (Scott et al., 2011; Conley et al., 2011; Negrello et al., 2013; Fu et al., 2012; Combes et al., 2012; Dye et al., 2014; Bussmann et al., 2015; Harris & Harris, 2011; Harris et al., 2012; Yang et al., 2017, 2018, 2019a).

Overall, an estimated 500 or more strong lenses have been discovered. These LPs are therefore likened to rare, highly luminous, pearls in the cosmic ocean of hundreds of billions of galaxies. They are selected across the entire sub-mm sky, with number densities of 0.01 - 0.1 deg^{-2} (Vieira et al., 2013; Harrington et al., 2016). Using a Tully-Fisher like relationship, as suggested by Harris et al. (2012), to estimate the magnification factor (μ) for 24 LPs in our sample, using GBT CO(1-0) data, we find $\bar{\mu} \sim 26 \pm 13$ estimated in Harrington et al. (2018) and also Chapter 4. Interestingly, μ is weakly correlated to the spatial extent of lensing morphology observed in the *HST* images, providing further confidence to our higher estimate of the magnification factors as compared to the SPT/*Herschel* lensed dusty galaxy sample ($\bar{\mu} \sim 7$). These LPs have large magnification factors estimated simply based on the size of the Einstein radius (in some cases >10"), however extensive follow-up has also confirmed the nature of strong lensing magnification, $\mu > 10 - 30$ in published/ongoing lens modeling (e.g. Frye et al., 2019).

1.4.2 Differential lensing effects

The effects of a possible spatially varying magnification factor may result in flux amplification of certain regions of the lensed galaxy of interest. Here we briefly describe some of these caveats, as this will be further discussed in Chapter 4.

The total size of the emitting region of the low-excitation and higher-excitation emission lines of CO may vary intrinsically in the source plane, therefore if these emitting regions are disproportionately distributed along the caustic, the observed fluxes could yield differential magnifications. That is, the more compact emission traced by higher-J CO transitions may be magnified by a factor that is significantly different than the diffuse, low-excitation gas (Blain, 1999; Serjeant, 2012; Hezaveh et al., 2012), if it lies closer, on average, to the caustic. As AGN/QSOs have extreme luminosities centrally located within the host galaxy, these point-like objects may be subject to stronger differential lensing than starburst galaxies. This would lower the probability that such a distinction is made between the magnification factor for higher-J CO versus the low-J CO emitting regions. This is because the source of the higher-J emission in AGN/QSOs is likely confined to a concentrated region near the center of mass of the host galaxy, whereas the starburst galaxies have more extended reservoirs that may be well-mixed, and both low-J and high-J lines may be magnified differentially in a similar manner, on average. Differential lensing may be more pronounced when comparing low- and high-J CO line fluxes, however the bulk of this work is focused on global properties such as the total molecular gas mass – which is most sensitive to the lowest-J CO line measurements. High angular resolution imaging in the future is required to investigate differential lensing. We therefore focus on the observed quantities.

Due to the extreme starburst nature of the lensed *Planck*-selected starburst galaxies, the molecular

ISM may have a large volume filling factor of gas, suggesting a smooth distribution of SF on galactic scales (Kennicutt, 1998; Kennicutt & Evans, 2012). An explicit accounting of this would require assigning a unique magnification factor to each measurement of the dust continuum and a magnification factor per velocity channel for the CO/[CI] lines to model the de-magnified integrated fluxes (see e.g. Leung et al., 2017). Recent studies have shown a similar magnification factor for the low-J CO/adjacent dust continuum (Cañameras et al., 2017b), while others show a non-negligible 20-40% differential magnification of low-mid-J CO/dust continuum (Yang et al., 2019b). It is clear that every lens configuration is a unique system, and therefore a coherent set of lens models is required for the lower-excitation versus the higher-excitation molecular/atomic gas at matching spatial resolution and S/N to diagnose these effects more systematically. However, in this study the effective source radius, described below, is directly connected to the apparent flux within the source solid angle, and is used as input to the model. For our two component modelling, we cannot explicitly determine the differential lens magnification factor, as the intrinsic ratio of the emitting radius for each component may be different from the modelled ratio. Thirteen out of the 24 lensed *Planck* starburst galaxies presented here have lens models developed based on a wide range of high-angular resolution *HST* near-IR data and/or ground-based optical/near-IR follow-up of the foreground and lensing environment (Díaz-Sánchez et al., 2017; Frye et al., 2019). A small subset of the lensed *Planck* selected starburst galaxies have a range of marginally resolved to highly resolved (down to beam sizes, θ ~0.1 - 0.2″) mm-radio interferometric dust continuum and/or single-line CO imaging to also aid lens modelling efforts (Geach et al., 2015, 2018; Bussmann et al., 2015; Cañameras et al., 2017a,b, 2018a). Overall, these systems have flux-weighted total magnification factors ranging between 10-40 (Table 4.1).

The lack of magnification factor estimates derived for each of the emission lines, in addition to multiple magnification factor estimates derived from sampling the rest-FIR thermal continuum emission, restricts our analyses to the magnified (apparent) quantities. Harris et al. (2012) used a "Tully-Fischer" line luminosity/line-width relation to offer an empirical perspective on estimating the unknown magnification of the CO(1-0) line measured in 24 *Herschel*-selected, strongly lensed galaxies. There may be an intrinsic dispersion among the lensed *Planck* selected galaxies along this empirical relation, and the inclination angle is unaccounted for, yet we can use equation 2 of Harris et al. (2012) to estimate the lens magnification factor based on our GBT detected CO(1-0) line measurements. We derive the line full-width at half-maximum (FWHM) using a simple 1-D Gaussian model fit to the velocity line profiles as done by (Harrington et al., 2018). In the case of LPs-J0305, LPs-J0226, LPs-J105353 and LPs-J112713, there is no available CO(1-0) line data. Therefore, we use the value of $L'_{\rm CO(1\text{-}0)}$ from the best-fit, minimum-χ^2 *Turbulence* model and the measured FWHM from the low-J CO line data. We report the derived magnification factors in Table 4.1. This magnification factor estimate, which is usually 1.5-3× higher than previously reported results, has systematic uncertainties in estimating the lens magnification estimate could be more than 50% based ont he intrinsic scatter within the calibration sample used in Harris et al. (2012).

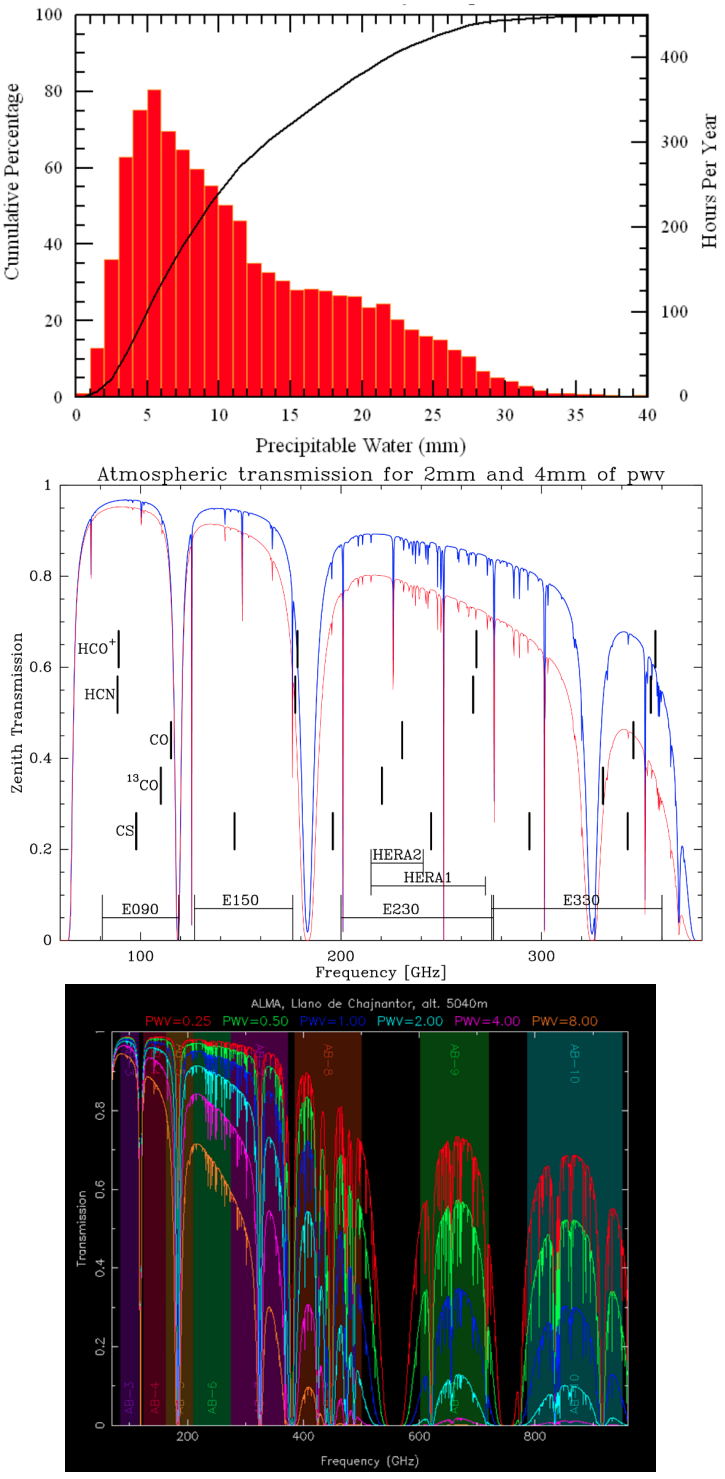

Figure 1.9: Atmospheric conditons as shown by a model of the atmospheric transmission as a function of frequency or wavelength for the the Green Bank Telescope in the US, the IRAM 30m telescope in Spain and the APEX telescope site, situated at the ALMA site in the Atacama desert in Chile. Depending on the site, the atmospheric transmission changes dramatically for different values of precipitable water vapour (PWV).

1.5 Single dish spectroscopic observations in the (sub)millimeter wave regime

This thesis work has a significant observational component, with hundreds of hours of first-hand observations with world-class single-dish radio telescopes. Before closing this introduction section, I will briefly capture the nature of such observations and the important considerations when obtaining the data used in this thesis work. Upon successful proposals early into the start of my dissertation work, I was able to soon-after acquire data first-hand with the Green Bank Telescope (GBT) in Green Bank, West Virginia, United States, IRAM 30m telescope in the Sierra Nevada mountains outside of Granada, Spain and Atacama Pathfinder Experiment (APEX) telescope located in the Atacama desert of northern Chile.

1.5.1 Observing conditions at sky frequencies of 30 - 420 GHz

A radio antenna is a large voltmeter, and it is the power received in units of antenna temperature that is eventually converted into physical flux density units. A telescope antenna has a diameter and an effective surface area to collect electromagnetic radiation at an observed frequency/wavelength. The area of an antenna is optimized to selectively filter incoming radiation from within the primary beam of the telescope. This primary beam arises from a diffraction-limited pattern. One can consider the reception pattern of constructive and destructive interference as any wave passes through an aperture and interacts with itself at integer offsets to the wave period, with an inverse dependence on the size of the aperture. In the same way, as an electromagnetic wave passes through a telescope aperture it results in a diffraction pattern of reception. It is helpful to remember that this pattern is interchangeable, as if one were to consider a telescope as an emitting source (for example, in radar applications) rather than a receiving source. The emitting/receiving "beam" is determined by the size of the antenna aperture and the wavelength. The beam size, typically measured in minutes of arc or seconds of arc, is given as, in the diffraction limit:

$$\Theta \propto \lambda / D, \tag{1.25}$$

where D is the effective diameter of the telescope, whereas the wavelength of a sinusoidal wave, λ, and frequency, ν, are inversely proportional via the speed of light, c.

Relatively higher frequencies (~250 GHz or greater) are difficult to observe as the atmosphere at those frequencies can be unstable across the sky. This is largely due to random turbulent air motions and a strong variation in the incoming signal due to varying amounts of water along the line of sight. Therefore, when there is low precipitable water vapor, corresponding to a lower opacity, it is best to conduct higher frequency observations. Sometimes the sky is clear and dry but there are wind gusts at 150 km/h forcing the telescope to be stowed. Typical observing restrictions at sites of the three main telescopes I observed with are seen in Figure 1.9. At the top is the Green Bank Telescope (100m unblocked aperture), located in Green Bank West Virginia, US, in which 80-115 GHz (mm) weather conditions can be seen to encompass an extremely small percentage of their cumulative hours of observing conditions. I primarily observed between 29-40 GHz (8-10mm) to detected redshifted CO(1-0) line emission. In the middle is the much more favorable site in the Sierra Nevada mountain range outside Granada, Spain, where the IRAM 30m telescope is located (2850m above sea level). I

primarily used this telescope to observe between 100-350 GHz, in which Figure 1.9 shows that an extremely low PWV value is required for atmospheric transmission to be above 75%. Hence, the best observing days are limited to a few days to weeks (typically after snow storms and in December-March). The bottom figure is an atmospheric model of the transmission at frequencies all the way up to 900 GHz, derived from the excellent observing conditions of the high (5100 m) and dry site of the Atacama desert in Northern Chile. The APEX telescope was used as a single 12m dish to employ a range of receivers/instruments and to demonstrate the need for an array at the Atacama desert, such as ALMA.

To maintain an accurate telescope pointing and focus model for optimized on-target observations, it is common to correct for pointing every one to three hours by choosing a bright nearby source close to where the science observations are targeted. Every two to four hours (and one or two hours after sunrise and sunset), a bright source needs to be observed to correct for the focus of the telescope mirrors. Meter-sized secondary, or tertiary, mirrors involved in redirecting the light beam to the receiver are shifted by a fraction of a millimeter to optimize the sensitivity of the telescope.

1.5.2 Spectroscopic observations at radio-to-millimeter frequencies

Radio antennae are often equipped with a range of instruments to conduct specific science goals. Since the early 2000s there has been a rapid advancement in spectroscopic capabilities thanks to breakthrough developments in hardware and technology. Sensitive cameras operating at millimeter frequencies allowed for the continuum detection of distant, star-forming galaxies, effectively measuring the thermal dust emission from these distant sources – 'continuum' referring to the broadband average over a range of frequencies. Since these discoveries, these continuum observations have been frequently followed-up with spectroscopic measurements to accurately confirm their exact distances through detections of molecular/atomic lines. Spectroscopy allows one to measure the signal from individual atoms or molecules in a galaxy to directly study both radiative and kinematic properties. All of the observations I conducted utilized superheterodyne receiver technology. Almost 100 years ago this type of receiver technology was invented (in 1918 by Edwin Armstrong), and it is still the standard method of tuning for all major electronics.

Rather than use physical components to filter different frequencies to overcome those two issues, a superheterodyne receiver operates by the concept of a beat frequency. This is the difference between two frequencies. For a desired frequency of observation, i.e. a so-called "tuning", the receiver system mixes the sky signal with an intermediate frequency. Mathematically this process is one of constructive and destructive interference, and can be manipulated to select desired frequency channels, as in a car stereo. To generate such a beat frequency, a signal of known frequency (e.g. an input sinusoidal wave) is injected into the system. This injected frequency down-converts the observed frequencies to lower frequencies, which can be more easily processed digitally.

Radio/sub/mm single dish antennae observe electromagnetic radiation as it enters into the telescope aperture and is re-directed to a focus. The light is not received continuously, as each receiver needs to sample the incoming data stream for a given bandwidth of measurable frequencies. The sampling rate limits the amount of information gathered in one unit of time. In the late 1990's and early 2000's, the frequency bandwidth available to the spectroscopic receivers was less than 1 GHz in the radio to

mm regime. If there was a redshift error on the order of 10% or greater, the redshifted line would fall outside of the observable bandpass. This hard limit in technology restricted the efficiency to confirm spectroscopic redshifts and further study the molecular/atomic gas properties at high-redshift. Nowadays, for many receivers, there is an instantaneous bandwidth of 16 GHz per polarization. The light from a distant galaxy is unlikey to be polarized so the orthogonal polarizations measured by the receivers can be combined and when averaged decrease the noise by a factor of $\sqrt{2}$. When tuning, the spectrometers have 8 GHz of bandwidth per sideband, with the line to be observed within one of these sidebands.

The time allotted for any telescope should be optimized as efficiently as possible. Yet realistically, there are natural physical limits. One such limit is the time it takes to change a receiver on a telescope, or to change a tuning setup within a single receiver. Through the process of identifying which frequencies the spectral lines are redshfited to, taking into considerationg the variations in atmospheric transmission, I optimized over 150 receiver tuning setups with the IRAM 30m and APEX telescopes. The sensitivity of one sideband may be better than the other, and sometimes it is not possible to measure the redshifted line close to the center of the sideband. This thesis work consists of a sample of more than twenty galaxies at redshifts spanning $z \sim 1-3.6$. I therefore designed the optimal observing strategies, taking into consideration the following: (i.) Which sources were going to be available to observe above 25-30 degrees elevation, and for how long, (ii.), testing different tuning set-ups to know how close to the edge I can place the receiver tuning in order to fully detect the spectral line – and to minimize noise from the edge of the receiver; (iii.) designing receiver tunings which would be usable for as many combinations of sources/lines, without having to change tuning/receiver. Thus, for example, I may observe the CO(9-8) line from one galaxy, while another galaxy is slowly rising in the sky as the Earth rotates. Soon after, I would then observe the second galaxy of interest after it has risen in the sky, which may have, e.g., a [CI](1-0) line redshifted into a different sideband for the same tuning.

CHAPTER 2

Structural outline and motivation

The molecular gas to stellar mass fraction within the ISM of star-forming galaxies has decreased significantly since the peak epoch of the co-moving cosmic SFR density at $z = 1-3$. This suggests swift stellar mass assembly at high-z occurred, leaving many open questions regarding the heating/cooling mechanisms for sustaining/quenching star formation. Multiple ISM diagnostics are therefore needed to investigate the influence of the far-IR radiation fields dominated by newly formed young massive stars. The advancement of wide-bandwidth spectrometers has now allowed the possibility to investigate such extreme conditions in distant galaxies in lines other than CO to develop a more cohesive picture of the multi-phase ISM during the starburst episodes of galaxy evolution. It is believed at some point all massive galaxies, $M_\star > 10^{9.5}$ $M_\odot$, have experienced such a starburst time in their evolution.

The overall focus of my dissertation work is on characterizing the extremely luminous star-formation processes through observations and modeling of spectral line emission arising both from the cool molecular ISM, and the warm ionized ISM of strongly lensed, dusty star-forming galaxies. I focus primarily on the cool ISM, and thereby characterize the physical gas properties for the sample of lensed *Planck*-selected galaxies, which themselves are unique stellar manufacturing factories in the early Universe.

- In Chapter 3, we examine the cool molecular gas reservoirs of the *Planck* selected-high-z star-forming systems. This is the result of a pilot survey to measure the faint CO(1-0) line emission of a sub-sample of Planck selected galaxies from Harrington(2016) using the GBT. This ground-state CO transition is vital for determining the bulk molecular gas mass. This is an important parameter due to the fact that most of the baryonic mass is in molecular form (not stellar mass) for these distant starbursting galaxies. The success of this pilot study (Harrington et al., 2018) led to a plethora of follow-up opportunities to study the more highly excited CO line transitions in a systematic manner.

- Chapter 4 is the culmination of many hundreds of hours of telescope time, which had its foundation in the results of Chapter 3. Based on these data, we systematically acquired detections of fourteen additional CO(1-0) lines in a follow-up program with the GBT (for context, currently there are less than 100 CO(1-0) line detections of $z > 1$ galaxies). With a firm constraint on the

ground-state CO line emission, we then set out to target the expected peak of the CO excitation ladder, using the 70 - 350 GHz frequency coverage of the IRAM 30m telescope, in a subset of the brightest LPs. This led to multiple follow-up programs based on the repeated success of each of the previous programs to easily detect CO(4-3; 5-4; 6-5; 7-6) lines. As many high-z galaxies only have one or two low-J CO lines, we intended on systematically measuring the rise, peak and fall of the CO ladder for this rich sample of lensed galaxies. To do this, we utilized the IRAM 30m *and* APEX 12m telescopes, accessing low-J to high-J CO lines. The latter are redshifted into higher and higher frequencies. The estimate of a total ∼1000 hours of telescope time across all programs led to such a legacy value dataset and analyses for the high-z galaxy evolution community (Harrington et al., 2018, 2019, and Harrington et al. (submitted)). This chapter includes the non-LTE radiative transfer modeling of both the dust and molecular gas, *simultaneously*. We perform a robust suite of modelling procedures using both a turbulence driven gas density PDF framework, as well as a more simplistic two-component model to study ∼ 200 CO and [CI] lines in 24 LPs.

- Chapter 5 highlights a case study demonstrating the usefulness of far-IR fine-structure lines to study both the cool molecular and the warm ionized ISM of the LPs, and high-z star-formation. Based on the sensitivity of the APEX telescope, and the excellent observing conditions in the Atacama Desert of Northern Chile, we detected the first [NII]205um emission line from a galaxy between $0.4 < z < 3.9$, from the coeval AGN/starburst galaxy in our sample, the LPs-J0209. With a robust constraint on the molecular gas properties from the work presented in Chapters 4 and 5, we are able to provide a unique insight into the ionized gas conditions, as opposed to only the cool molecular star-forming fuel supply. This study has led to a series of follow-up APEX proposals and successful observations.

- Chapter 6 is a summary within the context of the larger field of galaxy evolution. The focus of the outlook is on both the immediate follow-up work and also promising avenues in this field of research for the next decade to come.

CHAPTER 3

Total Molecular Gas Masses of *Planck - Herschel* Selected Strongly Lensed Hyper Luminous Infrared Galaxies

This chapter is a reproduction of the article of the same title that has been published in Monthly Notices of the Royal Astronomical Society under the reference:

- Harrington, K.C., Yun, M.S., Magnelli, B, et al. 2018, MNRAS, 474, 3866.

The manuscript, found here, is reproduced under the non-exclusive right of re-publication granted by the Oxford University Press to the authors of the original article in MNRAS. To ensure open access to the article the peer-reviewed, published version has been uploaded to astro.ph (1711.10827).

3.1 Abstract

We report the detection of CO(1-0) line emission from seven *Planck* and *Herschel* selected hyper luminous ($L_{IR(8-1000\mu m)} > 10^{13} L_{\odot}$) infrared galaxies with the Green Bank Telescope (*GBT*). CO(1-0) measurements are a vital tool to trace the bulk molecular gas mass across all redshifts. Our results place tight constraints on the total gas content of these most apparently luminous high-z star-forming galaxies (apparent IR luminosities of $L_{IR} > 10^{13-14} L_{\odot}$), while we confirm their predetermined redshifts measured using the Large Millimeter Telescope, *LMT* ($z_{\rm CO} = 1.33 - 3.26$). The CO(1-0) lines show similar profiles as compared to $\rm J_{up} = 2 - 4$ transitions previously observed with the *LMT*. We report enhanced infrared to CO line luminosity ratios of $< L_{IR}/L'_{CO(1-0)} >= 110 \pm 22\, L_{\odot}(K\ km\ s^{-1}\ pc^{-2})^{-1}$ compared to normal star-forming galaxies, yet similar to those of well-studied IR-luminous galaxies at high-z. We find average brightness temperature ratios of $< r_{21} >= 0.93$ (2 sources), $< r_{31} >= 0.34$ (5 sources), and $< r_{41} >= 0.18$ (1 source). The r_{31} and r_{41} values are roughly half the average values for SMGs. We estimate the total gas mass content as $\mu M_{H2} = (0.9 - 27.2) \times 10^{11} (\alpha_{CO}/0.8) M_{\odot}$, where μ is the magnification factor and $\alpha_{\rm CO}$ is the CO line luminosity to molecular hydrogen gas mass conversion factor. The rapid gas depletion times, $< \tau_{\rm depl} >= 80$ Myr, reveal vigorous starburst activity, and contrast the Gyr depletion timescales observed in local, normal star-forming galaxies.

3.2 Introduction

Most of the stars in the local universe formed out of tremendous cool gas reservoirs ($M_{gas} \sim 10^{10-11} M\odot$, $T \sim 10 - 100$ K) in the interstellar medium (ISM) of high redshift ($1 < z < 3.5$) galaxies with intense star-formation (SF) (Carilli & Walter, 2013).

Massive, dusty star forming galaxies at high-z (DSFGs; $M_{dust} \sim 10^{8-9}$ $M_{\odot}$) are typically gas-rich galaxies selected via their bright observed (sub)-mm fluxes (also known as SMGs). The rest-frame far-IR (FIR)-mm luminosity associated with the thermal dust emission (Efstathiou et al., 2000; Johnson et al., 2013) (re-radiated far-UV radiation) traces the total star-formation (SF) activity, while the extreme star-formation rates (SFRs) in these IR luminous galaxies are likely due to a sustained supply of cool gas from the intergalactic medium (IGM). The dense molecular ingredients of the ISM thereby limits the timescale for extended starburst (SB) activity, with short-lived SB episodes of 10's-100's of Myr. These are believed to often include gas-rich mergers that induce star formation via tidal torques, which drive gas infall and subsequent collapse. The most active SB galaxies at $z \sim 2$ contribute key insights into galaxy evolution and structure formation, as their massive gas reservoirs play a key role in the bulk stellar mass growth in their ISM environments, and as a result are believed to be the progenitors to massive elliptical/spheroidal galaxies and clusters at low-z (Casey et al., 2014).

The SMG population can be accounted for by major or minor-merger dominated starbursts (Baugh et al., 2005a; Swinbank et al., 2008) in some semi-analytic models. Others suggest that the observed population is a heterogeneous mix of early and late stage major mergers and blending of passive star-forming disc galaxies. The brightest SMGs are likely early-stage mergers, exchanging a significant amount of molecular material for continued star formation (Hayward et al., 2012; Narayanan et al., 2015). SMGs typically have high gas mass fractions, $M_{\rm gas}/M_{\star}$, up to 80% (Carilli & Walter, 2013).

CO line measurements are vital for directly probing the fuel for these star-forming galaxies, i.e. the total molecular gas mass, at the peak of the co-moving SFR density ($z \sim 2 - 3$). The gas accretion history of growing dark matter (DM) halos in cosmological simulations (Kereš et al., 2005) agrees well with the observed evolution of the CO luminosity function, as Decarli et al. (2016) find a peak redshift for CO luminous galaxies at $z \sim 2$, comparable to the peak of the co-moving star formation rate density.

The CO (J= $1 \rightarrow 0$) transition accounts for both the dense and most diffuse molecular gas, and has traditionally been calibrated to trace the bulk H_2gas mass (via collisional excitation with the H_2gas). The observed CO line luminosity, L'$_{\rm CO}$, to H_2 mass conversion factor, $\alpha_{\rm CO}$, (Carilli & Walter, 2013; Bolatto et al., 2013), is calibrated to this transition, making observations of CO(1-0) important for determining the total H_2mass content at high-z.

The number of high-z sources with galaxy integrated CO(1-0) detections is sparse (see Scoville et al., 2017; Carilli & Walter, 2013), although it is accumulating (e.g. Carilli et al., 2002; Hainline et al., 2006; Harris et al., 2012; Thomson et al., 2012; Fu et al., 2013; Aravena et al., 2013; Sharon et al., 2016; Decarli et al., 2016; Huynh et al., 2017), with approximately 60 to date. Resolved imaging of this lowest rotational transition of CO (e.g. Riechers et al., 2011; Lestrade et al., 2011) in high-z SMGs indicates that the total molecular gas can extend up to 30 kpc for merging systems. Only the most active star forming sources with apparent $L_{\rm IR} \geq 10^{12-14}L_{\odot}$ at $z > 1$ can be observed at this fundamental CO rotational transition. These apparent luminosities are often due to strong lensing. The strong lensing effect (usually with magnification factor, $\mu = 10 - 30X$) (e.g. Bussmann et al., 2013, 2015; Geach et al., 2015; Spilker et al., 2016), yields shorter integration times to provide secure detections of the molecular gas in both strongly lensed, intrinsically bright and faint, but highly

magnified, normal star-forming systems.

The far-IR/sub-mm *Herschel* Astrophysical Terahertz Large Area Survey (H-ATLAS) (Eales et al., 2010) and the Herschel Multi-tiered Extragalactic Survey (HerMES) (Oliver et al., 2012), together covering about 650deg^2, and the 2500 deg^2 mm South Pole Telescope (*SPT*, Carlstrom et al., 2011) have paved the way forward in discovering a rare population of gravitationally lensed DSFGs (e.g. Planck Collaboration et al., 2011a; Wardlow et al., 2013; Vieira et al., 2013; Weiß et al., 2013; Negrello et al., 2017a), as well as an intrinsically bright, unlensed population. Cañameras et al. (2015) and Harrington et al. (2016) have exploited the all-sky sensitivity of *Planck* to find the most luminous high redshift galaxies currently known in the *Planck* era – all of which are gravitationally lensed.

Here we present galaxy integrated, CO(1-0) measurements of seven $z > 1$ galaxies using the Green Bank Telescope (*GBT*). This is a pilot study for a larger program to identify a large sample of extremely luminous high-z SMGs identified by the all-sky *Planck* survey. In our original pilot study (Harrington et al., 2016), our goal was to identify sources that have the probability to be gravitationally lensed given their high flux densities in the 3 SPIRE bands of 250, 350, 500μm e.g. the S_{500} or $S_{350} \geq$ 100 mJy (e.g. Wardlow et al., 2013). We have previously obtained one $J_{up} = 2 - 4$ transition for all seven of the sources presented in this study using the Redshift Search Receiver (RSR) on the *LMT*. The majority of these sources have apparent $\mu L_{\rm IR} > 10^{14.0-14.5}$ $L_\odot$ making them some of the most luminous sources currently known (Harrington et al., 2016; Cañameras et al., 2015). Our goals in this study are to confirm the *LMT* CO redshift, measure the CO(1-0) line emission to constrain our estimate of the H_2masses and begin analysing the CO spectral line energy distributions (CO SLEDs). We will first review our sample selection and previous observations, as described in detail in Harrington et al. (2016), and then we will outline our CO(1-0) observations using the VErsatile GBT Astronomical Spectrometer (VEGAS) instrument on the *GBT*. Afterwards we report our measured and derived gas properties using the CO(1-0) line emission and supplementary *LMT* CO data, followed by a discussion. We adopt a Λ CDM cosmology with $H_0 = 70$ km s^{-1} Mpc^{-1} with $\Omega_{\rm m} = 0.3$, and $\Omega_\Lambda = 0.7$ throughout this chapter.

3.3 Sample

In a search for the most extreme, and thus rare, star-forming galaxies at $z > 1$, we exploit the full-sky sub-mm coverage offered by the the *Planck* Catalog of Compact Sources (PCCS). The highest frequency observed by *Planck* (857 GHz / 350 μm) contains a dataset of $\sim$ 24,000 point source objects (Planck Collaboration et al., 2014). From this dataset we limit our searches to point sources at Galactic latitude $|b| > 30$ deg to minimize the Galactic source contamination. This filtered sample is then cross-correlated with the combined catalogs of three *Herschel* large area surveys: *Herschel* Multi-tiered Extragalactic Survey (HerMES, Oliver et al., 2012), *Herschel* Stripe 82 Survey (HerS-82, Viero et al., 2014), and the dedicated *Planck* follow-up *Herschel* DDT “Must-Do" Programme: “The *Herschel* and *Planck* All-Sky Source Snapshot Legacy Survey”.

The details of our selection method can be found in Harrington et al. (2016) for the *Planck* - *Herschel* counterparts with $S_{350} \geq 100 mJy$ in our initial follow-up during the Early Science Campaign 2 for the *LMT*. In brief, we cross-matched *Planck-Herschel* counterparts within 150". In total there were 350 *Herschel* counterparts to 56 *Planck* sources within 150". The higher spatial resolution of *Herschel* allowed us to pinpoint the position of the *Planck* point sources, enabling follow up studies.

For 8/11 galaxies observed with the *LMT* we detected a single, compact source using the AzTEC

Source ID	RA	DEC	$\mu L^{\star}_{IR}$	*GBT* RX	Dates	Int. Time (On-Source)	$< T_{sys} >$
	J2000	J2000	$(10^{14} L_{\odot})$		2016	mins	K
PJ142823.9	14h28m23.9s	+35d26m20s	0.19 ± 0.04	Q	2/12;2/19	336	100
PJ160722.6	16h07m22.6s	+73d47m03s	0.14 ± 0.03	Q	2/12;2/19	216	75
PJ105353.0	10h53m53.0s	+05d56m21s	2.9 ± 0.4	K_a	3/30	100	40
PJ112714.5	11h27m14.5s	+42d28m25s	1.1 ± 0.2	K_a	3/30	84	40
PJ120207.6	12h02m07.6s	+53d34m39s	1.4 ± 0.3	K_a	3/30	80	40
PJ132302.9	13h23m02.9s	+55d36m01s	1.2 ± 0.2	K_a	3/30	96	40
PJ160917.8	16h09m17.8s	+60d45m20s	2.0 ± 0.4	K_a	3/26	92	35

Table 3.1: Sources and *GBT* Observations Summary. Q band receiver frequency coverage: 38.2-49.8 GHz. K_a band receiver frequency coverage: 26.0-40 GHz. * L_{IR} is the far-infrared luminosity integrated between 8-1000 μm.

1.1mm camera. Subsequently we detected a strong CO line with the RSR spectrometre. We make use of the 3 SPIRE bands of *Herschel* (250, 350, 500 μm) and the additional *LMT* observations to derive apparent $\mu L_{\rm IR} > 10^{13.0-14.5} L_{\odot}$ at $z_{\rm CO} = 1.33 - 3.26$. The current sample in this *GBT* study consists of observations of only seven of the original eight targets.

3.4 *GBT* Observations

Based on our RSR spectroscopy, two of our sources have redshifted CO(1-0) (i.e. rest-frame 115.27 GHz) line emission in the range of the Q band receiver (38.2 – 49.8 GHz) on the *GBT*. The other five sources fall within the K_a band receiver (26.0 – 40 GHz). We used the low-resolution 1500 MHz bandwidth mode of the backend spectrometre, VEGAS. The raw channel resolution corresponds to 1.465 MHz, or $\sim$ 16 km s^{-1} in K_a band, using 1024 channels. Observations between February and March, 2016, took place in typical weather conditions. For both Q and K_a band observations, we used a SubBeamNod procedure, nodding the 8m *GBT* sub-reflector every 6 seconds between each receiver feed for an integration time of four minutes. In most cases, this 4 minute procedure was repeated back-to-back for up to an hour to achieve the ON source integration times presented in Table 3.1. The atmosphere becomes highly variable at the frequencies within Q and K_a band, therefore we observed pointing sources roughly every hour. The routine pointing and focus procedures allowed us to assess the best azimuth and elevation corrections, as well as the best focus values for the peak line strength measurements.

After total-power switching for the standard $(ON - OFF)/OFF$ GBTIDL calculations, we include the observatory's atmospheric model, which tracks zenith opacity as a function of frequency and time. Each scan is corrected for the atmospheric time and frequency variations on the sky, given zenith opacity $\tau_{\rm sky}$ and elevation, EL:

$$T_{\rm antenna} = T_{\rm sys} \times e^{\frac{\tau_{\rm sky}}{\sin({\rm EL})}} \times \frac{\rm (ON\text{-}OFF)}{OFF}. \tag{3.1}$$

The elevation ranges for Q and K_a band spanned 33 – 84 deg and 28 – 73 deg , respectively. The typical T_{sys} values ranged from 67-134 K in Q band, and 30 - 45 K in K_a band. To convert the measured antenna temperature in $T_{\rm A}^{*}$ to flux density we use the calibration factor derived for *GBT*: Q band scales as 1 K / 1.7 Jy, K_a band as $1K/1.6Jy$.

We used a high-pass filter to remove very low-frequency ripples in the overall baseline without

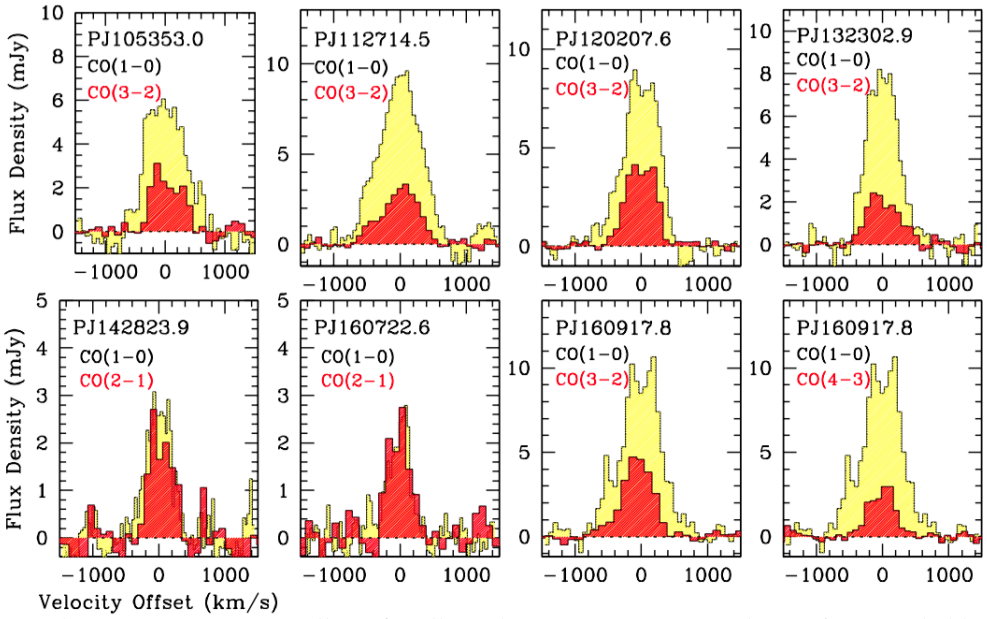

Figure 3.1: The RSR CO spectra (yellow) for all 7 galaxies (Harrington et al., 2016) are scaled by J_{up}^2 and overlaid (red) onto the GBT CO spectra (yellow) in this study. The comparable line widths and spectral features are coincident. PJ160918 has both its CO(4 – 3) and (3 – 2) lines compared to the (1 – 0) line emission.

removing the line emission. The width of the high-pass filter was at least twice the expected full-width at half maximum (FWHM) of the CO line based on our *LMT* RSR spectra. We utilised Gaussian smoothing to decrease the resolution by a factor of 4, resulting in a 5.86 MHz ($\sim 50\,kms^{-1}$ for K_a) channel resolution. In this smoothing step, each channel was treated as independent to avoid correlations in the noise of neighboring channels. As the high-pass filter removes the low-frequency ripples, and not the mid-frequency baseline ripples, we then fit and remove a baseline ($n_{\rm poly} = 2 - 3$) to the emission free regions of the spectra. The resulting spectra can be seen in Fig. 3.1. We adopt a 30% total uncertainty given a 15-20% flux calibration error, typical 5-10% pointing/focus drifts and atmospheric losses and a conservative 10-15% for the baseline removal due to the variations across the bandpass at the observed frequencies.

3.5 Results: CO (1 – 0) Line Properties

We detect CO(1-0) at $S_{\rm peak}/{\rm N}_{channel} > 7$ from each of our seven targets at the expected redshifts. We first derive the observed central frequency by fitting a single Gaussian to the CO(1-0) line emission, confirming the exact redshifts of these *Planck-Herschel* identified galaxies, which had previously been derived using only one CO line from the *LMT* (Table 3.2). The spectroscopic redshifts span from $1.33 < z < 3.26$. Our new *GBT* measurements further support our previous redshift determinations from the combination of panchromatic photometry (WISE-11 and 22 μm, *Herschel* SPIRE 250, 350, and 500 μm, AzTEC 1100 μm and NVSS/FIRST radio) and single CO line observations (see Appendix A of (Harrington et al., 2016)).

We find that the CO(1-0) lines show nearly identical profiles and widths as the $J_{up} = 2 - 4$ CO lines, with FWHM = [375–740 km s^{-1}] (see Fig. 3.1). It is unlikely that there is a significant amount of gas

ID	ν_{obs} (GHz)	$z_{\mathrm{CO(1-0)}}$	ΔV (km/s)	$S\Delta V^{\dagger}$ (Jy km/s)	S_{ν} Peak (mJy)	$\mu L'_{\mathrm{CO}}$ (10^{10} K km s^{-1}pc^2)
PJ105353.0	28.7712	3.0053 ± 0.00016	738 ± 38	4.3 ± 1.3	6.2 ± 1.9	170 ± 60
PJ112714.5	35.6248	2.2352 ± 0.00006	736 ± 20	7.4 ± 2.2	9.3 ± 2.8	178 ± 63
PJ120207.6	33.4970	2.442 ± 0.00007	602 ± 21	5.5 ± 1.7	8.9 ± 2.7	154 ± 55
PJ132302.9	33.7350	2.4165 ± 0.00006	540 ± 17	4.7 ± 1.4	8.4 ± 2.5	129 ± 46
PJ142823.9	49.5766	1.3254 ± 0.00005	436 ± 25	1.2 ± 0.4	2.9 ± 0.9	11 ± 4
PJ160722.6	46.4115	1.4838 ± 0.00006	374 ± 27	1.0 ± 0.3	2.4 ± 0.7	12 ± 4
PJ160917.8	27.0911	3.2567 ± 0.00014	705 ± 31	7.6 ± 2.3	9.8 ± 2.9	343 ± 121

Table 3.2: Summary of CO(1-0) VEGAS Measurements. T_A^* to flux density using the *GBT* : Q band is 1K/1.7 Jy, Ka band is 1K/1.6 Jy. The reported redshifts correspond to the values obtained after velocity offset corrections. The line widths reported indicate the FWHM values after correcting for the instrumental resolution. This correction was on average less than 1% due to large observed line widths. † The integrated value obtained within the interval of ±1500 km s^{-1}from the center.

that excites the CO(1-0) but not, e.g. the CO($3-2$). Therefore, the similar line emission FWHM and line profiles suggests that both transitions are tracing co-spatial volumes.

We calculated the line luminosity, $L'_{\mathrm{CO(1-0)}}$, using Eq. (3) by Solomon et al. (1997). Since the CO lines are not exactly Gaussian, we also integrated the spectra within ±1500 km s^{-1}to compute $S_{\mathrm{CO}}\Delta V$. The corresponding Gaussian derived values of $S_{\mathrm{CO}}\Delta V$ are the same within 1-sigma. Some of the measured apparent L'_{CO} are amongst the brightest, if not the brightest, for all $z > 1$ QSO, SMG, LBG, including the SPT DSFGs (Aravena et al., 2016), as well as $z < 1$ ULIRGs, nearby spirals, and low-z starburst galaxies (Carilli & Walter, 2013). These bright apparent luminosities suggest that our galaxies have been strongly magnified.

3.6 Discussion

3.6.1 CO Spectral Line Energy Distributions (SLEDs)

In Fig 3.2 we plot the ratio of the line integrated intensity of the higher-J CO $S_{\mathrm{CO}}\Delta V$ to our CO(1-0) $S_{\mathrm{CO}}\Delta V$. All of our galaxies show sub-thermalised excitation conditions. Up to $J \leq 3$, we find these values to be consistent with both the lower end of the SMG excitation distribution (Bothwell et al., 2013; Carilli & Walter, 2013) and the upper end of the MW (Fixsen et al., 1999). The uncertainty of the MW measurements and the physical intrinsic SMG dispersion overlap for $J \leq 4$. Without higher-J CO lines, where SMGs and the MW differ strongly, it is a challenge to disentangle which of these two ISM conditions dominate our galaxies.

We parametrized these CO SLEDs in terms of brightness temperature, or CO line luminosity, ratios,

$$r_{up,1} = \frac{T_B(J_{upper} > 1)}{T_B(1-0)} = \frac{L'_{CO}(J_{upper} > 1)}{L'_{CO}(1-0)}.$$

For two sources with only r_{21} we found $< r_{21} >= 0.92$, while the remaining five sources have $< r_{31} >= 0.34$. Finally, for the one source with a CO($4-3$) line observation, we found $r_{41} = 0.18$, similar to what has been reported in Hainline et al. (2006) for an SMG of similar redshift (i.e.

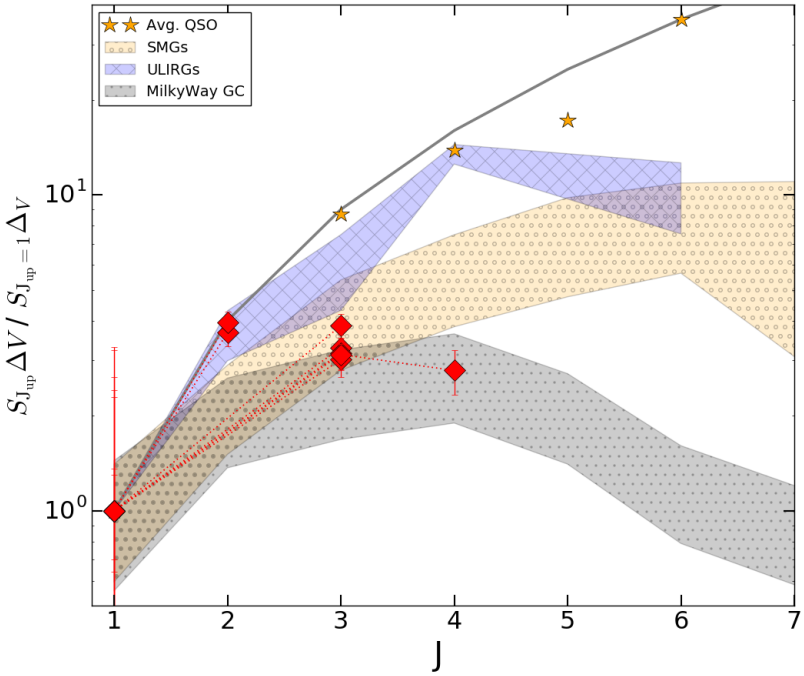

Figure 3.2: Here we plot the velocity-integrated line intensity ratios of J_{up}/J= 1, normalised to the CO(1-0) derived integrated flux for the current sample. Our seven galaxies (red diamonds) are within the spread for average SMGs (Bothwell et al., 2013) (yellow), and can be compared to the low-z (U)LIRG population (Papadopoulos et al., 2012a) (blue), and the Milky Way center (Fixsen et al., 1999) (gray). All regions contain the dispersion between the 25th and 75th percentile of the distribution of the CO(1-0) normalised integrated flux. Yellow stars show the average QSO values out to J = 6 (Carilli & Walter, 2013).

ID	$L(IR)/L'_{CO(1-0)}$ $L_\odot/(Kkms^{-1}pc^2)$	$r_{up,1}$	μM_{ISM} $(10^{10}M_\odot)$	μM_{H2} $(\alpha_{CO}4.3, 0.8)(10^{10}\ M_\odot)$	τ_{depl}-CO $(\alpha_{CO}4.3, 0.8)$ (Myr)	τ_{depl}-ISM (Myr)
PJ105353.0	170 ± 65	$0.36 \pm 0.13[r_{31}]$	624 ± 156	[732, 136] ± [259, 54]	[239, 44]	203
PJ112714.5	62 ± 25	$0.29 \pm 0.10[r_{31}]$	160 ± 40	[764, 142] ± [270, 27]	[636, 118]	133
PJ120207.6	91 ± 38	$0.4 \pm 0.14[r_{31}]$	452 ± 113	[663, 123] ± [234, 30]	[442, 82]	302
PJ132302.9	93 ± 36	$0.31 \pm 0.11[r_{31}]$	215 ± 54	[557, 103] ± [196, 23]	[425, 79]	164
PJ142823.9	168 ± 69	$0.88 \pm 0.36[r_{21}]$	97 ± 24	[49, 9] ± [17, 4]	[228, 42]	452
PJ160722.6	121 ± 50	$0.95 \pm 0.38[r_{21}]$	52 ± 13	[50, 9] ± [18, 5]	[331, 62]	344
PJ160917.8	58 ± 24	$0.35 \pm 0.13[r_{31}]$	465 ± 116	[1473, 274] ± [521, 85]	[694, 129]	219
PJ160917.8	–	$0.18 \pm 0.06[r_{41}]$	–	–	–	–

Table 3.3: Gas Properties.Unknown lensing amplification μ is reflected in the derived CO luminosity and H_2 mass. ISM masses were calculated following Scoville et al. (2016b), scaled to our AzTEC 1.1mm photometry with a fixed dust temperature of 25 K.

$z \sim 3.3 - 3.5$). As noted in (Frayer et al., 2011), there is a wide-range in the observed $r_{31} = 0.1 - 1$ in the local starburst population. The fact that our galaxies fall in the lower end of the SMG excitation distribution, while being some of the most luminous sources currently known, suggests that they may not be exceptional SMGs, but more strongly magnified sources.

In Harrington et al. (2016) we showed that all of these sources fall within the parameter space for SF powered luminosity (rather than AGN) in a mid-IR to far-IR color-color diagnostic plot (Kirkpatrick et al., 2013). Using their CO SLED we can further rule out the presence of a powerful QSO in our galaxies, as typical QSO host galaxies with powerful AGN activity often exhibit thermalised line ratios out to $CO(4-3)$ (e.g Riechers et al., 2006; Weiß et al., 2007a). However, we caution that most QSO hosts with a good coverage in the CO SLED are strongly lensed objects selected in the optical/NIR. This may result in a bias towards the excitation conditions within the central region. Sharon et al. (2016) show there is a statistical similarity between the r_{31} values reported for SMGs and AGN in their sample. However, the line ratios in their sample have a global average (AGN and SMG) 3 times higher for r_{31} (in fact close to thermalised: $< r_{31} >= 0.9$) as compared to our sources. This suggests that their sample might consist of hybrid SMG/AGN galaxies. Our CO SLEDs are currently limited out to J = 3 or 4, therefore we cannot rule out the presence of an AGN.

3.6.2 Ratio of IR Luminosity to CO Line Luminosity

The observable $\mu L_{IR}/\mu L'_{CO(1-0)}$ ratio serves as a proxy for SF efficiency (SFE), and stands independent of the unknown magnification factor [1]. The integrated IR emission (8-1000μm) reflects the bulk star-forming activity, while the CO line luminosity indicates the amount of gas supplying the ongoing star formation.

Using the value of this ratio we place our sample in the context of SB versus typical star-forming galaxies at different z, IR and CO line luminosity (Fig 3.3; e.g. Genzel et al., 2010). We measure the $\mu L_{\rm IR}/\mu L'_{\rm CO(1-0)}$ ratio as (58-170) $\rm L_\odot/(K\,kms^{-1}pc^2)$, with $< 110 \pm 22 >$ $\rm L_\odot$ / K km s^{-1}pc^{-2} (see Fig 3.3). The average value of our galaxies is closer to 140 $L_\odot/(Kkms^{-1}pc^2)$ observed in SB galaxies, rather than 30 $L_\odot/(Kkms^{-1}pc^2)$ observed in typical star-forming galaxies (Solomon & Vanden Bout, 2005; Genzel et al., 2010; Frayer et al., 2011). From this we conclude that the $L_{\rm IR}/L'_{\rm CO(1-0)}$ values obtained for this subset of *Planck-Herschel* sources have enhanced ratios with respect to typical star-forming galaxies, as expected from their large apparent $L_{\rm IR}$ (Cañameras et al., 2015; Harrington et al., 2016).

We note that our sample exhibits slightly lower ratios on average compared to both the highly excited system, HFLS-3 ($z \sim 6$ Riechers et al., 2013), as well as the lensed SPT DSFGs (Aravena et al., 2016) (Fig 3.3). Roughly half of the strongly lensed, dusty *Herschel* galaxies (Harris et al., 2012) are consistent with our sample and lie within the yellow shaded region for SB systems. In contrast, more than half of the SPT sources have excess $L_{\rm IR}$-to-$L'_{\rm CO(1-0)}$ Aravena et al. (2016), although the dispersion is similar for both H-ATLAS and SPT samples. Our seven *Planck-Herschel* sample are unusual as they lack a similar dispersion. This may reflect the ability of the all-sky sub-mm sensitivy and coverage of the *Planck* survey in detecting the rare galaxies that are, on average, more strongly lensed than the similarly selected H-ATLAS sample.

While the SPT lensed galaxies are a similar population at high-z with comparable L_{IR}, due to

[1] We assume, without high angular resolution imaging of the two luminosity sources, that the CO(1-0) emitting region and the pervasive dust content are on average co-spatial.

different selection methods (350 μm versus mm), the average redshift of their sample is significantly shifted towards a higher value compared to our sample: $< z >= 3.9$ and $< z >= 2.3$, respectively. At such a high redshift, $z \sim 4$, a MW type galaxy would be subject to non-negligible dust heating due to the CMB (da Cunha et al., 2013), and may contribute to the higher L_{IR}-to-$L'_{CO(1-0)}$ values observed in the SPT sample. At $z \sim 4$, the CMB temperature is also a sufficient background to radiatively excite the cool reservoirs of CO, particularly the J= $1 \rightarrow 0$ ground state rotational transition, resulting in a dimming of the observed CO line emission. Because (sub)-mm flux measurements are made against the CMB, the contrast in the CO $(1-0)$ line integrated intensity via collisional excitation (typically with H_2molecules), compared with the radiatively excitated CO gas from the CMB background becomes more severe beyond $z = 4$. About 80% of the CO $(1-0)$ emission can be recovered against the CMB at $z = 2-3$, but only 50-60% just beyond $z = 4$ if there would be a gas kinetic temperature of 40 K (da Cunha et al., 2013).

We caution that the effects of the CMB alone cannot account for the differences observed in these luminosity-luminosity ratios, as the H-ATLAS and SPT sample have a similar spread in their $L_{\rm IR}$-to-$L'_{\rm CO(1-0)}$ values. The similar redshift range of the 12 H-ATLAS sample compared to the sample of 7 *Planck-Herschel* galaxies in this study reveals that the CMB effects cannot explain this offset. The excitation conditions of a multi-phase, multiple gas component ISM are also expected to change for each galaxy. One would expect that the density and kinetic temperature of the CO $(1-0)$ emitting gas (and the gradients across the galaxy) to factor into the total attenuation of the CO $(1-0)$ line emission (e.g. Tunnard & Greve, 2017) and any self-shielding. As the intense star-forming conditions during the redshifts indicated in these three samples (SPT, H-ATLAS, *Planck-Herschel*) will give rise to a dynamic set of ISM conditions, these varying gas excitation conditions will therefore have non-negligible effects in the observed $L_{\rm IR}$-to-$L'_{\rm CO(1-0)}$ values.

3.6.3 Total gas mass from $L'_{\rm CO(1-0)}$

CO is the second most abundant molecule in the ISM after the highly abundant molecular hydrogen, H_2, and the CO(1-0) line emission is the most direct proxy for H_2as it traces even the most diffuse gas. Our galaxy integrated CO(1-0) line luminosity is converted to a total molecular gas mass assuming an α_{CO} conversion factor (see review by Bolatto et al., 2013). It is common to use a standard ULIRG conversion, i.e. $\alpha_{CO} = 0.8$, for star bursting SMG/DSFGs at high-z, although we reference a standard Galactic value in Table 3.3. The similarity of the $L_{\rm IR}/L'_{\rm CO(1-0)}$ ratios observed in our sample and those of local ULIRGs seems to further support the use of a starburst-like $\alpha_{\rm CO}$ conversion factor, even if the centrally compact, concentrated nuclei in local ULIRGs may not be representative of the entire ISM environments in our galaxies. We found $\mu M_{\rm H2} = (0.9-27.4) \times 10^{11} {\rm M}_{\odot} (\alpha_{CO}/0.8)$, which are amongst the largest apparent gas contents measured at high-z, even if a lensed magnification of an order of magnitude is taken into account (see Carilli & Walter, 2013).

We also compare our CO-based gas mass to the ISM gas mass estimates using the empirical calibration from measured rest-frame dust continuum (e.g. Scoville et al., 2016b, 2017). Using our AzTEC 1.1mm photometry ($\nu_{\rm obs}$ = 272 GHz $\rightarrow$ rest-frame 250-470μm), we compute the ISM mass using Eq. 14 of Scoville et al. (2017). The ISM masses we report scatter predictably around the values obtained from a ULIRG or Galactic conversion factor, suggesting that the value for $\alpha_{\rm CO}$ varies intrinsically from galaxy to galaxy. Later we will revisit this empirical calibration to compare the CO line luminosity to the specific luminosity at rest-frame 850μm.

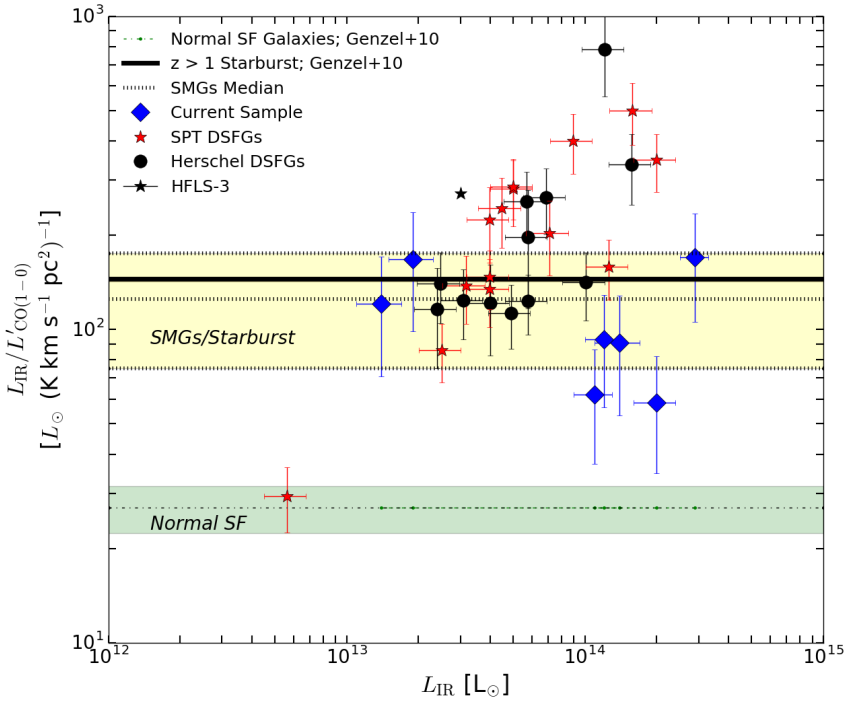

Figure 3.3: Here we present the $L_{\rm IR}/L'_{\rm CO(1\text{-}0)}$ ratios of our sample compared with known, lensed *Herschel* and SPT DSFGs (Harris et al., 2012; Aravena et al., 2016), the highly excited HFLS-3 (Riechers et al., 2013) and the median for all SMGs ($125 \pm 50 L_\odot/Kkms^{-1}pc^{-2}$) compiled in the literature by Frayer et al. (2011) (shaded yellow). We plot 2σ boundaries taken from Genzel et al. (2010) for starburst ($140\ L_\odot/Kkms^{-1}pc^{-2}$) and typical star-forming galaxies ($30\ \ L_\odot/K\,kms^{-1}pc^{-2}$). The average for our seven targets in this study is $110 \pm 22\ L_\odot/(Kkms^{-1}pc^2)$.

3.6.4 Gas Depletion Time Scales

The amount of time for a galaxy to consume its total molecular gas, given its current galaxy integrated star formation rate, is its so-called depletion time, or gas consumption time scale, $\tau_{\rm depl} = \mu M_{\rm H2}/\mu SFR$. This inverse SFE reflects the nature of the SF activity of a galaxy, and is a measure that stands independent of the magnification factor in the same way for the $L_{\rm IR}$-to-CO$(1-0)$ line luminosity ratios above.

To derive our SFR estimates we used the integrated 8-1000μm SED and the empirical calibration (Kennicutt, 1998) to convert $L_{\rm IR}$ to SFR – adopting a Kroupa IMF. The values we obtain are, uncorrected for magnification amplification, $\sim 1500 - 30700\ M_\odot yr^{-1}$ (Harrington et al., 2016). Combined with the CO-based gas masses reported above, this suggests a depletion time scale of $\tau_{\rm depl} \sim 80$ Myr These actively evolving galaxies represent a special mode of rapid starburst activity. This is consistent with short gas depletion times observed on the order of $\tau_{depl} = 10 - 100$ Myr (e.g. Genzel et al., 2015a; Béthermin et al., 2016; Aravena et al., 2016; Scoville et al., 2016b), and also with typical

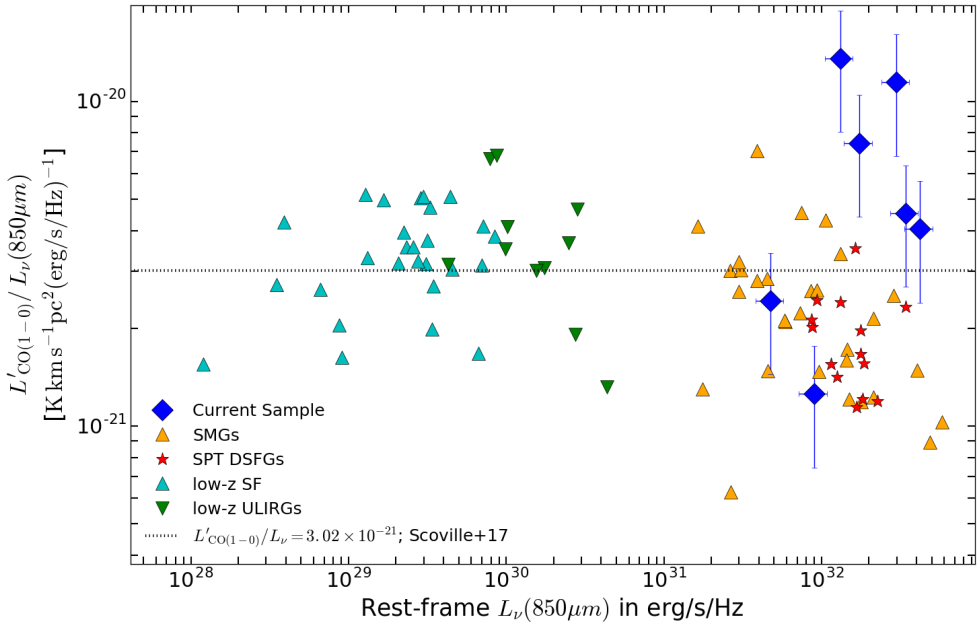

Figure 3.4: We compare our measured $L'_{\rm CO(1\text{-}0)}$ to rest-frame $L_{\nu(353GHz/850\mu m}$ in our sample to the low-z star-forming galaxies (Dale et al., 2012; Young et al., 1995), local ULIRGs (Mentuch Cooper et al., 2012; Chu et al., 2017; Sanders et al., 1989, 1991; Solomon et al., 1997), $z \sim 2$ SMGs (Greve et al., 2003; Ivison et al., 2011; Harris et al., 2012; Riechers et al., 2011; Lestrade et al., 2011; Thomson et al., 2012; Fu et al., 2013; Aravena et al., 2013; Thomson et al., 2015), and lensed SPT galaxies (Aravena et al., 2016) with global measurements of CO(1-0) – or CO(2 – 1) for some SPT sources, where we used $r_{21} = 0.9$ when applicable. We overplot the best fit linear relation from Scoville et al. (2017): $L'_{\rm CO(1\text{-}0)} = 3.02 \times 10^{-21} L_{\nu 850}$.

galaxy-galaxy crossing time ($\sim$ 100Myr; (Scoville et al., 2016b)). The rapid $\tau_{\rm depl}$ in these galaxies at high-z rival the $\tau_{\rm depl} = 2.2$ Gyr timescales for normal star-forming galaxies at $z = 0$ (Leroy et al., 2013).

3.6.5 Global Gas to Dust Comparison

The ratio of measured $L'_{\rm CO(1\text{-}0)}$ to rest-frame specific luminosity at 850μm serves as a foundation for converting the optically thin Rayleigh-Jeans dust continuum, observed in the (sub)-mm, into total ISM mass (Scoville et al., 2017, 2016b, 2017). To infer the rest-frame 850μm of our galaxies, and thus to compare them to the empirical relation, we use the far-IR SED model fit procedure described by Harrington et al. (2016), fitting the *Herschel* SPIRE 250-500 μm and AzTEC 1.1mm photometry with a modified blackbody (Eq. 14 Yun & Carilli, 2002) (Fig. 3.4). Several of $z \sim$ 2-3 galaxies lie above the empirical calibration obtained by Scoville et al. (2017). In Scoville et al. (2017) the SED analyses was redone using the published sub-mm photometry and CO(1-0) line emission for the 30 normal low-z star-forming galaxies (Dale et al., 2012; Young et al., 1995), 12 low-z ULIRGs (Mentuch Cooper et al., 2012; Chu et al., 2017; Sanders et al., 1989, 1991; Solomon et al., 1997), and 30 SMGs (Greve et al., 2003; Ivison et al., 2011; Harris et al., 2012; Riechers et al., 2011; Lestrade et al., 2011;

Thomson et al., 2012; Fu et al., 2013; Aravena et al., 2013; Thomson et al., 2015) at comparable redshifts to our sample. This empirical relation, based primarily on galaxies with solar metallicities, was recently validated using ~ 70 main-sequence, low-z star-forming galaxies (Hughes et al., 2017). Without optical or FIR fine-structure emission lines we cannot directly constrain the metallicities of our sample. However, we do not expect these galaxies to have sub-solar metallicities given their large apparent dust masses ($\mu M_{\rm d} = [0.1 - 2] \times 10^{10} M_{\odot}$) and given the empirical mass-metallicity relationship out to high-z (Geach et al., 2011; Saintonge et al., 2016a).

The SMG/DSFG population predominantly falls below the 1:1 relation, making our small sample the first to populate the upper envelope–which corresponds to a higher amount of observed CO gas per unit 850μm dust emission. The highest value of $L'_{\rm CO}/L_{850}$ observed in the SMG population compiled by Scoville et al. (2017) is the 350μm selected source in Ivison et al. (2011). Two of our galaxies are above the observed scatter, while three of our galaxies exhibit extreme CO luminosities compared to their rest-frame dust luminosity. A larger sample is undoubtedly required to further unveil if, as suggested by our sample, there is a larger intrinsic scatter at high-z, particularly at $\log(L'_{\rm CO(1\text{-}0)}) > 10.5\ K\ km\ s^{-1}\ pc^2$ and $\log(L_{\nu 850}) > 31.5\ ergs^{-1}Hz^{-1}$. To compare to the SPT-DSFGs with J$\leq$ 2 CO line detections (Aravena et al., 2016), we take their 18 galaxies with consistent sampling of 0.25-1.4mm photometry, similar to our 0.25-1.1mm data, and fit their FIR-mm SEDs as described above. Those SPT galaxies with only CO(2 − 1) were converted to $L'_{CO(1-0)}$ using an $r_{21} = 0.9$.

The relatively high $L'_{\rm CO}/L_{850}$ ratios observed in our galaxies indicate larger gas-to-dust mass (GDMR) ratios than observed in previous samples (Fig. 3.4). Converting the AzTEC 1.1mm continuum measurement into dust mass, assuming $T_{\rm d} = 25$K, we found GDMRs in the range [40-200] using the CO-based gas mass ($\alpha_{\rm CO} = 0.8$), compared with the average GDMR of ~ 230 from the 1.1mm derived ISM mass (Scoville et al., 2017). This range is both consistent, though slightly larger, than observed in local galaxies with solar metallicities (Leroy et al., 2011; Draine et al., 2007). Assuming instead a Galactic $\alpha_{\rm CO} = 4.3$, we would infer extremely high GDMRs (up to 1100), only observed in local, greatly metal-poor dwarf galaxies. The assumption of $\alpha_{\rm CO}$, as well as the choice of dust temperature in the ISM mass calculations ultimately determines the derived GDMRs.

3.7 Conclusions

Using VEGAS on the *GBT*, we have successfully measured the CO(1-0) line emission for seven of the most gas-rich SMGs/DSFGs studied to date. The key results of this study can be summarised as:

- We have confirmed the previously determined spectroscopic redshifts reported by Harrington et al. (2016)
- The linewidths/profiles for the low-J RSR and CO(1-0) VEGAS measurements are nearly identical; therefore the emitting regions are likely co-spatial, with $< FWHM >= 590$ km s^{-1},
- The CO SLEDs of the galaxies in our sample are indicative of a gas component with sub-thermal excitation conditions: CO line luminosity ratios of $< r_{21} >= 0.92$ (2 sources), $< r_{31} >= 0.34$ (5 sources), and $r_{41} = 0.18$ (1 source)
- We find enhanced $L_{\rm IR}/L'_{\rm CO(1\text{-}0)}$ ratios with respect to normal star-forming systems, as we report an average value of $110 \pm 22\ L_{\odot}/(Kkms^{-1}pc^2)$, comparable to the median of other well studied SMGs.

With the CO(1-0) line emission we place tight constraints on the total molecular gas mass, and allow future CO SLED analyses to benefit from having the fundamental rotational transition observed. The large gas masses obtained are $\mu M_{\rm H2} = (0.9 - 27) \times 10^{11} (\alpha_{\rm CO}/0.8)\ {\rm M}_{\odot}$. The average gas depletion time we find is $\tau_{\rm depl} \sim 80$ Myr. These extremely luminous IR galaxies (with $L_{\rm IR} \geq 10^{13-14} {\rm L}_{\odot}$) exhibit rapid depletion timescales, and we are likely capturing this light from a relatively short-lived starburst episode.

CHAPTER 4

Observations and Modelling of Cool, Turbulent, Molecular Gas in Lensed *Planck*-Selected Starburst Galaxies at $z \sim 1 - 3.5$

The contents of this chapter are based on an upcoming publication in The Astrophysical Journal (ApJ), under the title " Turbulent, Molecular Gas in Lensed *Planck*-Selected Starburst Galaxies at $z \sim 1 - 3.5$":

- Harrington, K.C., Weiß, A., et al. (revised version submitted to ApJ September 18, 2020)

4.1 Abstract

Dusty star-forming galaxies at high redshift ($1 < z < 3$) represent the most intense star-forming regions in the Universe. Key aspects to these processes are the gas heating and cooling mechanisms. Although it is well known that these galaxies are gas-rich, little is known about the gas excitation conditions, as only few detailed radiative transfer studies have been carried out due to a lack of line detections per galaxy. Here we examine these processes in a sample of 24 strongly lensed star-forming galaxies identified by the *Planck* satellite (*LPs*) at $z \sim 1.1 - 3.5$. We analyze 162 CO rotational transitions (ranging from $J_{up} = 1 - 12$) and 37 atomic carbon fine-structure lines ([CI]) in order to characterize the physical conditions of the gas in sample of *LPs*. We simultaneously fit the CO and [CI] lines, and the dust continuum emission, using two different non-LTE, radiative transfer models. The first model represents a two component gas density, while the second assumes a turbulence driven log-normal gas density distribution.

4.2 Introduction

Star-forming galaxies at redshifts $z \sim 1-3$ probe the cosmic epoch when most of the stellar mass assembly in the Universe took place (Madau & Dickinson, 2014, and references therein). A better understanding of star formation (SF) during this epoch is therefore imperative to understand SF across cosmic time. Locally, less than 5% of the galaxy population has a star formation rate (SFR) that is significantly higher than the empirical main-sequence for star-forming galaxies, i.e. the tight correlation (∼0.3 dex) between the SFR and stellar mass, $M_\star$ (Brinchmann et al., 2004; Noeske et al., 2007; Elbaz et al., 2007; Goto et al., 2011; Sargent et al., 2012; Whitaker et al., 2012, 2014; Salmon et al., 2015). These often-called starburst galaxies, with an infrared (IR) luminosity $L_{\rm IR} \sim 0.1-5\times10^{12}$ $L_\odot$ (e.g. Sanders & Mirabel, 1996; Downes & Solomon, 1998), become increasingly more common at high-z . In fact, (sub)mm number counts reveal that galaxies with $L_{\rm IR} > 10^{12-13}$ $L_\odot$, at $z > 0.5$, are many hundreds of times more likely to exist than in the local Universe (Blain et al., 2002; Chapman et al., 2005; Béthermin et al., 2012; Magnelli et al., 2013; Casey et al., 2013; Geach et al., 2013; Simpson et al., 2014; Strandet et al., 2016; Casey et al., 2014). Meanwhile, the cosmic molecular gas density also peaks at $z \sim 1-3$ (Decarli et al., 2014; Walter et al., 2014; Lentati et al., 2015; Decarli et al., 2016; Riechers et al., 2019; Liu et al., 2019). This suggests a strong link between molecular gas and SF. Rest-frame far-infrared (FIR) measurements of spectral lines and thermal dust continuum emission have been used to investigate the cooling and heating processes of the interstellar medium (ISM) in star-forming galaxies, however the physical conditions at high-z is still, in general, poorly investigated (Popesso et al., 2012; Bothwell et al., 2013; Carilli & Walter, 2013; Genzel et al., 2013; Yang et al., 2017; Tacconi et al., 2018, 2020; Lenkić et al., 2020; Aravena et al., 2020).

Turbulence regulates SF within cold and dense molecular clouds in most star-forming regions, and turbulence-regulated feedback seems to properly describe the main characteristics of the star-forming ISM (Shu et al., 1987; Elmegreen & Scalo, 2004; Krumholz & McKee, 2005; McKee & Ostriker, 2007; Krumholz, 2014). A log-normal probability distribution function (PDF) is often used to describe both the molecular gas velocity dispersion and volume density (Vazquez-Semadeni, 1994; Padoan et al., 1997; Ostriker, 1998; Klessen, 2000; Wada & Norman, 2001; Kowal et al., 2007; Narayanan et al., 2008b,a; Krumholz et al., 2009a; Molina et al., 2012; Hopkins et al., 2013). This is because the turbulent activity sets the local gas density as a consequence of randomly distributed shocks that compress the gas. This processes eventually converge towards a log-normal distribution of density due to the central-limit theorem (Vazquez-Semadeni, 1994; Kevlahan & Pudritz, 2009; Krumholz, 2014). Such turbulent models are supported by observational evidence using optically thin, diffuse *and* dense molecular gas tracers of clouds within the Milky Way (e.g. Ginsburg et al., 2013). A commonly used simplification to deal with these complex models is to adopt the Large Velocity Gradient (LVG) approximation (Goldreich & Kwan, 1974; Scoville & Solomon, 1974) to model the photon escape probabilities within large-scale velocity flows. This assumption is applicable for clouds in the Milky Way, where the local thermal motions are much smaller than flow velocities, although non-local thermodynamic equilibrium (non-LTE) gas conditions may be present. The radial motion assumed in early applications of non-LTE LVG models would lead to higher SF efficiencies than observed, leading to the conclusion that a form of turbulent feedback must be present in the ISM to regulate SF (Zuckerman & Evans, 1974; Zuckerman & Palmer, 1975). In addition, turbulent motion is set at the 'driving scale' (e.g. Elmegreen & Scalo, 2004; Scalo & Elmegreen, 2004), determined by the largest physical size of the system. Diverse studies have found that gas turbulence increases as a function of

z, suggesting such star-formation processes cannot be maintained for long periods of time (several orbital times) – particularly in the most extreme star-forming galaxies (Kassin et al., 2012; Wisnioski et al., 2015; Johnson et al., 2018; Übler et al., 2019). How the turbulent ISM behaves at high-z , given the strong cosmic evolution of star-forming gas, is still an open question.

Star-forming galaxies at high-z may have turbulent SF extending many kiloparsecs beyond their center, with total molecular gas masses up to an order of magnitude larger than local starbursts (Tacconi et al., 2006; Hodge, 2010; Ivison et al., 2010; Hodge et al., 2016; Kirkpatrick et al., 2017b). Therefore, it is crucial to derive the bulk molecular gas mass content in these host galaxies in order to properly quantify the SF activity as a function of the molecular gas properties. The main challenge in studying the star-forming gas is that cloud collapse requires cold environments, with T $\leq$ 100 K, yet the lowest energy transitions of H_2 are much higher than these temperatures. Therefore H_2 is unable to trace the total column density (i.e. total mass) of gas (e.g. 1-30% of the gas column density; Roussel et al., 2007). Carbon Monoxide (CO) is the second most abundant molecule in the ISM and is almost exclusively excited by collisions with H_2. Since it is one of the primary tracers of the H_2 gas column density, it offers a unique opportunity to study these cold gas properties in star-forming galaxies.

The CO line luminosity to molecular gas mass conversion factor, $\alpha_{\rm CO}$, has been reviewed by several detailed studies (Magdis et al., 2011; Genzel et al., 2012; Narayanan et al., 2012; Schruba et al., 2012; Bolatto et al., 2013; Hunt et al., 2015; Amorín et al., 2016; Accurso et al., 2017). The CO(1-0) and CO(2-1) rotational transitions, and their less optically thick isotopologues (^{13}CO, C^{18}O), have been vital in determining the $L'_{\rm CO}$-to-$M_{\rm H_2}$ conversion factor, $\alpha_{\rm CO}$. The Galactic value is $\alpha_{\rm CO} \sim 4$ M$_\odot$ (K km s^{-1} pc^2)$^{-1}$, whereas the canonical value for local starburst galaxies is $\alpha_{\rm CO}$ ~0.8 M$_\odot$ (K km s^{-1} pc^2)$^{-1}$ (Downes & Solomon, 1998). CO traces diffuse and dense gas, however the atomic carbon, fine-structure line transitions ([CI] lines) are able to trace mostly diffuse gas (Glover & Clark, 2012; Israel et al., 2015). [CI] is an additional tracer capable of determining the molecular H_2 gas mass (Weiß et al., 2003, 2005a). Efforts to calibrate the [CI] transitions as a tracer of the molecular gas mass, and attempts to constrain the gas-phase carbon abundance, have grown significantly, including high-z massive star-forming galaxies on the main-sequence and bright quasars (Walter et al., 2011; Alaghband-Zadeh et al., 2013; Bothwell et al., 2017; Dannerbauer et al., 2019; Valentino et al., 2020). This is mostly based on the relative increase in detection efficiency of the [CI] ground transition as it gets redshifted at $z > 1$ into mm wavelengths, due to the higher photon energy in the [CI] lines. This makes it easier to detect than the faint ground-state CO(1-0) line. For the cold (T ~ 20 K) and low density ($\log(n(H_2)) \sim 2$ cm^{-3}) ISM, dominating the emission in the Milky Way (Dame et al., 1986; Bronfman et al., 1988; Fixsen et al., 1999; García et al., 2014), the CO(1-0) line luminosity has traditionally been used as a tracer of the total molecular gas content (Bolatto et al., 2013), as higher molecular rotational levels are poorly populated under these conditions. Following early studies in the Milky Way, this approach has been widely applied to determine the molecular gas content in nearby star-forming galaxies. The general scenario may differ for higher excitation gas (or increased SF activity), as the higher-J level populations can contribute a more significant fractional contribution to the CO partition function. For intense star-forming environments, where the mean gas density is larger than 10^{3-4} cm^{-3} and/or the gas kinetic temperature is higher than 20 K, the CO(2-1) and CO(3-2) and even higher rotational transitions begin to contribute a higher fraction to the partition function, as less molecules sit at the $J_{\rm up}$ = 1 state. Thus, these low-J lines can trace comparable, if not

larger, fractions of the total CO column densities (and thus more molecular gas) as the CO(1-0) line. This highlights the need to measure multiple CO transitions and conduct a proper modelling of the line intensities to obtain meaningful conversion factors for star-forming galaxies at $z > 1$.

Local measurements of the CO ladder in large samples of star-forming and starburst systems have been conducted using the *Herschel*SPIRE (and HIFI; Rangwala et al., 2011; Liu et al., 2015; Kamenetzky et al., 2016; Rosenberg et al., 2015; Lu et al., 2017). On average, the majority of the SF in local starburst galaxies is confined to the central few hundred parsecs of the Galactic nucleus. Most extreme IR luminosities in the local Universe are induced by merger-driven processes, although, in general, there is a strong presence of warm and diffuse molecular gas (see e.g. Downes & Solomon, 1998), well-traced by the mid-to-high-J CO lines (Rosenberg et al., 2015; Kamenetzky et al., 2016). Constraints on such galaxy-wide molecular ISM properties at $z > 1$ have been limited to large integration times required to sample the low-, mid-, and high-J CO lines. Less than twenty years ago, only ~40 galaxies at $z > 1$ had been detected in CO emission (Solomon & Vanden Bout, 2005; Omont, 2007). Carilli & Walter (2013) reviewed ~ 200 galaxies, most with a single line detection (J_{up} = 2-5). At the time, only eleven high-z galaxies had one (or both) [CI] line detection(s) (Weiß et al., 2005a; Walter et al., 2011; Carilli & Walter, 2013).

Strong gravitational lensing of high-z star forming galaxies offers a unique way to examine highly magnified molecular gas. The method for selecting strongly lensed dusty galaxy candidates, at $z > 1$, is primarily based on unusually bright (sub)mm fluxes compared to the expected steep drop-off in (sub)mm number counts (e.g. Negrello et al., 2007). This method has since identified a large number across the extragalactic sky, i.e. more than 100 lensed candidates at $z > 1$ (Ivison et al., 2010; Wardlow et al., 2013; Negrello et al., 2017b; Bussmann et al., 2013, 2015; Vieira et al., 2010; Weiß et al., 2013; Strandet et al., 2016; Cañameras et al., 2015; Harrington et al., 2016; Díaz-Sánchez et al., 2017; Bakx et al., 2018). The lensed population of dusty star-forming galaxies selected by the South Pole Telescope *SPT*, *Herschel* Space Observatory and *Planck* have now been detected in more than two CO transitions (e.g. Spilker et al., 2016; Strandet et al., 2017; Yang et al., 2017; Bakx et al., 2020, and this work). The *Herschel*-selected, strongly lensed galaxy sample (Bussmann et al., 2013) offered the first systematic approach to producing a statistically significant sample of CO/[CI] lines (Yang et al., 2017), followed by a compilation in 11 *Planck* and *Herschel* selected lensed galaxies (Cañameras et al., 2018b), including four galaxies with both [CI] lines detected (Nesvadba et al., 2019). The IR to CO luminosity relations of local starbursts and high-z star-forming galaxies explored by Greve et al. (2014) indicate that the ISM radiation field is an important component to consider when understanding CO line excitation, yet this investigation was limited to 23 unlensed and 21 lensed dusty star-forming systems – all with more than three frequency measurements of the dust continuum and usually a single CO line detection. Most previous studies used only single and/or double component gas emitting regions to reproduce the observed CO emission, excluding the simultaneous modeling of the available [CI] emission, but also ignoring the role of the dust continuum emission as a heating source of the gas.

In this chapter, we focus on our application of state-of-the-art non-LTE models to ~ 200 CO and [CI] emission lines, from single-dish line measurements, for a flux-limited sample of 24 lensed galaxies identified by the *Planck* satellite. This sample builds off of our pilot *Planck*and *Herschel*selection in Harrington et al. (2016), expanded since then (Berman et al. in prep.). We have selected 24 of these galaxies to investigate the physical gas conditions responsible for driving such bright apparent FIR

luminosities ($\mu_L L_{IR} > 10^{14}$ $L_\odot$). We have a systematic focus on detecting the rise, peak and turnover in the CO excitation ladder in order to investigate the gas volume densities and turbulent properties, the relationship between the gas kinetic temperature and dust temperature, and the derivation of α_{CO}. We follow a novel approach when modelling all emission lines detected based on a turbulence-driven gas density PDF. Unlike most high-z studies, we have simultaneously modelled these lines in the presence of both dust continuum radiation field and CMB radiation as background excitation sources. We first describe the sample selection and ancillary dust photometry of the 24 strongly lensed galaxies in our sample.We then provide the details of the novel GBT, IRAM 30m, and APEX single-dish measurements of the CO ladder, ranging from $J_{up} = 1 - 12$, and both [CI] lines. Later we provide a summary of the emission line profiles, and thereafter summarize the models and model assumptions. We then discuss our main results, and finally we provide an interpretation of the physical gas conditions of these extreme starburst galaxies, with further conclusions afterwards. We adopt a fiducial ΛCDM cosmology with $H_0 = 69.6\,\mathrm{kms^{-1}Mpc^{-1}}$ with $\Omega_m = 0.286$, and $\Omega_\Lambda = 1 - \Omega_m$ throughout this chapter (Bennett et al., 2014)[1].

4.3 Sample

4.3.1 Selection

Here we outline our sample of strongly lensed *Planck* selected, dusty star-forming galaxies, hereafter "*LPs*" (Table 4.1). Our sample of 24 *LPs* began with a *Planck*& *Herschel*cross-match identification of eight objects (8/24) with continuum detections at 857 GHz (Harrington et al., 2016) greater than 100 mJy. The remaining 16/24 *LPs* were selected based on continuum detections by *Planck*, at 857, 545 and/or 353 GHz in the maps of all the available, clean extragalactic sky. These bright *Planck* point sources were then analyzed through a filtering process using a WISE color selection for the four WISE bands (3.4μm, 4.6μm, 12μm, 22μm Yun et al., 2008, Berman et al in prep.). Other methods to identify strong gravitational lenses using (sub)mm data were independently verified by other teams using *Planck*& *Herschel*color criteria (Cañameras et al., 2015). The 24 *LPs* presented in these analyses include eight systems identified by Cañameras et al. (2015). The use of *Planck*and WISE data resulted in the discovery of the brightest known, dusty starburst galaxy at $z > 1$, the 'Cosmic Eyebrow' (Díaz-Sánchez et al., 2017; Dannerbauer et al., 2019), which has also been independently recovered as one of the *LPs* presented in this survey work. Note that LPs-J1329 corresponds to the location on the sky associated with the *Cosmic Eyebrow-A* lens component (Dannerbauer et al., 2019). Table 4.1 shows the size of the lensed emission for each of the *LPs*, in which there are 21/24 with lens sizes $\leq 10''$. Half of the *LPs* are galaxy-galaxy lenses, while the other half are a mix of cluster or group lensing. The foreground lens galaxies have a negligible contribution to the observed far-IR emission of the lensed galaxy (Harrington et al., 2016). The *LPs* have CO-based spectroscopic redshifts ranging from $z_{CO} \sim$ 1.1 - 3.6 (Harrington et al., 2016, 2018; Cañameras et al., 2018b, and this work). They are comparable or brighter in CO and FIR luminosity than other strongly lensed SPT (Strandet et al., 2016, 2017; Weiß et al., 2013) or *Herschel*-selected dusty star forming galaxies (Harris et al., 2012; Bussmann et al., 2013, 2015; Yang et al., 2017). The *Planck*& *Herschel*wavelength selections preferentially target $z \sim 2 - 3$ galaxies, versus the mm-selected SPT sources with a median closer to $z \sim 4$, al-

[1] We have used *astropy.cosmology* (Astropy Collaboration et al., 2018).

though with a wide range between $z \sim 2-7$ (Strandet et al., 2016; Spilker et al., 2016; Weiß et al., 2013).

Our selection method only picks out sub-mm bright point sources, and the WISE data assists us in interpreting that these systems do not have the same mid-IR characteristics as the luminous WISE-selected, dust-obscured QSOs (Tsai et al., 2015). The prevalence of a dust-obscured AGN within the *LPs* is uncertain, however Harrington et al. (2016) and Berman et al. (in prep.) have shown, using *WISE* and *Herschel*data (see methods in, e.g. Kirkpatrick et al., 2015), that the majority of the *LPs* have a substantial contribution to the total IR luminosity from SF activity instead of AGN activity (see also Cañameras et al., 2015). The dusty nature of the *LPs* has thus far resulted in the absence of stellar mass estimates, yet the extreme nature of their IR luminosities suggests that it would be reasonable to assume they would lie above the main-sequence for star-forming galaxies at these redshifts. We therefore consider them starburst galaxies, without alluding to an assumed SF history.

4.3.2 Continuum data

The observed dust continuum and spectral energy distribution are used to constrain the excitation conditions, and a database of continuum measurements between 250 μm and 2 mm is compiled from new and archival photometry by *Planck*, *Herschel*, ALMA, LMT, JCMT, and IRAM 30-m telescopes. All of the ancillary (sub)mm photometric data used in this work can be accessed in the upcoming online table. We also provide the modelled continuum data from Berman et al. (in prep.), and we refer the reader to more detailed information reported in the literature for previous (sub)mm observations with the SMA, NOEMA and ALMA for a sub-set of the *LPs* (Bussmann et al., 2013; Cañameras et al., 2015; Harrington et al., 2016; Su et al., 2017; Geach et al., 2018; Rivera et al., 2019; Díaz-Sánchez et al., 2017; Dannerbauer et al., 2019). With the exception of the sources with ALMA 1 mm imaging data that fully resolves the continuum structure with better than $1''$ angular resolution, all other photometry come from low resolution observations that do not resolve the dust emission. There are ten *LPs* with ALMA 1 mm continuum measurements (Berman et al. in prep.). Six of these ten also have LMT-AzTEC measurements, which agree well with the comparable ALMA detection. The continuum measurements at $\lambda_{\rm obs}$ = 1-2 mm come from LMT-AzTEC (1.1mm) and/or IRAM 30m-GISMO2 (2mm) observations (Cañameras et al., 2015; Harrington et al., 2016, Berman in prep), and in some cases archival SCUBA-2 850μm data was available (Díaz-Sánchez et al., 2017, Berman et al. in prep.).
The measured (sub)mm flux densities of 10s to 100s of mJy are so large that source confusion is not relevant. An exception is the *Planck* data with effective resolution of $5'$. Here we adopt the photometry and uncertainty which fully incorporates the confusion noise based on the measured local foreground, leading to the conservative photometric uncertainties for the *Planck* data. The majority of the *LPs* have ancillary *Herschel*-SPIRE (250μm, 350μm, 500μm) and/or mm-wavelength measurements, which are useful to constrain the peak wavelength and the long-wavelength tail of the thermal dust emission. Additionally, previous work by Harrington et al. (2016) has shown that a minimal fraction of the far-IR emission is expected to come from the foreground lens for these systems.

ID	RA	DEC	z_{fg}	$z_{<CO/[CI]>}$	μ_L	$\mu_L^\dagger$	Lens size
	J2000	J2000					$''$
LPsJ0116^{I}	01:16:46.77	-24:37:01.90	0.4	2.12453	-	23	~4.5^{GG}
LPs-J0209^{II,III,IV,V,VI,VII,VIII}	02:09:41.3	00:15:59.00	0.202	2.55274	7 – 22	58	~3^{GG}
LPs-J0226^{I}	02:26:33.98	23:45:28.3	0.34	3.11896	-	40	~3.5^{GG}
LPs-J0305^{I}	03:05:10.62	-30:36:30.30	0.1-0.5	2.26239	-	18	~2^{GG}
LPs-J0748^{I,IX,X}	07:48:51.72	59:41:53.5	0.402	2.75440	-	21	~13^{GC}
LPs-J0846^{I}	08:46:50.16	15:05:47.30	0.1	2.66151	-	27	~10^{GC}
LPs-J105322^{I,XI,XII,XIII}	10:53:22.60	60:51:47.00	0.837	3.54936	5 – 12	41	~6^{GG}
LPs-J105353^{II,XI,XIV,XV,XII,XIII,XVI}	10:53:53.00	05:56:21.00	1.525	3.00551	9 – 48	20	~1.5^{GG}
LPs-J112714^{II,XI,XII,XIII,XVII}	11:27:14.50	42:28:25.00	0.33-0.35	2.23639	20 – 35	25	~13^{GC}
LPs-J112713^{I}	11:27:13.44	46:09:24.10	0.415	1.30365	-	21	~1.5^{GG}
LPs-J1138^{I}	11:38:05.53	32:57:56.90	0.6	2.01833	-	10	~1^{GG}
LPs-J1139^{I,XI,XII}	11:39:21.74	20:24:50.90	0.57	2.85837	6 – 8	19	~1^{GG}
LPs-J1202^{I,XI,XII}	12:02:07.60	53:34:39.00	0.212	2.44160	-	25	~5-10^{GC}
LPs-J1322^{I}	13:22:17.52	09:23:26.40	-	2.06762	-	20	~10^{GC}
LPs-J1323^{II,XI,XII,XVI}	13:23:02.90	55:36:01.00	0.47	2.41671	9 – 12	25	~10^{GC}
LPs-J1326^{I,XVIII,XIX}	13:26:30.25	33:44:07.40	0.64	2.95072	4 – 5	33	~1.5^{GG}
LPs-J1329^{I,XX,XXI,XXII}	13:29:34.18	22:43:27.30	0.443	2.04008	9 – 13	31	~11^{GC}
LPs-J1336^{I}	13:36:34.94	49:13:13.60	0.28	3.25477	-	24	~1.5^{GG}
LPs-J1428^{II,XXIII,XXIV,XXV,XXVI,XXVII}	14:28:23.90	35:26:20.00	-	1.32567	-	4	~1^{GG}
LPs-J1449^{I}	14:49:58.59	22:38:36.80	-	2.15360	-	8	~10^{GC}
LPs-J1544^{I,XI,XII,XIII,XXVIII}	15:44:32.35	50:23:43.70	0.673	2.59884	10-17	10	~7^{GC}
LPs-J1607^{II}	16:07:22.6	73:47:03	0.65	1.48390	-	4	~1^{GG}
LPs-J1609^{II,XI,XII,XIII,XVI}	16:09:17.80	60:45:20.00	0.45	3.25550	12 – 16	44	~7^{GC}
LPs-J2313^{I}	23:13:56.64	01:09:17.70	0.56	2.21661	-	57	~3^{GG}

Table 4.1: Foreground lens redshfits as reported in references. $z_{<CO/[CI]>}$ is the average redshift of the *LPs*based on all CO/[CI] line detections. $\mu_L^\dagger$ Lens magnfication factor range. Measured with single line / single-band CO / dust emission or HST near-IR imaging. † = Estimated using Tully-Fischer method (Harris et al., 2012). ^{GG} = Galaxy-Galaxy lens. The lens arc size corresponds to the effective Einstein radius, or the inferred circular radius. ^{GC} = Galaxy-Galaxy Cluster (or group) lens. The lens arc size corresponds to the largest lens arclet or effective Einstein radius. **References:** I. Berman et al. (in prep), II. (Harrington et al., 2016), III. (Harrington et al., 2019), IV. (Geach et al., 2015), V. (Su et al., 2017), VI. (Geach et al., 2018), VII. (Rivera et al., 2019), VIII. Kamieneski et al. (in prep), IX. (Khatri & Gaspari, 2016), X. (Amodeo et al., 2018), XI. (Cañameras et al., 2015), XII. (Cañameras et al., 2018b), XIII. (Frye et al., 2019), XIV. (Cañameras et al., 2017a), XV. (Cañameras et al., 2017b), XVI. (Harrington et al., 2018), XVII. (Cañameras et al., 2018a), XVIII. (Bussmann et al., 2013), XIX. (Yang et al., 2017), XX. (Díaz-Sánchez et al., 2017), XXI. (Dannerbauer et al., 2019), XXII. (Iglesias-Groth et al., 2017), XXIII. (Borys et al., 2006), XXIV. (Iono et al., 2009), XXV. (Sturm et al., 2010), XXVI. (Stacey et al., 2010), XXVII. (Hailey-Dunsheath et al., 2012), XXVIII. (Nesvadba et al., 2019)

Telescope	Receiver	ν_{obs} [GHz]	Θ^a [$''$]
GBT 100m	K_a band	26 - 40	19 - 29
LMT 32m	RSR	75 - 115	21 - 31
IRAM 30m	E150	125 - 175	14 - 20
IRAM 30m	E230	202 - 274	9 - 12
IRAM 30m	E330	277 - 350	7 - 9
APEX 12m	PI230	200 - 270	23 - 31
APEX 12m	FLASH345/460	268 - 516	12 - 17

Table 4.2: Summary of single-dish telescopes and receivers used in this analysis. ^{a}Observed beam size.

4.4 Spectral Line Observations

The number of new line measurements we present in this work is ~70% of the following: 20 CO(1-0), 6 CO(2-1), 24 CO(3-2), 15 CO(4-3), 16 CO(5-4), 15 CO(6-5), 18 CO(7-6), 17 CO(8-7), 16 CO(9-8), 6 CO(10-9), 8 CO(11-10), 1 CO(12-11), 19 [CI](1-0) and 18 [CI](2-1). For a thorough analysis, we complemented our line observations with nearly 50 line measurements previously reported in the literature (Cañameras et al., 2015; Harrington et al., 2016; Cañameras et al., 2017b, 2018b; Harrington et al., 2018; Dannerbauer et al., 2019; Nesvadba et al., 2019, Berman et al. in prep.), for the *LPs* in our catalogue. In Table 4.2, we summarize the astronomical facilities, receiver names, observed bandwidths, and telescope's beam sizes involved in the data acquisition for this work. Table 4.2 also includes the beam size for the LMT and ALMA/Band 3 spectral line measurements to be presented in Berman et al. (in prep.). Both the LMT and ALMA/Band 3 observations had targeted the same CO transition, CO(2-1) or CO(3-2), with comparable line fluxes.

4.4.1 GBT, IRAM 30m and APEX Observations

We observed the CO(1-0) line with the Ka-band receiver on the Green Bank Telescope GBT (Pr. ID: 17B-305; PI: K. Harrington) between October 7 - 31, 2017, in Green Bank, West Virginia, U.S.A. under stable atmospheric conditions during both night and day hours. The observing procedure and data reduction is identical to that presented in Harrington et al. (2018); Dannerbauer et al. (2019), and we briefly describe the procedure below. We executed a SubBeamNod observing mode, with 4 min integration per scan. Each session started with a pointing and focus check, followed by a pointing every 1-1.5hr. Focus measurements were conducted every 3hr for longer observing sessions. We tuned the backend spectrometer, VEGAS, to its low-resolution, 1.5 GHz bandwidth mode. Using GBTIDL (Marganian et al., 2013) we computed all On-Off measurements and corrected for atmospheric attenuation. Each spectrum was inspected by eye after baseline subtraction (see Harrington et al., 2018), and roughly 10-15% of scans were dropped. After subtracting a baseline, and then averaging, we smoothed the spectra to ~ 100 km s^{-1}channel resolution.

We observed mid-high-J CO and [CI] emission lines in the sources available in the Southern

hemisphere using both the PI230 and dual-frequency FLASH 345/460 receivers on the APEX telescope in San Pedro de Atacama, Chile (Güsten et al., 2006). We used Max Planck Society observing time between 22 May and 28 September, 2018 (Pr. M-0101.F-9503A-2018; PI: Harrington), soon after the new telescope surface was installed and commissioned. Observations took place in a range of very good to reasonable weather conditions, i.e. precipitable water vapor (PWV) ~ 2-3mm for PI230 and PWV <2mm for FLASH+. FLASH (Heyminck et al., 2006b) is a 2 side-band (SB) dual-frequency heterodyne receiver with a single orthogonal linear polarization for each of the 345 GHz and 460 GHz atmospheric windows. Both the FLASH 345/460 channels have an upper and lower side-band with 4 GHz bandwidth. The PI230 receiver is a 2-sideband heterodyne receiver with a dual-polarization capability and 2×8 GHz bandwidth. We used a standard wobbler switching with a chopping rate of 1.5 Hz, and an azimuthal throw offset of 30". Each scan consisted of a hot/sky/cold calibration 600" off-source, followed by 12 subscans of 20s per on-source integration time. Focus checks were performed roughly every 3-4hr, whereas pointing checks on Jupiter or nearby star were performed every 1-2h (pointing accuracy within 2-3″). All data was recorded using the MPIfR eXtended bandwidth Fast Fourier Transform spectrometers (FFTS; Klein et al., 2006), and each of the scans were reduced and analyzed using the CLASS and GREG packages within the GILDAS software (Pety, 2005). The spectrum from each scan was smoothed to ~ 100 km s^{-1}channel resolution and assessed after subtracting a first-order baseline from the emission line-free channels. The baseline stability depends strongly on the observed frequency and/or weather conditions, therefore we dropped 10-25% of the scans before co-adding the base-line subtracted, rms-weighted spectrum.

We observed low-to-high-J CO and [CI] emission lines with the IRAM 30m telescope during three observing semesters (Pr. 187-16, 170-17, 201-18; PI: K. Harrington), between January 29th, 2017 and April 24th, 2019. Overall, weather conditions varied from excellent to poor, with the reference zenith opacity at 225 GHz, $\tau_{\nu 225\mathrm{GHz}} \sim 0.05 - 0.8$. We utilized all four of the EMIR receivers (Carter et al., 2012), E090, E150, E230 and E330, often with dual tuning modes to target more than one CO/[CI] emission line. In total, the EMIR receiver has a dual polarization, with a 16 GHz bandwidth backend spectrometer, the fast Fourier Transform Spectrometre (FTS200), and an 8 GHz bandwidth spectrometer, the WIde-band Line Multiple Auto-correlator (WILMA). The FTS200 has a finer channel resolution, however is subject to baseline instabilities such as platforming features in the bandpass. The WILMA has a lower native channel resolution and was used almost always alongside the FTS200 to verify observed line features. We carried out a standard wobbler switching observing mode with offset throws of 40″every second. Each wobbler switching mode procedure includes three, 5 minute integrations (i.e. twelve 25-s subscans). Pointing corrections were performed (e.g. Uranus, Venus, J1226+023, J1418+546) every 1-2hr, with azimuth and elevation pointing offsets typically within 1-3″. Focus measurements were repeated roughly 1.5hr after sunset/sunrise and every 3-4hr to correct for thermal deformations of the primary dish and/or secondary mirror. In the same manner presented in Harrington et al. (2019), all scans were reduced using GILDAS package, smoothed to ~ 50 − 150 km s^{-1}channel resolution, followed by a visual inspection of a baseline-subtracted spectrum and subsequent averaging of the rms-weighted spectrum. We dropped 5-20% of the scans per line due to unstable baselines or noise spikes, which may strongly depend on the specific tuning setup and weather.

4.4.2 Absolute Calibration Errors

In the following analyses we model the *apparent* (not corrected for lens magnification) velocity-integrated flux density, integrated across the entire line profile. We apply a total error based on the typical systematic uncertainties associated with pointed single-dish spectroscopic observations. These include: atmospheric instabilities (transmission varying on the order of seconds/minutes), pointing/focus corrections, baseline subtraction procedures, the calibration of the Jy/K gain conversion, receiver stability across the entire bandpass. For all CO(1-0) lines, we adopt a 25% uncertainty for systematic effects with the GBT (see Harrington et al., 2018; Frayer et al., 2018b). We adopt a 20% uncertainty for all APEX and IRAM 30m measurements less than $\sim$ 240 GHz and a 35% uncertainty for lines observed at higher frequencies. We add an additional 5-10% total uncertainty to those emission lines which were detected at the edge of the EMIR receiver capabilities and at lower atmospheric transmission. Despite careful pointing/focus/calibration measurements, we add an additional 5% total uncertainty to all integrated fluxes used in this study due to the heterogeneous observing conditions among all of the emission lines observed or reported in other studies. Sources LPs-J1322, LPs-J0846, LPs-J0748 have extended emission as detected by AzTEC 1.1mm continuum (Berman et al in prep.). Therefore, we measured the emission surrounding the reported RA/DEC, which we consider to be representative of the entire galaxy. As noted in Berman et al. (in prep.) for LPs-J1322, the ALMA measurements did not account for $\sim$ 35% of the LMT/AzTEC 1.1mm continuum flux due to its large Einstein Ring (also see Table 4.1 and Table 4.2). Therefore we have adopted an additional 35% total error for the lines in this source. High-frequency measurements may underestimate the total flux for the most extended *LPs* due to smaller beam-sizes and pointing errors. The conservative total uncertainties we adopt for these single-dish measurements thereby include a wide variation in the value of the flux density in an attempt to constrain the average global ISM properties.

4.5 Emission Line Profiles

Figure 4.1 shows an example set of low-to-high-J CO and [CI] line detections for LPs-J1323. The remaining figures for the line spectra for the *LPs* can be accessed online in the supplemental journal. In all of the 21/24 *LPs* with a [CI] line detection, the emission line profile matches that of the spectrally adjacent CO emission. Specific examples of this can be seen in the [CI](2-1)/CO(7-6) spectrally adjacent pair (see e.g. LPs-J0116, LPs-J0209, LPs-J0305, LPs-J0748, LPs-J1326). Most of the CO and [CI] lines have similar line-widths and shape. These spectrally resolved measurements indicate that the emitting regions follow the same large-scale dynamics, based on these spatially unresolved measurements.

Fig. 4.2 shows the measured velocity-integrated line fluxes, compared to our literature compilation (Carilli & Walter, 2013; Yang et al., 2017; Cañameras et al., 2015; Kirkpatrick et al., 2019). Many CO line measurements have now probed more than 2 - 3 orders of magnitude in the observed velocity-integrated line flux densities across this large sample of $\sim$ 270 galaxies at $z \sim 1 - 7$. The *LPs* are among the brightest CO sources on the sky, due to the magnification effects of strong lensing.

To characterize the velocity integrated flux density we calculate the full line-width at zero intensity

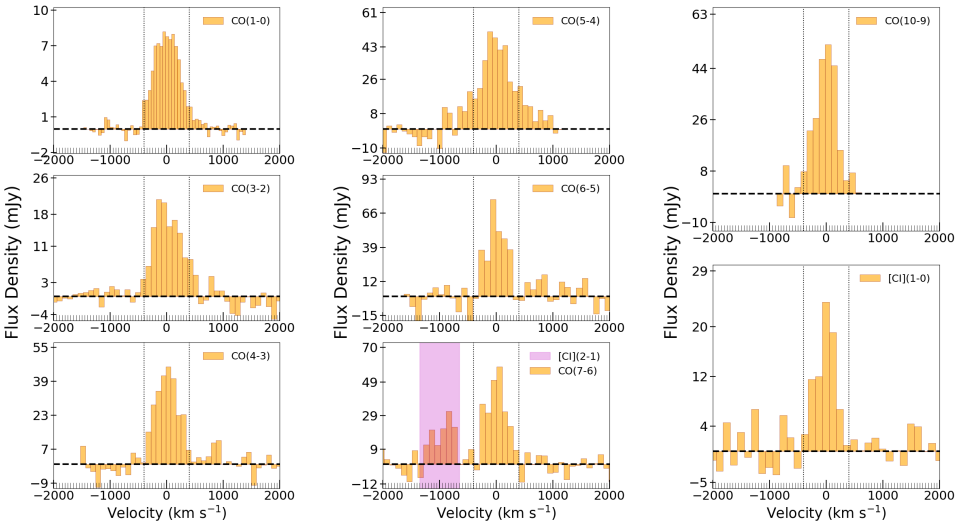

Figure 4.1: Apparent flux density versus velocity for the CO and [CI] line detections. The best fit models of all line and continuum data are shown for LPs-J1323 in Fig. 4.4. The CO(1-0) line was previously presented in Harrington et al. (2018). Spectra and best-fit models for the other *LPs* can be accessed online.

(FWZI) for all of the measured line fluxes (see Appendix A.1. We note that neither all spectra have similar line shapes between the sample of *LPs*, nor are all of the lines resolved at relatively high velocity resolution (e.g. 20-50 km s^{-1}), so we therefore avoid fitting simple 1-D Gaussian models to analyse the line-profiles. The mean and standard deviation of the FWZI for all of the CO lines for the entire sample of *LPs* is 851 ± 183 km s^{-1}. In Fig. 4.3, the FWZI is normalized to the FWZI of the CO(3-2) line to examine whether the line profiles may change as a function of J_{up}. The average value of this normalized FWZI decreases with increasing J_{up}, although the large total uncertainties for the lines do not reveal a statistically significant trend. The *LPs* with detections of higher-J CO lines show a similar line profile as seen in the emission lines of the lower-J rotational transitions. In some cases the FWZI of the high-J emission lines is narrower than the lower-J emission line profiles at comparable velocity resolution. This is apparent in LPs-J1336, as the CO(1-0; 5-4; 6-5; 8-7; 9-8; 10-9) emission lines have a comparable FWZI, whereas the strong detection of the CO(11-10) line reveals a FWZI that is roughly half. Narrow-line emission in the highest-J lines, compared to the lower-J lines, is observed in LPs-J0116, LPs-J0226, LPs-J1202, LPs-J1544. This is not seen in other systems with such high-J measurements. In 3/24 *LPs* with large lensing arcs, pointed observations may only partially cover the entire emitting region. Therefore the observed emission is assumed to be representative of the galaxy-scale ISM of the lensed galaxy. In these cases, additional uncertainties have been added to the observed integrated line fluxes (§4.4.2).

The lens magnification factor, μ_L, may have a different value for the low- and high-J CO lines, and thus may yield a potential differential lensing effect. Differential lensing of the diffuse and dense molecular gas traced by [CI] and CO may be negligible in most, if not all, of the *LPs* as the line profiles would have shown strong variations across the spectrally resolved line profiles. Since the average, normalized FWZI drops slightly (10 - 25%) from the median value for the

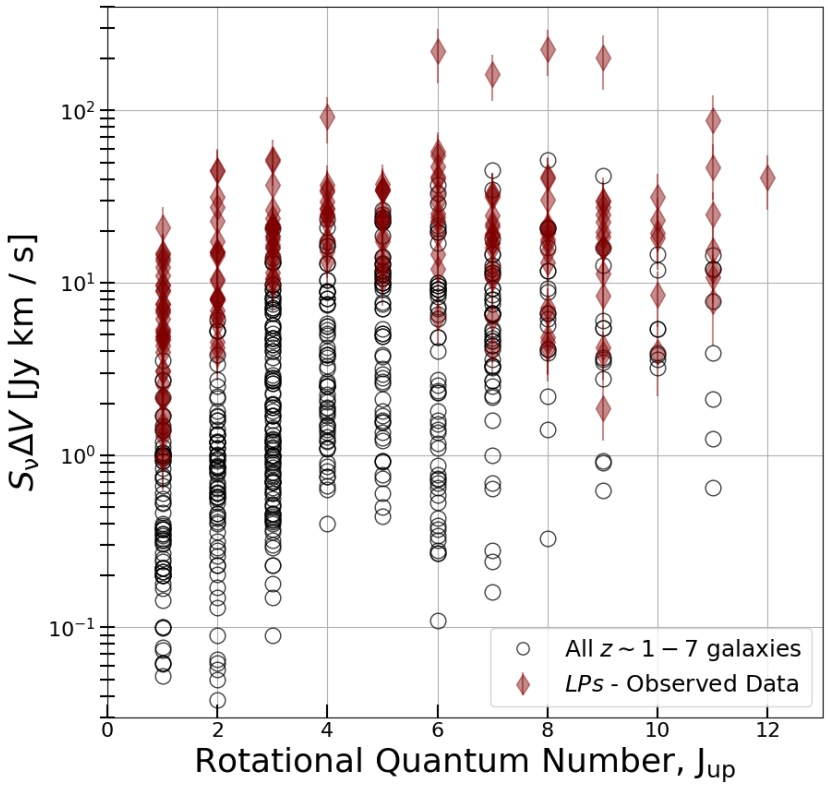

Figure 4.2: Velocity-integrated flux density (log-scale) measurements plotted versus the CO rotational quantum number, J_{up}, for the *LPs* (red diamond). The black circles show the *LPs* & K19 $z \sim 1 - 7$ sample, described in §4.5.

higher-J lines, such a change is not statistically significant given error uncertainties. Therefore, we are confident that differential lensing effects do not impact the general trends we present. The strong asymmetric lines may indicate[2] different magnification factors across the line profile (Leung et al., 2017), while the dust and CO may be slightly offset in the source plane (Rivera et al., 2019). These values will likely be the same for both the [CI] and CO lines, as the overall line shapes are similar. We note that Cañameras et al. (2018a) report a 5-10% difference in the flux-weighted mean magnification factor derived for the low-J CO and mm dust continuum, respectively, for 5/24 *LPs* presented in this work. For 2/24 *LPs* in this work, Cañameras et al. (2018a) reported less than 30% differential lensing of the dust and low-J CO. We are unable to de-magnify the sources for the analyses presented in this work, since there a magnification factor for different lines does not exist. Some lensed SPT-selected galaxies have a noted range from negligible differences in the magnification for different CO line transitions, up to a factor two (Apostolovski et al., 2019; Dong et al., 2019).

[2] Asymmetric lines could also indicate viewing a galactic system at a specific edge on orientation which covers an asymmetric portion of a rotating spheroidal disk or a significantly turbulent environment (e.g. Puschnig et al., 2020).

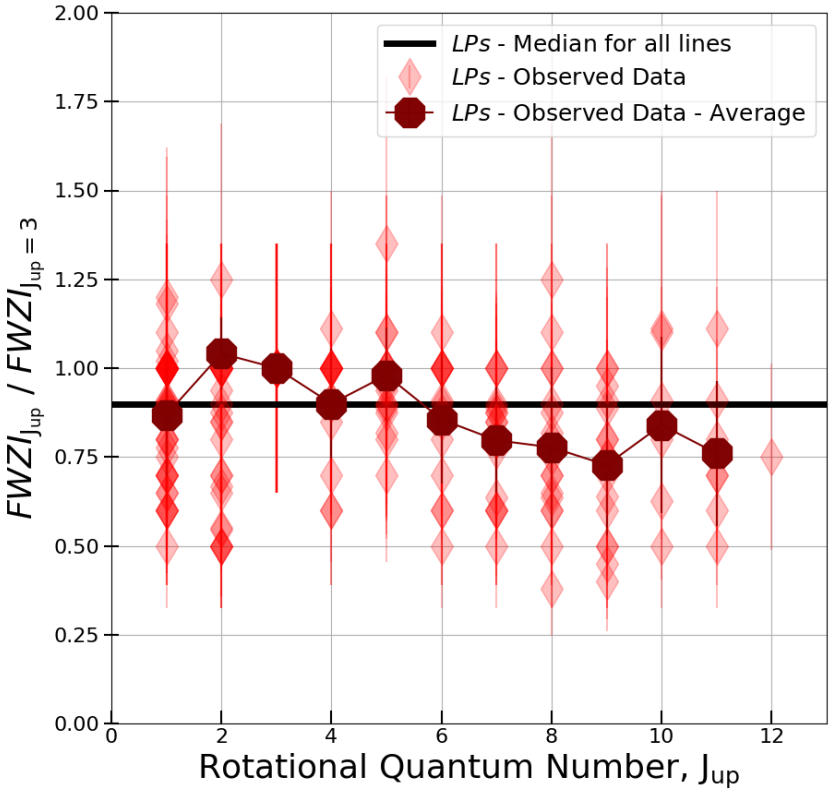

Figure 4.3: Apparent velocity-integrated flux density measurements plotted versus the CO rotational quantum number, J_{up}, for the *LPs* (red diamond). The gray squares show the CO line fluxes of other $z > 1$ galaxies (Carilli & Walter, 2013; Kirkpatrick et al., 2019).

4.6 Simultaneous Modeling of Line and Continuum Emission

We utilize two state-of-the-art radiative transfer codes to simultaneously model both the observed line fluxes and measurements of the thermal dust continuum emission. This enables us to study the gas excitation conditions for the *LPs* using (i.) a widely used approach to model two molecular gas components, and (ii.) a more realistic molecular ISM with a turbulence driven, lognormal density distribution for the gas density. The models we use are primarily derived from the equations presented in Weiß et al. (2007b). For the analyses in this work, the primary modification to those models is that the gas and dust are now modelled simultaneously. Below we summarize the main properties of these modelling tools. Details will be published elsewhere. We will first describe the model which considers two gas components. Afterwards we will summarize the second model, which includes many of the same input parameters as the first model, despite being a more physically motivated, modified version.

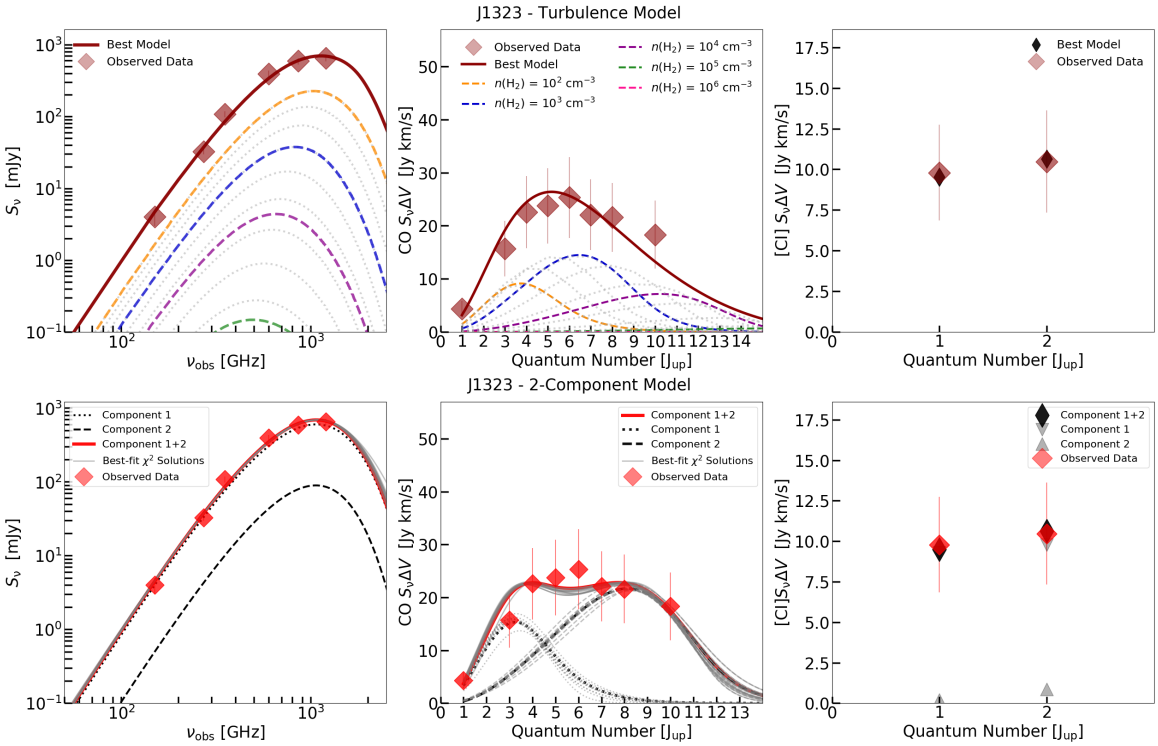

Figure 4.4: Best-fit, minimum-χ^2 model solution for LPs-J1323. **Top:** *Turbulence* model for the dust SED, CO and [CI] velocity-integrated line fluxes as determined by the best χ^2. For clarity, different dashed-colored curves denote the representative contributions to the density PDF for the molecular gas densities of $\log(n(H_2))$ = 2 (yellow), 3 (blue), 4 (purple), 5 (green) and 6 (pink) cm^{-3}. The gray-dashed lines represent the remaining LVG calculations (from the 50 total samples) which sample the gas density PDF (see §4.6). For the *Turbulence* model, these individual density contributions have a y-axis scaled by a factor 5 for both the dust and line SED to facilitate interpretation of the dominant gas density. All observed data are shown as red diamonds. The best-fit [CI] line fluxes are plotted over the observed data. All solid red lines indicate the total best-fit, minimum-χ^2 model. **Bottom:** *2-component* model curves for the lower excitation component (black dotted) and higher-excitation component (black dashed). The best-fit [CI] line flux from the lower-excitation component and higher-excitation component are denoted by a downward-facing and upward-facing gray triangle, respectively.

Parameters:	$\log_{10}(n_{H_2})$	T_{kin}	T_{kin} / T_{dust}	μR_{eff}	ΔV	κ_{vir}
Models:	[cm^{-3}]	[K]		[pc]	[km s^{-1}]	km s^{-1} pc^{-1} $cm^{3/2}$
2-component	1 – 7	15 – 600	0.5 – 6.0	0.1 – 19999	10 – 200	1.0 - 3.0
Turbulence	1 – 7	15 – 600	0.5 – 6.0	0.1 – 19999	10 – 200	1.0 - 3.0
	M_{ISM} / M_{dust}	CO / H_2	[CI] / H_2	$\beta_{T_{kin}}$	$\beta_{[CI]}$	β_{T_d}
2-component	120 – 150	1×10^{-4} – 2×10^{-4}	1×10^{-5} – 2×10^{-4}	–	–	1.8 – 2.0
Turbulence	120 – 150	1×10^{-4} – 2×10^{-4}	1×10^{-5} – 2×10^{-4}	-0.5 – -0.05	-5.0 – 0.0	1.8 – 2.0

Table 4.3: The ranges in parameter space explored in both models.

4.6.1 The *2-component* model parameters

Our first model is a simple non-LTE radiative transfer model, referred to as the "*2-component*" model. This model can, in principle, take into account an arbitrary number of molecular gas components. Nonetheless, due to the large number of coupled parameters and model degeneracies, we consider only two gas components, each with a unique, constant density. In Table 4.3 we summarize the range in parameter space we explore for both models. We consider 14 free parameters for the *2-component* model. Each of the two gas components in the *2-component* model has seven free parameters: $\log(n(H_2))$ (base 10), $T_{\rm kin}$, $\Delta V_{\rm turb}$, $\kappa_{\rm vir}$, $\sqrt{\mu_{\rm L}}R_{\rm eff}$, [CI]/$H_2$, and $T_{\rm kin}/T_{\rm d}$. Some of these parameters we have restricted specifically, as described below.

We parameterize the size of the emitting region by an effective radius which defines the apparent source solid angle $\Omega_{\rm app} = \mu_{\rm L}\,\frac{\pi R_{\rm eff}^2}{D_{\rm ang}^2}$ (e.g. Weiß et al., 2007b), using the angular diameter distance, $D_{\rm ang}$, $\mu_{\rm L}$ the magnification factor of the observed intensity, and $\sqrt{\mu_{\rm L}}R_{\rm eff}$ the apparent effective radius of the emission region. This apparent, effective disk radius would be equivalent to the intrinsic emitting region if the emission came from a filled aperture for an unlensed, face-on, circular disk (Weiß et al., 2007b). It is therefore a minimum radius, as the emission may come from an un-filled aperture which may be more widely distributed.

For each gas component, we consider a range of gas densities between $\log(n(H_2))$ = 1 - 6 cm^{-3}. We probe gas kinetic temperatures, $T_{\rm kin}$, ranging between the redshifted CMB radiation temperature and 600 K (corresponding to the highest energy CO transition we model ($J_{\rm up}$ = 15)). We account for the possible decoupling of the gas and dust by setting a limit on the gas kinetic temperature, as $T_{\rm kin} \geq 0.5T_{\rm d}$. The range we explore for this ratio of the gas kinetic temperature to the dust temperature ($T_{\rm kin}/T_{\rm d}$ = 0.5 - 6) is in agreement with theoretical work (see the review by Krumholz, 2014). In well-shielded regions that have $\log(n(H_2)) > 4.5$ cm^{-3} the molecular gas and dust may have a stronger coupling than in lower density environments. According to Krumholz (2014), within gas densities of $\log(n(H_2)) > 6$ cm^{-3} the gas and dust temperatures are expected to be nearly equivalent. We do not implement an explicit relationship between $T_{\rm kin}/T_{\rm d}$ and the gas density.

The systemic velocity gradient, $\delta v/\delta r$, and the molecular gas density together define dynamically bound or unbound systems, parameterized by the virial parameter, $\kappa_{\rm vir}$, (Goldsmith, 2001; Greve et al., 2009; Papadopoulos et al., 2012a). The virial parameter, $\kappa_{\rm vir}$, is a relationship between turbulent and

gravitational energy, and couples the velocity gradient and H_2 gas volume density. We explore a range corresponding to a physically bound molecular medium, up to a marginally unbound system, with $\kappa_{\rm vir} = 1 - 3$. The $\Delta V_{\rm turb}$ parameter in the *2-component* model calculations is, by definition, a mathematical term required for dimensional homogeneity.

We leave the carbon abundance as a free parameter, probing ranges consistent with diffuse to dense giant molecular clouds (GMC) abundances of [CI]/H_2 = $1{\times}10^{-5}$ - $2{\times}10^{-4}$. We assume an average Galactic disk value for the CO gas-phase abundance in the range of CO/H_2 = 1 - $2{\times}10^{-4}$ to be consistent with the typical molecular abundance of giant molecular clouds in the Milky Way (Scoville & Young, 1983; Wilson et al., 1986; Blake et al., 1987). Instead of allowing the gas-to-dust-mass ratio parameter to range freely, we restrict this to a value between $GDMR = 120 - 150$ (Draine, 2011); i.e., consistent with the observed value in the Milky Way (Draine, 2011). Recent studies (Casey et al., 2014, and references therein) suggest that massive star-forming galaxies represent high density cosmic regions at $z = 1 - 3$. The fiducial value of solar metallicity, Milky-Way type values, are supported by our selection criteria to study extremely dusty star-forming galaxies with sufficient metal enrichment at high-z . We may therefore expect the *LPs* to have already accumulated at least a near-solar metallicity in a relatively short amount of time (Cen & Ostriker, 1999; Bothwell et al., 2016). Some derived quantities, such as the $GDMR$ and the α conversion factor, will depend on metallicity (Narayanan et al., 2012). For galaxies with $2 - 3\times$ solar metallicity, the total gas mass comparisons would be impacted by a relative linear decrease in both the $GDMR$ and overall gas mass estimates from [CI] and CO.

4.6.2 Computing the line and continuum fluxes

We model the line fluxes of the CO(1-0) to CO(15-14) transitions, corresponding to upper state energy levels $E_{\rm u}$ = 5.5 - 663.4 K. We use the collisional rate coefficients from Flower & Pineau des Forêts (2001) to solve for the balance of excitation and de-excitation from and to a given energy state. While we compute the relative level populations of CO (and [CI], if detected), we also solve for the observed dust SED. We account for two background continuum sources: i.) the CMB radiation at the respective redshift, with $T_{\rm CMB} = 2.73\times(1 + z_{\rm source})$ K, and ii.) the IR radiation field. We simply solve for the gas kinetic temperature and dust temperature without modeling any specific heating mechanism. We note that theoretical and observational studies suggest the overall molecular ISM of a starburst/AGN galaxy could also be influenced by cosmic rays or X-rays (Meijerink et al., 2007, e.g.), and these heating mechanisms may be influential in determining the value we derive for the gas kinetic temperature.

The apparent line flux densities, $\mu_{\rm L} S_{\rm CO/[CI]}$, are directly proportional to the physical apparent source solid angle and line brightness temperatures, $T_{\rm b}$. In the non-LTE, LVG framework we calculate the full radiative description of the $T_{\rm b}$, although it is classically defined by its equivalent representation on the Rayleigh-Jeans side of the emitting spectrum, i.e. $h\nu_{\rm obs} << kT_{\rm b}$. The values of $T_{\rm b}$ we compute depend on the gas volume density, the kinetic temperature, and the gas-phase abundance per velocity gradient in the LVG description. Altogether, the values of $T_{\rm b}$ are used to model the observed line fluxes:

$$\mu_{\rm L} S_{\rm CO/[CI]} = \frac{T_{\rm b}\, 2k\nu_{\rm obs}^2 \Omega_{\rm app}}{c^2\,(1+z)}, \tag{4.1}$$

with c the speed of light, z redshift, $\nu_{\rm obs}$ the observed frequency of the CO or [CI] line and k the Boltzmann constant.

We parameterize the observed dust continuum radiation field by the dust temperature, $T_{\rm d}$, dust emissivity index, $\beta_{\rm T_d}$, apparent dust mass and source solid angle. The latter three parameters also characterize the wavelength at which the dust opacity becomes unity, ${\lambda_0}^3$. We note that λ_0 is not a free parameter in our model, but can be computed from the apparent dust mass and source solid angle via Eq.4.2. For simplicity, we restrict the $\beta_{T_{\rm d}}$ to a value between $\beta_{T_{\rm d}} = 1.8 - 2.0$ in both models to be consistent with previous studies of the *LPs* (Cañameras et al., 2015; Harrington et al., 2016). These values are also in agreement with the Milky Way average (Planck Collaboration et al., 2011b) and other studies of local and high redshift star-forming galaxies (Casey et al., 2014)[4].

We then compute the full radiative transfer analysis for the two components in the *2-component* model to derive both the dust opacity and line opacities in each calculation. The larger component can overlap with the more compact component, and we therefore take into account this difference when computing the overall dust SED (see e.g. Downes & Eckart, 2007). We keep the same frequency dependent dust emissivity index, $\beta_{T_{\rm d}}$, for each component. The dust optical depth is calculated using equations 2 and 3 of Weiß et al. (2007b), assuming a frequency dependent dust mass absorption coefficient, $\kappa_{\rm d}$ [cm^2 g^{-1}] (Kruegel & Siebenmorgen, 1994a); yielding

$$\tau_\nu = \frac{\kappa_{\rm d}\mu_{\rm L}M_{\rm d}}{\Omega_{\rm app}D_{\rm ang}^2} = \frac{0.4(\nu_{\rm r}/250{\rm GHz})^{\beta_{T_{\rm d}}}\,\mu_{\rm L}M_{\rm d}}{\Omega_{\rm app}D_{\rm ang}^2}. \tag{4.2}$$

We connect the modelled line and continuum fluxes by using the derived dust opacity and inferred CO (or [CI]) gas column density to calculate the H_2 gas column density, using equation 7 of Weiß et al. (2007b). The *GDMR* parameter is ultimately used to link the overall line fluxes and dust continuum in a self-consistent manner. We recall that the $T_{\rm kin}/T_{\rm d}$ parameter also links the line and continuum emission properties. We applied a prior for some of the *LPs*, with dust photometry limited mostly to *Planck* measurements, so that the dust SED turns over beyond rest-frame flux-densities of $\sim S_{>6000{\rm GHz,rest}}$ (i.e. rest-frame $\sim$50μm for the $z \sim 2-3$ *LPs*). This is in agreement with the physical conditions with which our model is sensitive to, i.e. the rest-frame FIR to mm wavelengths – rather than near- and mid-IR wavelengths. This restriction also prevents a largely unconstrained (and also unphysical) solution space, with extremely high apparent FIR luminosity ($\mu_{\rm L}L_{\rm FIR:40-120\mu m} > 10^{16}$ L$_\odot$)[5]. Note, dusty high-z star-forming galaxies, with full coverage of their thermal dust SED, fully support this prior (Strandet et al., 2016).

4.6.3 The *Turbulence* model parameters

The second model, hereafter the "*Turbulence*" model, is more sophisticated in describing the molecular ISM. It has nine free parameters, and is represented as a single gas component described by a gas

[3] λ_0 is directly proportional to the dust column density.

[4] $\beta_{\rm T_d}$ is subject to large uncertainties in dust grain size distributions (Draine, 2011).

[5] This is comparable to setting an upper limit for the dust temperature.

density PDF. We also model the line and continuum emission simultaneously in this model, including all of the same input parameters. For the *Turbulence* model, the effective radius connects the source solid angle to the gas density PDF, which makes this model distinct from the *2-component* model. In contrast, the *2-component* model simply treats the gas density and the source solid angle as completely independent parameters, and also does not draw an explicit connection between the gas density and gas kinetic temperature.

We explore a broad range of values for the H_2 gas volume density in the *Turbulence* model, $\log(n(H_2))$ = 1 - 10 cm^{-3}, with a restricted range for the mean density of the density PDF to values of $\log(n(H_2))$ = 1 - 6 cm^{-3}. The mean molecular gas density thereby determines the other model parameter to describe the global mean ISM properties of the *LPs*. We sample the best-fit, minimum-χ^2 *Turbulence* model density PDF by 50 bins. Each of the 50 gas densities are proportional to a solid angle that is occupied by that specific density bin. Therefore, each density corresponds to a radius – such that the sum of all areas is normalized to the input source solid angle. This implies that the model fit values for the dust and line SEDs are the sum of 50 individual LVG calculations which have used the value for each of those densities to calculate the relative emission properties. These altogether sum to the total line and continuum emission that has been measured.

There are two unique parameters for the *Turbulence* model, $\beta_{\rm [CI]}$ and $\beta_{T_{\rm kin}}$. The power-law index, $\beta_{\rm [CI]}$, constrains the value of the carbon abundance relative to [CI]/H_2 (Weiß et al., 2003). We express $\beta_{\rm [CI]}$ as a power-law of the density to describe the expected decreasing value of the carbon abundance for increasing molecular gas volume density (see e.g. Hollenbach & Tielens, 1999; Glover & Clark, 2012; Goldbaum et al., 2016). These chemical network calculations show that atomic carbon quickly disappears from the gas phase, and is transformed into other molecules, as the cloud becomes denser. We further explore the justification of this parameter in §4.7.3. The $\beta_{T_{\rm kin}}$ parameter couples the gas kinetic temperature to the gas volume density by a power-law index, $\beta_{T_{\rm kin}}$, as $T_{\rm kin} \propto \log(n(H_2))^{\beta_{T_{\rm kin}}}$, such that the more diffuse gas tends to have higher gas kinetic temperatures. This functional behavior has been well-studied in magneto-hydrodynamical simulations (Krumholz, 2014). The modelled galaxy-wide turbulent velocity dispersion, $\Delta V_{\rm turb}$, is a free parameter in the *Turbulence* model. Although similar to the *2-component* model, here it determines the width of the log-normal gas density PDF that is centered on the mean molecular gas density.

4.6.4 Fitting

We use the parameter ranges in Table 4.3 to model the observed data using a Bee Algorithm optimisation procedure (Pham & Castellani, 2009), as used in Strandet et al. (2017). In this optimisation procedure, each model iteration attempts to solve for the observed data by exploring a number of model calculations (hereafter 'bees') based on the free parameters. These 'bees' have a random initialisation within the defined parameter space, and record the model parameters with the best reduced χ^2 value, as determined by the dust, CO and [CI] data. The parameter space is further explored by 'bees' which provide a fine sampling around the best χ^2 regions, while other 'bees' continue to evaluate the parameter space randomly to avoid being trapped in a local minimum during each iteration. We evaluate $\sim 10^5$ models in each modelling procedure (for either the *2-component* or *Turbulence* model). To avoid repeatedly obtaining the same best-fit, minimum-χ^2 values, and also to avoid remaining fixed in a narrow solution-space within the posterior probability distribution of

each parameter, we re-generate this entire procedure multiple times, resulting in ~2 million model evaluations per galaxy for each of the *2-component* or *Turbulence* models. To describe the mean, global gas excitation conditions of the *LPs*, we refer primarily to the mean quantities and the standard deviation for the sample (Table 4.5). The quantities presented in Table 4.5 are based on the total χ^2-weighted mean parameter values for each of the individual *LPs*, as evaluated for each parameter value from the ~2 million models. The general trends and conclusions are not affected by the choice of the total χ^2-weighted mean and standard deviation of the global properties we derive, as opposed to, e.g. the median (50th percentile) values. Since we present the modelling of spatially unresolved, galaxy integrated measurements, with large absolute calibration errors (§4.4.2), we adopt this mean quantity to reflect the average galaxy-wide properties based on the limitations of our data.

4.7 Model Results

The best-fit, minimum-χ^2 models for all of the *LPs* can be accessed online, and we show an example below, for LPs-J1323 (Fig. 4.4). We plot this best-fit model values for the dust SED, CO spectral line energy distribution (line SED) and both ground-state [CI] velocity-integrated line fluxes. For the dust SED and CO line SEDs in the *Turbulence* model we also plot the relative contribution from each of the density PDFs. To facilitate comparison to the total observed best-fit model, we arbitrarily increase the y-axis value for each density component to scale the individual LVG calculations. These calculations, representative of different densities sampling the gas density PDF, are shown in different colors to visualize which mean density dominates the observed intensities. The accompanying figure for the best-fit *2-component* model shows the true y-axis values for the relative contributions from component one and component two – which add to the total observed data points.

4.7.1 CO Line SEDs

The majority of the *LPs* show a broad peak in the CO line SED at $J_{up} = 4 - 6$. The *LPs* show systematically higher excitation than the CO line SEDs in most local IR-bright, spiral galaxies, as well as many of the local radio/X-ray AGN host galaxies (van der Werf et al., 2010; Papadopoulos et al., 2012a; Spinoglio et al., 2012; Rosenberg et al., 2015; Liu et al., 2015; Kamenetzky et al., 2016). The observed dust emission arises from molecular gas with $\log(n(H_2))$ = 2-3 cm^{-3}, while the observed CO excitation ladders are dominated by $\log(n(H_2))$ = 3-4 cm^{-3}. There is sustained CO excitation out to $J_{up} = 9 - 11$ in most of the *LPs*. For this emission, molecular gas with $\log(n(H_2))$ = 4-5 cm^{-3} is dominant (see e.g. LPs-J0209, LPs-J1329, LPs-J1138).

To examine the dispersion in gas excitation conditions, Fig. 4.5 shows all of the best-fit, minimum-χ^2 *Turbulence* model-derived CO velocity-integrated line fluxes, normalized by the sum of all $J_{up} = 1 - 15$ velocity-integrated line fluxes. This normalisation indicates the relative strength between various line transitions among the sample, and we will present a more quantitative classification of the broad range in gas excitation conditions in §4.8.1. Using the velocity integrated line fluxes, we can calculate the line luminosity of CO or [CI] in terms of the area-integrated line surface brightness, $L'_{CO/[CI]}$. We calculate this value using the standard equations presented in Solomon et al. (1997). The ratio of this value for

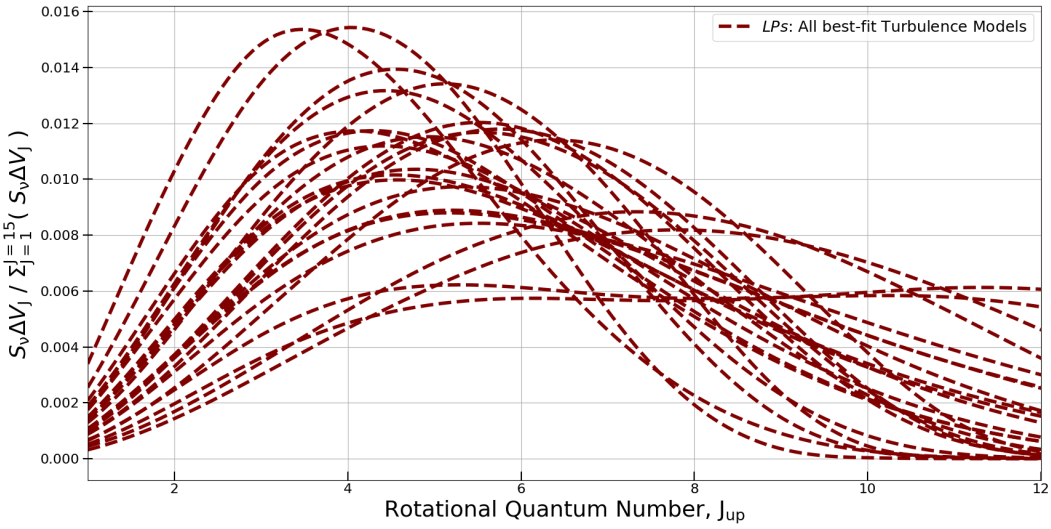

Figure 4.5: Best-fit, minimum-χ^2 *Turbulence* models for the CO velocity-integrated line fluxes, normalized by the sum of all $J_{up} = 1 - 15$ velocity-integrated line fluxes, for all of the *LPs*.

any two CO transitions will provide an average estimate of the intrinsic brightness temperature, T_b, ratio within the CO emitting gas. For the two lowest rotational transitions, this ratio is often close to unity for active star-forming systems (Carilli & Walter, 2013), assuming that the two lines have the same spatial extent on average with the same T_b, such that the two lines are thermalized. Table 4.4 shows the best-fit, minimum-χ^2 model derived line ratios from our physically motivated *Turbulence* model, yielding systematically derived values for the brightness temperature ratios corresponding to the ratio of $L'_{CO(J_{up}-(J_{up}-1))}/L'_{CO(1-0)}$, denoted as $R_{J_{up},1} = 1$. Table 4.4 summarizes the mean and standard deviation of the *LPs* sample from these best-fit, minimum-χ^2 *Turbulence* models, and we will discuss Table 4.4 in more detail in §4.8.1.

4.7.2 Physical gas properties of the *LPs*

CO and [CI] Line Opacities

We now focus on the best-fit values for the CO and [CI] line opacities, as derived in the *2-component* model. In the LVG approximation, we consider an emitting region of gas that is excited due to both the collisional interactions and the external radiation field. The observed line fluxes are computed using the line opacities, τ and the standard LVG assumption of the escape probability method formalism, which defines the probability of a photon escaping or entering the medium. As noted in other studies (Scoville & Solomon, 1974), this probability is proportional to $(1 + \tau)^{-1}$.

The observed line and continuum fluxes are determined by the relevant gas-phase abundance(s), volume density and the molecular gas kinetic temperature (i.e. the Maxwellian velocity distribution). Overall, these effects shape the value of the line opacity, specifically as

J_{up}	LPs	LPs+K19	K19:	CW13	CW13
	Mean Best-fit Model	Median	All sources	SMG	QSO
1	1	1	1	1	1
2	0.88 ± 0.07	0.73 ± 0.10	0.78 ± 0.13	0.85	0.99
3	0.69 ± 0.12	0.75 ± 0.11	0.78 ± 0.14	0.66	0.97
4	0.52 ± 0.14	0.46 ± 0.07	0.49 ± 0.10	0.46	0.87
5	0.37 ± 0.15	0.36 ± 0.06	0.34 ± 0.07	0.39	0.69
6	0.25 ± 0.14	0.28 ± 0.04	0.31 ± 0.06	-	-
7	0.17 ± 0.12	0.18 ± 0.03	0.21 ± 0.04	-	-
8	0.11 ± 0.09	0.08 ± 0.02	0.11 ± 0.03	-	-
9	0.07 ± 0.07	0.07 ± 0.02	0.14 ± 0.04	-	-
10	0.04 ± 0.05	0.07 ± 0.02	0.08 ± 0.04	-	-
11	0.02 ± 0.04	0.05 ± 0.02	0.12 ± 0.03	-	-
12	0.02 ± 0.03	0.02 ± 0.01	-	-	-

Table 4.4: Mean and 1-σ standard deviation of the brightness temperature ratios among the sample of 24 *LPs* based on the best-fit *Turbulence* models. "LPs+K19" column is the median value calculated from all observed CO lines, normalised by a common FIR luminosity, in the *LPs* & K19 sample of $z \sim 1-7$ galaxies. The "All sources" (z = 1 - 7) sample of Kirkpatrick et al. (2019). The values from the sample presented in Carilli & Walter (2013) for both high-z (sub)mm bright CO emitters (SMG) and quasars (QSO). Note, the entire Carilli & Walter (2013) sample is included in the most up-to-date *LPs* & K19 sample of $z \sim 1-7$ galaxies.

$$\tau_{\rm CO/CI} \propto \frac{\rm N(mol)[cm^{-2}]}{\Delta V_{\rm turb}[\rm kms^{-1}]} \propto \frac{n(\rm H_2)[cm^{-3}] \times [mol]/[H_2]}{\delta v/\delta r[\rm km\,s^{-1}/pc]}, \tag{4.3}$$

where 'N(mol)' is, here, the CO or [CI] gas column density, $\Delta V_{\rm turb}$ is the galaxy-wide turbulent velocity, $\delta v/\delta r$ is the large-scale, systemic velocity gradient, of the molecular/atomic gas, and '$n(\rm H_2)$' is the $\rm H_2$ gas volume density.

Figure 4.6 shows, for all *LPs*, the line opacities we derive for the upper state levels for each line transition from the best-fit, minimum-χ^2 *2-component* model results. We confirm the common assumption that the CO lines are optically thick and the atomic carbon fine-structure lines are optically thin. The CO line opacity depends on both the level population in the upper energy level state (the effective CO column density) and the galaxy-wide turbulent velocity dispersion. For a fixed column density, the higher the turbulent velocity, the lower the line opacity (see e.g. Narayanan & Krumholz, 2014). As shown for both components in each of the *LPs*, the CO line opacity first increases with $\rm J_{up}$ before it decreases progressively as the individual level populations are less frequently excited out to higher-J.

Fig. 4.6 also shows that the CO lines often do not freely radiate their emission, i.e. they are still optically thick, until $\rm J_{up} = 6-8$ and $\rm J_{up} = 8-15$ in components one and two, respectively. The more highly excited second component remains optically thick beyond $\rm J_{up} = 15$ in some cases. Also, as the second component is warmer and denser, the $\rm J_{up} = 0$ and $\rm J_{up} = 1$ levels are less populated, thereby more systems may exhibit optically thin CO(1-0) line emission in this more highly excited

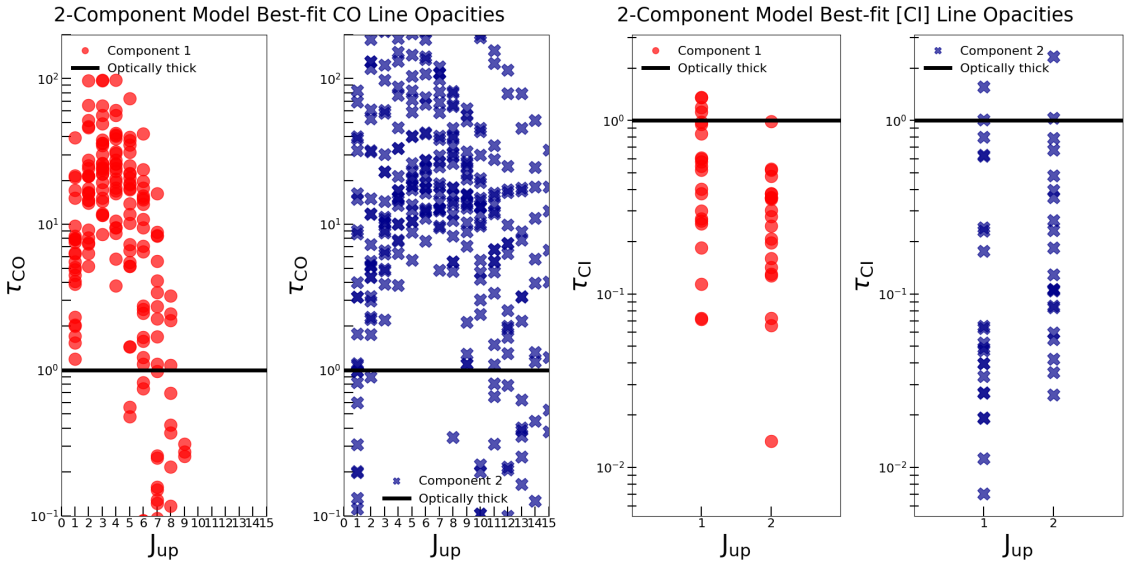

Figure 4.6: Best-fit results from the *2-component* model for the calculated line opacities. **Left:** CO line opacity versus rotational quantum number, J_{up}. **Right:** [CI] line opacity versus quantum level number. The solid black line indicates an optical depth of unity. The average best-fit, minimum-χ^2 model uncertainty is smaller than the marker size.

component. In general, beyond CO(8-7), the contribution to the total CO partition drops significantly and molecules will populate those higher states less frequently on average.

Importantly, the gas does not need to be diffuse in order to be optically thin. In fact, the second component, which we discuss later to be the denser component (§4.7.2), has more instances of the CO(1-0) line being optically thin. The lower density gas has a higher opacity, and a CO partition function that is weighed heavily by the lower-J lines. Our results show that as the density increases, the lines become more distributed across the CO partition function, which results in optically thin CO(1-0) line emission in the denser gas. This is consistent with theoretical work of Narayanan & Krumholz (2014), which had utilized both hydrodynamic simulations and radiative transfer analyses in order to calculate the CO line excitation for various idealized disk and merger galaxies at $z > 1$.

Characterizing the molecular ISM properties

Table 4.5 shows the mean and standard deviation value across the sample of *LPs* for the main free parameters. Note, the median values for the sample of *LPs* does not differ within the uncertainties. The *LPs* have a mean H_2 gas density and galaxy-wide mean turbulent velocity of $<\log(n(H_2))>= 4.3 \pm 0.9$ cm^{-3}, and $< \Delta V_{\rm turb} >= 125 \pm 40$ km s^{-1}, respectively. The mean value of the gas kinetic temperatures for both components in the *2-component* model are roughly equivalent to the mean kinetic temperature using the *Turbulence* model – despite the inherent differences in the physical assumptions of each model.

Using the derived dust temperature, we find the mean ratio of $< T_{\rm kin}/T_{\rm d} >= 2.6 \pm 1.3$. For mean

Parameter	Unit	Mean value (N = 24) LPs	
$\log(n_{H_2})$	cm^{-3}	4.31	0.88
T_{kin}	K	119.98	77.23
T_d	K	44.67	9.74
T_{kin}/T_d	-	2.58	1.30
κ_{vir}	km $s^{-1}pc^{-1}$ $cm^{3/2}$	1.45	0.36
ΔV_{turb}	km s^{-1}	125.17	39.98
$\sqrt{\mu_L}R_{eff}$	pc	13533.33	3147.00
$GDMR$	-	130.00	4.20
M_{ISM}	$M_\odot$	2.68E+12	1.28E+12
[CI]/[H_2]	-	6.82E-05	3.04E-05

Table 4.5: The mean and standard deviation for all χ^2-weighted mean parameter values across the sample of *LPs* – each of which the mean value calculated from ~2 million model evaluations.

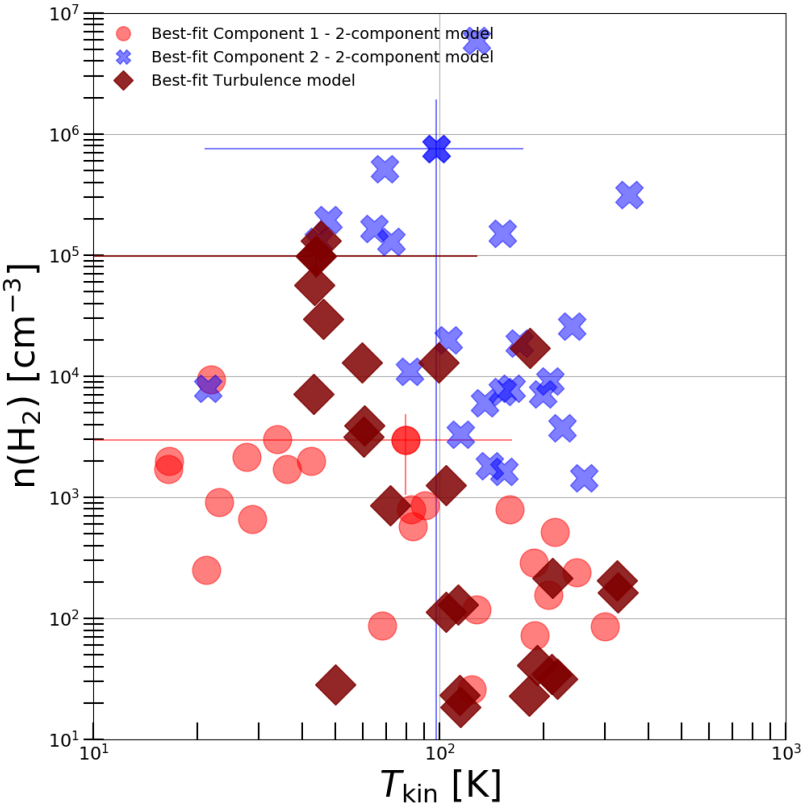

Figure 4.7: Best-fit, minimum-χ^2 solutions for the H_2 gas volume density and gas kinetic temperature derived for the *2-component* and *Turbulence* models (log-log-scale). We also show representative errors for both models.

densities above $\sim 10^{4.5}$ cm^{-3}, the value of $T_{\rm kin}/T_{\rm d}$ converges closer to unity as the molecular gas and dust become coupled (Goldsmith, 2001). This is indeed derived for the denser component, i.e. component two, which has a higher mean density, but lower $T_{\rm kin}/T_{\rm d}$, for the *2-component* model. This is also consistent in the *Turbulence* model results, as the *LPs* with higher mean density have lower values of $T_{\rm kin}/T_{\rm d}$. The mean apparent radius of the *LPs* is found to be $\sqrt{\mu_{\rm L}}R_{\rm eff} \sim 10 - 15$ kpc for the *Turbulence* model. For the *2-component* model, we derive a mean effective radius of $\sqrt{\mu_{\rm L}}R_{\rm eff} \sim 8.5$ kpc and ~ 3.3kpc, for the more diffuse and denser components, respectively.

We explore the relationship between the value of $T_{\rm kin}$ and H_2 gas density in Fig. 4.7. We plot the best-fit, minimum-χ^2 solutions obtained for both components in the *2-component* model. We also compare to the best-fit, minimum-χ^2 model results from the more physically motivated *Turbulence* model. In general, for the *2-component* model, the first component tends to have a lower H_2 gas density than the second component. There is a large dispersion in the value of $T_{\rm kin}$ for both components, although the first component tends to have more values at lower $T_{\rm kin}$. Since we find a similar range in $T_{\rm kin}$ for both components, it is clear that indeed the higher-J CO lines are driven mostly by the fact that the densities are higher, and that the $T_{\rm kin}$ plays a secondary role. This relation between the second component of the *2-component* model, and the observed high-J CO transitions is shown for all of the *LPs* in the online supplemental version to this manuscript. As shown, the second component may be largely unconstrained and have best-fit, minimum-χ^2 solutions for the density which are unlikely based upon examination of the more realistic results for the *Turbulence* model. Fig. 4.7 also shows that for the best-fit, minimum-χ^2 values of the H_2 gas density for the *2-component* model, the second component is always denser than the first. We find that the dominant emitting component associated with the excitation of the lower-J CO lines, has a mean volume density $\log(n(H_2)) = 2.2 - 3.7$ cm^{-3}, while the second component has a mean volume density between $\log(n(H_2)) = 3.2 - 6.4$ cm^{-3}, consistent with the observed trends in the line opacities seen in Fig. 4.6. Altogether, the *LPs* have a pervasive, dense, and highly active ISM with an average gas kinetic temperature $< T_{\rm kin} >= 120 \pm 77$ K. The median values for both components in the *2-component* model are ~ 81 km s^{-1}and ~ 137 km s^{-1}, for component one and two respectively. The Kendall's tau coefficient $\tau = 0.05$ indicates the gas kinetic temperature of component one and two are uncorrelated. This suggests that the diffuse (component one) and dense (component two) gas, although both relatively warm, share a distinct range of temperatures. The 2-sample Kolmogorov-Smirnov test also confirms that the gas kinetic temperatures likely share a different distribution for component one and two, respectively, with a p-value of 0.06[6].

To evaluate the apparent FIR luminosities we compute the integrated rest-frame FIR (40-120μm) dust SED. As noted above in §4.6, in the *Turbulence* model we add together the 50 LVG calculations which sample the mean gas density PDF (constant $GDMR$ for each calculation), to further derive the total dust SED. We calculate a wide range in apparent FIR luminosities among the *LPs* of $\mu_{\rm L}L_{\rm FIR} = 8 - 470 \times 10^{12}L_\odot$, with the corresponding dust temperatures of ~40 - 50 K. The contribution, per component, of the FIR luminosity is approximately divided among the *LPs* for the *2-component* model. The more highly excited component contributes ~50% of the total $\mu_{\rm L}L_{\rm FIR}$, on average, with a large dispersion. Following the traditional method in Kennicutt & Evans (2012) we integrate the total IR luminosity between 8-1000μm to derive a mean apparent $\mu_{\rm L}SFR = 35.6 \pm 4.4 \times 10^3$ M$_\odot$yr^{-1}.

[6] A p-value of 0.05 or less allows one to reject the null hypothesis that the two samples of kinetic temperatures come from the same distribution.

With an average magnification factor of 20, this would correspond to an intrinsic mean SFR for the *LPs* of order 1500 $M_{\odot}yr^{-1}$.

The dust opacity for the *LPs* becomes unity at wavelengths comparable to what is expected, i.e. ≥ rest-frame 100 μm, based on studies of the optically thick dust within the ISM of local and high-z star-forming systems (Blain et al., 2003; Huang et al., 2014; Lutz et al., 2016; Greve et al., 2012; Spilker et al., 2016; Hodge et al., 2016; Simpson et al., 2017). Overall, there is a range of λ_0 from a few tens of μm to ∼100-300 μm for both component one and component two, with the latter having significantly warmer dust temperatures and higher gas column densities, on average. In particular, we find a range of values between $N_{H_2} \sim 1$ - $10{\times}10^{23}cm^{-2}$ and $N_{H_2} \sim 0.5$ - $50{\times}10^{24}cm^{-2}$ for component one and component two, respectively. We estimate the effective optical extinction, A_V (in magnitudes), using the result for the Milky Way from Güver & Özel (2009), i.e.

$$N_H(cm^{-2}) = 2.2 \times 10^{21} A_V. \tag{4.4}$$

We find a value of $A_V > 450$, for a fiducial value of $N_{H_2} \sim 1 \times 10^{24} cm^{-2}$ for the *LPs*. The H_2 gas column densities in the second component of the most extreme *LPs* resembles regions similar to local starbursts and even comparable to the rare, highly dust enshrouded local starbursts exceeding $N_{H_2} \sim 10^{24-25} cm^{-2}$ (Sanders & Mirabel, 1996)). The *2-component* model does not recover small regions, and therefore any emission from such compact, high gas column density, galactic nucleus regions would not dominate the total emission. In fact, the *Turbulence* model indicates the smallest regions, corresponding to the highest gas density, contribute a negligible amount to the total line and dust SEDs (Fig. 4.4). It is often assumed that for dusty star-forming galaxies, with SFRs $> 100 - 1000\,M_{\odot}\,yr^{-1}$, that the thermal dust emission transitions from optically thick to optically thin beyond wavelengths of $\sim 100\mu m$ or more (Casey et al., 2018). This assumption is also verified in local star-forming systems (e.g Downes et al., 1993; Scoville et al., 2014, 2016a), but is difficult to constrain based on limited observations of individual high-z systems. This is often because of an sufficient sampling of the peak and tail of the thermal dust emission, as well as spatially unresolved measurements which cannot constrain the emitting size to compute accurate column densities. The spatially unresolved nature of this study is therefore a caveat in our derivation of both λ_0 and N_{H_2}.

Total molecular ISM mass estimates

We define the total, apparent, molecular gas mass[7], $\mu_L M_{ISM}$, based on our non-LTE radiative transfer LVG calculations of the H_2 gas column density and the effective radius. The H_2 gas column density is directly proportional to the volume density, $n(H_2)$, multiplied by the equivalent path-length of the molecules, i.e. $\Delta V_{turb}(\delta v/\delta r)^{-1}$, and therefore yields, together with the effective radius,

$$\mu_L M_{ISM} \propto \frac{\mu_L\, R_{eff}^2\,[pc^2] \times n(H_2)\,[cm^{-3}] \times \Delta V_{turb}\,[kms^{-1}]}{\delta v/\delta r\,[km\,s^{-1}/pc]}. \tag{4.5}$$

The systemic velocity gradient, $\delta v\,/\delta r$, is averaged across the modelled molecular gas component, which is assumed to fill the source solid angle. This corresponds to the mass of each component,

[7] Corrected by the Helium abundance, a factor 1.36 (Allen, 1973).

i.e. the total mass for the *2-component* model is the sum of both components. The *Turbulence* model density PDF is sampled by 50 density bins, each of which has an associated solid angle and allows for 50 individual mass calculations. The total $\mu_{\rm L} M_{\rm ISM}$ is the sum of all of the masses corresponding to the full density PDF. We use the value of $\mu_{\rm L} M_{\rm ISM}$ derived in the *Turbulence* model to estimate a range for the mean total molecular ISM mass of $\mu_{\rm L} M_{\rm ISM} = 3.6{\times}10^{11} - 1.6{\times}10^{13}$ M$_\odot$. The *2-component* model-derived $\mu_{\rm L} M_{\rm ISM}$ is broadly consistent with the *Turbulence* model, although the latter tends to be larger up to a factor ∼1.5. The inherent power-law dependence between density and gas kinetic temperature of the *Turbulence* model prevents over-dense solutions for the mean density in the log-normal PDF, and thus drives a realistic turnover in the CO line intensity at higher-J. Therefore, in the *Turbulence* model, there is more diffuse gas, on average, which contributes a larger fraction to the total molecular ISM mass. In contrast, the *2-component* model tends to fit the higher-J lines with a stronger contribution from the second, denser component, which contributes less to the total mass.

The mass of the more highly excited component in the *2-component* model (i.e. component two) can be thought of as a tracer of dense molecular gas (Gowardhan et al., 2017). The best-fit, minimum-χ^2 model solutions in our sample of *LPs* indicate a median and mean value of $M_{\rm ISM,c2}/M_{\rm ISM,total} = 25$ and 30%, respectively, for this proxy for the dense molecular gas fraction believed to be more closely associated with current SF. Therefore the more diffuse/less-excited component carries most of the mass. The larger mass fraction for component one is due to the larger size of that component, which scales non-linearly with the mass (Eq. 4.5).

The *LPs* have an average apparent total molecular gas mass $\mu_{\rm L} M_{\rm ISM} = 2.5{\times}10^{12}$ M$_\odot$. If this would be transformed into stars, this theoretical gas depletion time, $\tau_{\rm dep}$, results in a timescale on the order of $\tau_{\rm dep} =< \mu_{\rm L} M_{\rm ISM} > /< \mu_{\rm L} SFR >= (2.5{\times}10^{12})/(35.4{\times}10^{3}) \sim 70$ Myr. This rapid depletion timescale is an order of magnitude lower than the 1 Gyr gas depletion time observed in local star-forming galaxies (Leroy et al., 2013; Saintonge et al., 2013, 2016b), in agreement with the strong redshift dependence summarized by Tacconi et al. (2018, 2020). This further supports the notion that these systems lie above the main-sequence for star-forming galaxies at $z \sim 2 - 3$ (Whitaker et al., 2012). We use the derived values for $\sqrt{\mu_{\rm L}} R_{\rm eff}$ to also calculate the surface gas mass density $\Sigma_{M_{\rm ISM}} = \mu_{\rm L} M_{\rm ISM}/\pi(\sqrt{\mu_{\rm L}} R_{\rm eff})^2 \sim$ 800 - 22000 M$_\odot$ pc^{-2}. Note the magnification factors cancel to first-order. The total mean values of some of the *LPs* may be largely unconstrained, due to the lack of either ancillary [CI] data, strong dust photometric support (other than *Planck*data alone), or an insufficient amount of CO line detections. These *LPs* sample the higher-end of the observed molecular gas mass surface densities when compared to local star-forming galaxies (Schmidt, 1959; Downes & Solomon, 1998; Kennicutt & Evans, 2012; Bolatto et al., 2013, also see §4.8.2). The active star-forming regions of the *LPs* are, however, extended by 25 - 100× larger in area, with an intrinsic emitting size radius of order a few kpc (∼3 kpc; see §4.8.2).

4.7.3 Atomic Carbon Gas Excitation

In total, 21/24 *LPs* have one or both of the [CI] emission lines detected. Only 5/24 *LPs* have a single carbon line detection, while the remaining 16/24 *LPs* have measurements of both fine-structure lines. The [CI] measurements of the *LPs* represent the brightest apparent [CI] line fluxes reported at high-z (Brown & Vanden Bout, 1992; Barvainis et al., 1997; Weiß et al., 2003, 2005a; Walter et al., 2011;

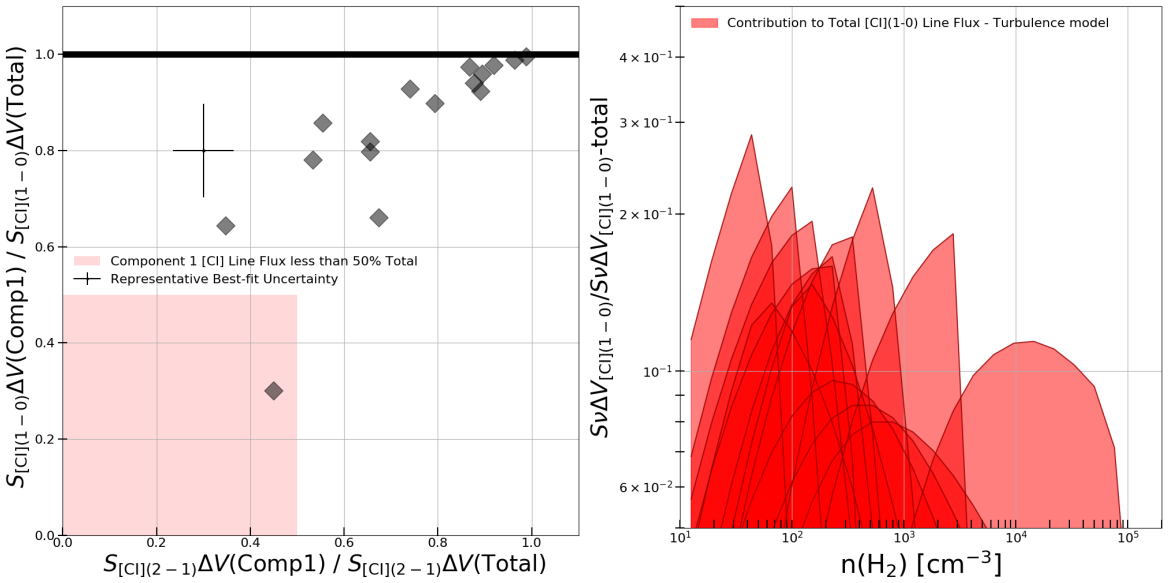

Figure 4.8: **Left:**Relative [CI](1-0) and [CI](2-1) line flux densities for component 1 versus the combined line flux densities for both components in the *2-component* model. The red-square indicates that both [CI] lines predominantly arize from the denser component, i.e. component 2. **Right:** For each of the *LPs* we plot (log-log-scale) the relative contribution to the total [CI](1-0) line flux derived in the *Turbulence* model, from the 50 individual [CI](1-0) line fluxes corresponding to the 50 H_2 densities which sample the density PDF.

Alaghband-Zadeh et al., 2013; Bothwell et al., 2017; Yang et al., 2017; Andreani et al., 2018). Strong turbulent mixing of the cool neutral media in the ISM may likely occur in these turbulent *LPs* (Xie et al., 1995), allowing for enriched [CI]/H_2 abundances in the interiors of molecular clouds, and thus strong [CI] emission. Both theoretical and observational studies have demonstrated the reliability of using [CI] to trace the overall kinematics of the cold gas, as well as to determine the total molecular gas mass (Papadopoulos & Greve, 2004; Weiß et al., 2005a; Tomassetti et al., 2014; Glover & Clark, 2014; Glover et al., 2015; Israel et al., 2015; Israel, 2020). The latter requires knowledge of the atomic carbon excitation temperature, $T_{\rm exc}$, and gas-phase abundance, [CI]/H_2, to accurately convert the [CI] line emission to the atomic carbon mass, $M_{\rm C}$, and further to the total molecular gas mass $M_{\rm ISM}$ (Weiß et al., 2003, 2005a).

We first examine which density phase the [CI] line emission predominantly arises from. The left-hand side of Fig. 4.8 plots the relative integrated flux values for the [CI](1-0) and [CI](2-1) lines from component one, with respect to the total integrated flux value for both components combined, for the *2-component* model. We remove from the figure the 5 *LPs* with only a single [CI] line to avoid mis-interpreting our results. Almost all of the [CI](1-0) and [CI](2-1) line emission in the *LPs* comes from the first component. In general, the first component is best-traced by the [CI](1-0) line. In general, this indicates that the carbon lines can be reliable tracers of the bulk gas mass, since we have shown in §4.7.2 that the first component in the *2-component* model carries most of the total mass. One of the *LPs*, LPs-J1139, seems to have a significant contribution from the denser component as indicated by the low contribution to the overall [CI] line emission from component one. This is due to its unusually high [CI](2-1) to [CI](1-0) line ratio (Nesvadba et al., 2019), although the CO(7-6) line

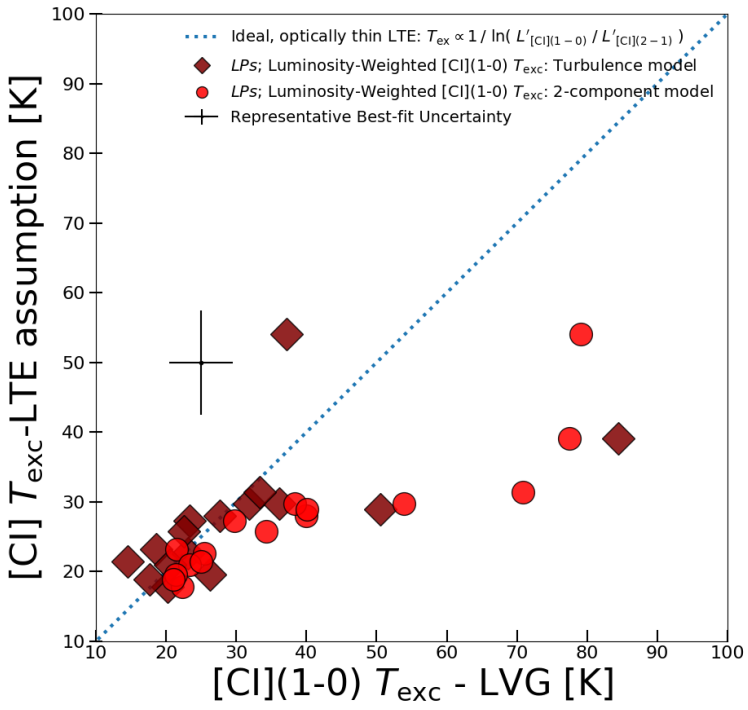

Figure 4.9: Luminosity-weighted excitation temperature of the atomic carbon [CI](1-0) line based on both the *2-component* model (red circle) and *Turbulence* model (maroon diamond) are shown on the x-axis. These values are compared to the predicted value based on the assumption of optically thin, LTE gas conditions (Schneider et al., 2003a).

reported by Cañameras et al. (2018b) appears to consistently under-predict the model-derived line flux density. The right-hand side of Fig. 4.8 further reveals the relationship between the [CI](1-0) velocity integrated line fluxes and H_2 density based on the *Turbulence* model. As suggested by the more simplistic *2-component* model, the *Turbulence* model shows that the diffuse gas, with $\log(n(H_2))$ = 2 - 3 cm^{-3}, is primarily responsible for the [CI](1-0) line emission. For such active star-forming systems, this implies that the carbon lines are well-suited to predominantly trace the diffuse molecular gas.

Next we investigate the atomic carbon T_{exc} for this diffuse molecular gas phase traced by the [CI] lines. In particular, our non-LTE analyses enables us to test the validity of the optically thin, LTE assumption framework that is commonly applied to detections of [CI] lines in star-forming galaxies. The measurement of both ground-state [CI] lines can, in principle, provide an independent estimate to constrain the carbon T_{exc} (Stutzki et al., 1997; Schneider et al., 2003a). The use of the carbon line ratio, $R_{[CI]} = L'_{[CI](2-1)}/L'_{[CI](1-0)}$, to determine T_{exc} requires two major assumptions: i.) that the line emission is optically thin and ii.) the lines are excited under LTE conditions, as defined in the Boltzmann Equation: $T_{exc,LTE} = 38.8/\ln(2.11/R([CI]))$ K (Stutzki et al., 1997; Schneider et al., 2003a). The value of T_{exc} can differ for each of the line transitions, i.e. the temper-

ature needed to recover the relative populations of the upper/lower levels from a Boltzmann distribution.

We briefly return to Fig. 4.6, based on our best-fit, minimum-χ^2 *2-component* models, to recall that the majority of the *LPs* have optically thin [CI](1-0) and [CI](2-1) lines. This also supports the capability of using the optically thin [CI] lines as a strong tracer of the bulk atomic carbon column density. We further calculate the value of the flux-weighted [CI](1-0) excitation temperature, $T_{\rm exc}$([CI](1-0)) using the relative integrated flux values from both components of the *2-component* model. In addition, we also calculate the equivalent flux-weighted [CI](1-0) line $T_{\rm exc}$ using the individual gas properties corresponding to the 50 density bins used to sample the density PDF derived in the *Turbulence* model.

We find that the average luminosity-weighted excitation temperature for $T_{\rm exc}$([CI](1-0)) $\sim$ 40 K for the *2-component* model and $T_{\rm exc}$([CI](1-0)) $\sim$ 32 K for the *Turbulence* model. Note, the mean value for $T_{\rm exc}$([CI](2-1)) $\sim$ 29 K for the *Turbulence* model. In the LTE assumption, $T_{\rm exc}$:= $T_{\rm exc}$[CI](1-0) = $T_{\rm exc}$[CI](2-1). The *LPs* have a systematically lower value of $T_{\rm exc}$[CI](2-1) than $T_{\rm exc}$[CI](1-0), up to 25-30% in some cases, reflecting those sub-thermal gas excitation conditions. Fig. 4.9 compares our derived, flux-weighted value of $T_{\rm exc}$[CI](1-0) using both models to the optically thin, LTE assumed value for the $T_{\rm exc}$, as presented in Stutzki et al. (1997); Schneider et al. (2003a). In general, our model-derived values agree with the ideal framework of assuming the atomic carbon excitation occurs within optically thin, LTE gas conditions, yet we find that some of the *LPs* would have had systematically under-predicted values of the carbon $T_{\rm exc}$ under these ideal assumptions. This emphasizes the importance in non-LTE modelling to better understand the sub-thermal excitation of the cold atomic and molecular ISM in star-forming galaxies. Our results for $T_{\rm exc}$ can also be compared with the recent large compilation of all local and high-z star-forming systems with [CI] detections (Valentino et al., 2020). They assume the same LTE assumptions as in Schneider et al. (2003a), yielding $T_{\rm exc}$ of $\sim$ 25 K with a moderate dispersion. This includes the high-z starburst/quasar sample of Walter et al. (2011), which had an average excitation of $\sim$ 30 K when using the same optically thin, LTE assumptions.

There are 5/16 *LPs* with both [CI] detections for which the *Turbulence* model still predicts low excitation temperatures of the [CI](1-0) line of $\leq$20 K. These are therefore over-predicted according to the simplified LTE assumption. We note that the low values of $T_{\rm exc}$ in these *LPs* are accompanied by their relatively low line ratios between the [CI](2-1) and [CI](1-0). At values of $T_{\rm exc} \leq 20$ K, Weiß et al. (2005a) demonstrated that the atomic carbon mass estimate will increase exponentially. Many of the *LPs* show substantially sub-thermal gas excitation, as shown from the $T_{\rm exc}$[CI](1-0) values. This may be due to the enhanced molecular gas kinetic temperatures with respect to the carbon excitation temperature, $T_{\rm kin}/T_{\rm exc}$[CI](1-0) $\sim$ 4. Therefore, blind LTE assumptions would have strongly impacted the inferred total carbon mass and relative abundance in those galaxies by about an order of magnitude. If the [CI] lines are completely dominated by sub-thermal gas excitation, the model-derived value of $T_{\rm exc}$ will be higher by up to a factor of 2-3 in the *2-component* model. There is considerably less scatter in the *Turbulence* model, which is likely due to the differences in these models when deriving the carbon gas-phase abundance.

We recall that we have restricted the CO/H_2 abundance to a Milky Way value of $\sim 10^{-4}$, close to that of local star-forming systems with CO/H_2 = 0.5 - 1 $\times 10^{-4}$. We do, however, allow the value of [CI]/H_2 to vary as a free parameter in both models. We find, for the *Turbulence* model, the sample

mean for the *LPs* of $< [CI]/H_2 >= 6.82 \pm 3.04 \times 10^{-5}$. To better understand the *2-component* model, we note that if the value of $[CI]/H_2$ were increased in the second component to match that of the first component, then the [CI] emission would always be close to LTE (since the H_2 density of component two is always higher than the first component (Fig. 4.7). The *2-component* model solves this by reducing the value of $[CI]/H_2$ in the second component, so that the emission is dominated by the sub-thermally excited emission from the first component. Thus, the value of $[CI]/H_2$ in the second component must be lower, otherwise the models would result in higher than observed line ratios. This is one of the main criteria for the *Turbulence* modelling procedure, which realistically forces the gas-phase carbon abundance to decrease with increasing H_2 densities according to a power-law relation.

At high-z , knowledge of the excitation conditions and abundance of carbon is often the main source of uncertainty. The mean value of $[CI]/H_2$ we find for the *LPs* is comparable to previous estimates by local/high-z studies, although typically this has been achieved via the inferred H_2 mass from single (low-J) CO transitions (Weiß et al., 2005a; Walter et al., 2011; Valentino et al., 2020). We caution that there is an order of magnitude dispersion in $[CI]/H_2$ among the *LPs*, which has strong implications for the inferred conversion from the [CI] line luminosity to M_{ISM} in star-forming galaxies (as discussed in §4.8.2). Some high-z carbon gas-phase abundance estimates are a few $\times 10^{-5}$ (Walter et al., 2011), which are broadly consistent with that of low-z galaxies. This suggests that the starbursts and QSO have at least solar gas-phase metallicities or higher (Gerin & Phillips, 2000; Weiß et al., 2001; Israel & Baas, 2002, 2003). Overall, we find values often lower than the abundance derived in the solar neighborhood of $[CI]/H_2 \sim 3.5 \times 10^{-4}$ (Anders & Grevesse, 1989). In some cases, the *LPs* show similar $[CI]/H_2$ abundances to the cold Milky Way CO-faint clouds, with $\sim 1 - 2 \times 10^{-5}$ (Frerking et al., 1989; Keene et al., 1997).

4.8 Discussion

4.8.1 Molecular gas excitation at high-z

Classifying the gas physical conditions in the *LPs*

Fig. 4.5 shows that the *LPs* offer a rich perspective into the wide range of gas excitation properties of CO for high-z star-forming galaxies. Overall, there seems to be a continuous distribution in gas excitation conditions for this sample of *LPs*. The high magnification therefore allows us to probe an intrinsically heterogeneous mix of dusty star-forming galaxies. Following the classification scheme defined by Rosenberg et al. (2015) for the diverse sample of local IR-luminous star-forming galaxies, we apply the parameter, hereafter "x_{class}", to quantify the range of excitation conditions in these 24 *LPs*. This parameter specifically characterizes the drop-off slope, after the expected peak of the CO line SED of J_{up} = 5 - 7. For each individual galaxy, we compare the relative line luminosity strength (in $L_\odot$) of the higher-J CO(J_{up} = 11 - 13) lines versus the mid-J CO(J_{up} = 5 - 7) lines:

$$x_{class} = \frac{L_{CO(11-10)} + L_{CO(12-11)} + L_{CO(13-12)}}{L_{CO(5-4)} + L_{CO(6-5)} + L_{CO(7-6)}}, \tag{4.6}$$

with three excitation classes defined as $x_{class1} = [< 0.33]$, $x_{class2} = [0.33, 0.66]$, and $x_{class3} = [> 0.66]$. The sample of *LPs* indeed shows a broad range of excitation conditions based on these three

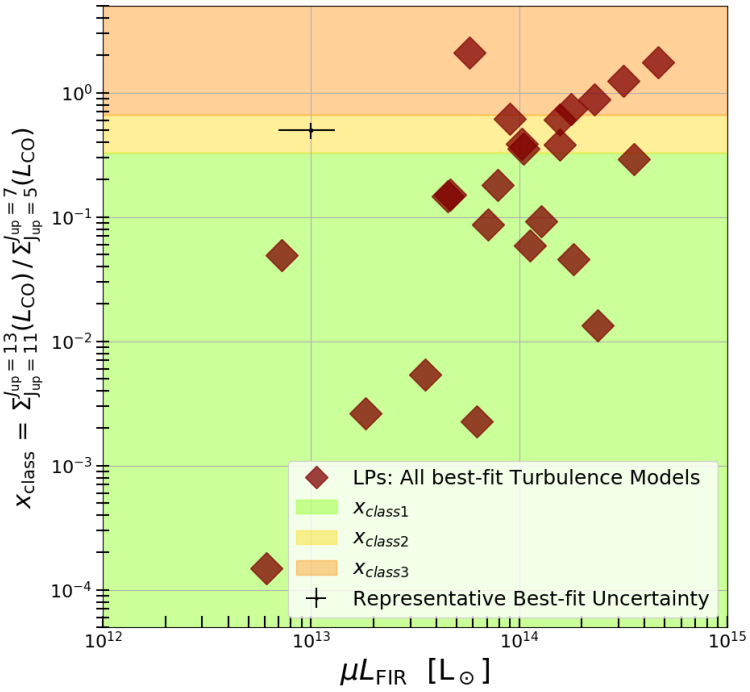

Figure 4.10: Plot (log-log-scale) between $x_{\rm class}$ and FIR luminosity, based on the best-fit, minimum-χ^2 *Turbulence* models. For details on the classification scheme, see §4.8.1 and Eq. 4.6.

different CO line SED classifications, with a continuum of $x_{\rm class}$ values. In total, there are 14 *LPs* within $x_{\rm class1}$, five *LPs* within $x_{\rm class2}$ and five *LPs* within $x_{\rm class3}$. We note that the three $z \sim 1$ *LPs* are all in $x_{\rm class1}$, however the distribution of z and classification is well-mixed for the $z = 2 - 3.5$ sub-sample. Fig. 4.10 shows the classification versus the FIR luminosity, indicating a clear relation between these two quantities, despite the strong incompleteness in our flux-limited sample of *LPs*, based on their selection criteria. The correlation we observe, between $x_{\rm class}$, or more broadly the CO line ratios, and the FIR luminosity is consistent with previous studies of star-forming galaxies (Greve et al., 2014; Rosenberg et al., 2015).

Mean CO brightness temperature ratios at $z > 1$

The CO line luminosities, $L'_{\rm CO}$, normalized to the CO(1-0) line, are often used to study the global gas excitation conditions of a galaxy and the line SEDs (e.g. Bothwell et al., 2013). Here we use our dataset of the *LPs*, based on ~ 4 - 6 CO lines for each of the *LPs*, to better understand the CO line SEDs of such IR-bright, $z > 1$ galaxies. These $L'_{\rm CO}$ ratios are also used to scale the higher-J CO lines to the ground-state transition to infer the total molecular gas mass (Carilli & Walter, 2013). In Fig. 4.11 we use the *Turbulence* model to show all of the best-fit CO line luminosities, $L'_{\rm CO}$, normalized to the CO(1-0) line. We also show the stacked brightness temperature ratios of the lensed SPT sample

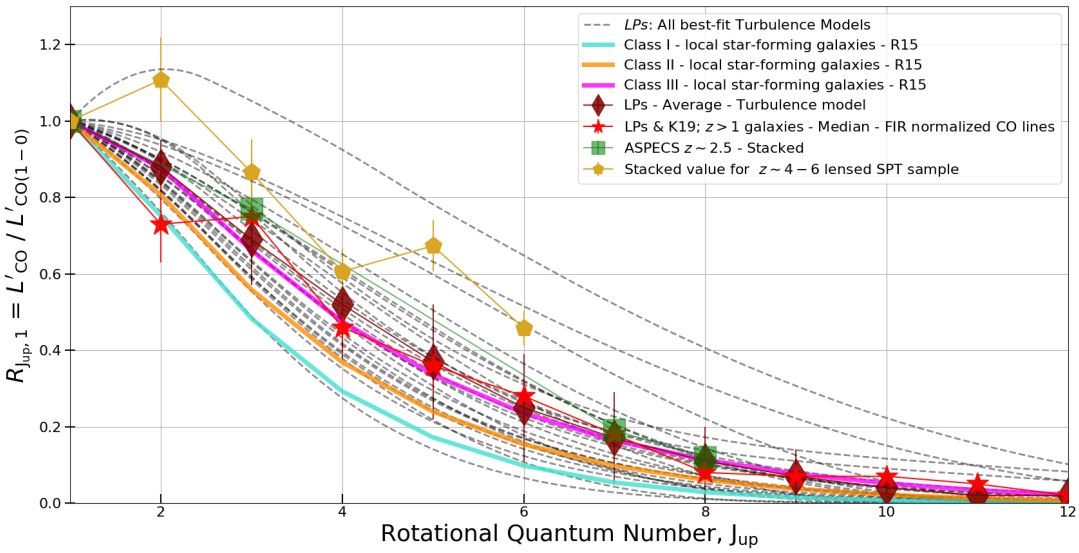

Figure 4.11: *Turbulence* model results for the best-fit, minimum-χ^2 model solutions for the CO line luminosities, $L'_{\rm CO}$, normalized to the CO(1-0) line, for the *LPs*. The average line ratios derived using the *Turbulence* model (maroon diamonds) are compared to the values from the *LPs* & K19 sample (red star), which are purely based on observations, with median line ratio values determined by normalizing each line by a common FIR luminosity. In addition, we plot representative local IR-bright star-forming galaxies from Rosenberg et al. (2015), with increasing classifications determined by their excitation conditions, from lowest to highest: Class I (light blue solid line), Class II (orange solid line) and Class III (magenta solid line). Yellow pentagons represent stacked values for the lensed SPT galaxies (Spilker et al., 2016), compared to the stacked value of $z \sim 2.5$ main-sequence star-forming galaxies (green squares) from the ASPECS sample (Walter et al., 2016; Riechers et al., 2020, Boogaard et al. submitted to ApJ).

(Spilker et al., 2016), and the stacked values of the unlensed, $z \sim 2.5$ main-sequence star-forming galaxies (Riechers et al., 2020, Boogaard et al. submitted to ApJ). The former tends to represent the higher gas excitation seen in a subset of the *LPs*. The latter, which considers only 7 sources in the stacked value, tends to agree with both the model-derived average values for $R_{3,1}$, $R_{7,1}$, and $R_{8,1}$. The *LPs* also show significantly higher line ratios than the $z \sim 1 - 2$, main-sequence star-forming galaxies in COSMOS field, for the available values of $R_{4,1} = 0.27$, $R_{5,1} = 0.21$, and $R_{7,1} = 0.06$ (Valentino et al., 2020)[8].

The local IR-bright star-forming galaxies from Rosenberg et al. (2015) are also shown in Fig. 4.11, according to their increasing classifications determined by their gas excitation conditions, from lowest to highest: Class I, Class II and Class. For reference the Milky Way has a global average value of $R_{3,1}$ of 0.28 ± 0.17 (Fixsen et al., 1999). The *LPs* show a broad range of gas excitation, although most have higher line ratios than both Class II and Class III galaxies, which are representative of most local (U)LIRGs (see also Papadopoulos et al., 2012a; Lu et al., 2014; Kamenetzky et al., 2016). We find

[8] Note, we have used a fiducial value of $R_{2,1} = 0.75$ to make this comparison, since only CO(2-1) line measurements are available.

that the mid-J CO lines have a mean $R_{6,1}$ of 0.25, consistent with the lower range of IR luminous star-forming galaxies. Papadopoulos et al. (2011) report values of $R_{3,1} = 0.67$ and $R_{6,1} = 0.2 - 1.6$ for local (U)LIRGs (Papadopoulos et al., 2012a). This is, overall, consistent with earlier studies and the value we obtain for the *LPs*. Local star-forming systems with $9 < \log(L_{\rm IR}) < 12$ show a median value of $R_{3,1}$ to be close to 0.5 (Mauersberger et al., 1999), with some 60 local barred galaxies and starbursts having an average value of $R_{3,1}$ close to 0.9 ± 0.1 (Yao et al., 2003). Overall, the line brightness temperature ratios for the *LPs* are usually not as high as one of the most IR luminous local starburst galaxies, M82 (Weiß et al., 2005b), which has a global average $R_{2,1}$, $R_{3,1}$, $R_{4,1}$ and $R_{5,1}$ of 0.98, 0.93, 0.85 and 0.75, respectively.

The sample mean and standard deviation are reported in Table 4.4. The *LPs* have line brightness temperature ratios that are often well-below unity (i.e. sub-thermal line excitation). Bothwell et al. (2013) previously interpreted the mean CO line SED of 32 $z > 1$ star-forming galaxies, by normalizing their CO line luminosities by a common FIR luminosity, while others normalized to a common measurement of the dust continuum at 1.4mm (Spilker et al., 2016). Based on our simultaneous modelling of the lines and continuum, we can test whether or not this is a valid method for building a mean line SED shape. The line ratios are sensitive to the FIR luminosity (see Fig. 4.10), yet different subsets of high-z sources do not have every line detected, and have different selection biases. Therefore, the FIR luminosity may be used to normalize each line detection in an attempt to remove these biases and to avoid physically misleading line ratios. It has been well-known that the FIR luminosity and CO line luminosity tend to increase with one another proportionally (Greve et al., 2012; Liu et al., 2015; Valentino et al., 2020).

To do this, we use the *LPs* & K19 $z \sim 1 - 7$ sample (hereafter "*LPs* & K19 sample"; $N_{gal} = 269$). To construct this compilation, we used our dataset for the *LPs* including the database compiled in Kirkpatrick et al. (2019), which includes most high-z galaxies with CO line detections (including Carilli & Walter, 2013; Pope et al., 2013; Aravena et al., 2014; Sharon et al., 2016; Yang et al., 2017; Frayer et al., 2018b; Perna et al., 2018; Kirkpatrick et al., 2019). Following previous studies, each CO line is normalized by a common FIR luminosity ($L_{\rm FIR} = 1 \times 10^{12.5}$ $L_\odot$). The values listed in Table 4.4 are derived using the *LPs* & K19 $z \sim 1 - 7$ CO line compilation, which consists of 90 CO(1-0) lines, 86 CO(2-1) lines, 128 CO(3-2) lines, 80 CO(4-3) lines, 68 CO(5-4), 73 CO(6-5), 63 CO(7-6), 39 CO(8-7), 33 CO(9-8), 14 CO(10-9), 15 CO(11-10) and 2 CO(12-11) high-z line measurements.

As shown in both Table 4.4 and Fig. 4.11, the average results from our best-fit, minimum-χ^2 *Turbulence* models are strikingly similar to the median brightness temperature ratios derived from the FIR luminosity-normalized lines we calculate from the CO line observations alone using the *LPs* & K19 sample, or the "All sources" sample (Kirkpatrick et al., 2019). In Table 4.4 we also reference the average line ratios, up to the $R_{5,1}$ ratio, from Carilli & Walter (2013), which is based on the available data for (sub)mm bright, star-forming galaxies (SMGs) and QSOs at the time. Although these values are often the most highly quoted for high-z line ratios, we also quote in Table 4.4 the more recent values reported by Kirkpatrick et al. (2019). The values from the latter are consistent with the low-mid-J CO line ratios reported by other recent studies of lensed, SMGs at $z > 1$ (Yang et al., 2017; Cañameras et al., 2018b).

At first glance, our results would seem to support this method of using the FIR luminosity to

normalize the CO lines to derive a mean CO line SED, however the sparse amount of well-sampled CO line SEDs per galaxy in the literature suggests that the three or more orders of magnitude dispersion in the observed line intensities (Fig. 4.2) all average out. The *LPs* & K19 $z \sim 1-7$ sample includes some of the brightest (sub)mm selected galaxies with multiple CO line detections, which further exaggerates the effects of averaging large samples of $z > 1$ galaxies Bothwell et al. (2013); Spilker et al. (2016); Yang et al. (2017); Cañameras et al. (2018b). As noted by Narayanan & Krumholz (2014), there can be a factor 5-10 difference in the CO line SEDs, at mid- to high-J transitions, for similarly selected, (sub)mm bright galaxies with the same integrated FIR luminosity. The broad range of excitation conditions and average line ratios we present for the *LPs* further highlights the notion that it is unlikely for their to be a template CO line SED for any $z > 1$ galaxy population. As noted throughout this work, our results agree with the theoretical models of Narayanan & Krumholz (2014) for the CO line SEDs of $z > 1$ star-forming galaxies, as parameterized by the SFR surface density. This suggests that in the absence of multiple CO line measurements, a SFR surface density estimate may be combined with limited line data, and further use the theoretical models of Narayanan & Krumholz (2014) to estimate the CO line SED.

4.8.2 Molecular gas mass estimates

Intrinsic Emitting Size Regions

One way to constrain whether or not the *LPs* are not only some of the most massive, gas-rich star-forming galaxies, but also perhaps the largest in size, is to cross-examine the model-derived radius with the intrinsic source size that might be expected from studies of star-forming galaxies at $z > 1$. As presented in §4.7.2, the mean value we derive from the *Turbulence* model for the radius of the modelled source emitting region is $\sqrt{\mu_{\rm L}} R_{\rm eff} \sim 10 - 15$ kpc. The intrinsic source size may differ, since we assume that the emission comes from a filled, face-on circular disk (see e.g. Weiß et al., 2007b) with an effective radius. This sets a lower limit to the true source size, as there is no information of how the gas and dust emission is distributed within the source solid angle. We therefore only consider the emission that is completely enclosed in the single dish beams, which corresponds to ~50 - 250 kpc physical diameter at these redshifts. We recall again the lens magnification factor estimates for the *LPs* in Table 4.1, as they will be used to estimate the intrinsic emitting size. For a reference, we derive an average value of $\mu_{\rm L}$ for the *LPs* using the upper limit value of $\mu_{\rm L}$ in Table 4.1. For galaxies without a published value of $\mu_{\rm L}$, we use the value based on the "Tully-Fischer" argument presented in Harris et al. (2012) and our CO(1-0) line measurements. The average lens magnification factor has a value of $\mu_{\rm L} \sim 20$. The expected, *intrinsic*, total line and continuum emitting size radius for all of the *LPs* $R_{\rm eff}/\sqrt{\mu_{\rm L}} = 13.5/\sqrt{20.4} \sim 3$ kpc. This size is consistent overall with the size of the dust continuum emission from massive star-forming galaxies at $z = 1 - 3$ (1 - 5 kpc, Simpson et al., 2015; Hodge et al., 2016; Oteo et al., 2016, 2017; Barro et al., 2016; Rujopakarn et al., 2016b; Fujimoto et al., 2017; Jiménez-Andrade et al., 2019b; Hodge & da Cunha, 2020).

We can further test the reliability of our *Turbulence* model if we consider two of the *LPs* with estimates of the intrinsic, lens model reconstruction of the source size, based on high-angular resolution data: LPs-J105353 (Cañameras et al., 2017b) and LPs-J0209 (Geach et al., 2018; Rivera et al., 2019).

As summarized in Harrington et al. (2019) for LPs-J0209[9], the lens model reconstruction from the low-J CO line image presented in both Geach et al. (2018); Rivera et al. (2019) suggests a molecular gas reservoir with an emitting radius of ∼ 1 - 2 kpc. The flux-weighted mean magnification factor derived for this source is ∼ 15, corresponding to an expected *intrinsic* emitting radius for LPs-J0209 of $R_{\rm eff}/\sqrt{\mu_{\rm L}} = 16.1/\sqrt{14.7} \sim 4$ kpc. Note that we are modelling the full extent of the CO(1-0) to CO(15-14) line emission. Therefore, our modelling is consistent with the independently derived source-plane radius derived from both the CO(4-3) and CO(3-2) emission lines within the overall uncertainties. Based on CO(1-0) line observations of high-z galaxies, the factor two difference can be accounted for, as the easily excited CO(1-0) line emission is expected to be more extended on average (Emonts et al., 2014; Spingola et al., 2020). LPs-J105353[10] is proposed to consist of two independent regions (roughly 1.5 kpc in length along the major axis) in the reconstructed source plane CO(4-3) line image (Cañameras et al., 2017b), each separated by ∼ 500 pc, corresponding to an intrinsic emitting size radius of ∼ 2 kpc. Our modelling would suggest an expected *intrinsic* emitting radius for LPs-J105353 of $R_{\rm eff}/\sqrt{\mu_{\rm L}} = 14.5/\sqrt{26.8} \sim 3$ kpc, which is consistent within the uncertainties considering both the lens model and our radiative transfer model. Thus, the intrinsic size may play a role in understanding the high apparent fluxes. A magnification factor of 50 would be required to reduce the mean value we derive from the *Turbulence* model, i.e. $\sqrt{\mu_{\rm L}} R_{\rm eff} \sim 10 - 15$ kpc, to match the more common size expected for $z > 1$ star-forming galaxies of ∼ 2 kpc. Since the average magnification factor for the *LPs* is ∼ 20, the size of these systems may be one of the primary physical parameters responsible for explaining their extreme IR luminosity.

Converting $L'_{\rm CO}$ and $L'_{\rm [CI]}$ to $M_{\rm ISM}$

We use the results of the more realistic *Turbulence* model (§4.7) to calculate the derived values of both $\alpha_{\rm CO}$ and $\alpha_{\rm [CI]}$ [hereafter without units attached to ease readability; $\rm M_\odot$ (K km s^{-1} pc^2)$^{-1}$] conversion factors between the line luminosity to total molecular gas mass, $M_{\rm ISM}$. We refer to these factors with respect to the ground-state transitions, CO(1-0) and [CI](1-0), unless otherwise noted. Fig. 4.12 shows the results for the value of $\alpha_{\rm CO}$ based on a representative set of low-to-high-J CO transitions, versus the minimum-χ^2 model solution for the total molecular gas mass, for all of the *LPs*. The CO(1-0) and CO(3-2) derived $\alpha_{\rm CO}$ values are less scattered than those derived from CO(9-8) and CO(11-10) transitions. This demonstrates that the lower-J lines are more reliable tracers of $M_{\rm ISM}$, as expected.

To consider the use of [CI] line emission as a tracer of $M_{\rm ISM}$, we recall the results in §4.7.3, in particular: i.) the [CI] lines are optically thin, and ii.) most of the carbon emission arises from the more diffuse line emitting region (i.e. component one from the *2-component* model) with $\log(n(H_2)) \sim 2 - 3$ cm^{-3} – which is the cold gas component responsible for the bulk of the total $M_{\rm ISM}$ (also see Fig. 4.8). The value of $\alpha_{\rm [CI](1-0)}$ can be used to convert the optically thin $L'_{\rm [CI](1-0)}$ measurement to $M_{\rm ISM}$, which we find an average value of $< \alpha_{\rm CI} >= 16.2 \pm 7.9$ for the *LPs* with both [CI] lines detected. Crocker et al. (2019) recently studied a sample of 22 local spiral galaxies, representing a wide range of SFR and stellar masses, using spatially resolved *Herschel* SPIRE observations of CO and [CI]. They found a lower value of $\alpha_{\rm [CI](1-0)} = 7.9$, with a factor 1.5-2 uncertainty. There

[9] Also referred to as the Red Radio Ring.
[10] Also referred to as PLCK G244.8+54.9.

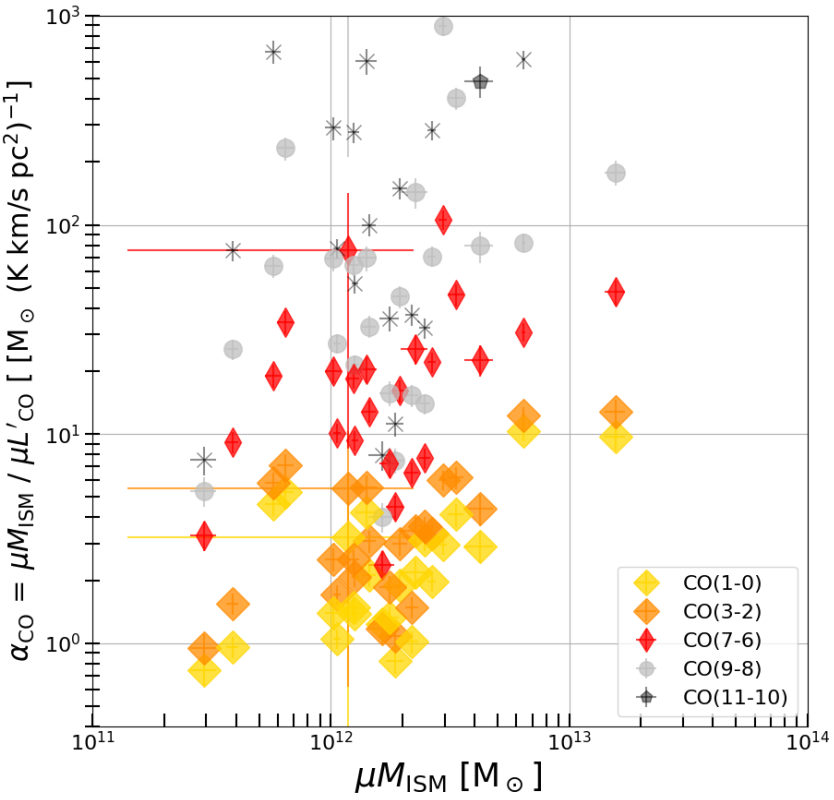

Figure 4.12: CO line to molecular gas mass conversion factor, α_{CO}, value versus μM_{ISM} for the CO(1-0) (gold diamond), CO(4-3) (orange diamond), CO(7-6) (thin red diamond), CO(9-8) (gray circle) and CO(11-10) (black cross) lines, as derived from the best-fit, minimum-χ^2 *Turbulence* models (log-log-scale).

are differences in these values of $\alpha_{[CI](1-0)}$ for the *LPs*, as compared to these less extreme local star-forming galaxies, yet this may be due to differences in the calibration. Our current work performs a full radiative transfer analysis, while Crocker et al. (2019) had used an intensity-intensity correlation between the low-J CO and [CI] line emission and an assumed value of α_{CO}. The latter was determined previously by (Sandstrom et al., 2013) for their sample based on an assumed spread in the *GDMR*. Another recent study used an alternative method to first measure [CI] and H_2 absorption lines from gamma-ray burst and QSO objects (Heintz & Watson, 2020). Thereafter they determine the value of $\alpha_{[CI](1-0)} \sim 21$ for an assumed solar metallicity, which is consistent with our derived values.

Based on the *Turbulence* model, we find an average value for the *LPs* of $< \alpha_{CO(1-0)} >= 3.4 \pm 2.1$, with a factor 10 dispersion and a mean value of $< \alpha_{CO(1-0)} >= 4.2$ for the galaxies with the best dust photometry and CO/[CI] line coverage. Note, the scatter in the conversion factors come from the scatter in the line luminosities and total molecular gas masses used to derive the mass-to-light conversion for each of the *LPs*. Therefore, a single conversion factor value would not reflect this

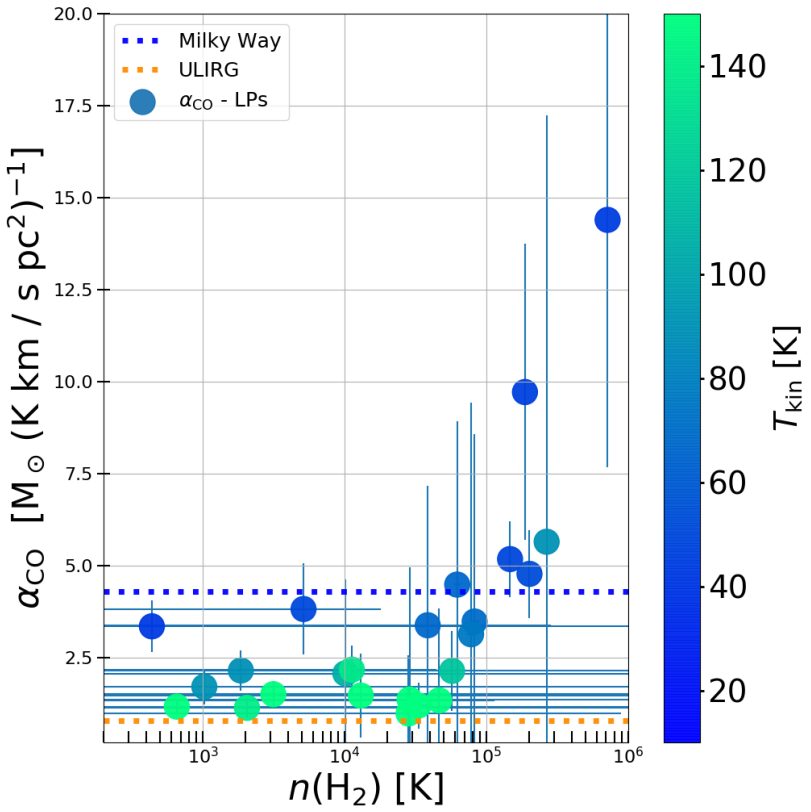

Figure 4.13: *Turbulence* model derived α_{CO} factor versus H_2 gas density (log-x scale). The colorbar denotes the gas kinetic temperature. These are the total χ^2-weighted parameter mean and standard deviation values derived from the ~2 million model calculations. The canonical ULIRG and Milky Way values for α_{CO} are α_{CO} = 0.8 and 4.3 M$_\odot$ (K km s^{-1} pc^2)$^{-1}$, respectively.

intrinsic dispersion among the sample.

Almost all of the *LPs* have a value of α_{CO} which is higher than the local IR (ultra)luminous star-forming galaxy (a.k.a "ULIRG") conversion factor of α_{CO} = 0.8 (Downes & Solomon, 1998). The ULIRG value was derived using similar LVG approximations using only the available low-J CO lines, as well as dynamical mass measurements of the concentrated nuclear starburst regions. The warm, diffuse and dense molecular gas that pervades the molecular medium of local IR luminous star-forming galaxies was not fully traced by the CO(1-0) and CO(2-1) lines Downes & Solomon (1998). The lower-J lines only trace the diffuse and warm gas under these active star-forming conditions, and therefore they correspond to lower values of α_{CO}. We have also shown this in our best-fit, minimum-χ^2 model CO line SEDs, where the CO(1-0) line emission arises mostly from the diffuse molecular gas with density $\log(n(H_2)) \sim 2$ cm^{-3}, while the gas at these lower densities has higher kinetic temperatures. A lower value of α_{CO} would be inferred for the *LPs* if limited to only the low-J CO lines tracing this warm and diffuse phase, and thereby neglecting the higher-density gas which is required to excite the higher-J CO lines. Therefore, our physical results are still consistent with the general conclusions in modelling the local ULIRGs (Downes & Solomon, 1998), yet we have modelled the substantial

contributions to the overall CO line SED from warm and dense gas of the order of $T_{\rm kin} \sim 120$ K and $\log(n(H_2)) = 4$ - 5 cm^{-3}. This explains why our overall result reflects higher values of $\alpha_{\rm CO} \sim 3.4$ for the *LPs*.

Fig. 4.13 shows our derived conversion factors as a function of both the mean H_2 gas density and gas kinetic temperature. Almost half of the 24 *LPs* have low values of $\alpha_{\rm CO} = 1 - 2$, and are associated with higher gas kinetic temperatures ($T_{\rm kin} > 120$K). The left-hand side of Fig. 4.13 shows a non-linear decrease in $\alpha_{\rm CO}$ as a function of increasing $T_{\rm kin}$, whereas the right-hand side of Fig. 4.13 suggests a strong rise in $\alpha_{\rm CO}$ for increasing H_2 gas density. We note that the system with one of the highest values is the known radio-AGN/starburst, LPs-J0209, and the highest redshift source in our sample, LPs-J105322 ($z \sim 3.5$) both have well sampled dust photometry and CO lines out to $J_{\rm up} = 11$ and both [CI] lines, yet we still derive the highest values of $\alpha_{\rm CO(1-0)} \geq 10$, albeit with larger uncertainty. In future work we will investigate the statistical relationship between $\alpha_{\rm CO}$ and these parameters. Since the LPs-J0209 source is known to have a compact radio AGN (Geach et al., 2015), future studies may explore the reasons whether or not star-forming galaxies with coeval AGN activity (Harrington et al., 2019) may tend to show higher values of $\alpha_{\rm CO}$. In fact, the AGN APM0827, has a relatively high value of $\alpha_{\rm CO} \sim 5$ and $\log(n(H_2)) \sim 5$ cm^{-3} (Weiß et al., 2007b).

The large range observed for the *LPs* suggests a strong diversity in gas excitation properties among this relatively small sample. It seems incorrect to assume a common value for high-z star-forming galaxies, as discussed previously in the context of a continuity of gas excitation conditions and the corresponding variation in the conversion factor (e.g. Casey et al., 2014). The two different values commonly applied have been based on a simplified bi-modal population of star-forming galaxies (e.g. Daddi et al., 2010), yet more complex two-population models are successfully reproducing several observed properties in observed high-z galaxies (Sargent et al., 2014). The latter may be tested with assumptions of a continuity in gas excitation conditions for different galaxy populations. Variations of the CO gas-phase abundance across a turbulent star-forming disk will alter the conversion factor (Wolfire et al., 2010; Shetty et al., 2011b; Narayanan et al., 2012), therefore it is possible for a wide variation in $\alpha_{\rm CO}$ to exist for a given gas column density. In general, the lower the metallicity, the higher the conversion factor will have to be in order to raise the relative unit mass per solar line luminosity to account for the low-abundance environment. The higher the metallicity, the lower the conversion factor (Wolfire et al., 2010; Bolatto et al., 2013; Narayanan & Krumholz, 2014).

In Fig. 4.14, we examine the relation between the derived $\alpha_{\rm CO}$ and $\alpha_{\rm [CI]}$ conversion factors with the gas mass surface density in the sample of *LPs*. The rather extreme galaxy-integrated surface gas mass densities for the *LPs* is accompanied by a wide range in the conversion factor we derive. Previous works (Tacconi et al., 2008) have suggested that as the gas mass surface density goes beyond 100 $M_\odot$ pc^{-2}, i.e. comparable to GMCs in the Milky Way and nearby galaxies, the values of $\alpha_{\rm CO}$ decreases. Fig. 4.14 indicates that our analyses suggest the possibility of a factor 10 dispersion of $\alpha_{\rm CO}$ between $\Sigma_{M_{\rm ISM}} = 10^{3-4}$ $M_\odot$ pc^{-2}, yet a positive trend. Since the CI emission is optically thin the conversion factor must increase. This drives the value we derive for $\alpha_{\rm [CI]}$ to higher values, which are comparable to the value of $\alpha_{\rm CO}$ for those low-metallicity nearby galaxies. The average value of $\alpha_{\rm CO}$ is slightly lower than the Galactic value (Bolatto et al., 2013). Overall, the sample mean value for the *LPs* is similar to the value of $\alpha_{\rm CO} = 3.6$ derived using clumpy disk dynamical mass model calculations

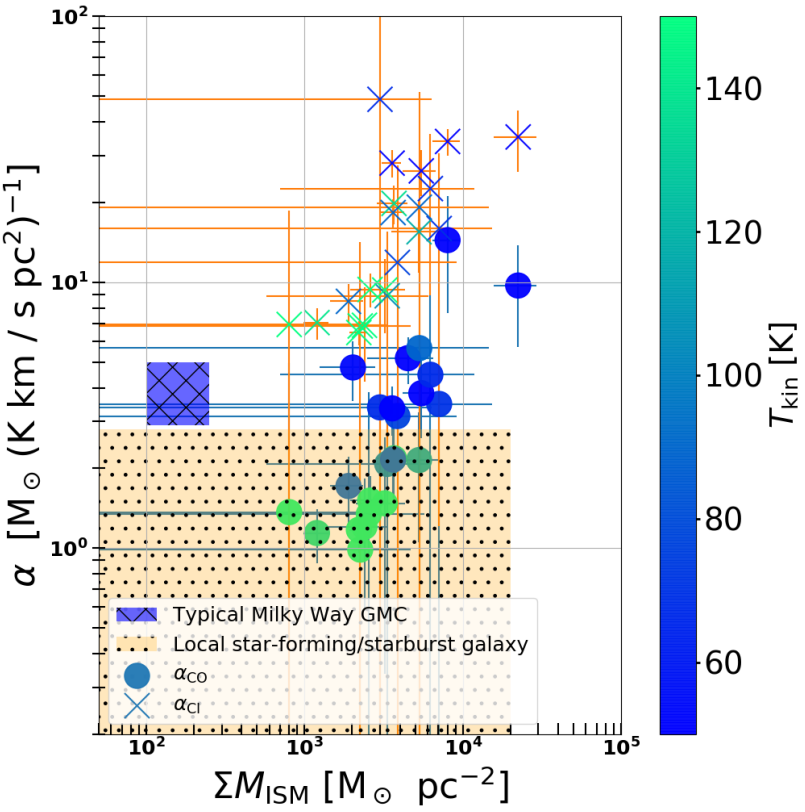

Figure 4.14: *Turbulence* model derived CO and [CI] line to molecular ISM mass conversion factors, plotted against the molecular ISM gas mass surface density, with α_{CO} and $\alpha_{[CI]}$ denoted as circles and crosses, respectively (log-log-scale). The colorbar denotes the gas kinetic temperature, T_{kin}. Also shown are the values for α_{CO} derived in the Milky Way and the local IR luminous star-forming systems (see Bolatto et al., 2013). Both plots report the total χ^2-weighted parameter mean and standard deviation values derived from the ~2 million model calculations.

for near-IR selected galaxies at $z \sim 1.5$ (Daddi et al., 2010). In general, lower T_{kin}, and both higher $\Sigma_{M_{ISM}}$ and $\log(n(H_2))$, seem to increase the value of α_{CO} based on our full radiative transfer modelling of the *LPs*. Comparable spatially resolved datasets would allow for such robust tests of functional forms between these parameters to enable a thorough comparison among this sample of *LPs*. For example, Maloney & Black (1988) considered $\alpha_{CO} \propto \sqrt{n(H_2)}/T_{kin}$, while others have proposed a weaker dependence on the gas kinetic temperature, i.e. $\alpha_{CO} \propto \sqrt{n(H_2)/T_{kin}}$ Shetty et al. (2011b).

Comparisons between M_{ISM} estimates derived from optically thin, dust continuum methods

The simultaneous modelling of the CO, [CI] and dust continuum emission enables a robust comparison to the inferred value of total molecular ISM mass, M_{ISM}, based only on the properties of the dust SED. Recently, there has been a growing set of methods using dust continuum measurements to infer the M_{ISM} in star-forming galaxies, although observations of dust and its effects have been used to derive gas column densities over many years. Previous studies have integrated information about the

visual extinction, gas-to-dust-mass ratio, the CO line luminosity to $M_{\rm ISM}$ conversion factor, $\alpha_{\rm CO}$, and observations of the thermal dust continuum along the assumed optically thin, Rayleigh-Jeans, side of the emission spectrum (Lilley, 1955; Heiles, 1967; Savage & Code, 1970; Aannestad & Purcell, 1973; Emerson et al., 1973; Hildebrand et al., 1977; Hildebrand, 1983; Young et al., 1986; Lonsdale & Hacking, 1987; Solomon & Sage, 1988; Scoville et al., 1991; Young & Scoville, 1991; Blain & Longair, 1993; Kruegel & Siebenmorgen, 1994b; Young et al., 1996; Solomon et al., 1997; Calzetti et al., 2000; Genzel et al., 2010; Leroy et al., 2011; Magdis et al., 2012; Scoville et al., 2014, 2016a, 2017; Tacconi et al., 2018; Coogan et al., 2019).

The use of a single-band dust continuum measurement to estimate $M_{\rm ISM}$ is based on the assumption that the rest-frame dust continuum emission is optically thin beyond $\lambda_{\rm rest} \geq 250\mu$m (recently highlighted by Scoville et al., 2014, 2016a, 2017). The method of Scoville et al. (2014, 2016a, 2017) (hereafter the "*1-mm method*"), uses the inferred rest-frame 850μm continuum emission, and derives an empirical calibration of the dust opacity per unit ISM mass. The total $M_{\rm ISM}$ estimate based on CO(1-0) line measurements is increasing for high-z star-forming galaxies, enabling further calibrations of this method. In the *1-mm method*, a Milky Way value of $\alpha_{\rm CO} = 6.5$ (Scoville et al., 1987, 2017) is applied for the absolute scaling from CO(1-0) line luminosity to the total $M_{\rm ISM}$. The *1-mm method* advocates using a cold, mass-weighted dust temperature, $T_{\rm d} = 25$ K (Scoville et al., 2014; Liang et al., 2018, 2019). With our detailed modelling, we are able to test this hypothesis.

Since our models provide the mass and the luminosity for each gas component, together with the dust temperature, we can compute the mass- and luminosity-weighted dust temperatures for each galaxy using:

$$\mathrm{T_{d-weighted}} = \frac{\Sigma_{\rm i=1}^{\rm i=N} W_{\rm i} T_{\rm d,i}}{\Sigma_{\rm i=1}^{\rm i=N} W_i}, \tag{4.7}$$

where $W_{\rm i}$ is the mass-weighted or luminosity-weighted value, $N = 2$ for the *2-component* model and $N = 50$ for the *Turbulence* model, since we have 50 individual calculations of the dust temperature and mass. The result of this calculation is shown in Fig.4.15, using the $L_{850\mu\rm m}$ value to calculate a luminosity-weighted dust temperature. Note, the dust temperature values we derive for the *LPs* span a range common to high-z dusty star-forming galaxies, therefore the high apparent IR luminosity for the *LPs* does not bias our results to sources with higher dust temperatures. We also note that the model derived dust temperatures we use to compute the luminosity-weighted value are also consistent, within 1-σ uncertainties, with previously determined values of the dust temperature using commonly applied modified black-body fits (Cañameras et al., 2015; Harrington et al., 2016).

Two immediate outcomes from this exercise are: 1.) the mass-weighted $T_{\rm d}$ value and luminosity-weighted $T_{\rm d}$ value for both models are remarkably consistent with one another, with a one-to-one correlation observed for all of the *LPs* when using the more realistic *Turbulence* model, and 2.) the mass-weighted $T_{\rm d}$ value for both models is consistently higher than the advocated value of $T_{\rm d} = 25$ K in the *1-mm method* for star-forming galaxies. The mass-weighted value was justified by Scoville et al. (2014) to reflect the fact that the dust grains exposed to strong radiative heating would represent a so-called luminosity-weighted dust temperature. We demonstrate, *using two separate models*, that it is instead justified to use the effective luminosity-weighted dust temperature, e.g. as derived in a dust

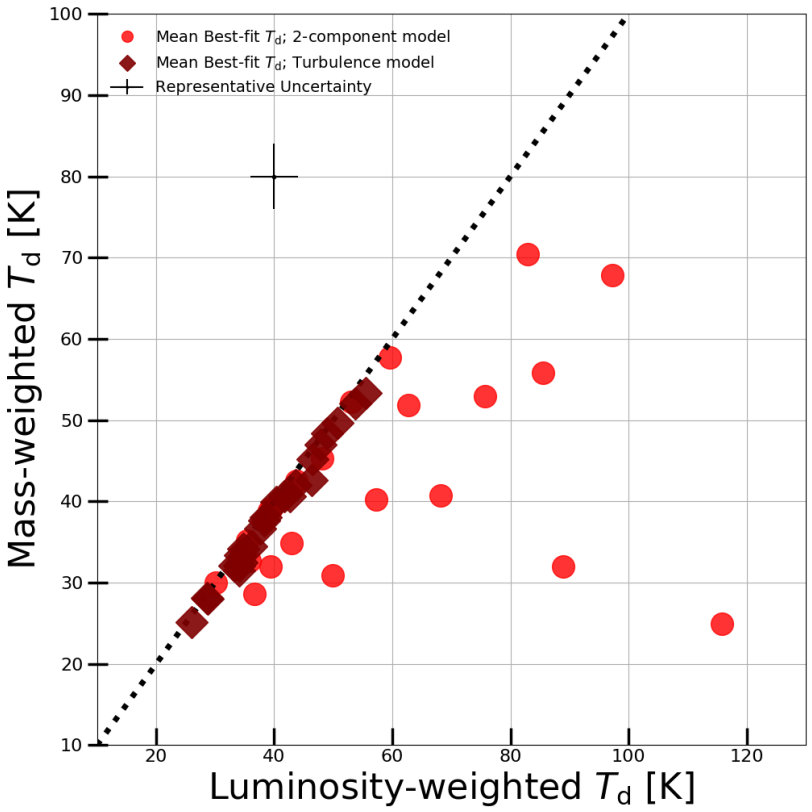

Figure 4.15: $L_{850\mu m}$-weighted dust temperature, T_d, versus the mass-weighted value of T_d for both the *2-component* model and the *Turbulence* model. The calculations are described in §4.8.2

.

SED fit, when using the *1-mm method* to calculate M_{ISM}. We find a one-to-one correlation among the mass-weighted and luminosity-weighted T_d values, indicating the dust mass in the *LPs* primarily consists of relatively warm diffuse gas, on contrast to the assumed cold diffuse dust content in the Milky Way. We stress, however, that the often-used optically thin MBB fit should not be used since it underestimates T_d compared to models with a realistic transition wavelength between the optically thin and optically thick emission regimes of the dust (Jin et al., 2019; Cortzen et al., 2020).

We further demonstrate the effects this may have in Fig. 4.16, which shows the value of $\mu_L M_{ISM}$ derived using three separate methods. The first two methods are our full radiative transfer calculations of $\mu_L M_{ISM}$, as computed using the *2-component* model and the *Turbulence* model. We compute the final estimate of $\mu_L M_{ISM}$ for the *LPs*, using the *1-mm method* and the respective AzTEC or ALMA ~1-mm dust continuum measurements (Harrington et al., 2016, Berman et al. in prep.), a mass-weighted T_d = 25 K and a value of β_{T_d} = 1.8 (which is consistent with our modelling procedure, §4.6). Overall, the *1-mm method* systematically over-predicts $\mu_L M_{ISM}$, consistent with other work (Liu et al., 2019). This confirms the assumed mass-weighted T_d in the *1-mm method* are too low to explain the *LPs*, as the value we use for the *GDMR* in our modelling is comparable to that used in the empirical calibration presented most recently in Scoville et al. (2017). In some cases, the discrepancy may be larger than a

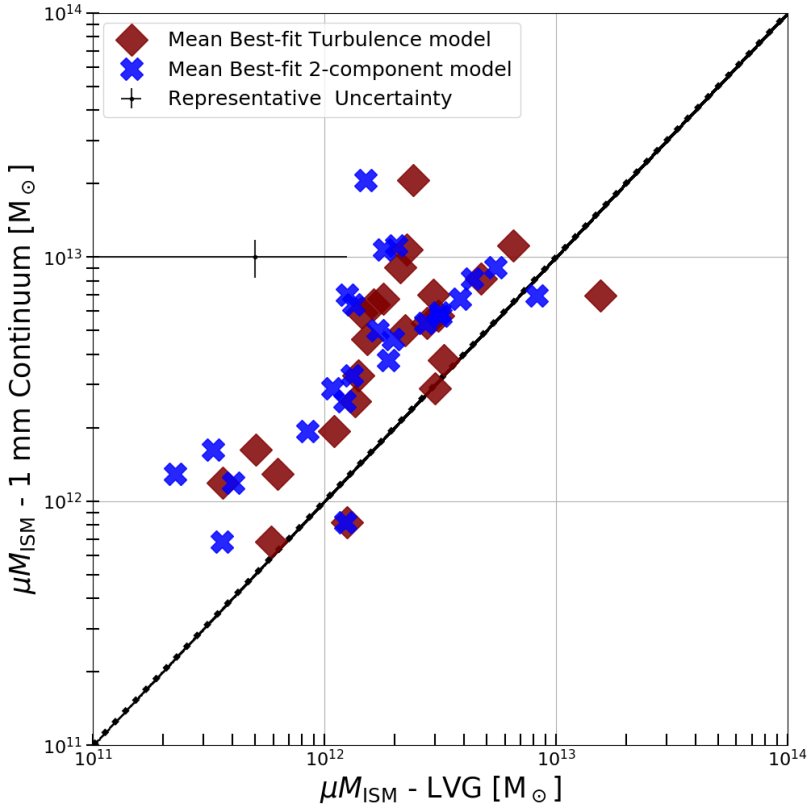

Figure 4.16: Mass-mass plot (log-log-scale) of apparent total molecular gas mass, $\mu_{\rm L} M_{\rm ISM}$, derived using three methods. The y-axis shows the result using a single continuum measurement of the thermal dust emission and an assumed mass-weighted $T_{\rm d} = 25$ K based on the scaling methods described in Scoville et al. (2017). The x-axis indicates the values of $\mu_{\rm L} M_{\rm ISM}$, as derived for both the *2-component* model and the *Turbulence* model.

factor two, and this is likely due to the large dispersion we find for the *LPs* for the average value of $\alpha_{\rm CO}$. In a recent study by Kaasinen et al. (2019), the rest-frame 850μm luminosity was also used to cross-calibrate the mass estimate. They found a factor of two discrepancy in the total molecular gas mass estimates using both spatially resolved CO(1-0) line emission, with an assumed $\alpha_{\rm CO} = 6.5$ M$_\odot$ (K km s^{-1} pc^2)$^{-1}$ and a spatially resolved dust continuum measurement used to infer the rest-frame 850μm emission and the *1-mm method* described above (assuming the same value of $\beta_{T_{\rm d}} = 1.8$ as we have used).

For many of the *LPs*, the value of $\alpha_{\rm CO}$ is less than the standard value used in the *1-mm method*. For global comparisons between galaxy populations, a single value was deemed appropriate, however, the estimate of $M_{\rm ISM}$ for high-z star-forming galaxies may be over- or under-estimated on average if the value of $\alpha_{\rm CO}$ is undetermined. The molecular gas and dust are, presumably, well-mixed in such turbulent star-forming systems (Krumholz et al., 2018). Since they are believed to trace one another, the single-band $\sim$ 1-mm, dust continuum method to derive the $M_{\rm ISM}$ has a clear advantage because it is more feasible to obtain a (sub)mm continuum detection of a high-z galaxy than it is to detect multiple CO lines and perform a non-LTE radiative transfer analysis to explicitly derive an estimate of $M_{\rm ISM}$. The strong dependencies on the assumed dust SED and gas excitation conditions are important

to consider when estimating $M_{\rm ISM}$, and therefore motivate further benchmarking between the various methods to derive $M_{\rm ISM}$ in high-z .

4.8.3 Heating, cooling and turbulence-regulated SF

SF occurs deep within molecular clouds, and this process requires cooling to aid gravitational collapse. At relatively high gas column densities, the kinetic energy transferred to CO molecules is converted to line photons which then radiate that energy away. Therefore we expect that CO line cooling is the dominant cooling process of the molecular gas-rich star-forming regions within the *LPs*. At lower column densities the far-IR fine-structure lines of singly ionized carbon, [CII], and neutral and doubly ionized oxygen, [OI] and [OIII], are often considered as the dominant coolants of the star-forming ISM (Hollenbach, 1985; Rosenberg et al., 2015; Díaz-Santos et al., 2016). The highly ionized and/or high temperature (and density) regions traced by these FIR fine-structure emission lines are not expected to contribute to the cooling of the gas and dust rich molecular gas traced by the CO line measurements of the *LPs*. The contribution of collisionally excited [CII] line cooling arises from neutral gas within dense PDRs, corresponding to $\log(n(H_2)) \sim 3$ cm^{-3} and T = 100 K (Hollenbach & Tielens, 1997; Goldsmith et al., 2012). Within the denser molecular gas phase we model in this work, we expect that collisional excitations between molecules is believed to play a stronger role as a gas heating term, as opposed to FUV heating from photodissociation regions (PDR) which lie between the HII regions and the cold molecular gas (Tielens & Hollenbach, 1985). In addition, Meijerink et al. (2011) demonstrate in a pure PDR model that the CO cooling fraction is 3% – 5%, while Rosenberg et al. (2015) noticed similar cooling power from the CO lines up to tens of percent of the total cooling budget[11]. They observed a strong CO cooling fraction, which does not show a deficit as observed in the FIR fine-structure lines.

To explore the nature, and possible source(s), of the energy for the total CO line cooling in the *LPs* we first calculate the sum $\Sigma_{\rm J_{up}=1}^{\rm J_{up}=15}(\mu_{\rm L} L_{\rm CO_{J_{up}}})$ for each CO line luminosity using the best-fit, minimum-χ^2 values from the *Turbulence* model (see Table A.2), and derive a range of values for the apparent CO cooling power for the *LPs* between $\Sigma\ (\mu_{\rm L} L_{\rm CO_{J_{up}}}) \sim 7 \times 10^{42}$ to $\sim 5 \times 10^{44}$ ergs s^{-1}. Our analyses of the *Turbulence* model results suggest that the global molecular ISM in the *LPs* often has an H_2 gas density $\log(n(H_2)) > 4$ cm^{-3}, and gas kinetic temperatures between 60 - 150 K. This implies that our estimate is specifically connected to the total cooling budget of this dense molecular gas phase. If we consider this cooling power to be continuous over the mean molecular gas depletion time, of the order of 70 Myr, the total energy emitted is of the order of $E_{\rm CO-70Myr} \sim 10^{59-60}$ ergs.

We can also estimate the turbulent kinetic energy of the molecular gas using the mean, intrinsic molecular gas mass we derived in § 4.7.2, and the mean turbulent velocity dispersion, resulting in $E_{\rm turb} = 0.5(M_{\rm ISM}/ < \mu_{\rm L} >= 20) \times \Delta V_{\rm turb}^2 \sim 10^{54-55}$ ergs. We recall our results for the *Turbulence* model, with the sample mean galaxy-wide, turbulent velocity dispersions for the *LPs* of $< \Delta V_{\rm turb} >= 125 \pm 40$ km s^{-1}, consistent with the second-moment velocity dispersion maps of line images for high-z star-forming systems (Leung et al., 2019b; Yang et al., 2019b; Talia et al., 2018; Venemans et al.,

[11] Without further information on the FIR fine-structure lines for the sample of *LPs*, we are unable to make a full comparison using the CO cooling budget alone.

2019; Tadaki et al., 2020; Neri et al., 2020; Jiménez-Andrade et al., 2020). This fiducial value of $E_{\rm turb}$ for a given mass and instantaneous turbulent velocity dispersion is 4-5 orders of magnitude lower than $E_{\rm CO-70Myr} \sim 10^{59-60}$ ergs. Therefore, over the 70 Myr, a considerable amount of energy is responsible for sustaining the continuous CO line emission.

As noted in Rosenberg et al. (2014), local IR luminous systems may have various sources of turbulent energy, e.g., merger activity, AGN and powerful outflows. Studies predict the coexistence of starburst and AGN activity, particularly at $z \sim 2$ (Hopkins et al., 2008), yet the *LPs* have been shown to be strongly powered by SF rather than an AGN (e.g. Harrington et al., 2016). Nonetheless, we can estimate the relative contribution of mechanical feedback energy from AGN outflow activity. As a reference, one of the most powerful radio-loud QSOs, 3C82, has a jet power of the order of 10^{47} ergs s^{-1} (Punsly et al., 2020). Theoretical studies which aim to reproduce the formation of local massive elliptical galaxies have indicated an AGN mechanical outflow energy estimate of the order of 10^{42-43} ergs, with a rate of $\sim 3{\times}10^{-5}$ Myr^{-1} (Gaspari et al., 2012). If we use this AGN episodic rate from Gaspari et al. (2012) and the jet power of 3C82, we estimate a total power of the order of 10^{58} ergs in 70 Myr – i.e. $\leq 10\%$ of the total energy radiated away by CO line emission. Note, it is unlikely that all of the mechanical jet power is continuous, nor is it directly transferred into the molecular gas of the ISM, since 3C82 has a biconical outflow orientation. The mechanical power from AGN jets may also impart a significant amount of energy in the form of galactic outflows, of the order of 10^{44-46} erg s^{-1} (Veilleux et al., 2009; Sharma & Nath, 2012; McNamara et al., 2014; Russell et al., 2016; Veilleux et al., 2020). The unconstrained nature of galactic outflows at high-z is still to be determined, as the mean gas densities may exceed the jet densities by four or five orders of magnitude (McNamara et al., 2016), and therefore is a caveat in this interpretation.

AGN may also produce a significant amount of X-ray heating (Meijerink et al., 2006, 2007). X-ray absorption effects between the rest-frame 2 - 30 keV energy range are pronounced at higher energies. The gas column densities we derive in §4.7.2 suggests that we are often in the Compton-thick regime beyond $N_{\rm H} > 10^{24}$ cm^{-2} (Hickox & Alexander, 2018). Currently, there is no constraint on the X-ray luminosity in the *LPs*, and we are aware of only one example of a radio-AGN, i.e. LPs-J0209 (Geach et al., 2015; Harrington et al., 2019). We also cannot rule out the possibility of a heavily dust obscured AGN, yet our sample of *LPs* have a strong selection function biased away from identifying strong QSOs (Yun et al., 2008; Harrington et al., 2016). Although there are limited X-ray studies of dusty star-forming galaxies at $z > 1$, we are able to estimate a possible energy from an assumed apparent X-ray luminosity, as derived from the apparent SFR for the *LPs* and a local ratio of $L_{\rm X:0.5-8keV}/SFR$ (Mineo et al., 2014). We use an assumed intrinsic spectral shape for a non-AGN X-ray contribution, with an X-ray absorbing gas column density of $N_{\rm H} \sim 10^{22}$ cm^{-2}, and infer an apparent X-ray luminosity of the order of 10^{43} ergs s^{-1}. This energy is consistent with other, $z \sim 2 - 3$, FIR detected X-ray AGN galaxies (Mullaney et al., 2011, 2012).

Since we expect much of the intervening gas column densities to be up to three orders of magnitude higher than this assumed value, this likely reflects an extreme upper limit. This corresponds to an apparent X-ray energy of the order of 10^{59} ergs. Although this is equivalent to the CO line cooling, when integrated across the fiducial 70 Myr timescale, it is a strong assumption for the X-ray luminosity to be continuous. Since this may be a strong upper limit, we can also conclude that X-ray luminosity from a non-AGN component is unlikely to be the primary heating mechanism to excite the gas-rich molecular ISM in the *LPs*.

Cosmic rays, unless inhomegenously distributed, are unlikely to regulate star-forming gas at physical scales larger than 100 pc – although the distribution and random diffusion of cosmic rays is highly uncertain (Thompson et al., 2006; Zweibel, 2013). Cosmic ray heating (see the review by Krumholz, 2014), is primarily one of the strongest gas heating mechanisms within cloud interiors when the dust temperatures are $\sim$ 20 K and the gas densities are $\sim$100-1000 cm^{-3}. Beyond gas densities of 10^4 cm^{-3}, the effects of dust grain-molecular gas energy exchange (via the IR radiation field and/or grain-molecule collisions) are predicted to become stronger, if not dominant over cosmic ray and far-UV (FUV) heating (Goldsmith, 2001; Krumholz et al., 2011; Narayanan & Krumholz, 2014). It appears that cosmic ray heating may not be pervasive throughout the ISM of the *LPs*, since their mean densities are above 10^4 cm^{-3}. Both observational and theoretical work suggests that the more diffuse gas, which can extend out to $\sim$ 10 kpc, may be strongly influenced by cosmic rays in dusty star-forming galaxies at $z \sim 2-3$ (Papadopoulos & Greve, 2004; Acciari et al., 2009; Abdo et al., 2010; Bisbas et al., 2015; Falgarone et al., 2017; Indriolo et al., 2018). The relative role of cosmic rays in driving the heating in high-z star-forming galaxies is currently unconstrained, which remains a caveat in this analysis. There is evidence to suggest that the UV radiation field strength determines the relative cosmic ray ionization rate, and for such galaxies it may be likely that the majority of the cosmic rays are confined to the local star-forming regions within the ISM because the UV radiation decreases faster than the inverse square of the distance from the ionizing source (Indriolo et al., 2018).

Our results for the sample mean value of $T_{\rm kin}/T_{\rm d} = 2-3$, on average, suggests galaxy-wide, turbulence-driven, mechanical heating as a signpost for the significantly high SF activity in these high-z galaxies. The $T_{\rm kin}/T_{\rm d}$ ratio parameter, to zeroth order, may be an interesting parameter to better understand the relative level of mechanical (traced by $T_{\rm kin}$) versus photoelectric heating (traced by $T_{\rm d}$). The local starburst galaxy, NGC6240, has a large CO line to continuum ratio driven by galaxy wide shocks (i.e. mechanical energy input; Papadopoulos et al., 2014). This scenario seems to be consistent with the large total line-widths (§4.5) and highly turbulent star-forming medium inferred for the *LPs*. Therefore some form of kinetic activity must be responsible to drive this ratio to higher values, which implies some form of kinetic energy density must sustained to distribute the significant molecular gas content within the ISM of the *LPs*. The values of $T_{\rm kin}/T_{\rm d} = 2-3$ are also found in the Milky Way regions with strong interstellar radiation field strengths, $G_0 = 10^5$, such as the Orion PDR regions (a peak density of $\log(n(H_2)) \sim 5$ cm^{-3}). These regions have a typical visual extinction $A_{\rm V} < 4$ (in mag). These optical extinctions correspond to low column densities, where most of the FUV radiation is absorbed (Hollenbach & Tielens, 1999, ; Fig. 16). We have already shown in §4.7.2 that the *LPs* have extinction values of the order of many hundreds of magnitude. Deeper within the PDR structure of Orion, corresponding to $A_{\rm V} > 4$, the $T_{\rm kin}/T_{\rm d}$ values decrease towards a value of unity or less (Hollenbach & Tielens, 1999, ; Fig. 16). Since we do not have values close to, or less than, $T_{\rm kin}/T_{\rm d} = 1$, we can conclude that FUV heating from PDRs is likely not the primary heating mechanism in the ISM of the *LPs*.

Other forms of heating mechanisms, therefore, seem to be required for the more intense star-forming galaxies like the *LPs*. Rosenberg et al. (2014) introduce an additional form of mechanical heating[12] to

[12] Note, Rosenberg et al. (2014) scale this simple mechanical heating term between a normalized value of 0 and 1, and combine this with their PDR model in order to match the LVG derived values of the $T_{\rm kin}$.

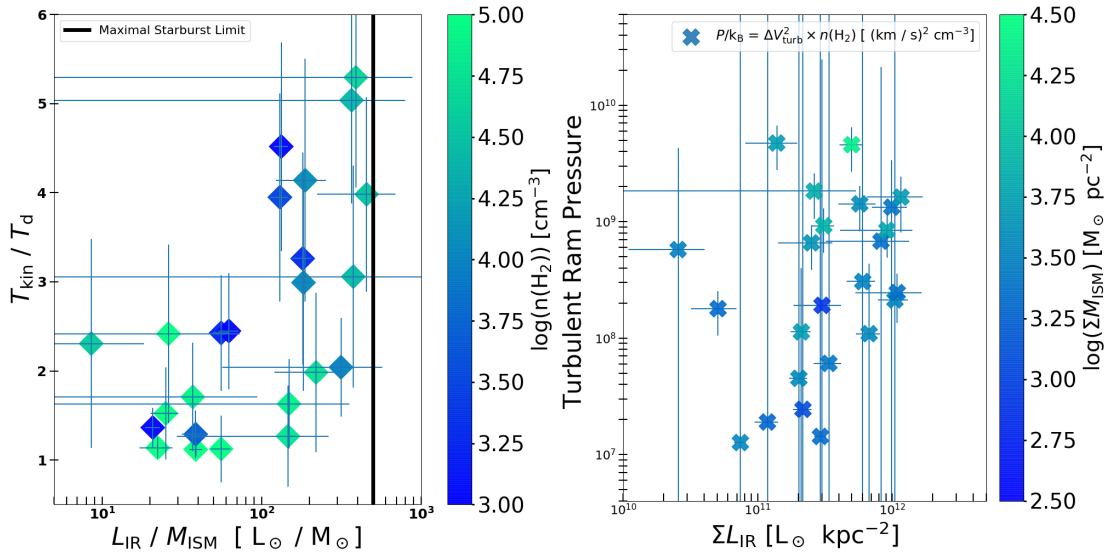

Figure 4.17: **Left:** T_{kin}/T_d parameter versus the SF efficiency proxy, i.e. the total IR luminosity to molecular ISM mass ratio, L_{IR}/M_{ISM}, derived using the *Turbulence* model, with the derived mean H_2 gas density in the colorbar axis (log-x scale). **Right:** Turbulent ram pressure versus the IR luminosity surface density, with the molecular gas mass surface density in the colorbar axis (log-log-scale). Both plots report the total χ^2-weighted parameter mean and standard deviation values derived from the ~2 million model calculations.

their PDR models in order to fit the observed line SED for the local starburst galaxy, NGC253. In fact, this mechanical heating term is required to account for more than two-thirds of the observed mid-high-J CO line fluxes. It is also required to also recover the solutions to their alternative LVG models, one of which corresponds to a molecular phase with $\log(n(H_2)) > 3.5$ cm^{-3}, and $T_{kin} = 60$ K. The PDR models alone could only reproduce a maximum gas kinetic temperature of 18 K when considering the gas density for the LVG model as an PDR input value. They argue the radiation field required to heat the gas photodissociates the CO molecules in the PDR in these models, the result is a factor of three lower value for the gas kinetic temperature between the PDR and LVG model results. Rosenberg et al. (2014) therefore argue there is a need for this additional mechanical form of heating. Rosenberg et al. (2014) do not fit for the dust temperature and T_{kin} simultaneously, so there is no direct comparison to our modelling procedure. Nevertheless, it is clear that PDRs are physically unlikely to be able to excite the observed line fluxes for the *LPs*. This is because the *LPs* have dust temperatures higher than the PDR-derived, maximum gas kinetic temperature of 18 K (in the case of $\log(n(H_2)) = 3.5$ cm^{-3}). We therefore infer that the T_{kin}/T_d parameter reflects a strong mechanical heating mechanism within the molecular ISM of the *LPs*, despite the fact that our model inexplicably accounts for the source of this mechanical energy.

Fig. 4.17 shows the T_{kin}/T_d parameter to the ratio of the total IR luminosity to molecular gas mass (i.e. a proxy of SFR per unit gas mass, hereafter SF efficiency "SFE"). The SFE is believed to strongly increase with increasing redshift, accompanied by a similarly strong evolution in the mass accretion rate for field galaxies at $z > 1$ (Scoville et al., 2017; Tacconi et al., 2020), as well as increased turbulent velocity dispersions and SN rates (Joung et al., 2009; Krumholz et al., 2018). The combined feedback from various stellar evolution processes are likely captured in the SFE parameter, therefore we expect that the value of T_{kin}/T_d will increase with higher values of SFE. The left-hand side of Fig. 4.17

shows some of the *LPs* approaching the limits of a maximal starburst [13]. Overall there is a range of values for the SFE of the *LPs*, corresponding to galaxies which would be considered main-sequence $z \sim 2-3$ star-forming galaxies, as well as the extreme outlier starburst galaxies (e.g. Genzel et al., 2010, 2015b; Tacconi et al., 2018, 2020). Higher values of the IR luminosity are proportional to the increase in SFR, and may therefore be an indicator for the mechanical energy input required to increase the values of $T_{\rm kin}/T_{\rm d}$. Indeed, Fig. 4.17 shows that as the SFE-proxy increases, there are more *LPs* with higher values of $T_{\rm kin}/T_{\rm d}$. The increased SFR in the *LPs* is expected to contribute a significant amount of energy from stellar feedback, both in the form of massive proto-stellar outflows and/or supernovae (SN) explosion shocks (McKee, 1989; Norman & Silk, 1980; Draine & McKee, 1993; Krumholz et al., 2006; Nakamura & Li, 2007; Krumholz et al., 2009a; Hopkins et al., 2011; Leung et al., 2020; Keller et al., 2020; Haid et al., 2019, 2018; Seifried et al., 2017) – all of which dissipate energy through a turbulent energy cascade towards smaller physical scales (Dobbs & Pringle, 2013; Van Loo et al., 2013). The *LPs* have a significant quantity of molecular gas, therefore we expect that this will dominate over the radiation pressure within the ISM[14]. Therefore we expect that mechanical stellar feedback (rather than radiative feedback) will likely have a strong contribution to the pervasive turbulent gas conditions within the ISM (Jacquet et al., 2011; Krumholz et al., 2012).

The total wind energy of an O-type star on the main-sequence of stellar evolution, combined with the rapid mass-loss rate of the more transient Wolf-Rayet evolutionary stage, results in a fiducial range of $\sim 10^{49-51}$ ergs in a 5 Myr lifetime (Leitherer et al., 1999; Chu, 2005; Smith, 2014; Ramachandran et al., 2019). As a reference, the intense star-forming region traced by the supergiant shell within IC2574, a nearby dwarf galaxy, has an estimated kinetic energy input of the order of about $\sim 3 \times 10^{53}$ ergs over a 1 Myr lifetime (Walter et al., 1998). We can estimate the stellar mechanical wind energy input using a fiducial value for the intrinsic SFR for the *LPs* of 1000 $\rm M_\odot\ yr^{-1}$ (see also §4.7.2) and an expected cumulative fraction of 0.2% by number for massive stars (Kroupa IMF Kroupa, 2002)[15]. The approximate stellar mechanical wind energy input is of the order of $\sim 1 \times 10^{52}$ ergs. SNe events occur at the end of the life-cycle of massive stars with initial stellar masses between $\sim 10-40$ $\rm M_\odot$ (Heger et al., 2003), each of which produces roughly 10^{51} ergs (Jones et al., 1999). If we assume that these massive stars consist of ~ 7 % of the total stellar mass fraction we derive a SNe rate of $\sim$6 SN $\rm yr^{-1}$ for the *LPs*, which is $\sim 300\times$ the value of the Milky Way (Diehl, 2018). For reference, the center of M82 has an estimated rate of ~ 0.1 SN $\rm yr^{-1}$ (Kronberg et al., 1981; Weiß et al., 1999).

We can further estimate the energy input from SNe to be on the order of 10^{59} ergs using the reference time-frame of 70 Myr. Therefore this value is an upper limit, since we do not expect that the injection of energy from SNe will be a continuous process. Nonetheless, this value is comparable with our simplistic estimate of the possible stellar mechanical wind energy input from young massive stars over 70 Myr, which are expected to provide a steady stream of mechanical energy throughout their lifetimes via stellar winds with terminal velocities of the order of 1000 km $\rm s^{-1}$(Puls et al., 2008). The direct impact of massive stars and SNe, however, may be biased towards their most immediate environments.

[13] A maximal starburst is a system within which radiation pressure overcomes the SF episode by disrupting ongoing SF activity, with a theoretical limit of $\mu_{\rm L} L_{\rm IR}/\mu_{\rm L} M_{\rm H_2} = 500\ \rm L_\odot/M_\odot$ (Thompson et al., 2005; Andrews & Thompson, 2011).

[14] Due to, e.g., Rayleigh-Taylor instabilities.

[15] Note, recent studies of high-z star-forming galaxies suggest there may be a top-heavy IMF (Romano et al., 2017; Zhang et al., 2018b).

It has also been shown theoretically that only a 1% fraction, or less, of the SNe energy output is transformed into turbulent energy (Iffrig & Hennebelle, 2015; Martizzi et al., 2016). Overall, the mixture of both SNe events occurring in parallel with the stellar evolution processes of the population of Wolf-Rayet stars and short-lived massive stars in young stellar associations can still potentially provide a large fraction of the necessary energy budget with respect to the value of $E_{CO-70Myr} \sim 10^{59}$ ergs. As well, the mechanical energy of E(massive stellar winds & SNe) $\sim 10^{59-60}$ ergs,i.e. 4-5 orders of magnitude larger than E_{turb}.

Despite the potentially strong energetic contributions from stellar evolution processes, massive stars may not be the only sources of such turbulent energy input. Gravity may play an equally important role in introducing a large amount of turbulent gas motion, which may sustain the relatively high turbulent velocity dispersions we derived for the *LPs*. The right-hand side of Fig. 4.17 shows the relationship between the IR luminosity surface density, $\Sigma_{L_{IR}}$, and the turbulent ram pressure for the *LPs*. The equivalent turbulent gas ram pressure is connected to the vertical stabilizing force in a marginally stable gas disk. This pressure will increase as the SF activity increases, according to turbulence-regulated SF models (Krumholz et al., 2009a; Bournaud et al., 2010; Krumholz et al., 2018). We use the mean values from the *Turbulence* model to calculate the turbulent ram pressure to be $P_{turb} = \Delta^2_{turb} \times n(H_2) = 10^{6.2-9.8}$ (km s^{-1})^2 cm^{-3}, which is significantly higher than the gas thermal pressure, $P_{th} = P/k = n(H_2) \times T_{kin} = 10^{2.9-6.9}$ K cm^{-3} (with k the Boltzmann constant). Many *LPs* have large uncertainties due to our lack of constraints on the molecular gas density and our total errors, and future work may refine these values for individual *LPs* using spatially resolved line measurements of the mean turbulent velocity dispersion. Both the Kendall's tau statistic, $\tau = 0.27$ and the Spearman's rank correlation, $r = 0.37$ indicate that there is only a mild positive correlation between the turbulent gas pressure across the range of $\Sigma_{L_{IR}} \sim 10^{11-12}$ L$_\odot$ kpc^{-2} for the *LPs*, if any. Since there is a large amount of turbulent energy present in the *LPs*, it is inferred that the thermal pressure equilibrium of clouds is negligible overall in terms of regulating the SF activity. This result is consistent with theoretical studies (e.g. Ballesteros-Paredes et al., 1999). It is important to measure the mean molecular gas thermal pressure, as it sets the background for thermal pressure balance throughout the ISM, as galaxies with higher than 50% molecular gas to atomic gas fractions are subject to collapse (Krumholz & McKee, 2005).

Our results indicate that the additional form of turbulent pressure is an important form of feedback to regulate the intense SF activity for these gas-rich *LPs*. Using equation A7 from Brucy et al. (2020) for the upper bound for possible turbulent power, Π_{SNe}, injected by a SNe:

$$\Pi_{SNe} \sim 4 \times 10^{37} (\Sigma_{M_{ISM}} / 10[M_\odot yr^{-1}])^{1.4} \, [\mathrm{ergs\,s^{-1}}]. \tag{4.8}$$

This yields a much lower estimate of the total turbulent energy input from SNe over the 70 Myr of $\sim 10^{56}$ ergs, still ~ 3 orders of magnitude less than $E_{CO-70Myr}$. This equation assumes the turbulence energy injection is proportional to the surface integrated SFR (Krumholz et al., 2018; Brucy et al., 2020). The high gas mass surface densities of the *LPs* can therefore produce much more power from stellar feedback than the highest explored values for the SFR ~ 100 M$_\odot$ yr^{-1} in the work of Brucy et al. (2020), therefore these estimates may reflect lower limits. Brucy et al. (2020) find that the large-scale turbulent energy injection has a much higher dependance on the gas mass surface densities, *by almost three orders of magnitude*. The general scenario is consistent with other studies, which find a more dominant turbulent energy contribution from large-scale motions instead of pure stellar

feedback (Bournaud et al., 2010; Renaud et al., 2012; Krumholz et al., 2018; Colling et al., 2018). We can loosely estimate this large-scale turbulent energy input based on the theoretical model values of Brucy et al. (2020) for a dense molecular medium, corresponding to $\sim 10^{40}$ ergs s^{-1}. We calculate, over 70 Myr, an estimate of $\sim 10^{55}$ ergs. This is one order of magnitude higher than the fiducial $E_{\rm turb}$ $\sim 10^{54-55}$ ergs we estimate above for the *LPs*. Therefore, a substantial amount of turbulence energy can also be supplied from large-scale disk motions.

Due to the conservation of angular momentum, any form of momentum injection into the molecular cloud surroundings will likely be radially transported towards the gravitational center of the galaxy. Indeed, mass accretion may play a primary role in increasing the level of turbulent energy within the ISM during these starburst episodes (Schmidt et al., 2016)[16]. The kpc-scale dynamics for these high-z gas-rich star-forming galaxies cause gravitational instabilities, and the turbulent driving from these processes may be a primary source of the bulk kinetic energy density (Silk, 1997; Schmidt et al., 2009; Bournaud et al., 2010; Krumholz & Burkhart, 2016; Krumholz et al., 2018; Colling et al., 2018; Brucy et al., 2020). These single-dish measurements offer a global view, or "top-down" perspective, of the molecular ISM conditions within the *LPs*. The gas mass surface density drives these high SFR and IR luminosity surface densities in "top-down" processes (Krumholz et al., 2018). The extreme gas mass surface densities may help to explain the extreme intrinsic IR luminosities exceeding 10^{13} $L_{\odot}$.

We expect that such massive galaxy-wide SF will act to re-stabilize the forming disk over a timescale of $\sim$ 100 Myr, meanwhile fresh gas is likely to be accreted, consumed or displaced within the ISM and/or in the form of massive galactic outflows (Quirk & Tinsley, 1973; Cox, 1981; Dopita et al., 1985; Larson, 1987; Ostriker et al., 2010; Veilleux et al., 2020). Altogether, such arguments for turbulence-regulated SF is consistent with evidence presented for both local (U)LIRGs and high-z starbursts. The local (U)LIRGs, with similar CO line SED coverage, require high amounts of mechanical energy / turbulent activity to sustain the higher-J CO line emission (e.g. Tacconi et al., 1999; Lu et al., 2014; Kamenetzky et al., 2016), while the 10 kpc-scale turbulent molecular gas reservoirs are believed to extend the starburst phase of high-z star-forming galaxies through the interplay of stellar/AGN feedback and intergalactic gas accretion (Falgarone et al., 2017).

4.9 Conclusions

In this work we have studied the physical gas properties of the molecular and atomic ISM at high-z . We have measured and compiled a legacy-value compendium of roughly 200 CO and [CI] spectral lines measured in a sample of 24 strongly lensed star-forming systems at $z \sim 1-4$, selected from the all-sky sub/mm *Planck*satellite (the *LPs*). To yield deeper insight into the molecular ISM excitation conditions, we systematically measured the multi-J line excitation of CO and [CI] using spatially unresolved, single-dish observations (i.e. IRAM 30m ([CI] and CO($J_{\rm up} = 3-11$)), GBT (CO(1-0)), and APEX ([CI] and CO($J_{\rm up} = 4-12$))).

This work is the first major effort to simultaneously fit all of the available spectral line and dust continuum observations. The vast majority of previous high-z studies have focused on non-LTE

[16] This is in addition to the turbulent motions generated from hydrodynamic gas motions causing gravitational shear forces.

radiative transfer modelling of a single or double component model of the observed line emission, excluding the thermal background from the IR radiation field. In this work we perform two complementary modelling procedures to model all of the line/continuum data: i.) a two-component molecular medium model, which enabled us to highlight the dominant properties of the more diffuse/quiescent and denser/highly excited gas, and ii.) a more realistic description of a molecular ISM which is described by a, turbulence-driven, molecular gas density PDF. Our main results are summarized as follows:

• The broad [CI] and CO lines ($< FWZI > \sim 850$ km s^{-1}) are strikingly similar in line shape, therefore these emission lines trace comparable galactic dynamics across the spatially unresolved, kpc-scales.

• We have derived the mean CO line brightness temperature ratios for the *LPs* out to the ratio of $L'_{\rm CO(12-11)}/L'_{\rm CO(1-0)}$, based on our best-fit, minimum-χ^2 *Turbulence* model. In addition, we have derived a set of median CO line brightness temperature ratios for a significant number of $z = 1 - 7$ galaxies with CO line detections, including the compilations by Carilli & Walter (2013) and Kirkpatrick et al. (2019). Although the median values are in excellent agreement with the average best-fit, minimum-χ^2 model derived values for the *LPs*, the wide range in CO excitation observed in individual galaxies implies that the use of an average (or median-based) value used for scaling L' measurements may be misleading when there is limited line/continuum data available.

• There is a wide range in the observed intensities for the CO rotational ladder, with an order of magnitude dispersion tracing a range of gas excitation in these lensed IR-luminous, star-forming galaxies. We further explored this wide dynamic range in observed gas excitation following the methodology presented by Rosenberg et al. (2015) for local IR luminous galaxies. We have thereby classified the CO excitation ladder with respect to the drop-off slope after the CO(5-4) transition by taking the ratio of the higher-J CO line luminosities to the mid-J CO line luminosities, and find the *LPs* probe more than 4 orders of magnitude in CO excitation. This classification increases to higher excitation as the derived FIR luminosity increases.

• There are 19 *LPs* with a [CI] line detection, while sixteen have both [CI] lines detected. Our non-LTE radiative transfer modelling of these lines suggests the [CI] lines are indeed optically thin, which is important for reliable calibrations to carbon gas column density and total mass. The two ground-state fine-structure carbon lines are sub-thermally excited, however. We demonstrate, using 16 *LPs* with both [CI] line detections, that the often-assumed LTE approximation to derive the carbon excitation temperature may under (or over) estimate the intrinsic carbon excitation temperature, depending on the gas excitation conditions of individual galaxies. We derived mean carbon gas excitation temperatures $T_{\rm exc} \sim 30$ and 40 K for the *Turbulence* model and *2-component* model, respectively. In some of the *LPs* we find values less than 20 K, and we would have misinterpreted the inferred total molecular gas mass if we had assumed the ideal, LTE prescription. We find, for the *Turbulence* model, the sample mean for the *LPs* of $< [[\rm CI]]/[\rm H_2] > \sim 6.8\times10^{-5}$, with a large dispersion.

• The average *intrinsic* size of the modelled gas and dust emitting region for the *Turbulence* model was derived to be $R_{\rm eff}(= 13.5)/\sqrt{\mu_{\rm L} \sim 20.4} \sim 3$ kpc. We have estimated the mean magnification using all of the available ranges derived for the *LPs* which have lens models. For the *LPs* without published magnification factors, we provide an estimate using the "Tully-Fischer" argument method presented by Harris et al. (2012), and our novel CO(1-0) line measurements. The intrinsic size for individual *LPs*

based on detailed lens modelling, agrees well with the expected intrinsic size derived in our modelling.

• We derived total molecular ISM masses in our modelling of the observed CO/[CI] lines and dust SED. Both of the modelling procedures are consistent in deriving $M_{\rm ISM}$, yet we find systematic offsets as the single-band 1-mm dust continuum method over-predicts the $M_{\rm ISM}$ derived using our robust modelling procedures. Our derived mean, mass-weighted, $T_{\rm d} \sim 40$ K for the sample of *LPs* does not suggest the use of the recommended mass-weighted $T_{\rm d} = 25$ K value when using a ~ 1 mm dust continuum observation to estimate the total molecular ISM mass. In fact, both of the modelling procedures indicate that the mass-weighted and luminosity-weighted $T_{\rm d}$ are close to identical, on average.

• We find a wide range in CO luminosity per mass, with a mean close to the Galactic value, i.e. $\alpha_{\rm CO} \sim 3.4$ M$_\odot$ (K km s^{-1} pc^2)$^{-1}$, however there is a large dispersion. Each system has a unique value of $\alpha_{\rm CO}$, disfavoring the use of a single value common for active star-forming galaxies at high-z Our modelling suggests the value of $\alpha_{\rm CO}$ increases with increasing gas mass surface density, as well as with gas volume density. The value of $\alpha_{\rm CO}$ decreases towards unity or less for increasing gas kinetic temperatures, specifically $T_{\rm kin}$ >120 K.

• The more realistic description of the turbulent molecular gas offers a picture of the excitation conditions of the ISM in the *LPs*. The large emitting regions are highly turbulent, as inferred by their mean turbulent velocity dispersion ($\Delta V_{\rm turb} > 125$km s^{-1}), and the gas kinetic temperature to dust temperature ratios $T_{\rm kin}/T_{\rm d} > 2.5$, on average, suggests the *LPs* require a significant amount of mechanical activity on >kpc scales (the driving scale) in conjunction with their massive molecular gas reservoirs. Since the inferred gas depletion time, $M_{\rm ISM}$/SFR, is of the order of 70 Myr, there must be a significant amount of gas, likely supplied from the CGM over the lifetime of this $\sim$ 100Myr starburst episode. The $T_{\rm kin}/T_{\rm d}$ ratio also increases with the inferred SF efficiency (i.e. $L_{\rm IR}/M_{\rm ISM}$), which suggests the kinetic input from increased SNe and stellar winds may also play a role in characterizing the overall mechanical heating in the ISM.

CHAPTER 5

The "Red Radio Ring": Ionised and Molecular Gas in a Starburst/Active Galactic Nucleus at $z \sim 2.55$

This chapter is a reproduction of the article of the same title that has been published in Monthly Notices of the Royal Astronomical Society under the reference:

- Harrington, K.C., Vishwas, A., Weiß, A., et al. 2019, MNRAS, 488, 1489.

The manuscript, found here, is reproduced under the non-exclusive right of re-publication granted by the Oxford University Press to the authors of the original article in MNRAS. To ensure open access to the article the peer-reviewed, published version has been uploaded to astro.ph (1906.09656).

5.1 Abstract

We report the detection of the far-infrared (FIR) fine-structure line of singly ionised nitrogen, [NII] 205μm, within the peak epoch of galaxy assembly, from a strongly lensed galaxy, hereafter "The Red Radio Ring"; the RRR, at z = 2.55. We combine new observations of the ground-state and mid-J transitions of CO (J_{up} = 1,5,8), and the FIR spectral energy distribution (SED), to explore the multi-phase interstellar medium (ISM) properties of the RRR. All line profiles suggest that the HII regions, traced by [NII] 205μm, and the (diffuse and dense) molecular gas, traced by the CO, are co-spatial when averaged over kpc-sized regions. Using its mid-IR-to-millimetre (mm) SED, we derive a non-negligible dust attenuation of the [NII] 205μmline emission. Assuming a uniform dust screen approximation results a mean molecular gas column density $> 10^{24}$ cm^{-2}, with a molecular gas-to-dust mass ratio of 100. It is clear that dust attenuation corrections should be accounted for when studying FIR fine-structure lines in such systems. The attenuation corrected ratio of $L_{\rm NII205}/L_{\rm IR(8\text{-}1000\mu\ m)} = 2.7 \times 10^{-4}$ is consistent with the dispersion of local and $z > 4$ SFGs. We find that the lower-limit, [NII] 205μm-based star-formation rate (SFR) is less than the IR-derived SFR by a factor of four. Finally, the dust SED, CO line SED and $L_{\rm NII205}$ line-to-IR luminosity ratio of the RRR is consistent with a starburst-powered ISM.

5.2 Introduction

Observational evidence reveals a synchronous peak, around $z \sim 2$, in both the cosmic co-moving star-formation rate (SFR) and super massive black hole accretion rate density (see e.g. Madau & Dickinson, 2014; Hickox & Alexander, 2018). Understanding this apparent co-evolution between active galactic nuclei (AGN) and star formation (SF) demands a deeper characterisation of the interstellar medium (ISM) in galaxies, such as the dynamics and spatial distribution of gas arising from different phases, as well as the relationship of ionised, molecular and stellar surface mass densities and their role in SF processes. Substantial theoretical work (Dalla Vecchia & Schaye, 2008; Scannapieco et al., 2012; Rosdahl et al., 2017) has also progressed in simulating the complex effects of black-hole, thermal, and kinetic feedback processes, while observations of ISM properties derived from a broad-band coverage are still required to form a complete impression of a galaxy that has both AGN and SF activity (Cicone et al., 2014, 2015, 2018). High-z star-forming galaxies (SFGs) at $z \sim 1-3$ typically show an increase in the molecular gas-to-stellar mass fractions (up to 50% or greater) (e.g. Tacconi et al., 2010, 2018). The spatial extent of SF within high-z SFGs can often exist out to large radii of ~ 2-10 kpc e.g. (Magdis et al., 2016; Elbaz et al., 2018b), exceeding the 0.1-1 kpc nuclear starburst (SB) regions of local (Ultra)Luminous InfraRed Galaxies ((U)LIRGs Sanders & Mirabel, 1996; Solomon et al., 1997; Solomon & Vanden Bout, 2005). Therefore global properties derived from measurements of the ionised and molecular ISM are needed to account for the total emission corresponding to the kpc-scale areas encompassed by high-z systems.

Studying the gas-rich, dusty star-forming galaxies (DSFGs) at $z > 1$ has largely focused on measurements of the molecular gas content via one or two CO lines (typically $J_{up} \leq 5$), and also the long-wavelength dust continuum, to understand the star-forming ISM, the total molecular gas mass and overall efficiency of SF (e.g. Genzel et al., 2010; Schinnerer et al., 2016; Scoville et al., 2017; Harrington et al., 2018; Leung et al., 2019a). The ionised ISM, however, has been largely unexplored at high-z, and therefore the complete picture of multi-phase gas processes required to disentangle the nature of SF in galaxies are poorly constrained. Far-IR fine-structure lines (FSLs) offer an additional probe of HII regions in obscured sites of SF, as they are less susceptible to dust attenuation when compared to optical or mid-IR lines (e.g. Fernández-Ontiveros et al., 2016). This motivates the use of these far-IR FSLs as powerful line diagnostics of the evolving ISM at high-z (Maiolino et al., 2005, 2009; Ferkinhoff et al., 2010, 2011; Riechers et al., 2014; Zavala et al., 2018; Zhang et al., 2018a; Marrone et al., 2018a; Vishwas et al., 2018; Zanella et al., 2018). Unfortunately, the atmospheric coverage of many important mid-/far-IR FSLs makes observations difficult to execute, if not impossible to observe from the ground.

The nitrogen atom has an ionisation energy $E_{i,\,N} = 14.53$ eV, and is therefore typically present with singly ionised hydrogen; $E_{i,\,H} = 13.6$ eV. The fine-structure splitting of the ground-state leads to two transitions at 121.898 μm and 205.178 μm; [NII] 122μm and [NII] 205μm, respectively[1]. In order to characterise the global ionised ISM properties, the low ionisation energy requirement of the far-IR [NII] emission lines makes them unique tracers of the low-excitation, warm ionised gas associated with HII regions and the ambient interstellar radiation field of the ISM. The physical

[1] The ground state ($^3P_0$) fine-structure splitting arises due to the unpaired electrons in the nitrogen atom. The $^3P_2$ and $^3P_1$ levels are only about 188 K and 70 K above ground, respectively.

and chemical evolution of the global ISM is influenced by supernova explosions and high mass-loss rates dispelled by stellar winds from massive OB and Wolf-Rayet type stars (e.g. McKee & Williams, 1997; Crowther, 2007; Puls et al., 2008). These, together with efficient rotational mixing within massive stars (Maeder & Meynet, 2000; Brott et al., 2011; Ekström et al., 2012), can quickly expose the products of stellar nucleosynthesis at the surface, thereby injecting substantial quantities of nitrogen into the ISM within a timescale of ∼10s Myr (Maeder & Meynet, 2000; Stanway & Eldridge, 2018).

The [NII] emission lines were first observed in the Milky Way by the COBE FIRAS spectrometre (Bennett et al., 1994), followed closely by KAO observations of the Galactic HII region G333.6-0.2 (Colgan et al., 1993). The [NII] 205μm line is also observable at rest velocities from the ground-based observatories at exceptional sites. Using the SPIFI spectrometer on the AST/RO telescope at South Pole, Oberst et al. (2006, 2011) mapped the [NII] 205μm line from the Carina Nebula and compared it with ISO LWS [NII] 122μm line maps to show the [NII] line originated from a low density ($n_{e^-} \sim 28$ cm^{-3}) ionized medium. High spatial-resolution, large-scale imaging of the Galactic plane were enabled by the sensitive PACS and SPIRE spectrometer on-board the *Herschel Space Observatory* (Goldsmith et al., 2015), and demonstrated that most of the [NII] line arises from extended, low density ($n_{e^-} \sim 10$ to 50 cm^{-3}) HII regions. Other efforts to use [NII] to derive average electron densities have been made in a range of local galaxies ($n_{e^-} \sim$ 20-100 cm^{-3}), for instance: M51 and Centaurs A, (Parkin et al., 2013), Ultra-luminous Infrared Galaxies ULIRGs (HERUS sample; Farrah et al., 2013), Dwarf galaxies (Cormier et al., 2015), KINGFISH galaxies (Herrera-Camus et al., 2016a) and other SFGs (Lu et al., 2017).

At high-z, observations of the [NII] 205μm line is largely limited to $z > 3.9$, where the line is red-shifted to wavelengths longer than 1mm, making ground based observations possible due to the more transmissive and stable atmosphere, with lower receiver noise temperatures. The current sample where this emission line is detected consists of twelve highly star-forming galaxies (Decarli et al., 2012, 2014; Combes et al., 2012; Rawle et al., 2014; Nagao et al., 2012; Béthermin et al., 2016; Pavesi et al., 2016, 2019; Lu et al., 2018), and there are at least five additional non-detections (see Walter et al., 2009; Riechers et al., 2013).

In this paper we report new spatially unresolved line detections from "The Red Radio Ring" (hereafter: the *RRR*) of [NII] 205μmline emission with the APEX telescope, complemented by CO(1-0), CO(5-4), and CO(8-7) line detections from the *Green Bank Telescope* (GBT) and IRAM 30m telescope. The [NII] 205μmline detection at the redshift, $z \sim 2.55$, in the *RRR* begins to bridge the gap between local detections and those at $z > 4$.

We structure this chapter as follows: we will first provide a brief outline of the nature of the galaxy presented in this study. We describe the [NII] and CO observations, and then present the results from the novel spectroscopic measurements. We will then discuss the [NII] derived SFR and the possibility for a co-eval AGN/SB, followed by our conclusions and outlook. Throughout this chapter we take for a point of reference a flat Λ CDM cosmology with $H_0 = 69.6\, kms^{-1}Mpc^{-1}$ with $\Omega_m = 0.286$, and $\Omega_\Lambda = 1 - \Omega_m$ (Bennett et al., 2014). Throughout the text, we use a magnification factor, $\mu = 15$, to report the intrinsic source properties unless otherwise noted. This value is derived from lens models using the highest spatial resolution data available for this source, i.e. $\mu = 14.7 \pm 0.3$, (Geach et al., 2018), and is consistent with other work (Rivera et al., 2019, ; Kamieneski et al. 2019, in prep.). The relative magnification factor, however, can change depending on the source plane distribution of every line and continuum tracer at varying rest frequencies.

5.3 The Red Radio Ring

the *RRR* was discovered by four independent teams: **(i)** the citizen science program *SpaceWarps* (Marshall et al., 2016) in a search for gravitational lensing features within deep (iJKs band) CFHT images in the *Herschel*-Stripe82 field (Geach et al., 2015); **(ii)** Harrington et al. (2016) identified this source after cross-matching *Herschel*-SPIRE and *Planck* images at 350μm in order to identify strongly lensed, DSFGs (Negrello et al., 2010; Fu et al., 2012; Planck Collaboration XXVII, 2015; Wardlow et al., 2013; Cañameras et al., 2015) and further confirmed with follow-up CO and millimetre dust continuum observations with the *Large Millimeter Telescope*; **(iii)** Nayyeri et al. (2016) present a similar selection of candidate lensed, DSFGs as Harrington et al. (2016), but with SPIRE 500μm images instead; and **(iv)** Su et al. (2017) identified the *RRR* as the brightest DSFG candidate (referred to as ACTJ0210+0016) in the 148, 218, and 278 GHz maps from the Atacama Cosmology Telescope (*ACT*), and presented follow-up CO(1-0) line observations with *Green Bank Telescope*/Zpectrometer.

The *RRR* is a strongly lensed radio-AGN/DSFG hybrid galaxy, magnified by a massive, foreground elliptical galaxy and a satellite companion at $z = 0.2019$ (Geach et al., 2015). The 1.4 GHz eMERLIN imaging ($\theta \sim 0.35$") revealed compact radio emission <250pc in the lens reconstructed source-plane image. The intrinsic specific radio luminosity $L_{1.4\,\mathrm{GHz}} \approx 10^{25}$ W Hz^{-1} suggests a radio-mode AGN (Geach et al., 2015). The wavelength corresponding to the peak line flux of the asymmetric low-J CO line profile corresponds to a redshift, z~2.553 for the *RRR* (Harrington et al., 2016; Su et al., 2017). Detailed strong lens modeling of the CO(3-2) emission resolved by NOEMA ($\theta \sim 0.75\times1.5$") suggests that the observed molecular gas emission arises from a rotating disk spread over ~3 kpc in the source-plane (Rivera et al., 2019). The source-plane reconstruction of the CO(4-3) line emission ($\theta \sim 0.25$") by Geach et al. (2018) provides evidence that the growth of the AGN is co-eval with the rapid SF. The molecular gas may dominate the galactic potential within these three kpc, which is further supported by Rivera et al. (2019).

5.4 Observations

5.4.1 GBT

The CO(1-0) line emission was observed using the Ka-band receiver on the GBT. Observations (GBT/17B-305; PI: K. Harrington) took place on October 22, 2017, under stable atmospheric conditions. We used the standard SubBeamNod procedure between the 8-m subreflector and the main dish, with 4 min integrations per scan. Pointing and focus were performed frequently before the SubBeamNod integrations. The backend spectrometer, VEGAS, was used to record the data from the Ka-band receiver, tuned to the expected CO(1-0) line frequency (in low-resolution, 1.5 GHz bandwidth mode; $\theta \sim 23$"). Subsequent data reduction was performed using GBTIDL (Marganian et al., 2013). All On-Off measurements were corrected for the atmospheric attenuation and afterwards treated in the same manner as in Harrington et al. (2018). We smoothed all spectra to 50 km s^{-1}channel resolution after averaging all low-order baseline subtracted spectra. The resulting on-source integration time was 1.25h. Flux accuracy was checked with the standard source Uranus and pointing stability

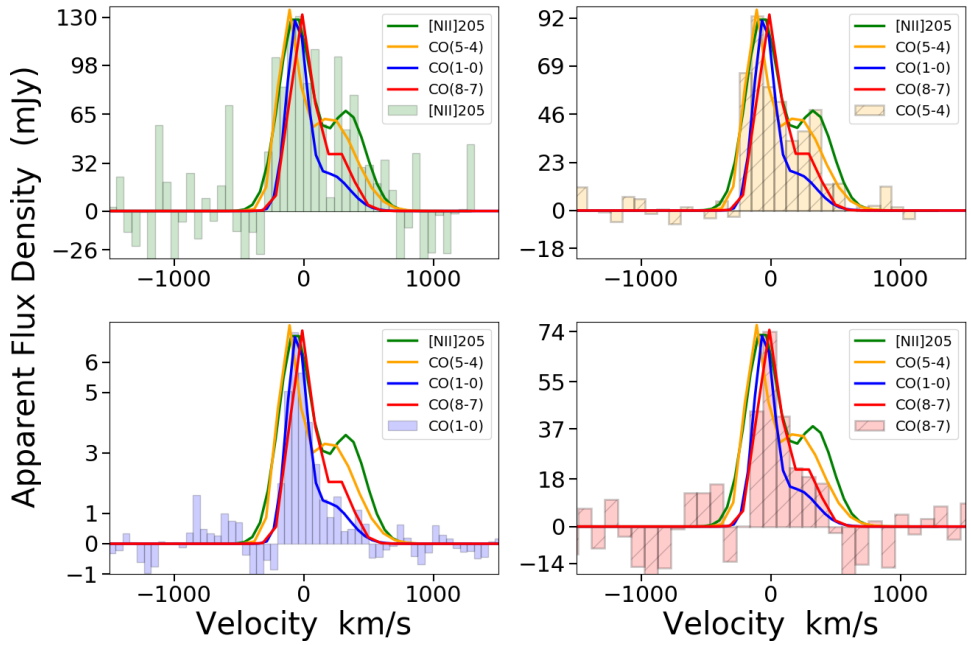

Figure 5.1: The spectra and two-component Gaussian fits for the [NII] 205μm(green; top left), CO(1-0) (blue; bottom left), CO(5-4) (orange; top right) and CO(8-7) (red; bottom right) lines. To aid comparisons among all line profiles, the best-fit Gaussian models have been re-scaled to the observed peak of each spectrum within each panel. The zero-point velocity is determined using $z = 2.553$.

with J0841+7053, J1310+3220, J1331+3030 and J1642+3948. We adopt a 25% uncertainty on the integrated line properties for systematic effects with the GBT (see Harrington et al., 2018; Frayer et al., 2018a).

5.4.2 APEX

To observe the [NII] 205μmemission line we used the FLASH$^+$ 460L single polarization receiver on the Atacama Pathfinder EXperiment (APEX) 12m telescope (Güsten et al., 2006). We used Max Planck Society observing time between 24 May and 17 July, 2018 (Pr. M-0101.F-9503A-2018; PI: Harrington), totaling 384 minutes of integration ($\theta \sim 15$"). FLASH (Heyminck et al., 2006a) is a 2 side-band (SB) dual-frequency heterodyne receiver with orthogonal linear polarizations, one for each of the 345 GHz and 460 GHz atmospheric windows. The FLASH observations were performed in good weather conditions, with precipitable water vapor < 1.5mm. Observations used standard wobbler switching with a chopping rate of 1.5 Hz, and an azimuthal throw offset of 30". Each scan consisted of a hot/sky/cold calibration 600" off-source, followed by 12 subscans of 20s per on-source integration time. Focus checks were performed regularly (every 3-5h), whereas pointing checks on a strong line/continuum source (e.g. Jupiter or nearby star) were performed roughly every 1-2h and yield a pointing accuracy within 2-3". To record the data we used the MPIfR eXtended bandwidth Fast Fourier Transform spectrometers (FFTS; Klein et al., 2006) with a 2× 2.5 GHz bandwidth for each of

the upper and lower receiver sidebands of spectra the FLASH receiver. All scans were reduced and analysed using the CLASS and GREG packages within the GILDAS[2] software distribution. Each scan was smoothed to ~ 90 km s^{-1} channel resolution and assessed by eye after a 1st order baseline polynomial subtraction (line-free channels). Only about 10% of the scans were removed for each set of spectra before co-adding the rms-weighted spectrum. We adopt an absolute uncertainty of 25% for all derived line properties to account for the variations in systematic behavior of the APEX observations at higher frequencies (e.g. atmospheric stability, baseline subtraction, pointing/focus corrections).

5.4.3 IRAM 30m

Observations with the IRAM 30m telescope took place across two observing semesters: Pr. 187-16 and Pr. 170-17 (PI: K. Harrington), starting on January 29th, 2017 we observed the CO(5-4) emission line in average weather conditions ($\tau_{\nu\,\mathrm{obs}} = 0.5 - 0.8$) for 30 minutes of integration. Subsequent observations were in excellent observing conditions ($\tau_{\nu\,\mathrm{obs}} < 0.04 - 0.2$) on December 13, 2017 for roughly 35 minutes integration to detect the CO(8-7) emission line. We used the E150 and E230 observing bands of the EMIR receiver, and utilised two backends: both the WIde-band Line Multiple Auto-correlator (WILMA) and the fast Fourier Transform Spectrometre (FTS200). Our observing mode consisted of a single EMIR band, capturing the dual polarization, 16 GHz bandwidth of the lower inner and lower outer (LI+LO), and upper inner and upper outer (UI+UO) sidebands with respect to the LO tuning frequency. To overcome the variable atmospheric conditions, we used the wobbler switching observing mode to perform offset throws of 40″every second. Each wobbler switching mode procedure includes three, 5 minute integrations (i.e. twelve 25-s subscans). Frequent focus and pointing checks were assessed (e.g. Uranus, Venus, J1226+023, J1418+546) every 1.5 to 2hr, with azimuth and elevation pointing offsets typically within 3″. The IRAM 30m beam sizes at the observed CO(5-4) and CO(8-7) line frequency are $\theta \sim 15$" and $\theta \sim 10$", respectively. The absolute uncertainty we adopt for the derived line properties from the IRAM 30m observations is 20% based on the dispersion of flux densities observed in pointing sources from ongoing monitoring at the telescope. All scans were reduced using GILDAS, smoothed to ~ 50 km s^{-1} channel resolution before being co-added.

5.5 Results

5.5.1 Intrinsic Line Properties

The observed [NII] 205μmemission line peaks at $\nu_{\mathrm{obs}}^{\mathrm{peak}} = 411.2485$ GHz. We integrate the full line profile to derive a total velocity integrated flux density of 4.3 ± 1.1 Jy km s^{-1}(using an antenna gain factor of 52.3 Jy/K). The CO(1-0) ($\nu_{\mathrm{obs}}^{\mathrm{peak}} = 32.4432 \pm 0.0001$ GHz) has a measured integrated flux of 0.18 ± 0.04 Jy km s^{-1}(antenna gain factor of 0.7 Jy/K). This is consistent with, albeit slightly higher than, the Zpectrometer measurement (0.11 ± 0.03 Jy km s^{-1}) of Su et al. (2017). The velocity integrated flux intensities for the CO(5-4) ($\nu_{\mathrm{obs}}^{\mathrm{peak}} = 162.212$ GHz) and CO(8-7) ($\nu_{\mathrm{obs}}^{\mathrm{peak}} = 259.484$ GHz) emission lines are 1.96 ±0.3 and 1.37 ±0.27 Jy km s^{-1}, using antenna gain factors of 6.69 and 8.38 Jy/K, respectively. We report in Tab. 5.1 the line luminosity (in $L_\odot$) and spatially integrated

[2] Software information can be found at: http://www.iram.fr/IRAMFR/GILDAS

	[NII]205μm	CO(1-0)	CO(3-2)[b]	CO(4-3)[c]	CO(5-4)	CO(8-7)
Redshift, z (peak)	2.55308 (0.0004)	2.55300 (0.0004)	2.5529 (0.00011)	2.5543 (0.0002)	2.5525 (0.0002)	2.55243 (0.0003)
Total Intrinsic Line Properties[a]:						
$S_\nu\Delta V$ [Jy km s^{-1}]	4.3 (1.1)	0.18 (0.04)	1.38 (0.28)	1.62 (0.32)	1.96 (0.3)	1.37 (0.27)
L'[10^{10} K km s^{-1} pc^2]	0.84 (0.21)	3.67 (0.92)	4.8 (1.2)	3.2 (0.8)	2.5 (0.6)	0.67 (0.19)
$L_{\rm line}$[10^8 L$_\odot$]	8.4 (2.0)	0.02 (4.3e-03)	0.64 (0.02)	1.0 (0.25)	1.5 (0.38)	1.6 (0.42)
Component A (peak):						
FWHM (km s^{-1})	293 (76)	179 (23)	-	-	165 (22)	154 (50)
Amplitude (mJy)	8.7 (1.3)	0.44 (0.07)	-	-	5.5 (0.7)	5.1 (2.0)
Center (km s^{-1})	-69 (34)	-55 (10)	-	-	-37 (6)	-20 (17)
Component B:						
FWHM (km s^{-1})	337 (170)	352 (230)	-	-	480 (116)	337 (353)
Amplitude (mJy)	4.5 (1.3)	0.09 (0.023)	-	-	2.10 (0.25)	1.5 (0.6)
Center (km s^{-1})	334 (72)	200 (118)	-	-	240 (60)	200 (188)

Table 5.1: Best-fit Gaussian Models and Line Properties. The velocities are measured with respect to $z = 2.553$, i.e. the peak velocity component. [a] Measured line properties corrected for magnification ($\mu = 15$). The systematic errors are listed in parenthesis for the velocity-integrated flux density and derived total line luminosities. The parenthessis associated with the FWHM, centroid, and amplitude for Gaussian components A and B are based on the residual errors to the model fit. [b] Su et al. (2017); Rivera et al. (2019) and [c] Geach et al. (2018), corrected for the cosmology used throughout this paper. Geach et al. (2018) report the redshift based on the mid-point full-width-at-zero-intensity of the observed CO(4-3) transition.

source brightness temperature (in K km s^{-1} pc^2) following Carilli & Walter (2013). We note that the peak line intensity frequencies are all consistent with $z = 2.5535 \pm 0.0006$.

Asymmetric line profiles are observed in all the high S/N ($S_{\rm peak}/N_{\rm rms} > 10$) line detections (CO 1-0, 5-4, 8-7; [NII] 205μm), therefore we fit two 1-D Gaussians to the line shapes to compare their respective full-width-at-half-maximum (FWHM), centroids and amplitudes. The best-fit models are overlaid on the CO and [NII] 205μmspectra in Fig. 5.1, while the best-fit parameters are listed in Tab. 5.1, together with the CO(3-2)[3] and CO(4-3) velocity integrated line flux densities from Rivera et al. (2019); Geach et al. (2018).

The line centroid and FWHM of the [NII] 205μmemission line are consistent with the observed CO(1-0) (tracing the total molecular gas mass), and the more highly excited, $J_{\rm up} > 3$, CO lines. In all lines, the red component is offset by about 250-450 km s^{-1}from the blue component. Differential lensing may yield differences in measured line ratios (Serjeant, 2012). However, without higher angular resolution observations for each transition, we assume the magnification factor does not change for each of the observed lines, such that the low-density diffuse HII regions traced by [NII] 205μmand the molecular gas traced by CO are considered to be co-spatial when averaged across kpc scales.

5.5.2 Far-IR Spectral Energy Distribution

Using data from the literature and various telescope archives, we compiled multi-band photometry tracing emission from the *RRR* in the (observed-frame) mid-infrared to mm-wavelengths (Geach et al., 2015; Harrington et al., 2016; Schulz et al., 2017; Su et al., 2017). We fit the observed SED with a single temperature modified blackbody (MBB) model combined with a Wien-side power-law slope, denoted as α, of which a value of $\alpha \sim 2$ is characteristic for SFGs (e.g., Casey et al., 2012). If an AGN torus is contributing a hot dust component, the MIR would show an

[3] As noted in Rivera et al. (2019), the CO(3-2) line flux for the LMT detection presented in Harrington et al. (2016) is unfortunately incorrect due to the early commissioning period and calibration uncertainties.

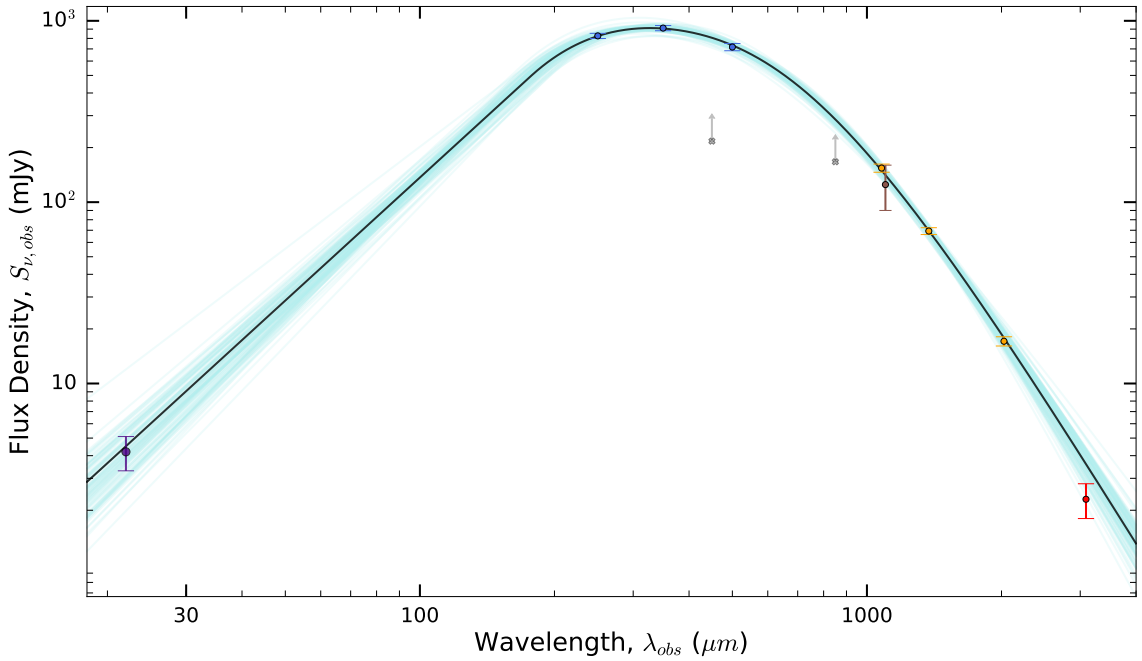

Figure 5.2: The best-fit modified blackbody SED model (black line) for the *RRR*. We also show multiple iterations of the models created by sampling the parameter space for the modified blackbody (cyan) that are representative of the degeneracies in the parameter space. Data included for the SED fit exercise is shown as colored circles with corresponding error bars: (indigo) WISE/W4, (blue) Herschel/SPIRE, (yellow) ACT (Su et al., 2017) and (red) CARMA (Su et al., 2017). For completeness, we show data that is not included for the SED fit - (gray cross as lower limits) measurements from SCUBA-2 presented in Geach et al. (2015) and (brown circle) is the average of the two AzTEC/LMT measurements from Geach et al. (2015) and Harrington et al. (2016).

Wavelength (μm)	Flux Density (mJy)	Instrument
22	4.2±0.9	WISE/W4
250	880±27	Herschel/SPIRE
350	991±30	Herschel/SPIRE
500	773±33	Herschel/SPIRE
850	167±4	JCMT/SCUBA (G15)
1078.4	154±8	ACT (278GHz, S17)
1100	95.5±6	LMT/AzTEC (G15)
1100	145±15	LMT/AzTEC (H16)
1375.2	69±3	ACT (218GHz, S17)
2025.6	17±2	ACT (148GHz, S17)
3090.6	2.3±0.5	CARMA (S17)

Table 5.2: Observed mid-IR to mm photometry for the *RRR*.Geach et al. (2015, G15), Harrington et al. (2016, H16), Su et al. (2017, S17).

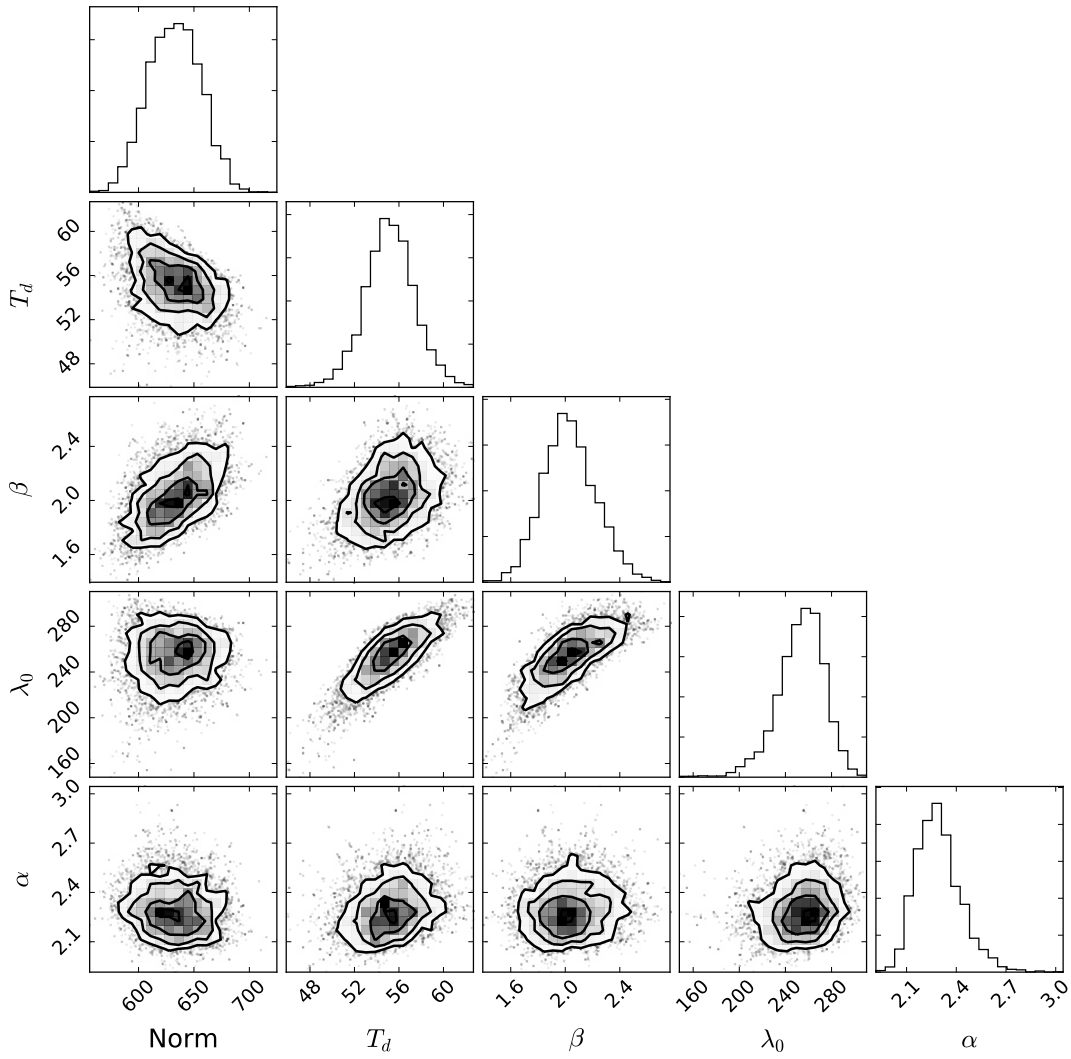

Figure 5.3: Posterior probability distribution for the SED model parameters: the value at which the dust opacity reaches unity is at rest-frame wavelength of λ_0, dust emissivity index, β, a single component dust temperature, $T_{\rm d}$, and the Wien-side power law slope for SFGs, α.

$L_{\rm IR\ (8\text{-}1000\mu\ m)}$	$L_{\rm FIR\ (40\text{-}120\mu\ m)}$	$\rm SFR_{IR}$	$\rm SFR_{[NII]205}$	$M_{\rm H_2}$	$M_{\rm min}(\rm H^+)$
$[10^{13} L_\odot]$	$[10^{13} L_\odot]$	$\rm M_\odot\ yr^{-1}$	$\rm M_\odot\ yr^{-1}$	$10^{10}\ \rm M_\odot$	$10^{10}\ \rm M_\odot$
$1.46^{0.07}_{-0.06}$	$0.82^{0.04}_{-0.03}$	2482 (992)	621^b	3.67 (0.9)	0.89

Table 5.3: The intrinsic (lensing-corrected) properties of the *RRR*. The reported values can be converted back to the apparent values by multiplying the average lensing magnification factor of μ=15 (Geach et al., 2018). The intrinsic SFR and $M(\rm H^+)$ are derived from the [NII] 205μmemission line, and are corrected by factor of 4.67 to account for the derived attenuation assuming a uniform dust screen approximation. The total and far-IR derived luminosities are derived from the dust SED modeling of the photometry from Harrington et al. (2016); Su et al. (2017); Rivera et al. (2019); Geach et al. (2015, 2018).

excess compared to the power law slope for a normal SFG (e.g. the WISE 'Hot DOGS' Tsai et al., 2015).

We retrieved the SPIRE photometer measurements from the SPIRE point source catalog (Schulz et al., 2017). We report the estimated uncertainties due to confusion rather than the systematic and statistical errors (which are <2%) as the SPIRE beam is large (18-35") and the diameter of the radio Einstein ring is roughly 5" (Geach et al., 2015). We find that the flux density measured with LMT/AzTEC varies by 50% between the two observations by Geach et al. (2015) and Harrington et al. (2016, see footnote 3 above). For the MBB fit, we use the average value of these measurements, with an uncertainty that encompasses the range of values reported, i.e., 125±35 mJy. We note that Geach et al. (2015) reported that the 450μm flux density measured with SCUBA was a factor of three smaller than that measured by SPIRE and hence this SCUBA measurement not included here. In comparison with the ACT 278 GHz measurement, we find that the 850μm SCUBA flux density, though a high significance detection, is most likely an underestimate, perhaps due to absolute flux calibration. We therefore ignore the SCUBA 850μm data point while performing the model fitting.

Fig. 5.2 shows the best-fit SED model of the *RRR*. In the following we quote the best-fit and the uncertainties based on the 16^{th}, 50^{th} and 84^{th} percentiles of the samples in the marginalized distributions for each of the parameters (see Fig. 5.3). We find the dust opacity reaches unity at rest-frame wavelength of $\lambda_0 = 254^{+17}_{-18}$ μm, with a dust emissivity index $\beta = 2.0^{+0.17}_{-0.17}$ and a dust temperature, $T_{\rm d} = 55^{+2.3}_{-2.2}$ K, Wien-side power-law slope $\alpha = 2.27^{+0.14}_{-0.11}$. The total *apparent* infrared luminosity (IR; 8 - 1000μm), $\mu L_{\rm IR} = 21.9^{+1.0}_{-0.89} \times 10^{13}$ $\rm L_\odot$, before correcting for the magnification factor, μ. The *apparent* far-infrared luminosity (FIR; 40-120μm), is $\mu L_{\rm FIR} = 12.3^{+0.41}_{-0.43} \times 10^{13}$ $\rm L_\odot$.

The value of $L_{\rm IR}$ / $L_{\rm FIR}$ is consistent with normal star-forming systems, i.e. $L_{\rm IR}$ / $L_{\rm FIR} \sim 1.5 - 2$ (Dale et al., 2001, ; see e.g. Leung et al. 2019b). Thus, the observed dust SED does not show strong signs of an AGN influence, e.g. no bright WISE/W4 counterpart. This suggests i.) that the compact radio-AGN, revealed by bright radio emission with a steep radio synchrotron slope of $\alpha_{\rm radio} = -1.1$ (Geach et al., 2015), does not significantly affect the overall IR luminosity of the *RRR*, or ii.) there is extreme dust obscuration of an AGN. Its intrinsic SFR can thus be estimated using $\mu = 15$ (Geach et al., 2018) and the standard calibration of the total IR to SFR, with $\rm SFR_{IR} = 1.7 \times 10^{-10} L_{IR}\ M_\odot\ yr^{-1}$; (Kennicutt, 1998). We find the $\rm SFR_{IR} = 2482 \pm 992\ M_\odot\ yr^{-1}$, taking into account the total error propagation for the average best-fit relative uncertainty on the IR luminosity (~3%), and the systematic errors for the photometric data points used in the modeling (~37%; Tab. 5.2).

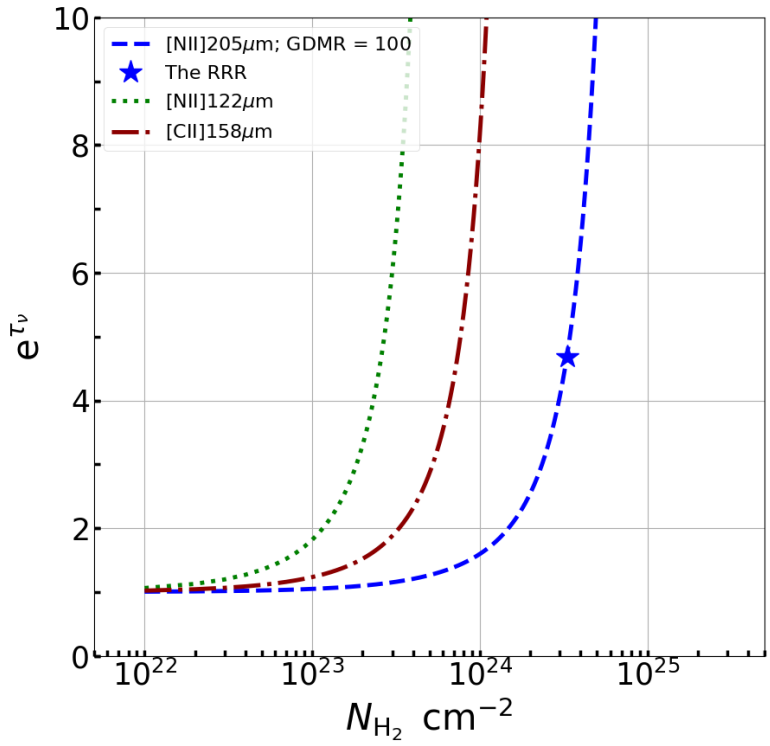

Figure 5.4: The dust attenuation correction as a function of mean molecular hydrogen column density. A single uniform dust screen approximation (with GDMR = 100; dust-emissivity spectral index, $\beta = 2.03$), evaluated at: the rest-wavelengths of the [NII] 205μm(green dotted line), the [NII] 122μm(blue dashed line) and [CII]158μm (red dashed-dotted line) line emission, including the result for the *RRR* (blue star).

Effects of Dust Attenuation

In the *RRR* the dust opacity reaches unity at the rest-frame wavelength of λ_0 =254μm . Such high opacity is consistent with that observed in other high-z DSFGs (Riechers et al., 2013), while slightly higher than e.g., AzTEC-3, which is a more normal star-forming galaxy at $z > 5$, (Riechers et al., 2014). The dust attenuation of the [NII] 205μmemission line is therefore not negligible, as pointed out by other studies of far-IR FSLs in quasars (QSOs) and DSFGs (Lamarche et al., 2017). We correct the line luminosity based on a single, uniform dust screen approximation, i.e., $L_{\mathrm{[NII]205}_{un-att.}} = e^{\tau_{205\mu m}} \times L_{\mathrm{[NII]205,\,obs.}}$. From our best-fit SED model, the opacity at rest-frame 205μm is $\tau_{205\mu\,\mathrm{m}} = (\lambda_0/\lambda)^\beta = 1.54$, which results in a uniform screen dust attenuation correction factor of $e^{\tau_{205\mu m}} \simeq 4.67$. The following corrections are considered an upper limit along the line of sight. In the scenario where the emitting gas is well mixed with dust, the mixed gas/dust attenuation correction factor would be $\tau_{205\mu\mathrm{m}}/(1 - e^{-\tau_{205\,\mu\,\mathrm{m}}}) = 1.96$.

Corrections to the observed far-IR FSL detections of the $z > 4$ systems are limited by the sparse sampling of their peak dust SED to accurately constrain the dust opacity at the relevant wavelength. The *RRR*, with its well-sampled dust SED, allows us to constrain the mean hydrogen column density

N_{H_2}. In the following analysis, we assume both a fixed gas-to-dust-mass ratio, GDMR = 100, and a simple uniform dust screen. The dust opacity is expressed in terms of the dust column density, N_d, and κ_ν, the mass absorption coefficient (Weiß et al., 2008). We express $N_d$as N_{H_2} multiplied by the mass of molecular hydrogen, m_{H_2}, divided by the GDMR:

$$\tau_\nu = \kappa_\nu \times N_{\rm d} = \kappa_\nu \times \frac{N_{\rm H_2} \times m_{\rm H_2}}{GDMR}, \tag{5.1}$$

where

$$\kappa_\nu = 0.04\,(\nu/250\ {\rm GHz})^\beta. \tag{5.2}$$

Figure 5.4 plots the dust attenuation correction as a function of the mean molecular hydrogen column density N_{H_2} at rest-frame wavelengths corresponding to the [NII] 205μm, [NII] 122μmand [CII]158μm emission lines. The equivalent H_2 gas column density in the *RRR* is $N_{H_2} = 3.3 \times 10^{24}\ cm^{-2}$.

The *RRR*, having high molecular gas column densities, will have corrections that can severely impact the use of both [NII] 205μmand [NII] 122μmemission lines as an electron density indicator. For example, based on this simple uniform screen approximation, the observed line ratio of [NII] 122μm/ [NII] 205μmin the *RRR* would need to be corrected by a factor of $e^{\tau_{122\mu m}}/e^{\tau_{205\mu m}} \approx 18$. An intrinsic [NII] 122$\mu$m/ [NII] 205$\mu$mline ratio of $\sim 4-5$, corresponding to an electron density of $n_{\rm e^-} \simeq 200$ cm^{-3} (e.g. in the local starburst, M82; Petuchowski et al., 1994), would thus yield an observed [NII] 122μm/ [NII] 205μmvalue of (4-5)/18 = 0.3. Neglecting dust opacity, one would associate such low observed line ratio to un-physically low densities, as it would lie below the minimum theoretical line ratio of ≈ 0.6, as derived for warm ionised regions with $n_{\rm e^-} << n_{\rm crit,\,205\,\mu m}$ (Goldsmith et al., 2015; Herrera-Camus et al., 2016a). Naturally, the *RRR*, but also all high-z systems resembling the *RRR*, i.e., having high column densities, would suffer from this effect. Dust opacity should not be neglected while studying far-IR FSL emission in high-z DSFGs.

Relative Cooling by [NII] 205μm Line Luminosity

Using the [NII] 205μmand IR luminosities, we calculate the attenuation corrected $L_{\rm [NII]205\,\mu\,m}/L_{\rm IR} = 2.7 \pm 1.0 \times 10^{-4}$, assuming the same magnification factor for both luminosities. The vast majority of the local and high-z galaxies do not correct for dust attenuation, therefore we use the apparent, attenuated value, $L_{\rm [NII]205\,\mu m}/L_{\rm IR} = 5.8 \pm 2.1 \times 10^{-5}$.

As seen in Fig. 5.5, this attenuated $L_{\rm [NII]205}/L_{\rm IR}$ ratio for the *RRR* is at the lower boundary of the mean range observed in local ULIRGs within the large scatter of $10^{-5} - 10^{-3}$ (Zhao et al., 2016). The large dispersion in the $L_{\rm [NII]205}/L_{\rm IR}$ ratio remains constant across all redshifts. Galaxies in Fig. 5.5 with the lowest values of $L_{\rm [NII]205}/L_{\rm IR}$ include strong QSOs at $z \sim 4$ (e.g. Decarli et al., 2012), as well as the local AGN, MrK231, which has at least a 20% AGN fraction contributing to its $L_{\rm IR} \approx 10^{12}$ L$_\odot$ (Fischer et al., 2010; Dietrich et al., 2018). SFGs at high-z have slightly large scatter, probing a range of up to a factor of five between low metallicity galaxies (Pavesi et al., 2019), DSFGs and a Lyman-α Emitter (Decarli et al., 2014).

The $L_{\rm [NII]205}/L_{\rm IR}$ ratio of the *RRR* more closely resembles that of local/high-z SB rather than that of local/high-z QSO/AGNs. To first order, the global ISM within the *RRR* is mostly powered by SF. We note, however, that this ratio is subject to a few caveats. Robust comparisons of this ratio between the *RRR* and to other systems can be affected by individual variations in attenuation effects and hard ionising radiation fields that determine the relative [NII] 205μmline emission. The bolometric input

to the total IR luminosity from a supermassive black hole accretion/activity could contaminate the apparent IR luminosities and reduce the observed line to total FIR luminosity, as seen in QSO-selected systems. However, this ratio may not decrease significantly if there is a narrow emission line region of an AGN contributing to the total [NII] 205μmline luminosity, as seen in the local selection of AGN via the [NII] 6584 Å / 6548 Å excess (Baldwin et al., 1981). Our dust SED model is consistent with that of a SB galaxy (Casey et al., 2012; Magnelli et al., 2014), yet the resemblance of such an SED can also be due to a large dust screen strongly attenuating the emission from an obscured, dusty AGN torus ($T_{\rm d} \approx 500$ K, Leung et al. 2018, submitted; Siebenmorgen et al., 2004, 2015; Feltre et al., 2012; Kirkpatrick et al., 2017a). Thus, the spatially unresolved measurement of $L_{\rm [NII]205}/L_{IR}$ ratio cannot exclusively select an AGN from a SFG.

In the local universe, the observed scatter correlates with the rest-frame $\log(f_{70\mu\,\rm m}/f_{160\mu\,\rm m})$ colour (Zhao et al., 2013, 2016). SFGs with colder colours have an average of $L_{\rm [NII]205}/L_{\rm IR} \sim 3 \times 10^{-4}$, while star-forming/SB galaxies with warmer colours have average values of the $L_{\rm [NII]205}/L_{\rm IR}$ ratio of $\sim 5 \times 10^{-5}$ (Zhao et al., 2016). We show in Fig. 5.5 the range observed in the local Universe within galaxies with a similar FIR colour as the *RRR* (see Fig. 3 in Zhao et al., 2016). The FIR colours can be interpreted as a proxy for the dust temperature. The ratio of the FIR FSL luminosity to IR luminosity in local ULIRGs, both with and without an AGN, reveals a so-called line-to-FIR-continuum "deficit", where the relative cooling efficiency of the line luminosity decreases with respect to the FIR continuum. This "deficit" increases for higher values of IR luminosity (warmer FIR colour) for [NII] 205μm, [NII] 122μm, [CII] 158μm, [OI] 63μm and [OIII] 88μm, with a two order of magnitude scatter for the [NII] lines (Malhotra et al., 2001; Graciá-Carpio et al., 2011; Díaz-Santos et al., 2017). The nature of this deficit can strongly depend on the location of dust grains along the line of sight to the line emitting region (Díaz-Santos et al., 2013, 2017), and that the "deficit" has a tight correlation to the relative compactness of the IR luminosity surface densities. This reflects the spatial concentration of dust-reprocessed far-UV through IR continuum photons, which diminishes the relative cooling power of the FIR FSL. Using the maximum radius of the *RRR* in the reconstructed source-plane from the best-fit lens model of $R_{\rm max} \simeq 2.6$ kpc (Geach et al., 2018), we infer a mean SFR surface density of $\Sigma_{\rm SFR}{}_{IR} = \frac{SFR_{\rm IR}}{\pi R^2_{\rm max}}$ of about 120 $\rm M_{\odot} yr^{-1} kpc^{-2}$. The high SFR surface density may indicate why the apparent, attenuated ratio of $\rm L_{[NII]205}/\ L_{IR}$ has a low value compared to the mean dispersion of local SFGs with similar rest-FIR colours (see green bar in Fig. 5.5).

5.5.3 CO Spectral Line Energy Distribution

The spectral line energy distribution (SLED) of CO can be a tool to distinguish extreme, highly excited QSO galaxies from galaxies that have molecular gas excitation dominated by SF activity (Daddi et al., 2015; Carilli & Walter, 2013). Fig. 5.6 compares the CO(1-0) normalised SLED of the *RRR* with the average spread amongst local ULIRGs, average DSFGs/SMGs, the Milky Way Galactic Centre, and well-known QSO powered systems at high-z (Weiß et al., 2007a; Fixsen et al., 1999; Papadopoulos et al., 2012a; Bothwell et al., 2013; Riechers et al., 2013). Compared with the Milky Way Centre and the average dusty SFG, the *RRR* shows high CO excitation. The CO SLED bears a resemblance to the even more extreme gas excitation in local ULIRGs (Papadopoulos et al., 2012a; Mashian et al., 2015; Rosenberg et al., 2015), but not as high as the local starbursts, M82 (Panuzzo et al., 2010) and NGC 253 (Hailey-Dunsheath et al., 2008), or the more normal SFG, NGC 891–all of which peak at CO(7-6) (Nikola et al., 2011b). The SLED is comparable to the average value of QSOs reported in the

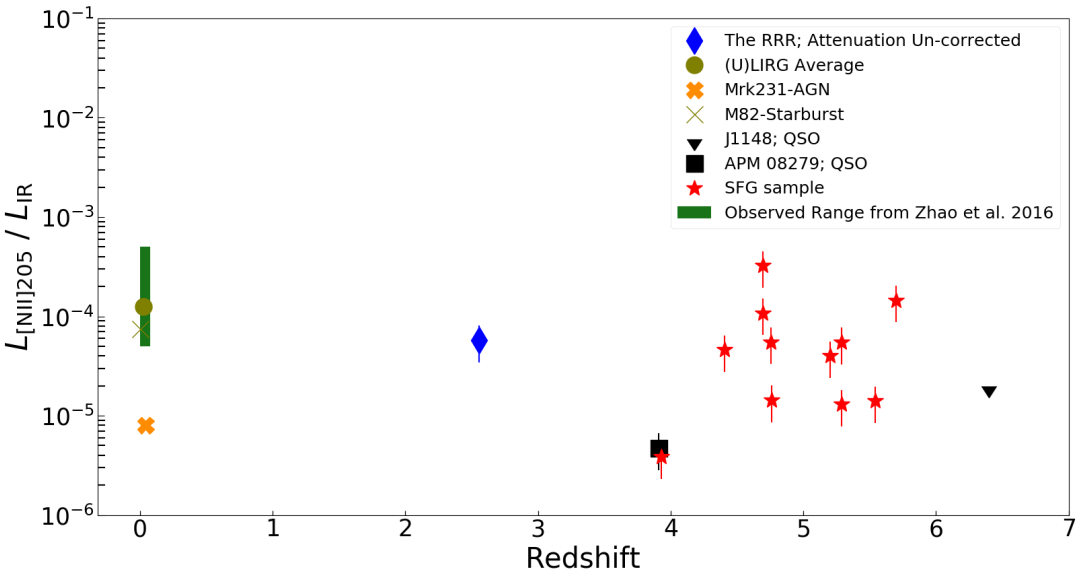

Figure 5.5: [NII] 205μmline luminosity to total IR (8-1000μm) luminosity ratio in various samples, probing a broad redshift range: local starburst, M82 (green 'x') and AGN, Mrk231 (orange 'x'), Walter et al. (2009); Decarli et al. (2012, 2014); Combes et al. (2012); Nagao et al. (2012); Béthermin et al. (2016); Pavesi et al. (2016, 2019); Lu et al. (2018) (red stars), including the attenuation corrected value for the *RRR*. We show the predicted dispersion observed in the local Universe by Zhao et al. (2016) within a sample of galaxies with similar far-IR colour as the *RRR* (green line).

review by Carilli & Walter (2013) out to $J_{up} = 5$. Its molecular gas excitation hints at the existence of a strong heating source. To account for the strong mid-J CO lines observed in NGC 253 and NGC 891, both Hailey-Dunsheath et al. (2008); Nikola et al. (2011b) both invoke the need for strong mechanical heating/shocks from a turbulent star-forming environment (see also Kamenetzky et al., 2016; Lu et al., 2017). The high-J turnover (at $J_{up} \geq 5$) and tail of the CO SLED indicates that the CO excitation is, however, not as extreme as in the highly excited QSO systems (Weiß et al., 2007a; Salomé et al., 2012).

5.5.4 Ionised and Molecular Gas Mass

Local [NII] measurements have found the electron density in the Milky Way to be $n_{e^-} = 33$ cm^{-3} (Goldsmith et al., 2015) and for local (U)LIRGs $n_{e^-} = 22\,cm^{-3}$ (Zhao et al., 2016). The minimum mass of ionised hydrogen can be approximated, after correcting for the line attenuation, using the high-temperature/high-density limit (see Ferkinhoff et al., 2011; Decarli et al., 2012). Using Eq. 1 in Decarli et al. (2012), we find $M_{\mathrm{min}(\mathrm{H}^+)} = 0.93 \pm 0.19 \times 10^{10}$ M$_\odot$. This assumes a gas phase nitrogen abundance of, $\chi(N) = N/H = 9.3 \times 10^{-5}$ (Savage & Sembach, 1996), determined by UV-absorption sight-lines towards massive stars in the Milky Way. We also assume that all the nitrogen is in the singly ionised state, i.e., $\chi(N) = \chi(N^+)$. To calculate the relevant fraction of ionised to molecular gas mass, we use the measured $L'_{\mathrm{CO(1-0)}}$ line luminosity converted to a total molecular gas mass. Here we assume a CO line to molecular hydrogen gas mass conversion factor, $\alpha_{\mathrm{CO}} = 1$ M$_\odot$ (K km s^{-1}pc^2)$^{-1}$,

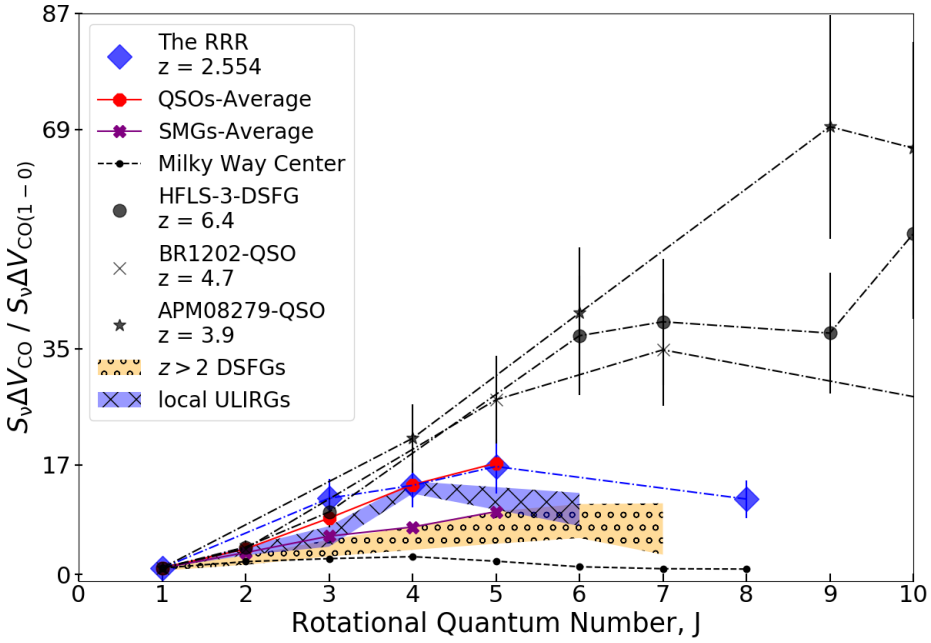

Figure 5.6: CO spectral line energy distribution (SLED), normalized to the ground-state CO(1-0) integrated flux density, of the *RRR* (blue diamonds), including local ULIRGs (Papadopoulos et al., 2012a), the Milky Way Centre (Fixsen et al., 1999) and high-z QSOs and DSFGs (Weiß et al., 2007a; Salomé et al., 2012; Bothwell et al., 2013; Riechers et al., 2013; Carilli & Walter, 2013).

appropriate for local starburst galaxies (Solomon & Vanden Bout, 2005; Downes & Solomon, 1998; Sanders & Mirabel, 1996)[4], and find $M_{\rm mol} = 3.67 \pm 0.9 \times 10^{10}$ M$_\odot$. To account for the total molecular gas mass, we correct by the additional mass-weighted contribution by He ($1.36 \times$ M$_{\rm H_2}$). The ionised to molecular mass fraction is 25%, consistent with other actively star-forming high-z systems (Ferkinhoff et al., 2011; Zhang et al., 2018a).

5.6 Discussion

5.6.1 Ionised Nitrogen as a SFR tracer

Despite the advantage of directly probing the ionising stars on timescales of ~10 Myr, Hα SFRs are often plagued by uncertainties from dust attenuation (Kennicutt, 1998; Calzetti et al., 2007). In dust-obscured galaxies, the attenuation-corrected Hα luminosity measurements significantly underestimate the overall SFR (e.g. Whitaker et al., 2017) derived from the total IR (8-1000μm) luminosity (Kennicutt, 1998; Kennicutt & Evans, 2012). In these dust-rich galaxies, the total IR luminosity has thus been seen as the ideal tracer of SFR because the dust-absorption cross section peaks at the wavelengths emitted by young stellar populations, and is re-emitted by dust in the far-IR wavelength regime (e.g

[4] A range has been reported for individual ULIRGs: α =0.6-2.6 (Downes & Solomon, 1998)

40-120μm, Helou et al., 1985). IR-derived SFRs trace the *characteristic, rather than instantaneous,* rates of SF on the order of 100 Myr, depending on the SF history. The total IR luminosity will be mostly dominated by the OB stellar population in starburst systems with less than a few 100 Myr gas consumption timescales (Kennicutt & Evans, 2012).

The far-IR FSLs have longer rest-wavelengths as compared to optical or near-IR tracers of SF, and the line photons may thus escape dust-obscured HII regions without being absorbed. This motivates the use of far-IR FSLs as faithful tracers of the most recent SF (Fernández-Ontiveros et al., 2016). For example, the [NII] derived SFR probes *quasi-instantaneous* star-formation rates corresponding to $\sim$ 30 Myr, i.e. the lifetimes of early B-stars.

Locally, however, [NII] may not be the ideal SFR tracer for galaxy integrated measurements, as it can trace a mixture of both ambient, diffuse ionised gas and ionised gas closely associated with SF. In contrast, [NII] may be a more accurate tracer of the global SFR in gas-rich, SFGs at high-z , as the latter contains star-forming environments that pervade the entire ISM. Indeed, these systems undergo rapid stellar mass assembly, with SF taking place throughout the entire galaxy (Magdis et al., 2016; Rujopakarn et al., 2016a; Elbaz et al., 2018b).

As first presented in Ferkinhoff et al. (2015), there is a physically motivated relation between the SFR and [NII] line emission for star-forming galaxies. This relation is further substantiated by an empirical relation between the observed [NII] line emission and the IR-derived SFR (Zhao et al., 2016). In ionisation bounded, low-density HII regions, the [NII] line emission is proportional to the ionising photon rate (modulo the N/H ratio), which in turn is proportional to SF. The low-z relation of [NII] line luminosity to SFR can be extended out to high-z only by making strong assumptions of both the fractional nitrogen abundance and ionised gas densities (Herrera-Camus et al., 2016a). Here we focus on the SFR estimate where the densities are below the critical density for [NII] 205μmemission line (44 cm^{-3} Goldsmith et al., 2015), and use Eq. 10 of Herrera-Camus et al. (2016a), assuming the collisional excitation coefficients from Tayal (2011), which yields

$$SFR_{[\mathrm{N\,II}]205\mu\,\mathrm{m}}\,[\,\mathrm{M_\odot}\ \ \mathrm{yr^{-1}}] = 1.98\times10^{-7}\,\frac{(N/H)_\odot}{(N^+/H^+)}\,\frac{L_{[\mathrm{N\,II}]205\mu m}}{\mathrm{L_\odot}}. \tag{5.3}$$

We estimate an attenuation, and magnification, corrected $\mathrm{SFR}_{[NII]205\mu m} = 621\ \mathrm{M_\odot\ yr^{-1}}$. However, both the nitrogen abundances in the *RRR* are unknown, and will affect this measurement significantly. The [NII] 205μmderived SFR is about four times smaller than the traditional IR-derived SFR (Tab. 5.3).

The SFR derived using Eq. 5.3 is, however, a lower-limit. The low-density assumption breaks down when the density reaches or even exceeds that of the critical density. This is a possibility for the *RRR*, as a strong SB could result in increased electron densities and an overlap of HII regions from widespread SF, yielding electron densities $> 10^4\mathrm{cm^{-3}}$(see Goldsmith et al., 2015; Herrera-Camus et al., 2016a). When the electron density is significantly higher than the critical density for the ground-state, the system is thermalised. Thus, the emission of photons is defined by the Boltzmann level population and the Einstein A-coefficient [5], saturating the [NII] 205μmline emission. Such high SFR surface density in the *RRR* (see § 4.2.2) implies the ISM has an electron density $n_{e^-} >> 100-1000\mathrm{cm^{-3}}$(Herrera-Camus et al., 2016a), i.e. an order of magnitude higher than the critical density of the [NII] 205μmemission line. To confirm that the disagreement between these two SFR estimates is simply due to high electron

[5] We assume all of the nitrogen is within low-density HII regions, as opposed to the hottest clusters of early O-type stars (which would result in most of the nitrogen residing in the [NII] or [NIV], rather than [NII]).

density in the ISM of the *RRR*, detection of the [NII] 122μmemission line will be needed.

5.6.2 Co-Evolution of AGN/SF in the *RRR*

The known compact radio-mode AGN, inferred from high spatial resolution eMERLIN observations (Geach et al., 2015), does not seem to halt the intense SF activity of the *RRR* (Geach et al., 2018). The unattenuated ratio of [NII] 205μmand IR luminosity is consistent with a SB galaxy, while the dust/CO SED also disfavors a strong AGN contaminating the IR spectrum (e.g. Salomé et al., 2012; Weiß et al., 2007a). The similitude in line profile shapes of the multiple CO lines and the [NII] 205μmline points at the co-existence of warm ionised and cold molecular phases across kpc scales.

As an example, the spatial co-existence of warm ionised regions traced by [NII] 205μm, and that of the dense and diffuse molecular gas traced by CO, can be considered similar to the gas phase mixing in the Central Molecular Zone (CMZ) on the scales of 100 pc (Kruijssen & Longmore, 2013; Ginsburg et al., 2018), and even in the immediate vicinity of Sgr-A* on the scale of 1 pc (Moser et al., 2017). Hence, the Galactic centre region may serve as a high-z galaxy analog (see also Swinbank et al., 2011; Kruijssen & Longmore, 2013). Thermal instability during AGN and SB phases in galaxies is one mechanism to explain how such a co-existence may be maintained over the long-term. Różańska et al. (2014) and Różańska et al. (2017) found that for certain parameter ranges (activity of a galactic nucleus, star cluster input), thermal instability operates[6] and essentially leads to the formation of the two-phase (warm–cold) medium, which is rather stable given the long heating and cooling timescales (Field, 1965). This can be one of the main sources of cold gas formation under the presence of stellar, supernova and AGN feedbacks (Tenorio-Tagle et al., 2013). Our global measurements represent the galaxy integrated average of the CO and [NII] 205μmline emission, such that it is not possible to access the relevant physical scales to compare directly to the CMZ. Geach et al. (2015, 2018) identify a compact radio AGN (<250 pc) and a galactic disk traced by CO(4-3), extended over 2.5-3 kpc, therefore the CO(5-4) line emission is almost certainly associated with this molecular disk. However, the relative contributions of the AGN and the large-scale galactic disk to the observed [NII] 205μmline emission remains to be resolved.

Such co-eval AGN/SF processes within galaxies is expected to be a part of the evolution of a massive galaxy such as the *RRR*, depicted by a short-lived, merger-induced SB that catalyses high AGN activity and black-hole growth (e.g. Hopkins et al., 2008). There is a range of co-eval AGN/SF processes that can be seen both locally and at high-z. In local systems, nuclear regions with high SF and low-AGN fractions are observed to co-exist based on various nebular line diagnostics e.g. (D'Agostino et al., 2018), while there is an inferred quenching of SF in local AGN hosts residing in massive elliptical galaxies (Baron et al., 2018). The increased excitation conditions within the narrow emission line regions of an unobscured AGN can ionise the entire ISM (Greene et al., 2011), and potentially quench SF. Therefore the use of ionised nitrogen as a tracer of SF may be unreliable because of the change in ionisation structure of nitrogen (depending on the slope of the ionisation parameter) in the presence of such a strong heating source. High-z galaxies, however, with large reservoirs of molecular gas ($> 10^{9-10}$M$_\odot$) can sustain ongoing SF even in the most extreme, optically bright, broad-line QSO systems (Glikman et al., 2015; Cresci et al., 2015). A systematic study of >100 gravitationally lensed QSOs ($z \sim 1-4$), Stacey et al. (2018) found most have both SF and AGN

[6] S-curve in the temperature–ionisation parameter plane ($T - \Sigma$), where the ionisation parameter Σ is defined as $\Sigma = P_{\rm rad}/P_{\rm gas}$, where $P_{\rm rad}$ and $P_{\rm gas}$ are radiation and gas pressure, respectively.

activity. Our conclusions suggest it is possible for both AGN and SB activity to co-exist, and this may be due to both thermal instability and the large molecular gas reservoir in the *RRR*.

5.7 Summary and Conclusions

We present the detection of [NII] 205μmin a strongly lensed AGN/SB galaxy at $z = 2.5535 \pm 0.0006$, obtained using the *APEX* telescope. We complement this detection with multiple CO line transitions (CO 1-0, 5-4, 8-7) to examine the global properties of the ionised and molecular gas in the *RRR*. Our main conclusions are:

• The line profiles for the CO and the [NII] 205μmemission lines have similar velocity components that can be explained by shared volumes, i.e. molecular clouds well-mixed with HII regions, suggesting the majority of the strong [NII] 205μmdetection is associated with SF.

• The non-negligible dust attenuation at rest-frame 205μm in the *RRR* suggests that these corrections need to be accounted for when interpreting far-IR FSLs in dust-rich systems at high-z. Assuming a uniform dust screen approximation results in a dust attenuation correction, $e^{\tau_{205\mu m}}$, of ~ 4.67 for the *RRR*. This implies a mean H_2 gas column density $> 10^{24}$ cm^{-2}, assuming a molecular gas-to-dust mass ratio of 100.

• We derived an attenuation corrected, minimum ionised gas mass, $M_{min}(H^+) = 0.89 \times 10^{10}(\frac{15}{\mu})$ $M_\odot$, assuming a high-density / high-temperature limit. This ionised gas mass corresponds to about 25% of the total molecular gas mass derived using the measured CO(1-0) line luminosity and $\alpha_{CO} = 1$ $M_\odot$ (K km s^{-1}pc^2)$^{-1}$.

• The attenuation corrected value of $L_{[NII]205\mu m}/L_{IR} = 2.7 \pm 1.0 \times 10^{-4}$, resembles the average values of SFGs rather than those with a known QSO influence.

• The IR SFR, $SFR_{IR} = 2482 \pm 992$ $M_\odot$ yr^{-1}, is a factor of four larger than the lower-limit SFR estimate from the attenuation corrected, [NII] 205μmline luminosity in the low-density regime: $SFR_{[NII]205\mu m} = 621$ $M_\odot$ yr^{-1}. This suggests the electron density is significantly high, or the assumed nitrogen abundance is significantly lower.

Utilising the [NII] 205μmline as a tracer of SF has a strong physical motivation, although the reliable application of local relations requires extensive calibration for high-z dusty SFGs. Future spatially resolved [NII] 205μmand [NII] 122μmobservations would help to isolate low-density vs. high-density HII complexes in the warm ionised medium (as seen in Spinoglio et al., 2015; Zhao et al., 2016) in order to aid future interpretations in this system.

CHAPTER 6

Conclusion and outlook

The physical conditions of the cold molecular gas in high-redshift star-forming galaxies is an important piece in the puzzle of how galaxies have formed and evolved over cosmic time. This PhD thesis examined these gas conditions for a relatively large sample of 24 infrared-bright lensed galaxies at redshift, $z \sim 2$.

Here I will briefly summarize the main points of this Ph.D. I first conducted a pilot study to measure and analyze the CO(1-0) emission line properties in a subset of these galaxies, with a focus on constraining the molecular gas masses. I further measured higher-J rotational transitions of CO, and both [CI] lines, in this sample in order to perform a joint modeling of the line spectral energy distributions and the IR/mm photometry. The overarching conclusion based on the results of this thesis work is that turbulence-regulated feedback is a key driver of the molecular gas emission in these high-redshift star-forming galaxies.

Further detailed studies of individual high-z ($z > 1$) dusty star-forming galaxies are still needed to describe the regulatory processes associated with intense bursts of star formation. To better understand these processes in the most dust-obscured sites throughout cosmic time, global and spatially resolved diagnostics need to be calibrated. Molecular gas distributions must be mapped at both low and high-z, and can then be compared with theoretical models of cloud fragmentation and collapse. With rapid inferred gas depletion times, dusty star-forming galaxies at $z > 1$ are ideal targets for investigating such phenomena. Most individual galaxies lack the suite of ISM diagnostics to better understand the driving mechanisms which sustain star-formation out to $\sim$ 10 kpc. With very large area (sub)-mm surveys, it is possible to detect these dusty galaxies using the natural microscope in space: i.e. strong gravitational lensing. This requires sensitive measurements of the rarest chance alignments between high-z systems and their massive foregrounds. These lensed galaxies maybe have line/continuum fluxes boosted by an order of magnitude or more, and larger samples are likely to be discovered in the coming decade.

Each strong lens system is an especial laboratory, enabling us to study the properties of in-situ star-forming regions. This makes the relatively large sample of *Planck*-selected galaxies in this thesis work a potential goldmine for probing a wealth of ISM line/continuum diagnostics with a modest amount of telescope time. Aside from CO/dust, far-IR fine-structure lines offer a powerful probe of

HII regions in obscured sites, while these strongly lensed galaxies would have the best opportunity to also detect fainter emission lines from molecules such as H_2O^+. The formation of H_2O via H_2O^+ intermediates makes H_2O^+ detections direct tracers of regions with ion-neutral reactions, and strong cosmic ray and/or X-ray ionization rates from obscured AGN in the ISM of local star-forming galaxies. Our complex radiative transfer modeling will be a useful tool to provide stronger insight into different gas heating mechanisms. Additional lines can be modeled in conjunction with the methodology presented in this thesis work, and the results can be compared with other possible physical models of the ISM in these galaxies. This would allow for better physical constraints of the dense molecular gas properties and heating mechanisms.

The legacy value data presented in this thesis has triggered a series of follow-up programs to resolve our understanding of these distant objects. The single-dish line measurements offer a spatially unresolved view into the global properties, and are vital for detection experiments prior to other spatially resolved observations with radio/(sub)-mm interferometer telescope arrays. I will briefly capture the promising outlook for future research based off of this thesis work:

- The GBT measurements of the CO(1-0) emission line has led to a successful proposal with the Very Large Array (VLA), in New Mexico, U.S.A., to spatially resolve (at 1" resolution) the CO(1-0) line emission in a subset of sixteen galaxies. A total of four of the sixteen sources were observed. This data will be reduced alongside other CO(1-0) line measurements in the VLA archive for other sources in the sample to assess the nature of the CO(1-0) emitting region and to trace the distribution and kinematics of the bulk molecular gas.

- The published results in Chapter 5 led to another successful proposal to use the APEX telescope in northern Chile, in order to measure more lines from singly ionized nitrogen. This line is useful in characterizing the mean ionized gas properties, and can be used to alternatively derive a SFR without integrating the dust SED. Four galaxies now have detections of the [NII]122μm line, which is among the largest number of lines for sample of $z \sim 1-3$ galaxies. Two galaxies have both [NII] line detections, which can allow for strong constraints on the nature of the ionized gas density. One such galaxy has a [CII] line detection with APEX, and the combination of [NII] and [CII] line measurements can be used to infer to what extent the ionized carbon emission arises from neutral versus ionized gas.

- The ALMA telescope, in northern Chile, is currently the most sensitive (sub)-mm interferometer in the world. It can reach extremely high spatial resolution, of just over over ten millionths of a degree, in the extended configurations to offer unique insight into the gas and dust from compact regions most closely associated with on-going star formation. There are many programs which have recently observed a subset of the sample in this thesis with ALMA, largely programs led by collaborators. Therefore, future work will include using both archival and proprietary data to study the spatially resolved gas and dust emission in order to better understand the distribution and concentration of star formation. Three galaxies have both VLA and ALMA data, which can be analysed together to offer robust view into the spatial distribution of radio through mm line/continuum emission. Three other galaxies in the sample also have

high-frequency observations planned, such that the APEX single dish measurement of [NII] will have complementary spatially resolved data.

- The SubMillimeter Array in Hawaii, U.S.A., offers a large frequency coverage and moderately high spatial resolution (down to $\sim$ 0.2") to further study the single-dish emission line detections presented in this thesis. There have been two approved SMA programs to measure the dust continuum emission, high-J CO lines and the [NII]205μm emission line in a total of three galaxies in the sample of this thesis. Partial observations have taken place already at 1-3" angular resolution, and the data will be reduced in the near-future. This work will be able to further study the physical size and conditions of the molecular and ionized gas in these extreme starburst galaxies at $z \sim 3$.

- The NOrthern Extended Millimeter Array (NOEMA) in Grenoble, France also offers sensitive 1 - 3 mm interferometric observations at moderately high spatial resolution (down to $\sim$ 0.3"). The strong CO and [CI] line measurements made using the IRAM 30m telescope motivated a follow-up program with NOEMA to measure two low-J CO lines and both [CI] lines to trace the diffuse and dense molecular gas in the ISM. In applying the radiative transfer models at-hand, it will be possible to estimate any spatial gradients in the gas excitation conditions on kpc scales. More than ten galaxies have recently been observed for both CO and [CI], at roughly 1" angular resolution. This angular resolution also complements that of the VLA CO(1-0) observations.

The future of ground-based near-IR and (sub)-mm astronomy is promising, as recently developed telescopes are now entering into their prime years of observing efficiency. The ALMA, SMA, and NOEMA (sub)-mm interferometric observations will therefore continue to be at the forefront of galaxy evolution studies in the coming years. Single-dish telescopes still offer a sensitive measurement of the extragalactic sky, and will likely be quite useful in the coming years to map large regions of the sky much faster than interferometers. The next-generation VLA will offer unprecedented sensitivity for future radio observations, eventually becoming the successor to the current VLA. In the future there will be another world-class radio telescope, the Square Kilometer Array. It is under construction in South Africa and Western Australia, yet, with a predicted thousands of antennae. The SKA precursor telescope in South Africa recently began observations, and when operating in the coming decade it will provide an unprecedented view of the low-frequency radio sky.

The advantage of space-based astronomy, in transcending the atmospheric limitations in ground-based observations, will further push the bounds of astrophysical research. The planned mission of the *James Webb Space Telescope* (*JWST*) will offer spectroscopic and photometric views of the near- and mid-IR Universe. Meanwhile, the optical/near-IR observations of the *HST* will continue, although the *HST* is now almost 30 years old. The planned far-IR mission of the so-called *Origins Space Telescope* will further complement the work of its predecessors, both the *Herschel Space Observatory* and *Planck* satellite telescope. Altogether, the combined efforts of ground- and space-based observations will continue to significantly advance the field of high-redshift galaxy evolution into the future.

APPENDIX A

Appendix

A.1 Tabulated properties

The following tables are the measured and derived emission line properties for the 24 lensed *Planck* selected galaxies, as presented in Chapter 4. The first table presents the redshift derived from the measured line, the velocity integrated flux density and subsequent line luminosities. The second table presents the *Turbulence* model derived velocity integrated flux densities, from the minimum-χ^2 models, for the CO rotational transitions corresponding to CO(1-0) up to CO(15-14). The subsequent, model-derived, line luminosities and line ratios are also shown.

ID	J_{up}	Line ID	Redshift	Error	$S_\nu \Delta V$	Error	L' [$\times 10^{10}$]	Error
		Line [J_{up}]			[Jy km/s]		[K km/s pc^2]	
LPsJ0116	1	CO(1-0)	2.12537	1.34E-04	4.68	1.64	1.06E+02	3.72E+01
LPsJ0116	3	CO(3-2)	2.12490	1.34E-04	51.10	10.22	1.29E+02	2.58E+01
LPsJ0116	6	CO(6-5)	2.12431	1.34E-04	55.20	16.56	3.49E+01	1.05E+01
LPsJ0116	7	CO(7-6)	2.12443	1.34E-04	33.25	9.98	1.54E+01	4.63E+00
LPsJ0116	8	CO(8-7)	2.12398	1.34E-04	30.34	10.62	1.08E+01	3.77E+00
LPsJ0116	9	CO(9-8)	2.12417	1.34E-04	19.72	6.90	5.54E+00	1.94E+00
LPsJ0116	2	[CI](2-1)	2.12443	1.34E-04	31.34	9.40	1.44E+01	4.33E+00
LPsJ0209	1	CO(1-0)	2.55301	1.61E-04	1.71	0.60	5.36E+01	1.88E+01
LPsJ0209	3	CO(3-2)	2.55280	1.61E-04	20.80	6.24	7.24E+01	2.17E+01
LPsJ0209	4	CO(4-3)	2.55300	1.61E-04	24.30	4.86	4.75E+01	9.50E+00
LPsJ0209	5	CO(5-4)	2.55352	1.61E-04	34.33	10.30	4.30E+01	1.29E+01
LPsJ0209	7	CO(7-6)	2.55341	1.61E-04	31.69	11.00	2.03E+01	7.03E+00
LPsJ0209	8	CO(8-7)	2.55241	1.61E-04	20.76	6.23	1.02E+01	3.05E+00
LPsJ0209	9	CO(9-8)	2.55217	1.61E-04	16.18	5.66	6.26E+00	2.19E+00
LPsJ0209	11	CO(11-10)	2.55160	1.61E-04	11.72	4.10	3.03E+00	1.06E+00
LPsJ0209	1	[CI](1-0)	2.55340	1.61E-04	9.62	2.89	1.65E+01	4.96E+00
LPsJ0209	2	[CI](2-1)	2.55341	1.61E-04	27.59	9.65	1.75E+01	6.13E+00
LPsJ0226	3	CO(3-2)	3.12000	1.97E-04	37.00	11.10	1.80E+02	5.41E+01
LPsJ0226	5	CO(5-4)	3.11946	1.97E-04	37.46	11.24	6.57E+01	1.97E+01
LPsJ0226	6	CO(6-5)	3.11945	1.97E-04	57.36	17.21	6.99E+01	2.10E+01
LPsJ0226	9	CO(9-8)	3.11841	1.97E-04	27.41	9.59	1.49E+01	5.20E+00
LPsJ0226	11	CO(11-10)	3.11791	1.97E-04	46.96	16.44	1.70E+01	5.96E+00
LPsJ0226	12	CO(12-11)	3.11852	1.97E-04	40.82	14.29	1.25E+01	4.36E+00
LPsJ0305	3	CO(3-2)	2.26300	1.43E-04	16.50	4.95	4.66E+01	1.40E+01
LPsJ0305	6	CO(6-5)	2.26292	1.43E-04	33.32	10.00	2.35E+01	7.06E+00
LPsJ0305	7	CO(7-6)	2.26259	1.43E-04	17.04	5.11	8.84E+00	2.65E+00
LPsJ0305	8	CO(8-7)	2.26168	1.43E-04	19.56	5.87	7.76E+00	2.33E+00
LPsJ0305	9	CO(9-8)	2.26157	1.43E-04	16.03	5.61	5.03E+00	1.76E+00
LPsJ0305	2	[CI](2-1)	2.26259	1.43E-04	8.01	2.40	4.12E+00	1.24E+00
LPsJ0748	1	CO(1-0)	2.75434	1.74E-04	2.58	0.90	9.18E+01	3.21E+01

ID	J_{up}	Line ID	Redshift	Error	$S_\nu \Delta V$	Error	L' [$\times 10^{10}$]	Error
LPsJ0748	3	CO(3-2)	2.75450	1.74E-04	17.90	5.37	7.09E+01	2.13E+01
LPsJ0748	5	CO(5-4)	2.75484	1.74E-04	22.81	6.84	3.25E+01	9.76E+00
LPsJ0748	7	CO(7-6)	2.75423	1.74E-04	15.93	4.78	1.16E+01	3.48E+00
LPsJ0748	8	CO(8-7)	2.75253	1.73E-04	4.86	2.19	2.71E+00	1.22E+00
LPsJ0748	9	CO(9-8)	2.75491	1.74E-04	11.27	5.07	4.97E+00	2.23E+00
LPsJ0748	1	[CI](1-0)	2.75559	1.74E-04	12.30	3.69	2.41E+01	7.22E+00
LPsJ0748	2	[CI](2-1)	2.75423	1.74E-04	17.53	5.26	1.27E+01	3.80E+00
LPsJ0846	1	CO(1-0)	2.66076	1.68E-04	2.16	0.75	7.25E+01	2.54E+01
LPsJ0846	3	CO(3-2)	2.66410	1.68E-04	20.90	4.18	5.35E+01	1.07E+01
LPsJ0846	4	CO(4-3)	2.66078	1.68E-04	33.77	10.13	7.09E+01	2.13E+01
LPsJ0846	5	CO(5-4)	2.66134	1.68E-04	17.51	5.25	2.35E+01	7.06E+00
LPsJ0846	7	CO(7-6)	2.66114	1.68E-04	18.63	5.59	1.28E+01	3.83E+00
LPsJ0846	8	CO(8-7)	2.66198	1.68E-04	17.16	6.00	9.02E+00	3.16E+00
LPsJ0846	1	[CI](1-0)	2.66087	1.68E-04	14.70	4.41	2.71E+01	8.13E+00
LPsJ0846	2	[CI](2-1)	2.66114	1.68E-04	15.03	4.51	1.02E+01	3.07E+00
LPsJ105322	3	CO(3-2)	3.54900	2.24E-04	21.90	6.57	1.32E+02	3.95E+01
LPsJ105322	4	CO(4-3)	3.54900	2.24E-04	29.60	8.88	1.00E+02	3.01E+01
LPsJ105322	5	CO(5-4)	3.54867	2.24E-04	34.67	10.40	7.51E+01	2.25E+01
LPsJ105322	6	CO(6-5)	3.54900	2.24E-04	41.30	12.39	6.25E+01	1.88E+01
LPsJ105322	7	CO(7-6)	3.55033	2.24E-04	24.54	8.59	2.72E+01	9.50E+00
LPsJ105322	9	CO(9-8)	3.54952	2.24E-04	18.56	8.35	1.24E+01	5.59E+00
LPsJ105322	10	CO(10-9)	3.54965	2.24E-04	3.99	1.80	2.16E+00	9.74E-01
LPsJ105322	11	CO(11-10)	3.54909	2.24E-04	7.83	3.52	3.51E+00	1.58E+00
LPsJ105322	1	[CI](1-0)	3.54900	2.24E-04	14.80	4.44	4.40E+01	1.32E+01
LPsJ105322	2	[CI](2-1)	3.55033	2.24E-04	22.90	8.01	2.52E+01	8.80E+00
LPsJ105353	1	CO(1-0)	3.00650	1.89E-04	3.99	1.40	1.65E+02	5.77E+01
LPsJ105353	3	CO(3-2)	3.00525	1.89E-04	14.10	4.23	6.46E+01	1.94E+01
LPsJ105353	4	CO(4-3)	3.00555	1.89E-04	26.90	8.07	6.99E+01	2.10E+01
LPsJ105353	5	CO(5-4)	3.00517	1.89E-04	26.35	7.90	4.35E+01	1.30E+01
LPsJ105353	6	CO(6-5)	3.00591	1.89E-04	40.45	12.13	4.64E+01	1.39E+01
LPsJ105353	7	CO(7-6)	3.00572	1.89E-04	32.18	11.26	2.71E+01	9.49E+00

ID	J_{up}	Line ID	Redshift	Error	$S_\nu\Delta V$	Error	L' [$\times 10^{10}$]	Error
LPsJ105353	8	CO(8-7)	3.00538	1.89E-04	40.51	12.15	2.61E+01	7.84E+00
LPsJ105353	9	CO(9-8)	3.00616	1.89E-04	30.11	10.54	1.54E+01	5.37E+00
LPsJ105353	10	CO(10-9)	3.00555	1.89E-04	31.60	11.06	1.31E+01	4.59E+00
LPsJ105353	11	CO(11-10)	3.00555	1.89E-04	24.80	8.68	8.50E+00	2.98E+00
LPsJ105353	1	[CI](1-0)	3.00369	1.89E-04	5.30	1.86	1.20E+01	4.20E+00
LPsJ105353	2	[CI](2-1)	3.00572	1.89E-04	8.22	2.88	6.87E+00	2.40E+00
LPsJ112713	2	CO(2-1)	1.30300	8.21E-05	14.40	4.32	3.32E+01	9.95E+00
LPsJ112713	3	CO(3-2)	1.30496	8.22E-05	18.83	5.65	1.93E+01	5.80E+00
LPsJ112713	5	CO(5-4)	1.30331	8.21E-05	22.79	7.97	8.40E+00	2.94E+00
LPsJ112713	1	[CI](1-0)	1.30332	8.21E-05	5.12	1.54	2.59E+00	7.77E-01
LPsJ112714	1	CO(1-0)	2.23571	1.41E-04	6.77	2.37	1.68E+02	5.89E+01
LPsJ112714	3	CO(3-2)	2.23546	1.41E-04	18.59	5.58	5.14E+01	1.54E+01
LPsJ112714	4	CO(4-3)	2.23621	1.41E-04	34.72	10.42	5.40E+01	1.62E+01
LPsJ112714	6	CO(6-5)	2.23630	1.41E-04	29.80	8.94	2.09E+01	6.27E+00
LPsJ112714	7	CO(7-6)	2.23683	1.41E-04	19.07	6.67	9.69E+00	3.39E+00
LPsJ112714	8	CO(8-7)	2.23745	1.41E-04	15.22	5.33	5.93E+00	2.07E+00
LPsJ112714	1	[CI](1-0)	2.23630	1.41E-04	11.10	3.33	1.51E+01	4.54E+00
LPsJ112714	2	[CI](2-1)	2.23683	1.41E-04	15.28	5.35	7.71E+00	2.70E+00
LPsJ1138	1	CO(1-0)	2.01824	1.27E-04	2.18	0.76	4.53E+01	1.59E+01
LPsJ1138	2	CO(2-1)	2.01800	1.27E-04	6.40	1.92	3.32E+01	9.96E+00
LPsJ1138	3	CO(3-2)	2.01800	1.27E-04	15.90	3.18	3.66E+01	7.33E+00
LPsJ1138	4	CO(4-3)	2.01870	1.27E-04	17.78	5.33	2.31E+01	6.92E+00
LPsJ1138	6	CO(6-5)	2.01851	1.27E-04	22.86	6.86	1.32E+01	3.95E+00
LPsJ1138	7	CO(7-6)	2.01850	1.27E-04	17.03	5.96	7.22E+00	2.53E+00
LPsJ1138	9	CO(9-8)	2.01807	1.27E-04	25.01	8.75	6.41E+00	2.24E+00
LPsJ1138	1	[CI](1-0)	2.01842	1.27E-04	4.73	1.42	5.39E+00	1.62E+00
LPsJ1138	2	[CI](2-1)	2.01850	1.27E-04	7.96	2.79	3.35E+00	1.17E+00
LPsJ1139	1	CO(1-0)	2.85832	1.80E-04	1.52	0.53	5.77E+01	2.02E+01
LPsJ1139	3	CO(3-2)	2.85800	1.80E-04	15.90	4.77	4.85E+01	1.45E+01
LPsJ1139	5	CO(5-4)	2.85920	1.80E-04	18.40	5.52	2.82E+01	8.46E+00
LPsJ1139	7	CO(7-6)	2.85920	1.80E-04	12.40	3.72	9.70E+00	2.91E+00

ID	J_{up}	Line ID	Redshift	Error	$S_\nu \Delta V$	Error	L' [$\times 10^{10}$]	Error
LPsJ1139	8	CO(8-7)	2.85905	1.80E-04	4.17	1.25	2.47E+00	7.42E-01
LPsJ1139	9	CO(9-8)	2.85538	1.80E-04	1.87	0.65	8.73E-01	3.06E-01
LPsJ1139	1	[CI](1-0)	2.85947	1.80E-04	5.43	1.63	1.13E+01	3.39E+00
LPsJ1139	2	[CI](2-1)	2.23630	1.41E-04	6.90	2.07	5.30E+00	1.59E+00
LPsJ1202	1	CO(1-0)	2.44124	1.54E-04	4.91	1.72	1.42E+02	4.98E+01
LPsJ1202	3	CO(3-2)	2.44179	1.54E-04	20.87	6.26	6.73E+01	2.02E+01
LPsJ1202	4	CO(4-3)	2.44195	1.54E-04	25.21	7.56	4.57E+01	1.37E+01
LPsJ1202	5	CO(5-4)	2.44157	1.54E-04	34.22	10.27	3.97E+01	1.19E+01
LPsJ1202	7	CO(7-6)	2.44163	1.54E-04	21.11	6.33	1.25E+01	3.75E+00
LPsJ1202	8	CO(8-7)	2.44210	1.54E-04	17.89	5.37	8.12E+00	2.43E+00
LPsJ1202	9	CO(9-8)	2.44136	1.54E-04	8.40	2.94	3.01E+00	1.05E+00
LPsJ1202	10	CO(10-9)	2.44072	1.54E-04	8.56	3.00	2.48E+00	8.69E-01
LPsJ1202	1	[CI](1-0)	2.44201	1.54E-04	9.08	2.72	1.44E+01	4.33E+00
LPsJ1202	2	[CI](2-1)	2.44163	1.54E-04	15.03	4.51	8.84E+00	2.65E+00
LPsJ1322	1	CO(1-0)	2.06680	1.30E-04	1.37	0.48	2.97E+01	1.04E+01
LPsJ1322	2	CO(2-1)	2.06760	1.30E-04	8.00	2.40	3.90E+01	1.17E+01
LPsJ1322	3	CO(3-2)	2.06760	1.30E-04	26.60	5.32	6.40E+01	1.28E+01
LPsJ1322	4	CO(4-3)	2.06751	1.30E-04	27.07	8.12	3.67E+01	1.10E+01
LPsJ1322	6	CO(6-5)	2.06754	1.30E-04	6.35	1.91	3.82E+00	1.15E+00
LPsJ1322	7	CO(7-6)	2.06766	1.30E-04	6.30	1.89	2.79E+00	8.36E-01
LPsJ1322	8	CO(8-7)	2.06783	1.30E-04	13.09	4.58	4.44E+00	1.55E+00
LPsJ1322	9	CO(9-8)	2.06845	1.30E-04	3.87	1.35	1.04E+00	3.62E-01
LPsJ1322	1	[CI](1-0)	2.06749	1.30E-04	6.94	2.08	8.25E+00	2.47E+00
LPsJ1322	2	[CI](2-1)	2.06766	1.30E-04	4.52	1.36	1.99E+00	5.96E-01
LPsJ1323	1	CO(1-0)	2.41697	1.52E-04	4.34	1.52	1.24E+02	4.33E+01
LPsJ1323	3	CO(3-2)	2.41682	1.52E-04	10.63	3.19	3.36E+01	1.01E+01
LPsJ1323	4	CO(4-3)	2.41668	1.52E-04	22.58	6.77	4.02E+01	1.21E+01
LPsJ1323	5	CO(5-4)	2.41720	1.52E-04	23.75	7.12	2.71E+01	8.12E+00
LPsJ1323	6	CO(6-5)	2.41698	1.52E-04	25.31	7.59	2.00E+01	6.01E+00
LPsJ1323	7	CO(7-6)	2.41659	1.52E-04	22.08	6.62	1.28E+01	3.85E+00
LPsJ1323	8	CO(8-7)	2.41660	1.52E-04	21.60	6.48	9.70E+00	2.91E+00

ID	J_{up}	Line ID	Redshift	Error	$S_\nu \Delta V$	Error	L' [$\times 10^{10}$]	Error
LPsJ1323	10	CO(10-9)	2.41651	1.52E-04	18.33	6.42	5.23E+00	1.83E+00
LPsJ1323	1	[CI](1-0)	2.41611	1.52E-04	9.79	2.94	1.53E+01	4.59E+00
LPsJ1323	2	[CI](2-1)	2.41659	1.52E-04	10.47	3.14	6.05E+00	1.82E+00
LPsJ1326	1	CO(1-0)	2.95041	1.86E-04	1.42	0.50	5.66E+01	1.98E+01
LPsJ1326	3	CO(3-2)	2.95100	1.86E-04	13.50	4.05	6.00E+01	1.80E+01
LPsJ1326	5	CO(5-4)	2.95106	1.86E-04	14.14	4.24	2.26E+01	6.79E+00
LPsJ1326	6	CO(6-5)	2.95040	1.86E-04	14.65	4.40	1.63E+01	4.88E+00
LPsJ1326	7	CO(7-6)	2.95101	1.86E-04	10.60	3.71	8.65E+00	3.03E+00
LPsJ1326	8	CO(8-7)	2.95033	1.86E-04	4.55	1.59	2.85E+00	9.96E-01
LPsJ1326	9	CO(9-8)	2.95017	1.86E-04	4.21	1.47	2.08E+00	7.28E-01
LPsJ1326	1	[CI](1-0)	2.95113	1.86E-04	9.00	2.70	1.98E+01	5.93E+00
LPsJ1326	2	[CI](2-1)	2.95101	1.86E-04	8.09	2.83	6.56E+00	2.30E+00
LPsJ1329	1	CO(1-0)	2.04021	1.29E-04	4.89	1.71	1.03E+02	3.62E+01
LPsJ1329	2	CO(2-1)	2.04000	1.29E-04	45.00	13.50	2.38E+02	7.14E+01
LPsJ1329	3	CO(3-2)	2.04000	1.29E-04	52.10	15.63	1.23E+02	3.68E+01
LPsJ1329	4	CO(4-3)	2.04002	1.29E-04	91.60	27.48	1.21E+02	3.63E+01
LPsJ1329	6	CO(6-5)	2.03998	1.29E-04	220.91	77.32	1.30E+02	4.54E+01
LPsJ1329	7	CO(7-6)	2.03998	1.29E-04	162.60	48.78	7.02E+01	2.11E+01
LPsJ1329	8	CO(8-7)	2.04012	1.29E-04	227.24	68.17	7.51E+01	2.25E+01
LPsJ1329	9	CO(9-8)	2.04006	1.29E-04	203.04	71.06	5.31E+01	1.86E+01
LPsJ1329	11	CO(11-10)	2.04093	1.29E-04	87.33	34.93	1.53E+01	6.12E+00
LPsJ1329	1	[CI](1-0)	2.03963	1.29E-04	21.07	6.32	2.44E+01	7.33E+00
LPsJ1329	2	[CI](2-1)	2.03998	1.29E-04	44.55	15.59	1.91E+01	6.69E+00
LPsJ1336	1	CO(1-0)	3.25313	2.05E-04	3.09	1.08	1.45E+02	5.09E+01
LPsJ1336	3	CO(3-2)	3.25400	2.05E-04	21.20	6.36	1.11E+02	3.32E+01
LPsJ1336	4	CO(4-3)	3.25400	2.05E-04	24.50	7.35	7.20E+01	2.16E+01
LPsJ1336	5	CO(5-4)	3.25465	2.05E-04	23.25	6.98	4.38E+01	1.31E+01
LPsJ1336	6	CO(6-5)	3.25490	2.05E-04	23.91	7.17	3.13E+01	9.38E+00
LPsJ1336	8	CO(8-7)	3.25642	2.05E-04	20.76	6.23	1.53E+01	4.58E+00
LPsJ1336	9	CO(9-8)	3.25597	2.05E-04	29.74	8.92	1.73E+01	5.19E+00
LPsJ1336	10	CO(10-9)	3.25539	2.05E-04	23.17	8.11	1.09E+01	3.82E+00

ID	J_{up}	Line ID	Redshift	Error	$S_\nu \Delta V$	Error	L' [$\times 10^{10}$]	Error
LPsJ1336	11	CO(11-10)	3.25612	2.05E-04	10.71	3.75	4.17E+00	1.46E+00
LPsJ1336	1	[CI](1-0)	3.25312	2.05E-04	7.51	2.63	1.94E+01	6.78E+00
LPsJ1428	1	CO(1-0)	1.32511	8.35E-05	1.29	0.45	1.23E+01	4.31E+00
LPsJ1428	2	CO(2-1)	1.32565	8.36E-05	4.23	1.27	1.01E+01	3.02E+00
LPsJ1428	3	CO(3-2)	1.32571	8.36E-05	10.51	3.15	1.11E+01	3.33E+00
LPsJ1428	5	CO(5-4)	1.32621	8.36E-05	12.85	3.86	4.90E+00	1.47E+00
LPsJ1449	1	CO(1-0)	2.15483	1.36E-04	0.99	0.35	2.32E+01	8.11E+00
LPsJ1449	3	CO(3-2)	2.15300	1.36E-04	20.90	6.27	5.40E+01	1.62E+01
LPsJ1449	4	CO(4-3)	2.15356	1.36E-04	17.50	5.25	2.91E+01	8.73E+00
LPsJ1449	6	CO(6-5)	2.15316	1.36E-04	12.01	5.50	6.41E+00	2.94E+00
LPsJ1449	7	CO(7-6)	2.15345	1.36E-04	19.20	7.68	9.13E+00	3.65E+00
LPsJ1449	9	CO(9-8)	2.15398	1.36E-04	22.50	12.50	7.21E+00	4.01E+00
LPsJ1449	1	[CI](1-0)	2.15341	1.36E-04	7.54	2.26	9.63E+00	2.89E+00
LPsJ1449	2	[CI](2-1)	2.15345	1.36E-04	6.39	1.92	3.02E+00	9.05E-01
LPsJ1544	1	CO(1-0)	2.59985	1.64E-04	2.12	0.74	6.84E+01	2.40E+01
LPsJ1544	3	CO(3-2)	2.59890	1.64E-04	11.50	3.45	4.12E+01	1.24E+01
LPsJ1544	4	CO(4-3)	2.59841	1.64E-04	15.21	4.56	3.07E+01	9.21E+00
LPsJ1544	5	CO(5-4)	2.59890	1.64E-04	10.50	3.15	1.37E+01	4.11E+00
LPsJ1544	7	CO(7-6)	2.59890	1.64E-04	4.10	1.23	2.70E+00	8.10E-01
LPsJ1544	8	CO(8-7)	2.59798	1.64E-04	7.15	2.15	3.61E+00	1.08E+00
LPsJ1544	1	[CI](1-0)	2.59890	1.64E-04	6.20	1.86	1.10E+01	3.29E+00
LPsJ1544	2	[CI](2-1)	2.59890	1.64E-04	5.80	1.74	3.81E+00	1.14E+00
LPsJ1607	1	CO(1-0)	1.48368	9.35E-05	0.96	0.34	1.13E+01	3.96E+00
LPsJ1607	2	CO(2-1)	1.48357	9.35E-05	3.87	1.16	1.14E+01	3.42E+00
LPsJ1607	3	CO(3-2)	1.48333	9.35E-05	9.80	2.94	1.28E+01	3.85E+00
LPsJ1607	5	CO(5-4)	1.48439	9.36E-05	12.06	3.62	5.70E+00	1.71E+00
LPsJ1609	1	CO(1-0)	3.25495	2.05E-04	7.10	2.48	3.34E+02	1.17E+02
LPsJ1609	3	CO(3-2)	3.25534	2.05E-04	23.77	7.13	1.24E+02	3.73E+01
LPsJ1609	4	CO(4-3)	3.25550	2.05E-04	36.90	11.07	1.09E+02	3.28E+01
LPsJ1609	5	CO(5-4)	3.25624	2.05E-04	35.39	10.62	6.67E+01	2.00E+01
LPsJ1609	6	CO(6-5)	3.25527	2.05E-04	47.12	14.14	6.16E+01	1.85E+01

ID	J_{up}	Line ID	Redshift	Error	$S_\nu\Delta V$	Error	L' [$\times 10^{10}$]	Error
LPsJ1609	8	CO(8-7)	3.25611	2.05E-04	41.16	12.35	3.03E+01	9.09E+00
LPsJ1609	9	CO(9-8)	3.25510	2.05E-04	16.03	4.81	9.32E+00	2.80E+00
LPsJ1609	10	CO(10-9)	3.25550	2.05E-04	19.60	6.86	9.30E+00	3.26E+00
LPsJ1609	11	CO(11-10)	3.25550	2.05E-04	15.46	5.41	6.02E+00	2.11E+00
LPsJ1609	1	[CI](1-0)	3.25550	2.05E-04	13.50	4.05	3.49E+01	1.05E+01
LPsJ2313	1	CO(1-0)	2.21653	1.40E-04	3.05	1.07	7.47E+01	2.61E+01
LPsJ2313	3	CO(3-2)	2.21700	1.40E-04	14.60	4.38	3.97E+01	1.19E+01
LPsJ2313	4	CO(4-3)	2.21680	1.40E-04	13.40	4.02	2.05E+01	6.15E+00
LPsJ2313	6	CO(6-5)	2.21731	1.40E-04	19.34	5.80	1.32E+01	3.95E+00
LPsJ2313	7	CO(7-6)	2.21627	1.40E-04	10.99	3.30	5.50E+00	1.65E+00
LPsJ2313	8	CO(8-7)	2.21794	1.40E-04	6.67	2.00	2.56E+00	7.67E-01
LPsJ2313	1	[CI](1-0)	2.21480	1.40E-04	14.03	4.21	1.88E+01	5.65E+00
LPsJ2313	2	[CI](2-1)	2.21627	1.40E-04	10.26	3.08	5.10E+00	1.53E+00

Table A.1: All spectral line observations were used to derive the line-integrated measurements within the integral regions indicated in §A.2.

Source ID	J_{up}	$S_\nu \Delta V$	L'_{CO}	L_{line}	R(J_{up},1)
		[km s^{-1}]	10^{10} [K km s^{-1} pc^2]	10^8 [$L_\odot$]	$L'_{CO(J_{up})}$ / $L'_{CO(1-0)}$
LPsJ0116-24	1	6.37E+00	1.45E+02	7.10E-01	1.00E+00
	2	2.18E+01	1.24E+02	4.85E+00	8.55E-01
	3	3.80E+01	9.61E+01	1.27E+01	6.64E-01
	4	4.89E+01	6.95E+01	2.18E+01	4.80E-01
	5	5.22E+01	4.75E+01	2.91E+01	3.28E-01
	6	4.84E+01	3.06E+01	3.24E+01	2.11E-01
	7	4.00E+01	1.86E+01	3.12E+01	1.28E-01
	8	2.94E+01	1.05E+01	2.62E+01	7.23E-02
	9	1.89E+01	5.32E+00	1.90E+01	3.68E-02
	10	1.03E+01	2.35E+00	1.15E+01	1.62E-02
	11	4.60E+00	8.66E-01	5.64E+00	5.98E-03
	12	1.50E+00	2.37E-01	2.00E+00	1.64E-03
	13	3.09E-01	4.16E-02	4.47E-01	2.87E-04
	14	4.87E-02	5.66E-03	7.58E-02	3.91E-05
	15	6.08E-03	6.16E-04	1.02E-02	4.26E-06
LPsJ0209+00	1	2.00E+00	6.25E+01	3.06E-01	1.00E+00
	2	7.49E+00	5.86E+01	2.30E+00	9.38E-01
	3	1.52E+01	5.27E+01	6.98E+00	8.43E-01
	4	2.32E+01	4.54E+01	1.42E+01	7.27E-01
	5	2.99E+01	3.74E+01	2.29E+01	5.99E-01
	6	3.34E+01	2.91E+01	3.08E+01	4.65E-01
	7	3.29E+01	2.10E+01	3.53E+01	3.37E-01
	8	2.82E+01	1.38E+01	3.46E+01	2.21E-01
	9	2.02E+01	7.83E+00	2.79E+01	1.25E-01
	10	1.12E+01	3.52E+00	1.72E+01	5.63E-02
	11	4.00E+00	1.04E+00	6.75E+00	1.66E-02
	12	7.33E-01	1.60E-01	1.35E+00	2.56E-03
	13	8.19E-02	1.52E-02	1.63E-01	2.43E-04
	14	7.67E-03	1.23E-03	1.65E-02	1.97E-05
	15	5.72E-04	7.99E-05	1.32E-03	1.28E-06
LPsJ0226+23	1	5.14E+00	2.25E+02	1.10E+00	1.00E+00
	2	1.95E+01	2.14E+02	8.38E+00	9.49E-01
	3	3.50E+01	1.71E+02	2.26E+01	7.58E-01
	4	4.53E+01	1.24E+02	3.90E+01	5.52E-01
	5	4.91E+01	8.63E+01	5.28E+01	3.83E-01
	6	4.85E+01	5.91E+01	6.25E+01	2.62E-01
	7	4.64E+01	4.16E+01	6.99E+01	1.85E-01
	8	4.54E+01	3.11E+01	7.80E+01	1.38E-01
	9	4.57E+01	2.48E+01	8.83E+01	1.10E-01
	10	4.62E+01	2.03E+01	9.93E+01	9.01E-02
	11	4.57E+01	1.66E+01	1.08E+02	7.37E-02
	12	4.30E+01	1.31E+01	1.11E+02	5.82E-02

Table A.2 continued from previous page

Source ID	J_{up}	$S_\nu \Delta V$	L'_{CO}	L_{line}	R(J_{up},1)
	13	3.82E+01	9.93E+00	1.07E+02	4.41E-02
	14	3.16E+01	7.08E+00	9.49E+01	3.14E-02
	15	2.46E+01	4.81E+00	7.92E+01	2.13E-02
LPsJ0305-30	1	2.71E+00	6.87E+01	3.37E-01	1.00E+00
	2	9.42E+00	5.98E+01	2.34E+00	8.70E-01
	3	1.67E+01	4.72E+01	6.25E+00	6.87E-01
	4	2.21E+01	3.50E+01	1.10E+01	5.09E-01
	5	2.45E+01	2.49E+01	1.52E+01	3.62E-01
	6	2.41E+01	1.70E+01	1.80E+01	2.48E-01
	7	2.17E+01	1.13E+01	1.89E+01	1.64E-01
	8	1.81E+01	7.20E+00	1.81E+01	1.05E-01
	9	1.41E+01	4.43E+00	1.58E+01	6.44E-02
	10	1.02E+01	2.60E+00	1.27E+01	3.78E-02
	11	6.92E+00	1.45E+00	9.46E+00	2.12E-02
	12	4.34E+00	7.66E-01	6.47E+00	1.12E-02
	13	2.45E+00	3.69E-01	3.96E+00	5.36E-03
	14	1.24E+00	1.61E-01	2.15E+00	2.34E-03
	15	5.08E-01	5.75E-02	9.48E-01	8.37E-04
LPsJ0748+59	1	2.94E+00	1.04E+02	5.12E-01	1.00E+00
	2	9.84E+00	8.75E+01	3.43E+00	8.37E-01
	3	1.66E+01	6.56E+01	8.68E+00	6.28E-01
	4	2.03E+01	4.50E+01	1.41E+01	4.31E-01
	5	2.01E+01	2.86E+01	1.75E+01	2.74E-01
	6	1.68E+01	1.66E+01	1.76E+01	1.59E-01
	7	1.21E+01	8.81E+00	1.48E+01	8.43E-02
	8	7.39E+00	4.11E+00	1.03E+01	3.93E-02
	9	3.60E+00	1.58E+00	5.65E+00	1.52E-02
	10	1.29E+00	4.58E-01	2.24E+00	4.39E-03
	11	2.97E-01	8.75E-02	5.70E-01	8.38E-04
	12	4.36E-02	1.08E-02	9.10E-02	1.03E-04
	13	4.42E-03	9.32E-04	1.00E-02	8.92E-06
	14	3.99E-04	7.25E-05	9.71E-04	6.94E-07
	15	2.91E-05	4.60E-06	7.58E-05	4.41E-08
LPsJ0846+15	1	3.08E+00	1.03E+02	5.07E-01	1.00E+00
	2	1.03E+01	8.70E+01	3.41E+00	8.41E-01
	3	1.75E+01	6.54E+01	8.66E+00	6.33E-01
	4	2.17E+01	4.56E+01	1.43E+01	4.41E-01
	5	2.26E+01	3.03E+01	1.86E+01	2.93E-01
	6	2.08E+01	1.94E+01	2.06E+01	1.88E-01
	7	1.76E+01	1.21E+01	2.03E+01	1.17E-01
	8	1.39E+01	7.33E+00	1.84E+01	7.09E-02
	9	1.03E+01	4.30E+00	1.53E+01	4.15E-02
	10	7.17E+00	2.41E+00	1.18E+01	2.33E-02

Table A.2 continued from previous page

Source ID	J_{up}	$S_\nu \Delta V$	L'_{CO}	L_{line}	R(J_{up},1)
	11	4.67E+00	1.30E+00	8.46E+00	1.26E-02
	12	2.82E+00	6.59E-01	5.57E+00	6.37E-03
	13	1.53E+00	3.05E-01	3.28E+00	2.95E-03
	14	7.48E-01	1.29E-01	1.72E+00	1.24E-03
	15	3.06E-01	4.58E-02	7.55E-01	4.43E-04
LPsJ1053+60	1	2.95E+00	1.60E+02	7.83E-01	1.00E+00
	2	1.07E+01	1.44E+02	5.66E+00	9.04E-01
	3	2.03E+01	1.22E+02	1.62E+01	7.66E-01
	4	2.89E+01	9.79E+01	3.07E+01	6.13E-01
	5	3.40E+01	7.36E+01	4.51E+01	4.61E-01
	6	3.41E+01	5.13E+01	5.43E+01	3.21E-01
	7	2.95E+01	3.27E+01	5.48E+01	2.04E-01
	8	2.17E+01	1.84E+01	4.61E+01	1.15E-01
	9	1.31E+01	8.74E+00	3.12E+01	5.47E-02
	10	6.09E+00	3.30E+00	1.61E+01	2.07E-02
	11	1.94E+00	8.71E-01	5.67E+00	5.46E-03
	12	3.76E-01	1.42E-01	1.20E+00	8.86E-04
	13	4.83E-02	1.55E-02	1.66E-01	9.71E-05
	14	5.31E-03	1.47E-03	1.97E-02	9.21E-06
	15	4.59E-04	1.11E-04	1.82E-03	6.94E-07
LPsJ1053+05	1	1.93E+00	7.98E+01	3.91E-01	1.00E+00
	2	7.36E+00	7.59E+01	2.98E+00	9.52E-01
	3	1.50E+01	6.86E+01	9.08E+00	8.60E-01
	4	2.32E+01	5.98E+01	1.88E+01	7.50E-01
	5	3.06E+01	5.04E+01	3.09E+01	6.32E-01
	6	3.58E+01	4.11E+01	4.34E+01	5.15E-01
	7	3.84E+01	3.23E+01	5.43E+01	4.05E-01
	8	3.79E+01	2.45E+01	6.13E+01	3.07E-01
	9	3.47E+01	1.77E+01	6.30E+01	2.21E-01
	10	2.92E+01	1.20E+01	5.89E+01	1.51E-01
	11	2.26E+01	7.70E+00	5.01E+01	9.66E-02
	12	1.57E+01	4.50E+00	3.80E+01	5.64E-02
	13	9.40E+00	2.30E+00	2.47E+01	2.88E-02
	14	4.75E+00	1.00E+00	1.34E+01	1.26E-02
	15	1.80E+00	3.31E-01	5.46E+00	4.15E-03
LPsJ1127+42	1	3.98E+00	3.67E+01	1.80E-01	1.00E+00
	2	1.30E+01	3.00E+01	1.18E+00	8.18E-01
	3	2.10E+01	2.15E+01	2.85E+00	5.87E-01
	4	2.41E+01	1.39E+01	4.35E+00	3.78E-01
	5	2.17E+01	7.99E+00	4.89E+00	2.18E-01
	6	1.54E+01	3.94E+00	4.17E+00	1.07E-01
	7	8.28E+00	1.56E+00	2.62E+00	4.25E-02
	8	3.01E+00	4.34E-01	1.09E+00	1.18E-02

Table A.2 continued from previous page

Source ID	J_{up}	$S_\nu \Delta V$	L'_{CO}	L_{line}	R(J_{up},1)
	9	5.53E-01	6.30E-02	2.25E-01	1.72E-03
	10	5.19E-02	4.79E-03	2.34E-02	1.31E-04
	11	3.31E-03	2.52E-04	1.64E-03	6.88E-06
	12	1.58E-04	1.01E-05	8.55E-05	2.76E-07
	13	5.26E-06	2.87E-07	3.08E-06	7.83E-09
	14	1.61E-07	7.60E-09	1.02E-07	2.07E-10
	15	3.73E-09	1.53E-10	2.52E-09	4.18E-12
LPsJ1127+46	1	4.06E+00	1.01E+02	4.95E-01	1.00E+00
	2	1.35E+01	8.41E+01	3.30E+00	8.33E-01
	3	2.23E+01	6.17E+01	8.16E+00	6.11E-01
	4	2.68E+01	4.17E+01	1.31E+01	4.13E-01
	5	2.71E+01	2.70E+01	1.65E+01	2.67E-01
	6	2.46E+01	1.70E+01	1.80E+01	1.68E-01
	7	2.08E+01	1.05E+01	1.77E+01	1.04E-01
	8	1.66E+01	6.46E+00	1.62E+01	6.40E-02
	9	1.27E+01	3.90E+00	1.39E+01	3.87E-02
	10	9.34E+00	2.33E+00	1.14E+01	2.31E-02
	11	6.64E+00	1.37E+00	8.90E+00	1.35E-02
	12	4.54E+00	7.87E-01	6.64E+00	7.79E-03
	13	2.98E+00	4.39E-01	4.71E+00	4.35E-03
	14	1.85E+00	2.36E-01	3.16E+00	2.34E-03
	15	1.08E+00	1.20E-01	1.98E+00	1.19E-03
LPsJ1138+32	1	1.91E+00	3.96E+01	1.94E-01	1.00E+00
	2	7.29E+00	3.78E+01	1.48E+00	9.55E-01
	3	1.34E+01	3.09E+01	4.09E+00	7.80E-01
	4	1.80E+01	2.34E+01	7.33E+00	5.90E-01
	5	2.05E+01	1.70E+01	1.04E+01	4.31E-01
	6	2.13E+01	1.23E+01	1.30E+01	3.10E-01
	7	2.11E+01	8.95E+00	1.50E+01	2.26E-01
	8	2.10E+01	6.82E+00	1.71E+01	1.72E-01
	9	2.14E+01	5.49E+00	1.96E+01	1.39E-01
	10	2.21E+01	4.60E+00	2.25E+01	1.16E-01
	11	2.27E+01	3.90E+00	2.54E+01	9.86E-02
	12	2.25E+01	3.25E+00	2.74E+01	8.20E-02
	13	2.12E+01	2.61E+00	2.81E+01	6.60E-02
	14	1.87E+01	1.98E+00	2.66E+01	5.00E-02
	15	1.55E+01	1.43E+00	2.35E+01	3.61E-02
LPsJ1139+20	1	2.14E+00	8.13E+01	3.99E-01	1.00E+00
	2	7.35E+00	6.97E+01	2.73E+00	8.57E-01
	3	1.28E+01	5.40E+01	7.15E+00	6.64E-01
	4	1.62E+01	3.83E+01	1.20E+01	4.71E-01
	5	1.64E+01	2.49E+01	1.52E+01	3.06E-01
	6	1.37E+01	1.44E+01	1.52E+01	1.77E-01

Table A.2 continued from previous page

Source ID	J_{up}	$S_\nu \Delta V$	L'_{CO}	L_{line}	R(J_{up},1)
	7	9.31E+00	7.21E+00	1.21E+01	8.86E-02
	8	4.92E+00	2.92E+00	7.31E+00	3.59E-02
	9	1.77E+00	8.31E-01	2.96E+00	1.02E-02
	10	3.56E-01	1.35E-01	6.61E-01	1.66E-03
	11	4.30E-02	1.35E-02	8.78E-02	1.66E-04
	12	3.73E-03	9.83E-04	8.30E-03	1.21E-05
	13	2.32E-04	5.21E-05	5.60E-04	6.41E-07
	14	1.33E-05	2.57E-06	3.45E-05	3.16E-08
	15	5.94E-07	1.00E-07	1.65E-06	1.23E-09
LPsJ1202+53	1	4.61E+00	1.34E+02	6.55E-01	1.00E+00
	2	1.51E+01	1.10E+02	4.29E+00	8.19E-01
	3	2.46E+01	7.94E+01	1.05E+01	5.94E-01
	4	2.92E+01	5.30E+01	1.66E+01	3.96E-01
	5	2.89E+01	3.35E+01	2.05E+01	2.51E-01
	6	2.53E+01	2.04E+01	2.16E+01	1.52E-01
	7	2.03E+01	1.20E+01	2.02E+01	8.98E-02
	8	1.51E+01	6.85E+00	1.72E+01	5.12E-02
	9	1.04E+01	3.74E+00	1.33E+01	2.79E-02
	10	6.64E+00	1.93E+00	9.43E+00	1.44E-02
	11	3.89E+00	9.33E-01	6.07E+00	6.98E-03
	12	2.04E+00	4.12E-01	3.48E+00	3.08E-03
	13	9.12E-01	1.57E-01	1.68E+00	1.17E-03
	14	3.41E-01	5.06E-02	6.78E-01	3.78E-04
	15	9.65E-02	1.25E-02	2.05E-01	9.32E-05
LPsJ1322+09	1	1.87E+00	4.04E+01	1.98E-01	1.00E+00
	2	6.27E+00	3.39E+01	1.33E+00	8.40E-01
	3	1.04E+01	2.50E+01	3.30E+00	6.18E-01
	4	1.25E+01	1.69E+01	5.31E+00	4.19E-01
	5	1.26E+01	1.10E+01	6.71E+00	2.71E-01
	6	1.14E+01	6.88E+00	7.28E+00	1.70E-01
	7	9.57E+00	4.23E+00	7.11E+00	1.05E-01
	8	7.57E+00	2.56E+00	6.42E+00	6.34E-02
	9	5.70E+00	1.52E+00	5.44E+00	3.77E-02
	10	4.11E+00	8.92E-01	4.36E+00	2.21E-02
	11	2.86E+00	5.13E-01	3.34E+00	1.27E-02
	12	1.91E+00	2.88E-01	2.43E+00	7.12E-03
	13	1.22E+00	1.57E-01	1.68E+00	3.87E-03
	14	7.41E-01	8.20E-02	1.10E+00	2.03E-03
	15	4.21E-01	4.06E-02	6.69E-01	1.00E-03
LPsJ1323+55	1	3.19E+00	9.09E+01	4.46E-01	1.00E+00
	2	1.11E+01	7.88E+01	3.09E+00	8.66E-01
	3	1.91E+01	6.06E+01	8.02E+00	6.66E-01
	4	2.44E+01	4.34E+01	1.36E+01	4.78E-01

Table A.2 continued from previous page

Source ID	J_{up}	$S_\nu \Delta V$	L'_{CO}	L_{line}	R(J_{up},1)
	5	2.63E+01	3.00E+01	1.84E+01	3.30E-01
	6	2.56E+01	2.03E+01	2.15E+01	2.23E-01
	7	2.33E+01	1.35E+01	2.27E+01	1.49E-01
	8	2.01E+01	8.94E+00	2.24E+01	9.83E-02
	9	1.66E+01	5.84E+00	2.08E+01	6.42E-02
	10	1.32E+01	3.78E+00	1.85E+01	4.15E-02
	11	1.02E+01	2.41E+00	1.57E+01	2.65E-02
	12	7.67E+00	1.52E+00	1.28E+01	1.67E-02
	13	5.52E+00	9.33E-01	1.00E+01	1.03E-02
	14	3.81E+00	5.55E-01	7.44E+00	6.11E-03
	15	2.49E+00	3.16E-01	5.20E+00	3.47E-03
LPsJ1326+33	1	2.10E+00	8.42E+01	4.13E-01	1.00E+00
	2	6.88E+00	6.88E+01	2.70E+00	8.17E-01
	3	1.12E+01	4.98E+01	6.59E+00	5.92E-01
	4	1.31E+01	3.28E+01	1.03E+01	3.90E-01
	5	1.27E+01	2.03E+01	1.24E+01	2.41E-01
	6	1.07E+01	1.19E+01	1.26E+01	1.42E-01
	7	8.28E+00	6.76E+00	1.14E+01	8.03E-02
	8	5.92E+00	3.70E+00	9.28E+00	4.40E-02
	9	3.93E+00	1.94E+00	6.93E+00	2.31E-02
	10	2.41E+00	9.65E-01	4.72E+00	1.15E-02
	11	1.36E+00	4.52E-01	2.94E+00	5.37E-03
	12	6.97E-01	1.94E-01	1.64E+00	2.30E-03
	13	3.08E-01	7.31E-02	7.85E-01	8.68E-04
	14	1.19E-01	2.43E-02	3.25E-01	2.88E-04
	15	3.69E-02	6.58E-03	1.08E-01	7.82E-05
LPsJ1329+22	1	6.31E+00	1.33E+02	6.54E-01	1.00E+00
	2	2.86E+01	1.51E+02	5.92E+00	1.13E+00
	3	5.97E+01	1.40E+02	1.85E+01	1.05E+00
	4	9.30E+01	1.23E+02	3.85E+01	9.21E-01
	5	1.23E+02	1.04E+02	6.39E+01	7.83E-01
	6	1.47E+02	8.62E+01	9.12E+01	6.46E-01
	7	1.60E+02	6.92E+01	1.16E+02	5.19E-01
	8	1.63E+02	5.40E+01	1.35E+02	4.05E-01
	9	1.56E+02	4.08E+01	1.46E+02	3.06E-01
	10	1.40E+02	2.96E+01	1.45E+02	2.22E-01
	11	1.18E+02	2.06E+01	1.34E+02	1.55E-01
	12	9.20E+01	1.35E+01	1.14E+02	1.01E-01
	13	6.48E+01	8.13E+00	8.72E+01	6.09E-02
	14	4.02E+01	4.35E+00	5.82E+01	3.26E-02
	15	2.01E+01	1.90E+00	3.12E+01	1.42E-02
LPsJ1336+49	1	2.83E+00	1.33E+02	6.53E-01	1.00E+00
	2	1.01E+01	1.19E+02	4.66E+00	8.92E-01

Table A.2 continued from previous page

Source ID	J_{up}	$S_\nu \Delta V$	L'_{CO}	L_{line}	R(J_{up},1)
	3	1.82E+01	9.50E+01	1.26E+01	7.12E-01
	4	2.41E+01	7.09E+01	2.22E+01	5.31E-01
	5	2.70E+01	5.08E+01	3.11E+01	3.81E-01
	6	2.71E+01	3.55E+01	3.75E+01	2.66E-01
	7	2.54E+01	2.44E+01	4.10E+01	1.83E-01
	8	2.26E+01	1.66E+01	4.17E+01	1.25E-01
	9	1.92E+01	1.12E+01	3.99E+01	8.39E-02
	10	1.58E+01	7.45E+00	3.64E+01	5.59E-02
	11	1.26E+01	4.91E+00	3.20E+01	3.68E-02
	12	9.75E+00	3.19E+00	2.70E+01	2.39E-02
	13	7.29E+00	2.03E+00	2.18E+01	1.52E-02
	14	5.22E+00	1.26E+00	1.68E+01	9.42E-03
	15	3.56E+00	7.45E-01	1.23E+01	5.59E-03
LPsJ1428+35	1	1.29E+00	1.23E+01	6.02E-02	1.00E+00
	2	4.62E+00	1.10E+01	4.31E-01	8.95E-01
	3	8.64E+00	9.13E+00	1.21E+00	7.43E-01
	4	1.19E+01	7.08E+00	2.22E+00	5.76E-01
	5	1.34E+01	5.09E+00	3.12E+00	4.14E-01
	6	1.25E+01	3.31E+00	3.50E+00	2.69E-01
	7	9.69E+00	1.88E+00	3.16E+00	1.53E-01
	8	5.86E+00	8.72E-01	2.18E+00	7.09E-02
	9	2.36E+00	2.78E-01	9.90E-01	2.26E-02
	10	4.50E-01	4.29E-02	2.10E-01	3.49E-03
	11	4.65E-02	3.66E-03	2.38E-02	2.98E-04
	12	3.51E-03	2.32E-04	1.96E-03	1.89E-05
	13	1.99E-04	1.12E-05	1.21E-04	9.15E-07
	14	1.04E-05	5.09E-07	6.82E-06	4.14E-08
	15	4.58E-07	1.94E-08	3.20E-07	1.58E-09
LPsJ1449+22	1	1.43E+00	3.34E+01	1.64E-01	1.00E+00
	2	5.17E+00	3.01E+01	1.18E+00	9.01E-01
	3	9.80E+00	2.54E+01	3.36E+00	7.60E-01
	4	1.39E+01	2.02E+01	6.33E+00	6.05E-01
	5	1.63E+01	1.51E+01	9.28E+00	4.54E-01
	6	1.64E+01	1.06E+01	1.12E+01	3.18E-01
	7	1.45E+01	6.88E+00	1.16E+01	2.06E-01
	8	1.11E+01	4.03E+00	1.01E+01	1.21E-01
	9	7.04E+00	2.03E+00	7.23E+00	6.07E-02
	10	3.49E+00	8.14E-01	3.98E+00	2.44E-02
	11	1.21E+00	2.33E-01	1.52E+00	6.99E-03
	12	2.45E-01	3.97E-02	3.35E-01	1.19E-03
	13	3.07E-02	4.23E-03	4.54E-02	1.27E-04
	14	3.22E-03	3.84E-04	5.14E-03	1.15E-05
	15	2.72E-04	2.82E-05	4.65E-04	8.46E-07

Table A.2 continued from previous page

Source ID	J_{up}	$S_\nu \Delta V$	L'_{CO}	L_{line}	R(J_{up},1)
LPsJ1544+50	1	3.11E+00	1.00E+02	4.92E-01	1.00E+00
	2	9.44E+00	7.62E+01	2.99E+00	7.59E-01
	3	1.36E+01	4.88E+01	6.46E+00	4.87E-01
	4	1.36E+01	2.75E+01	8.63E+00	2.74E-01
	5	1.09E+01	1.41E+01	8.61E+00	1.40E-01
	6	7.30E+00	6.55E+00	6.93E+00	6.53E-02
	7	4.22E+00	2.78E+00	4.67E+00	2.77E-02
	8	2.07E+00	1.05E+00	2.62E+00	1.04E-02
	9	8.27E-01	3.30E-01	1.18E+00	3.29E-03
	10	2.51E-01	8.11E-02	3.97E-01	8.08E-04
	11	5.35E-02	1.43E-02	9.31E-02	1.43E-04
	12	7.70E-03	1.73E-03	1.46E-02	1.72E-05
	13	7.76E-04	1.48E-04	1.59E-03	1.48E-06
	14	6.89E-05	1.14E-05	1.52E-04	1.13E-07
	15	4.91E-06	7.07E-07	1.16E-05	7.05E-09
LPsJ1607+73	1	1.05E+00	1.24E+01	6.09E-02	1.00E+00
	2	3.87E+00	1.14E+01	4.47E-01	9.19E-01
	3	7.53E+00	9.86E+00	1.30E+00	7.94E-01
	4	1.10E+01	8.08E+00	2.53E+00	6.51E-01
	5	1.33E+01	6.26E+00	3.83E+00	5.04E-01
	6	1.38E+01	4.52E+00	4.78E+00	3.64E-01
	7	1.25E+01	3.01E+00	5.05E+00	2.42E-01
	8	9.70E+00	1.79E+00	4.48E+00	1.44E-01
	9	6.18E+00	9.01E-01	3.21E+00	7.26E-02
	10	2.95E+00	3.48E-01	1.70E+00	2.80E-02
	11	8.75E-01	8.54E-02	5.56E-01	6.88E-03
	12	1.49E-01	1.22E-02	1.03E-01	9.84E-04
	13	1.70E-02	1.19E-03	1.27E-02	9.56E-05
	14	1.66E-03	1.00E-04	1.34E-03	8.07E-06
	15	1.31E-04	6.89E-06	1.13E-04	5.55E-07
LPsJ1609+45	1	4.60E+00	2.16E+02	1.06E+00	1.00E+00
	2	1.60E+01	1.88E+02	7.38E+00	8.69E-01
	3	2.81E+01	1.47E+02	1.94E+01	6.79E-01
	4	3.63E+01	1.07E+02	3.35E+01	4.93E-01
	5	3.94E+01	7.42E+01	4.55E+01	3.43E-01
	6	3.84E+01	5.02E+01	5.32E+01	2.32E-01
	7	3.48E+01	3.35E+01	5.62E+01	1.55E-01
	8	2.99E+01	2.20E+01	5.52E+01	1.02E-01
	9	2.47E+01	1.43E+01	5.12E+01	6.63E-02
	10	1.96E+01	9.23E+00	4.52E+01	4.26E-02
	11	1.51E+01	5.88E+00	3.83E+01	2.72E-02
	12	1.12E+01	3.68E+00	3.11E+01	1.70E-02
	13	8.07E+00	2.25E+00	2.42E+01	1.04E-02

Table A.2 continued from previous page

Source ID	J_{up}	$S_\nu \Delta V$	L'_{CO}	L_{line}	R(J_{up},1)
	14	5.55E+00	1.34E+00	1.79E+01	6.17E-03
	15	3.61E+00	7.57E-01	1.25E+01	3.50E-03
	1	3.00E+00	7.33E+01	3.59E-01	1.00E+00
LPsJ2313+01	2	9.55E+00	5.84E+01	2.29E+00	7.96E-01
	3	1.50E+01	4.06E+01	5.38E+00	5.55E-01
	4	1.69E+01	2.58E+01	8.10E+00	3.52E-01
	5	1.59E+01	1.56E+01	9.53E+00	2.12E-01
	6	1.33E+01	9.04E+00	9.56E+00	1.23E-01
	7	1.02E+01	5.10E+00	8.57E+00	6.97E-02
	8	7.33E+00	2.80E+00	7.02E+00	3.82E-02
	9	4.90E+00	1.48E+00	5.27E+00	2.02E-02
	10	3.03E+00	7.41E-01	3.62E+00	1.01E-02
	11	1.73E+00	3.50E-01	2.28E+00	4.78E-03
	12	8.93E-01	1.52E-01	1.28E+00	2.07E-03
	13	3.99E-01	5.77E-02	6.20E-01	7.88E-04
	14	1.53E-01	1.91E-02	2.56E-01	2.61E-04
	15	4.65E-02	5.06E-03	8.34E-02	6.91E-05

Table A.2: Best-fit CO excitation ladders,as determined from the best model solution in the top 1% of the best χ^2 solutions. The model error for each value is of order 5% based on the dispersion of best-fit values within the top solutions.

A.2 Spectra and Best-fit models

The following figures are the combined set of observations and model-fits for the observed and modelled spectral lines.

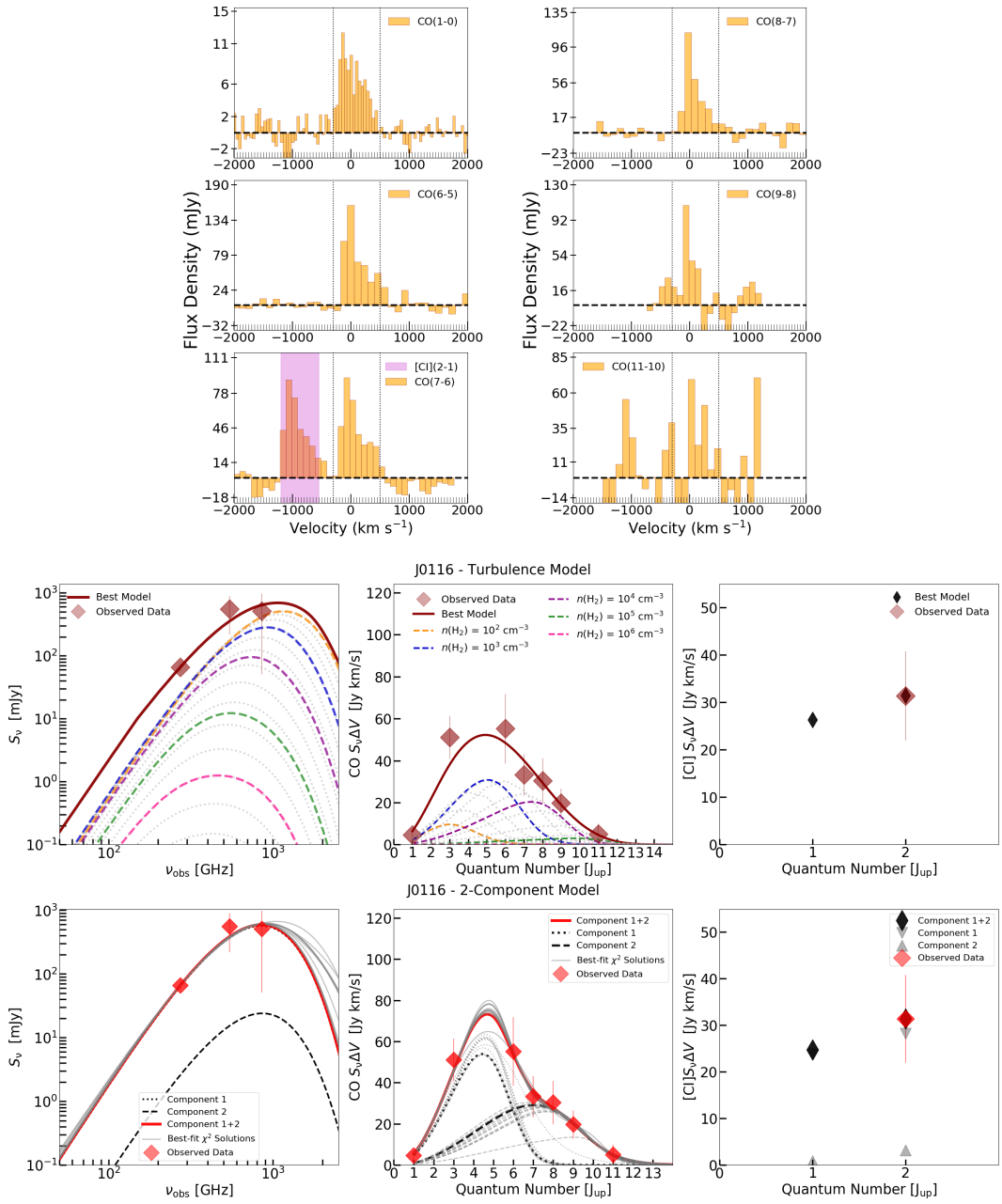

Figure A.1: LPsJ0116. **Top:** Apparent flux density versus velocity for the CO and [CI] line detections. We also model the CO(3-2) line measurement presented in Berman et al. (in prep). **Middle:** Best-fit, minimum-χ^2 model solution for the *Turbulence* model for the dust SED, CO and [CI] velocity-integrated line fluxes. For clarity, different dashed-colored curves denote the representative contributions to the density PDF for the molecular gas densities of $\log(n(H_2))$ = 2 (yellow), 3 (blue), 4 (purple), 5 (green) and 6 (pink) cm^{-3}. The gray-dashed lines represent the remaining LVG calculations (from the 50 total samples) which sample the gas density PDF. For the *Turbulence* model, these individual density contributions have a y-axis scaled by a factor 5 for both the dust and line SED to facilitate interpretation of the dominant gas density. All observed data are shown as red diamonds. The best-fit [CI] line fluxes are plotted over the observed data. Solid red lines denote the total best-fit, minimum-χ^2 model. **Bottom:** *2-component* model: lower excitation component (black dotted) and higher-excitation component (black dashed). The best-fit [CI] line flux from the lower-excitation component and higher-excitation component are a downward-facing or upward-facing gray triangle, respectively.

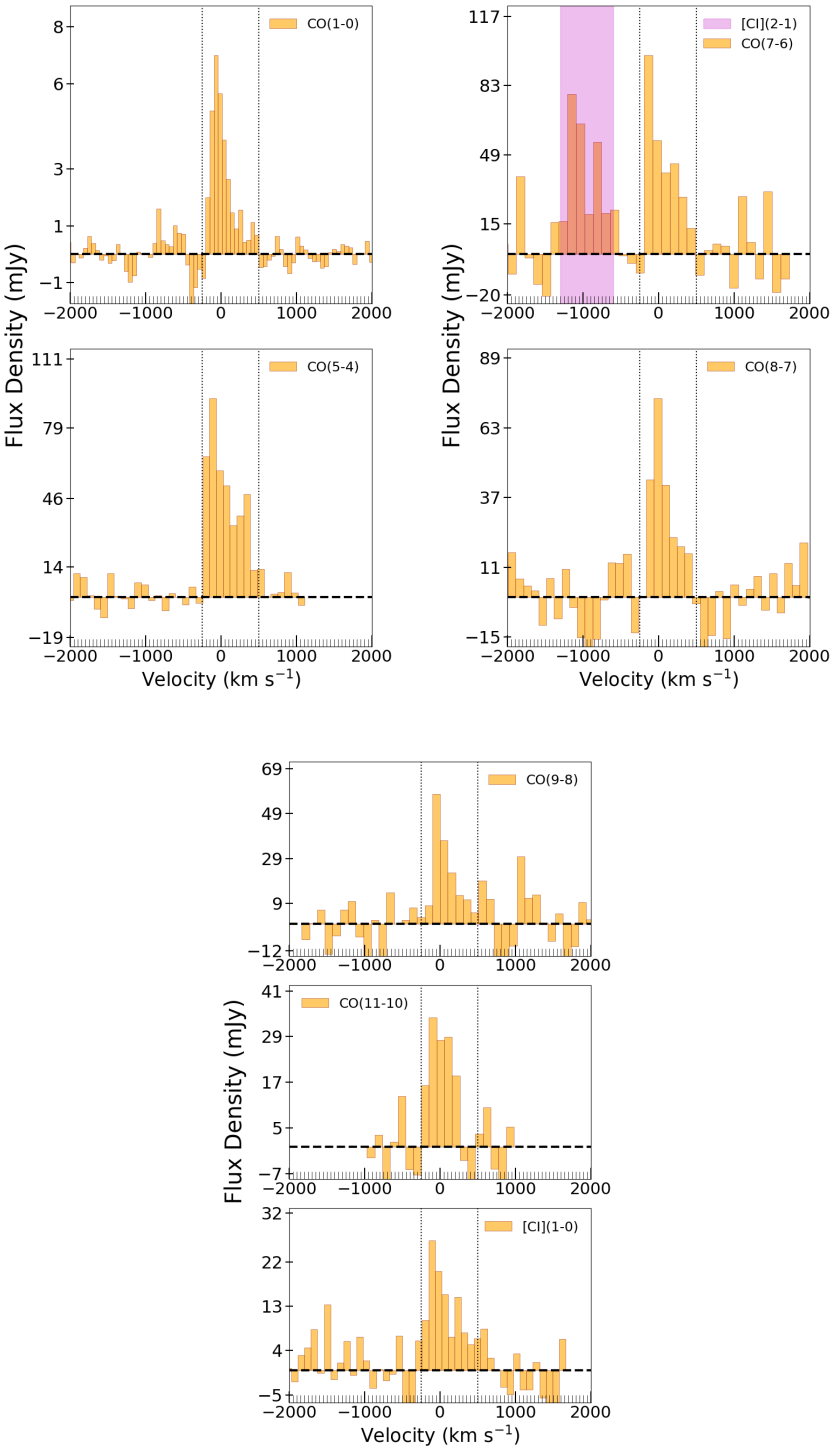

Figure A.2: LPsJ0209. These CO(1-0), CO(5-4) and CO(8-7) line spectra are also presented in Harrington et al. (2019). The CO(3-2) line measurement is also presented in Harrington et al. (2016), yet here we use the updated calibration of the original LMT spectra, consistent with that reported in Rivera et al. (2019). We also model the CO(4-3) line emission reported in Geach et al. (2018).

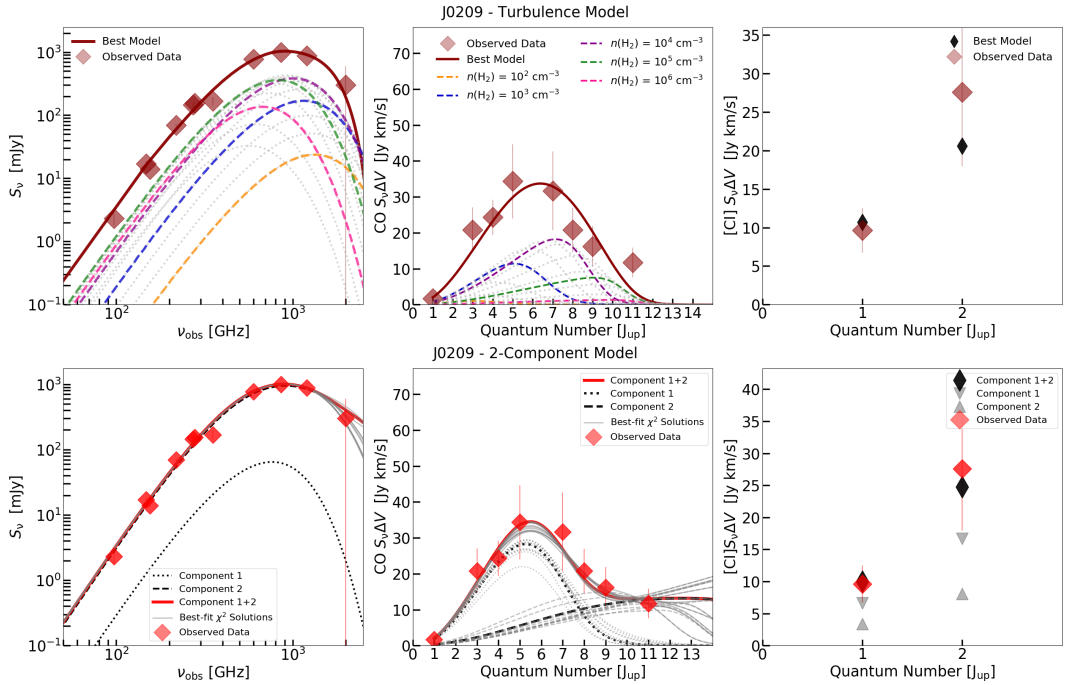

Figure A.3: LPsJ0209 continued.

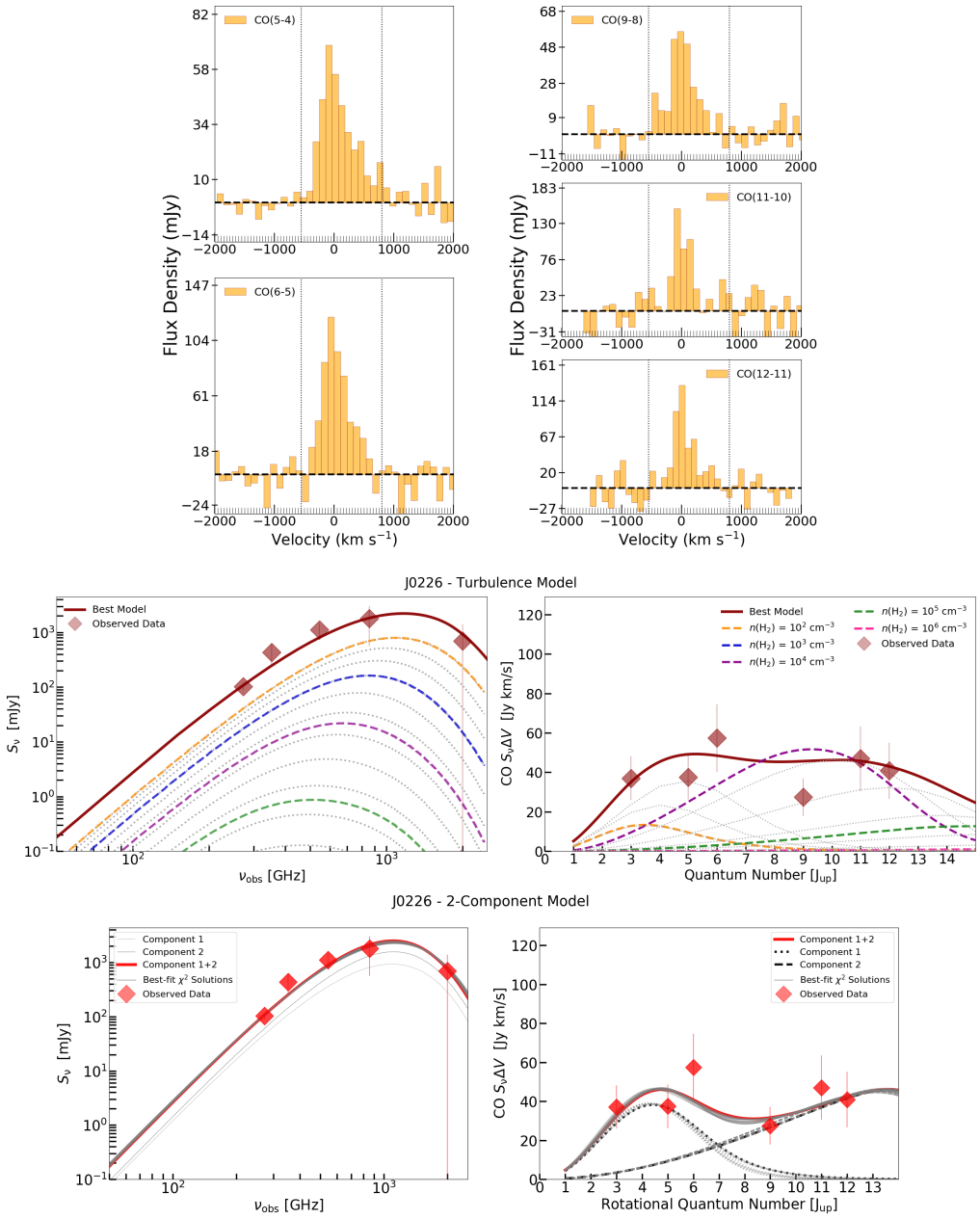

Figure A.4: LPsJ0226. We also model the CO(3-2) line measurement presented in Berman et al. (in prep).

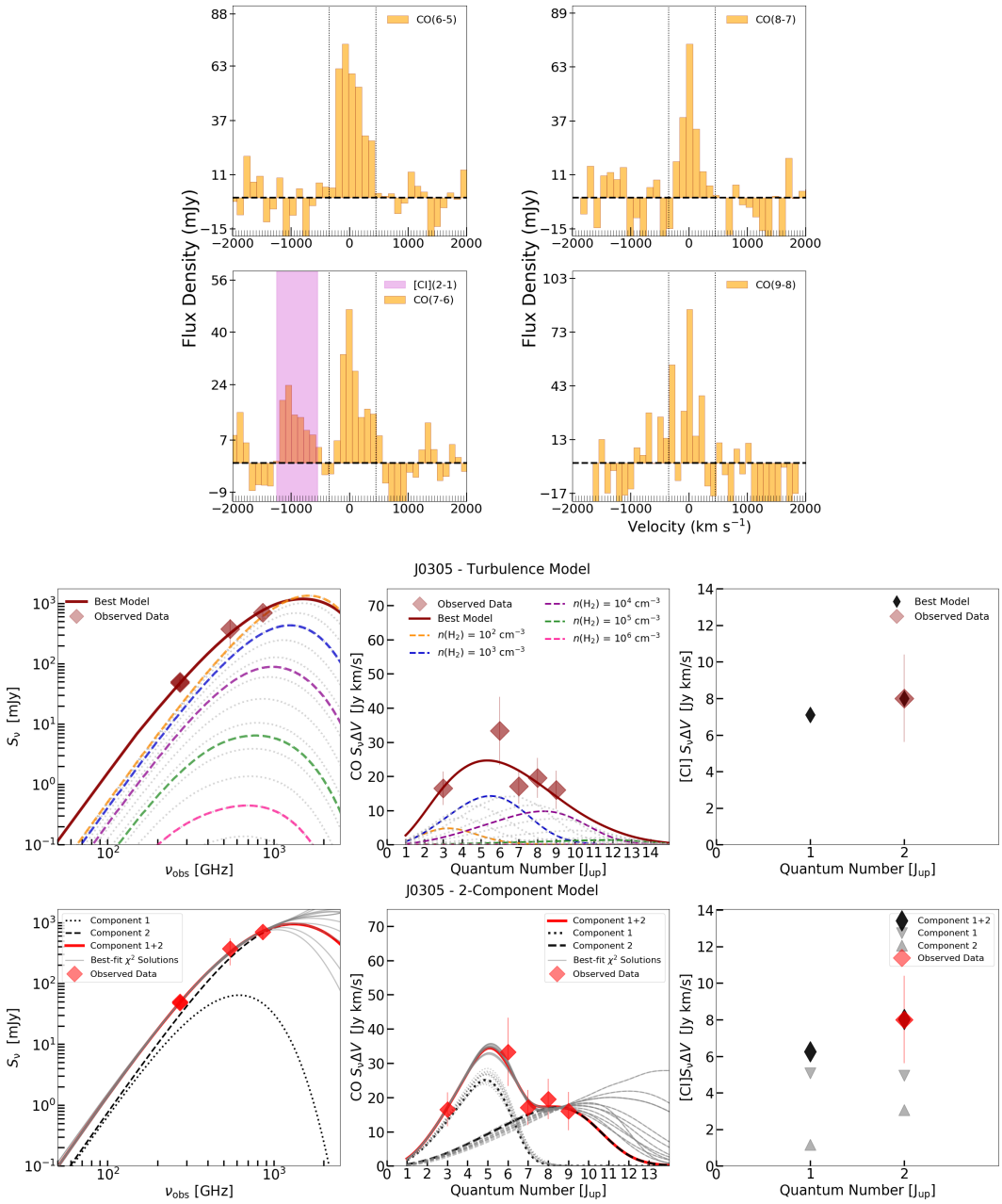

Figure A.5: LPsJ0305. We also model the CO(3-2) line measurement presented in Berman et al. (in prep).

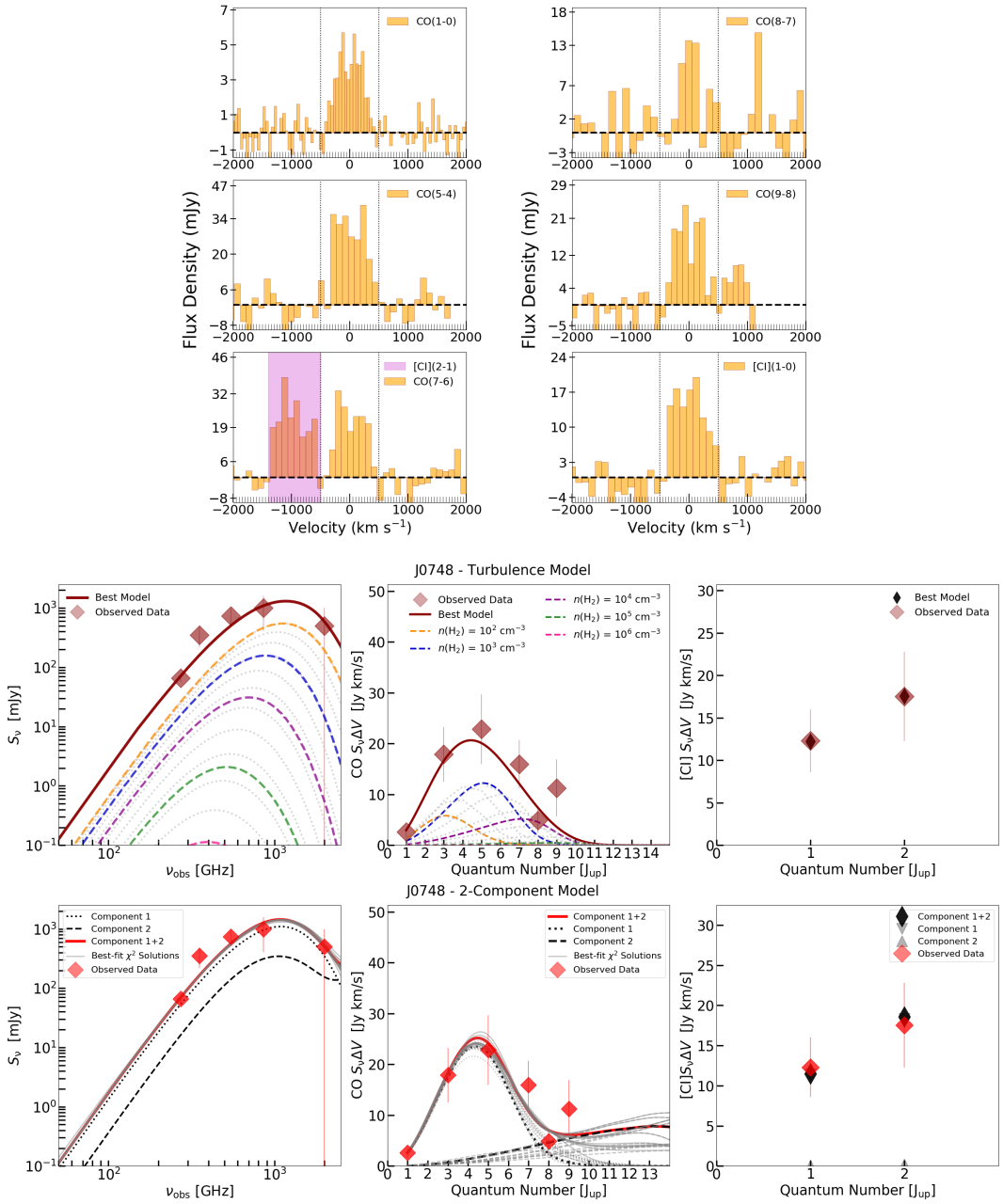

Figure A.6: LPsJ0748. We also model the CO(3-2) line measurement presented in Berman et al. (in prep).

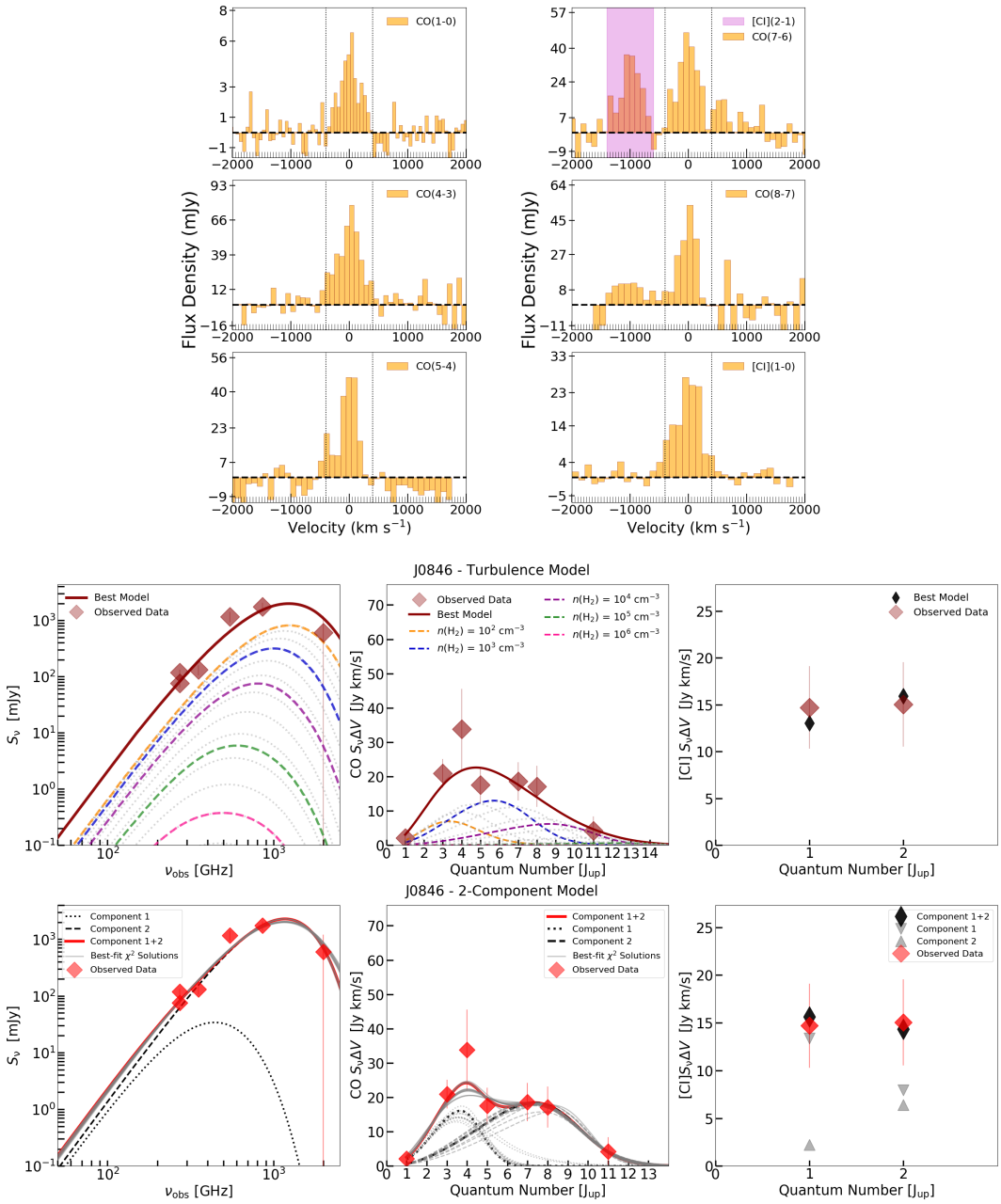

Figure A.7: LPsJ0846. We also model the CO(3-2) line measurement presented in Berman et al. (in prep).

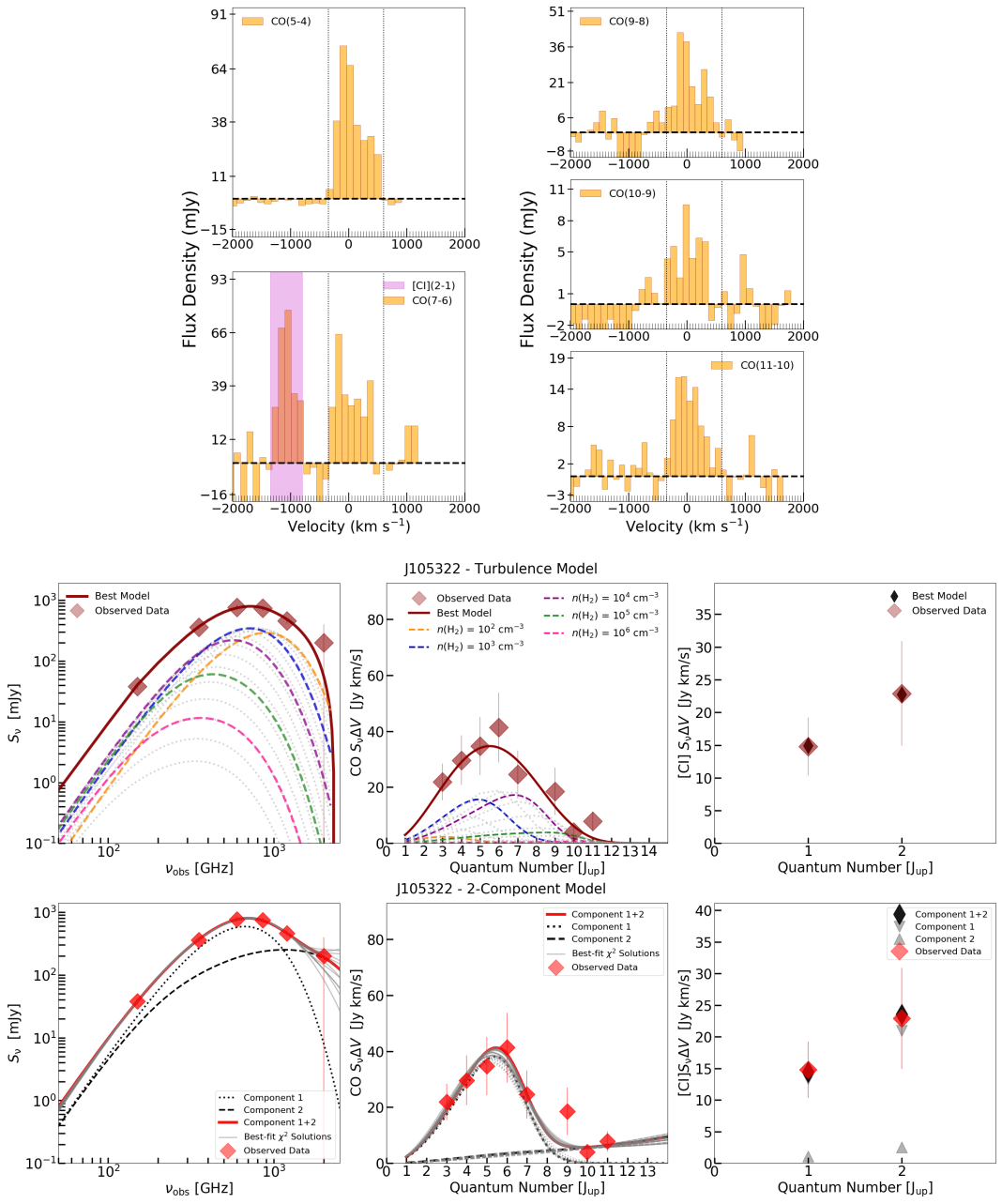

Figure A.8: LPsJ105322. We also model the CO(3-2) and CO(4-3) line measurements presented in Berman et al. (in prep), in addition to the [CI](1-0) and CO(6-5) line measurement from Nesvadba et al. (2019); Cañameras et al. (2018b).

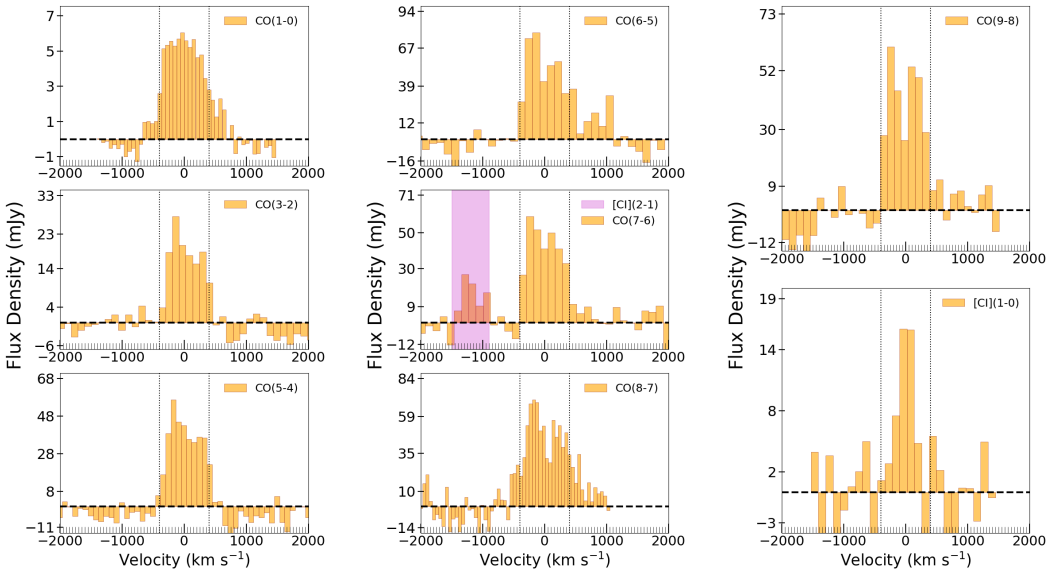

Figure A.9: LPsJ105353. We also model the CO(1-0) and CO(3-2) line measurements presented in Harrington et al. (2018, 2016), in addition to the CO(4-3), CO(10-9) and CO(11-10) line measurement from Cañameras et al. (2018b).

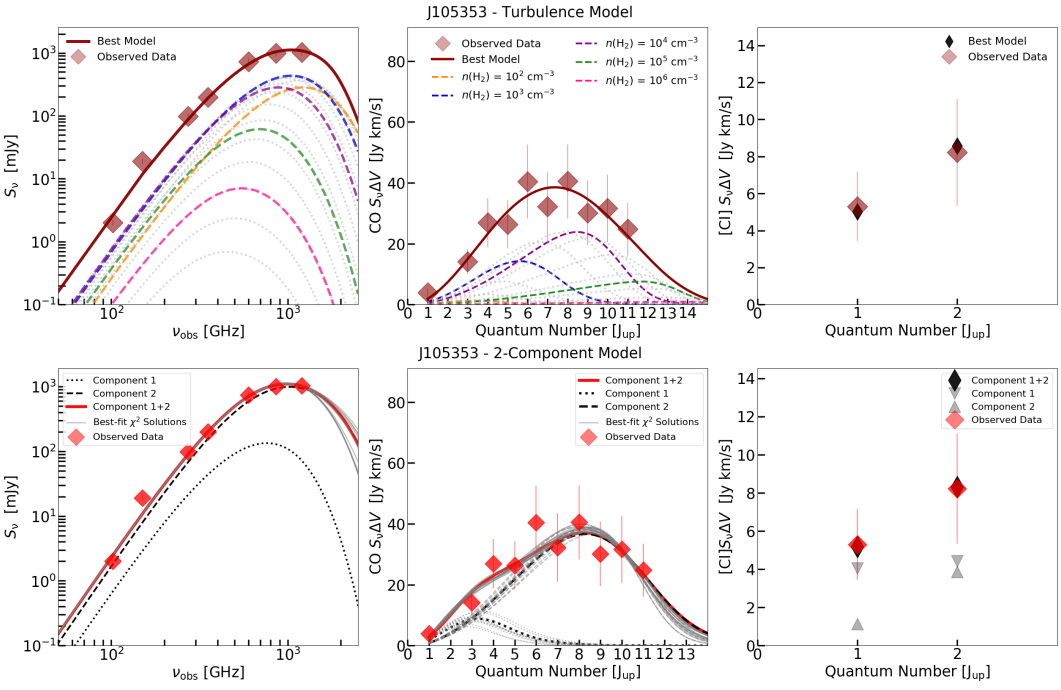

Figure A.10: LPsJ105353 continued.

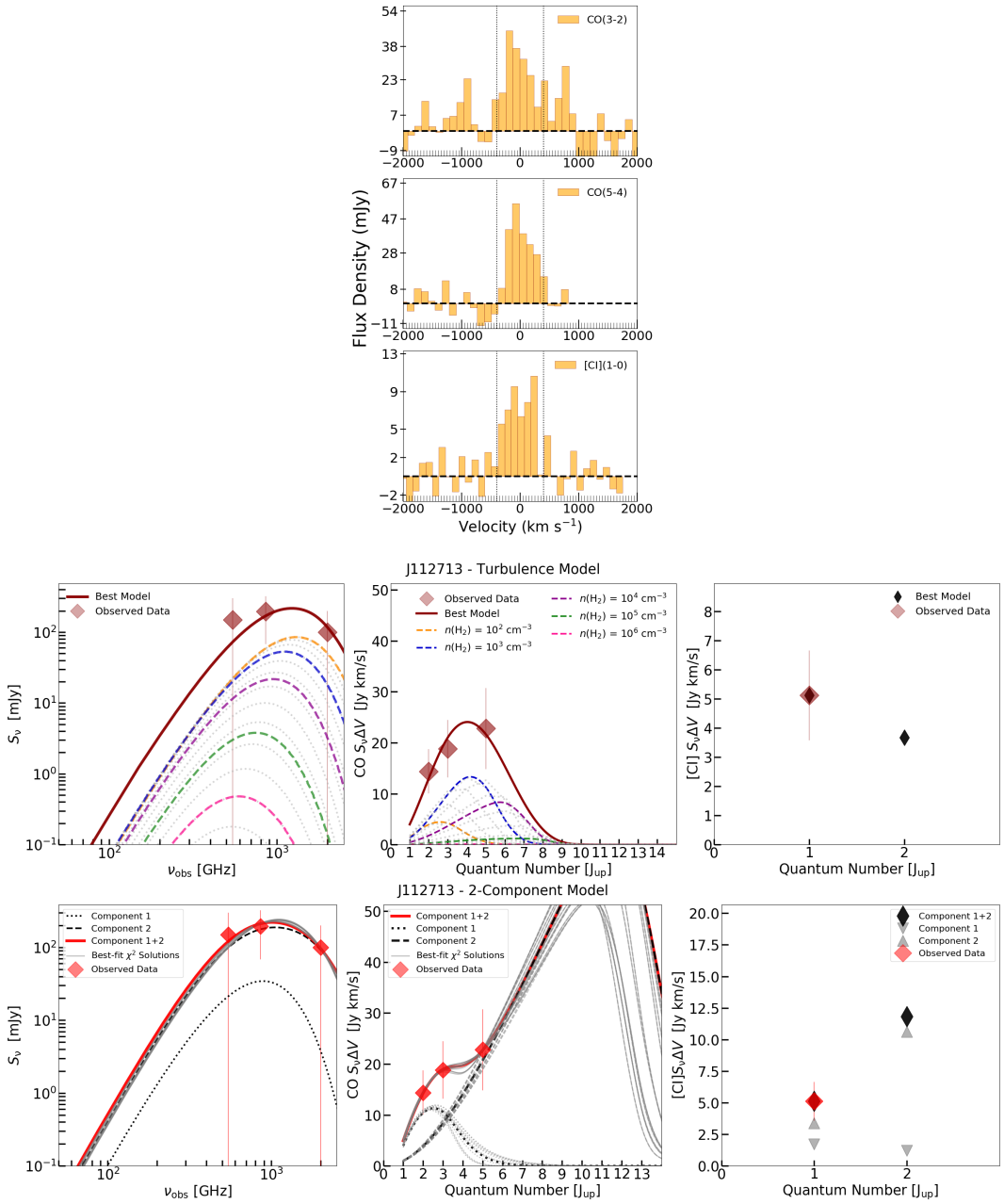

Figure A.11: LPsJ112713. We also model the CO(2-1) line measurements presented in Berman et al. (in prep.).

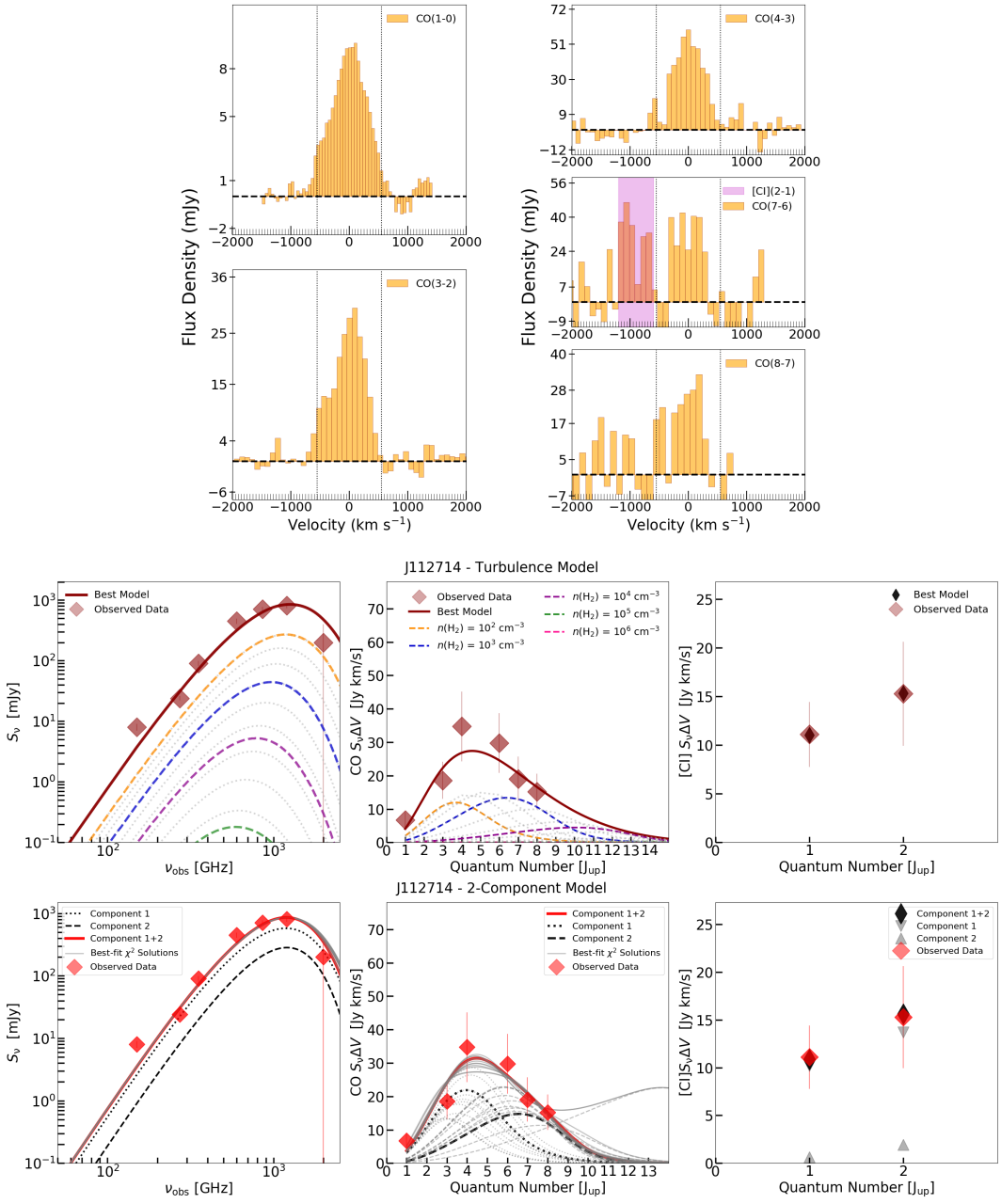

Figure A.12: LPsJ112714. We also model the CO(1-0) and CO(3-2) line measurements presented in Harrington et al. (2018, 2016), in addition to the [CI](1-0) and CO(6-5) line measurements from Nesvadba et al. (2019); Cañameras et al. (2018b).

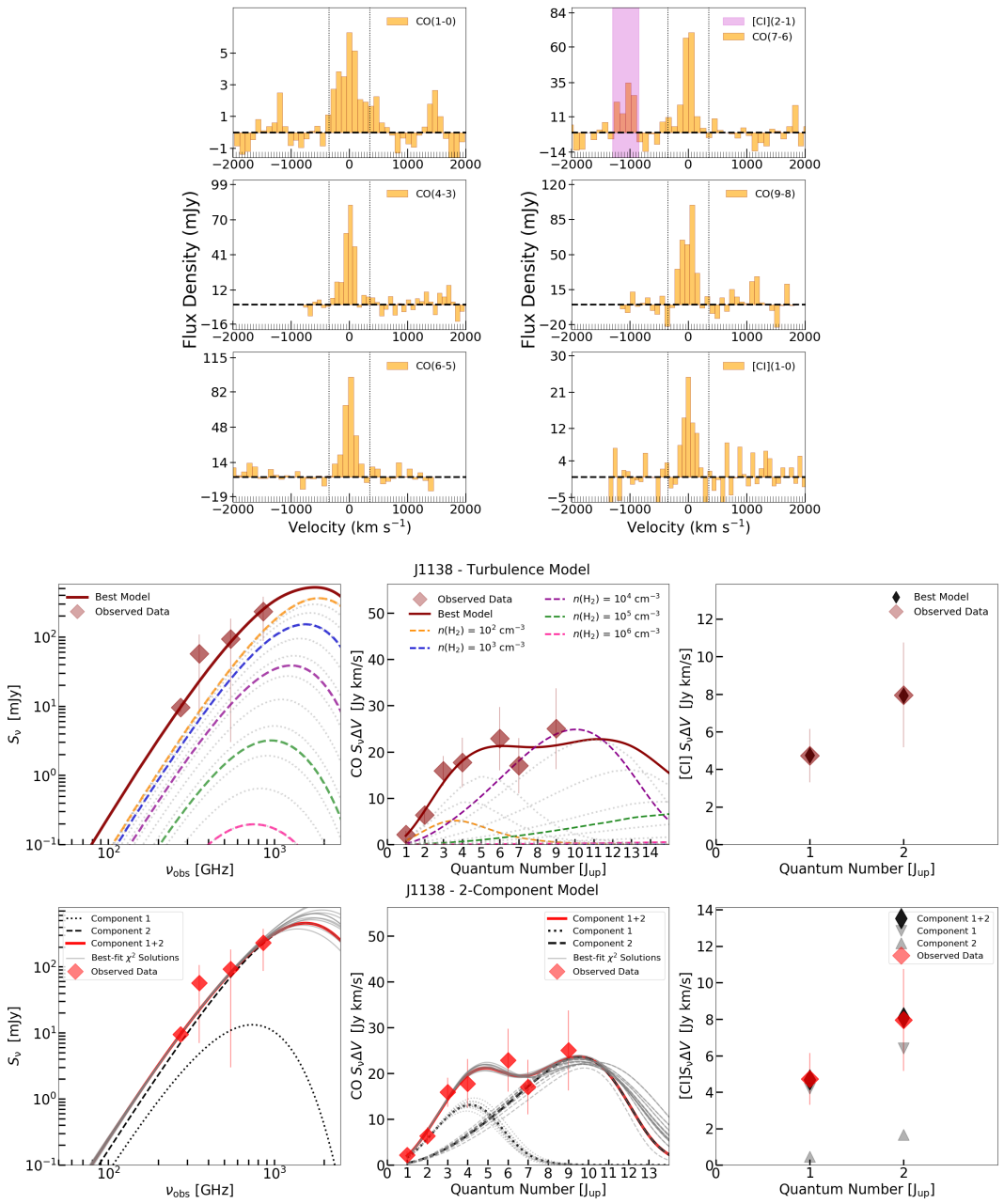

Figure A.13: LPsJ1138. We also model the CO(2-1) and CO(3-2) line measurements presented in Berman et al. (in prep.).

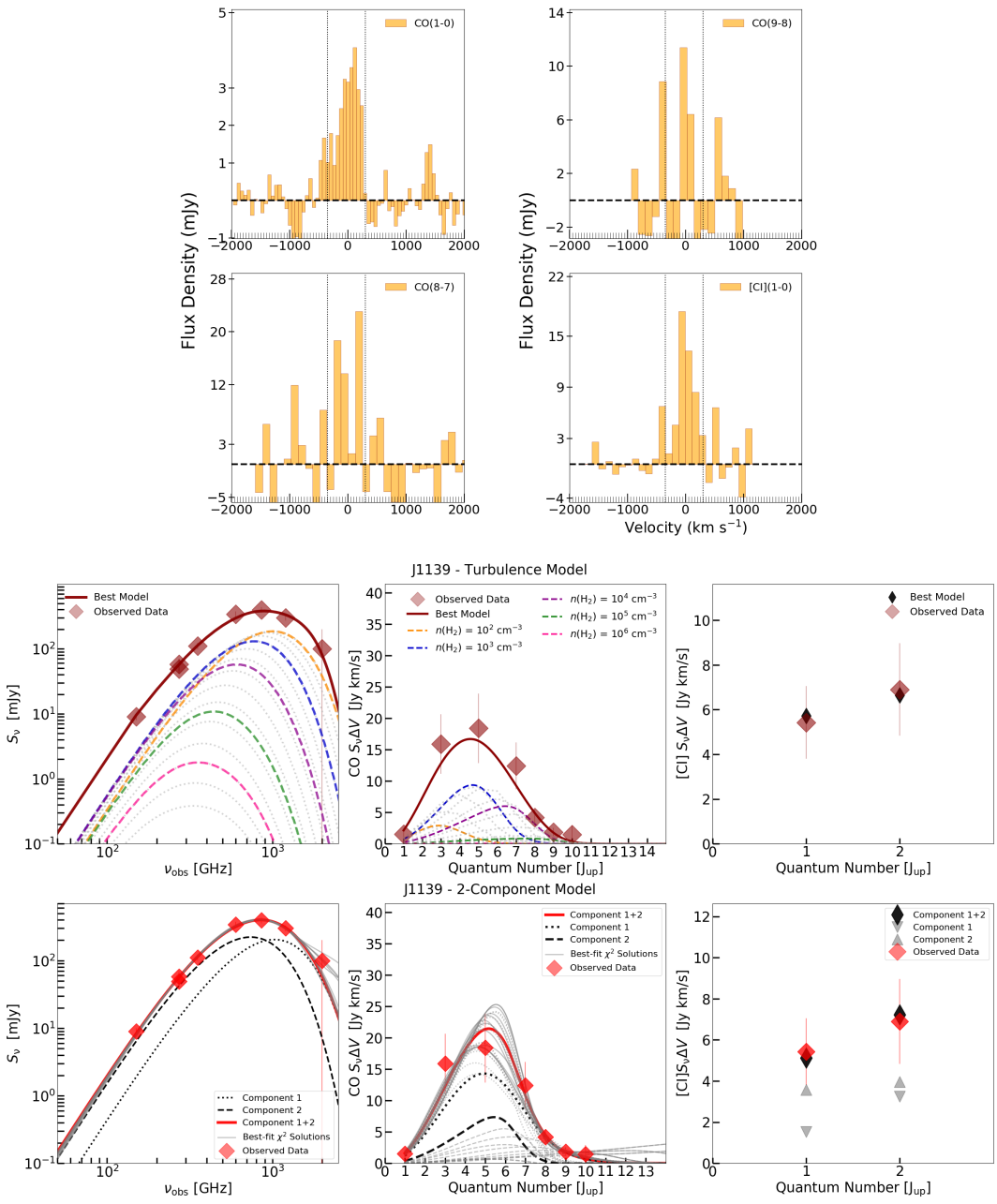

Figure A.14: LPsJ1139. We also model the CO(3-2) line measurements presented in Berman et al. (in prep.), in addition to the previously reported [CI](2-1) line (Nesvadba et al., 2019) and the CO(5-4) and CO(7-6) line measurements from Cañameras et al. (2018b).

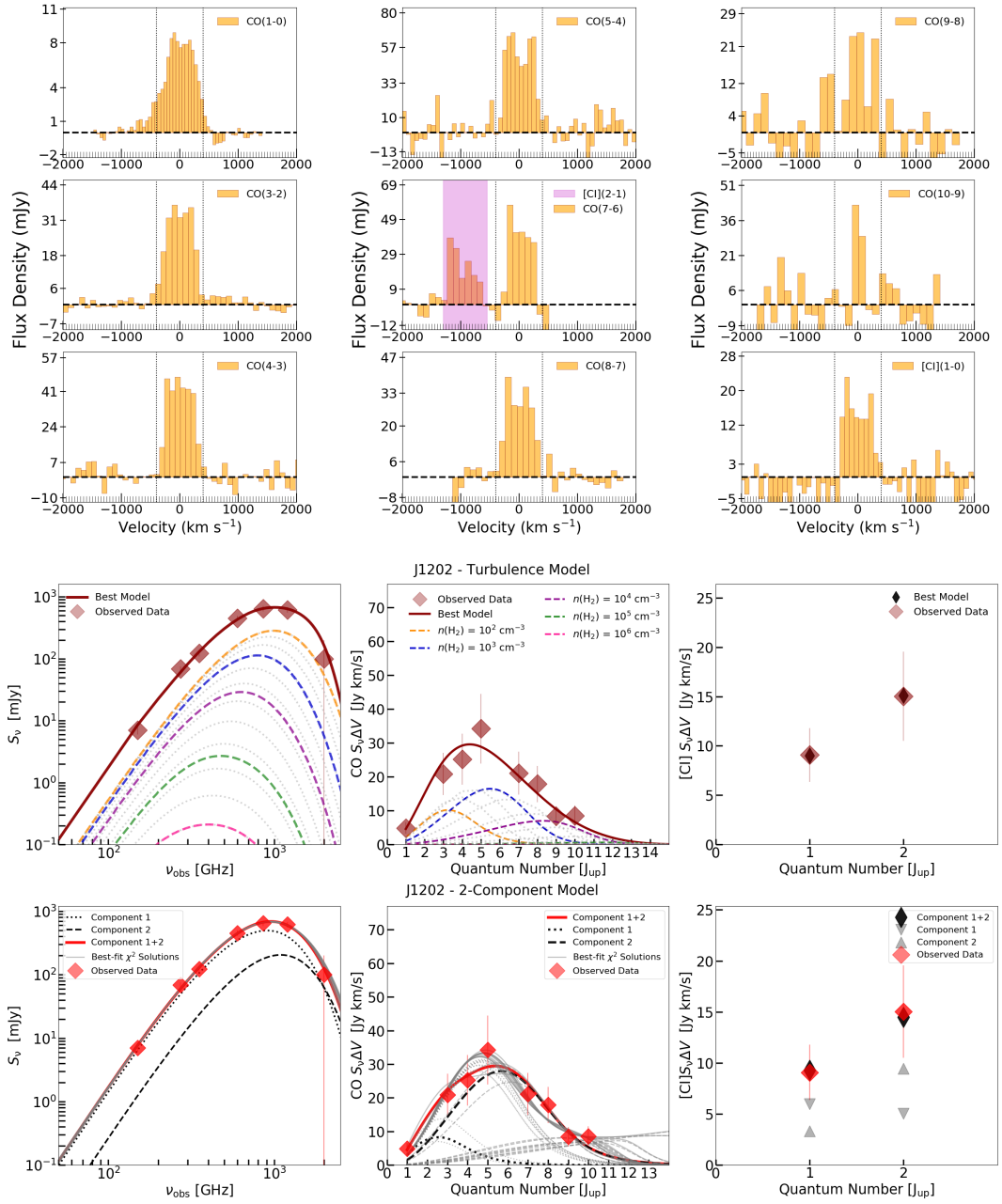

Figure A.15: LPsJ1202. We also model the CO(1-0) and CO(3-2) line measurements presented in Harrington et al. (2018, 2016).

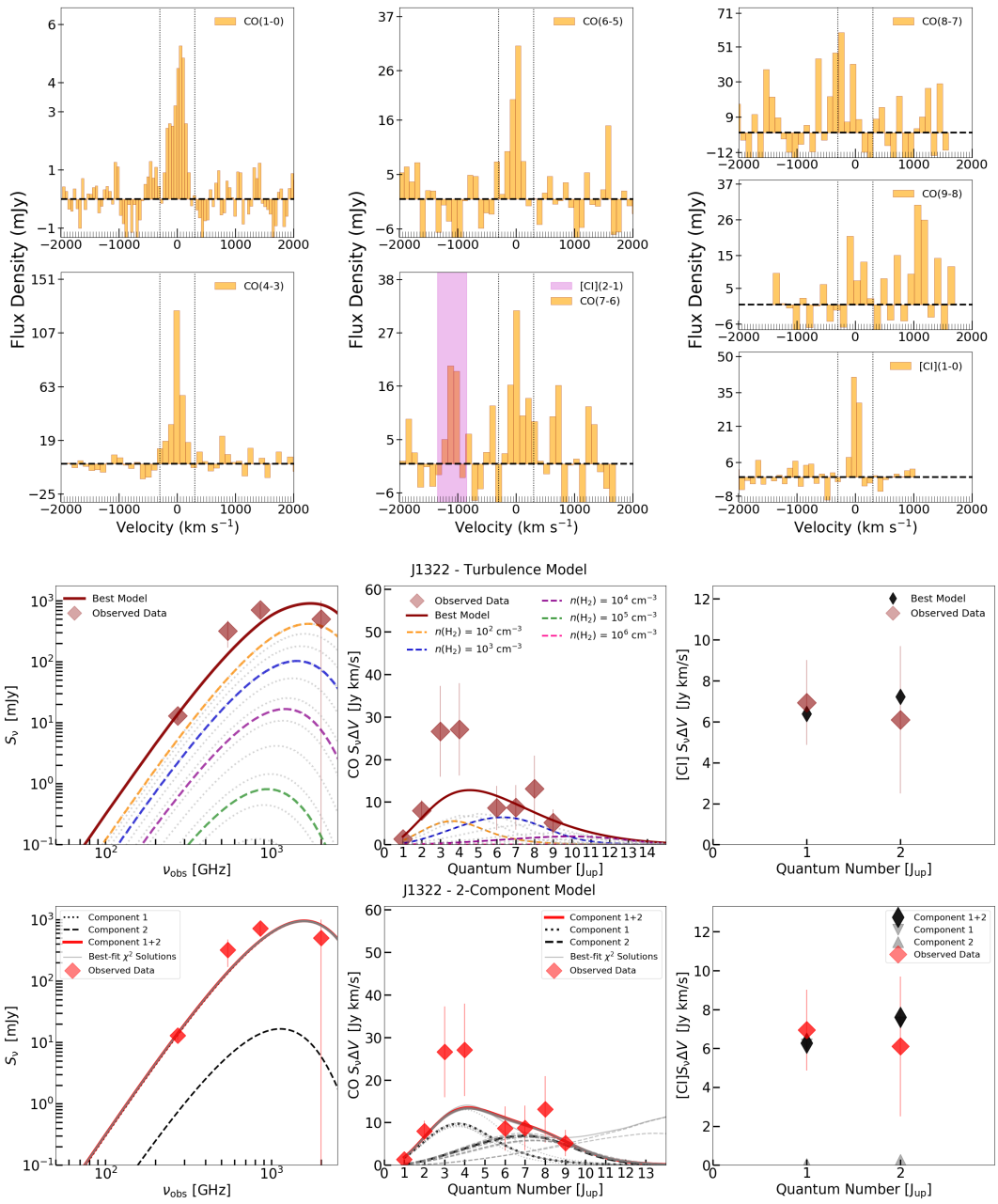

Figure A.16: LPsJ1322. We also model the CO(2-1) and CO(3-2) line measurements presented in Berman et al. (in prep).

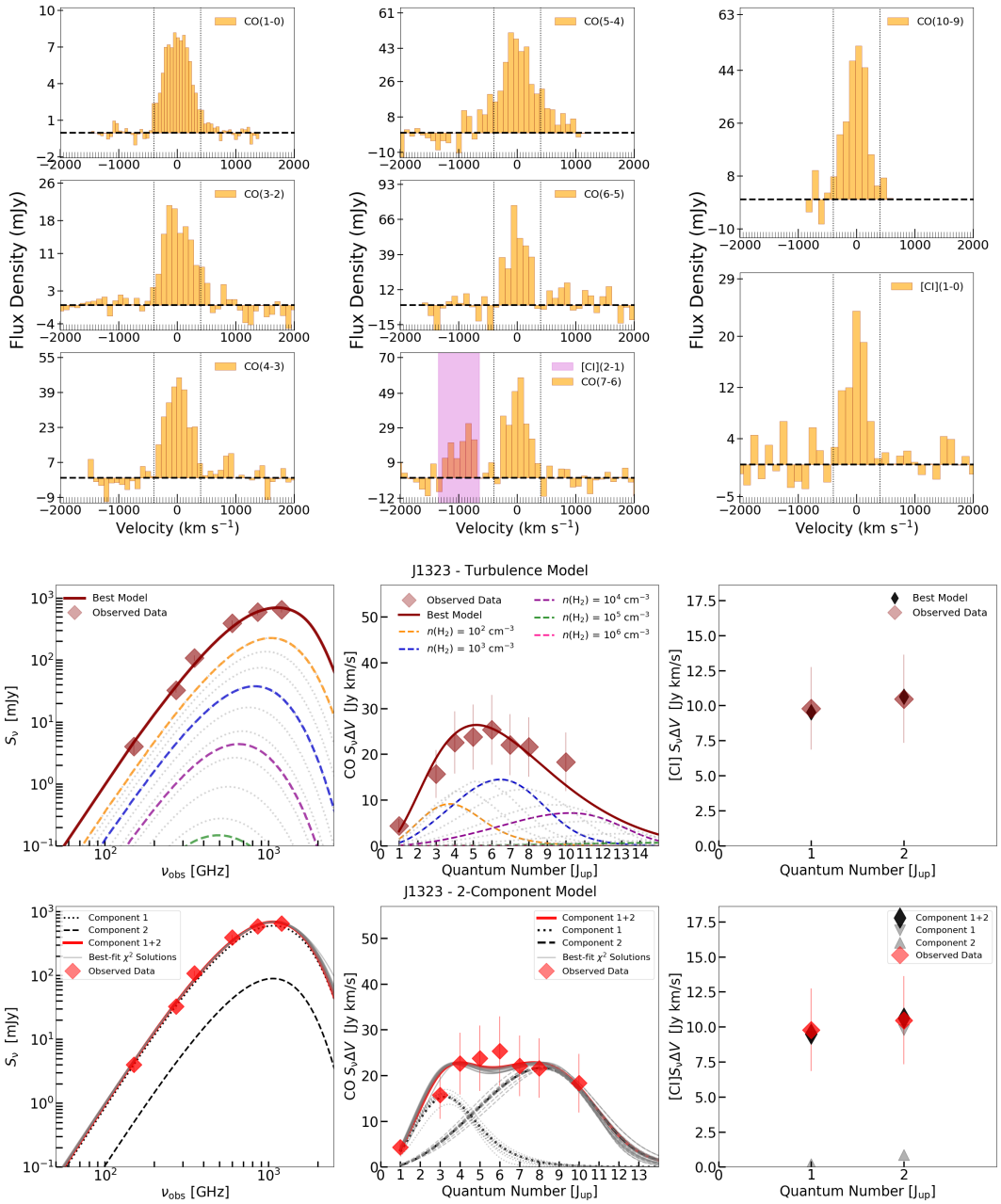

Figure A.17: LPsJ1323. We also model the CO(1-0) and CO(3-2) line measurements presented in Harrington et al. (2018, 2016), in addition to the CO(8-7) line measurement reported in Cañameras et al. (2018b).

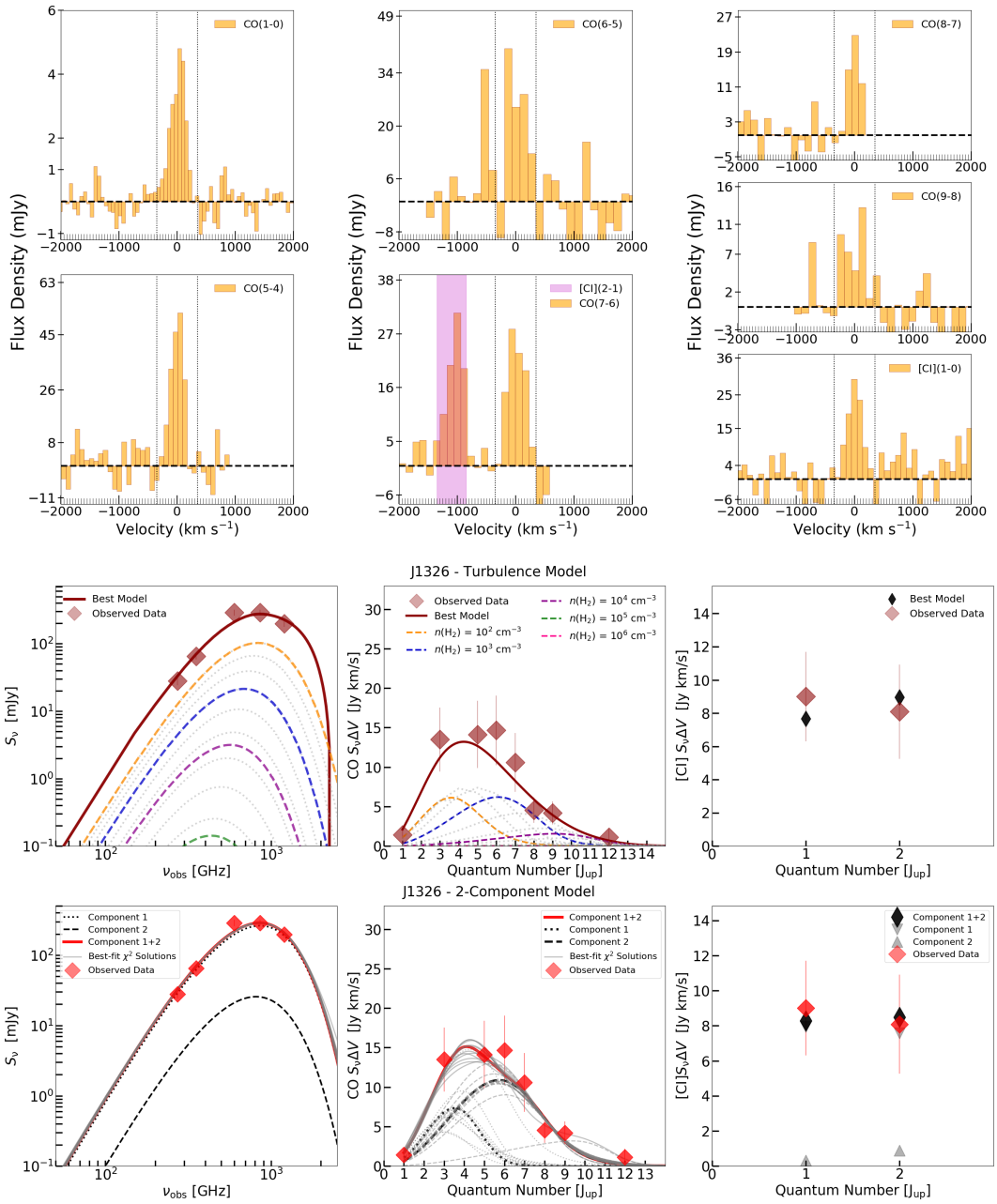

Figure A.18: LPsJ1326. We also model the CO(3-2) line measurement presented in Berman et al. (in prep.).

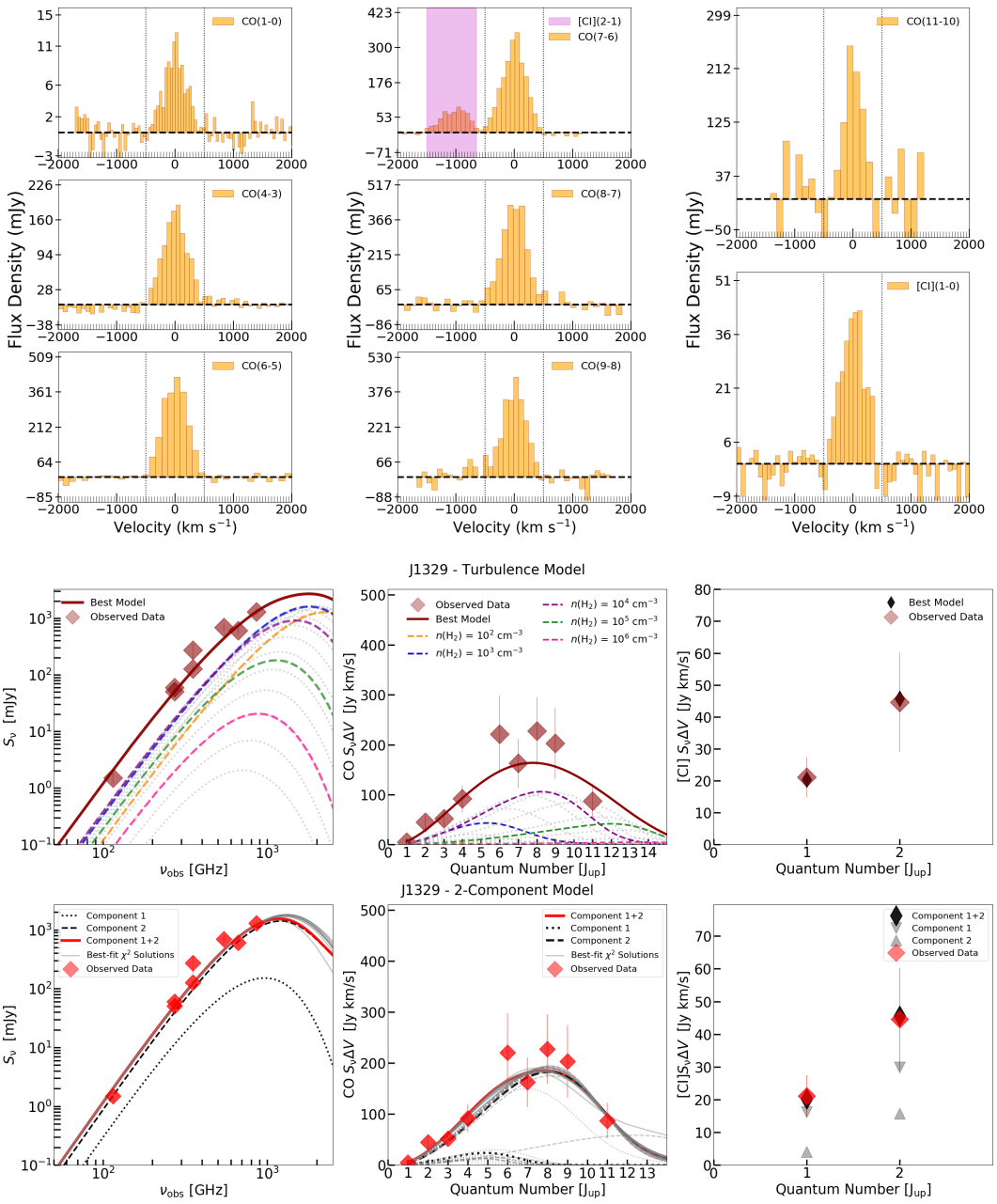

Figure A.19: LPsJ1329. These CO(1-0), [CI](1-0) and CO(4-3) spectra are also presented in (Dannerbauer et al., 2019). We also model the CO(2-1) line measurement presented in Berman et al. (in prep.).

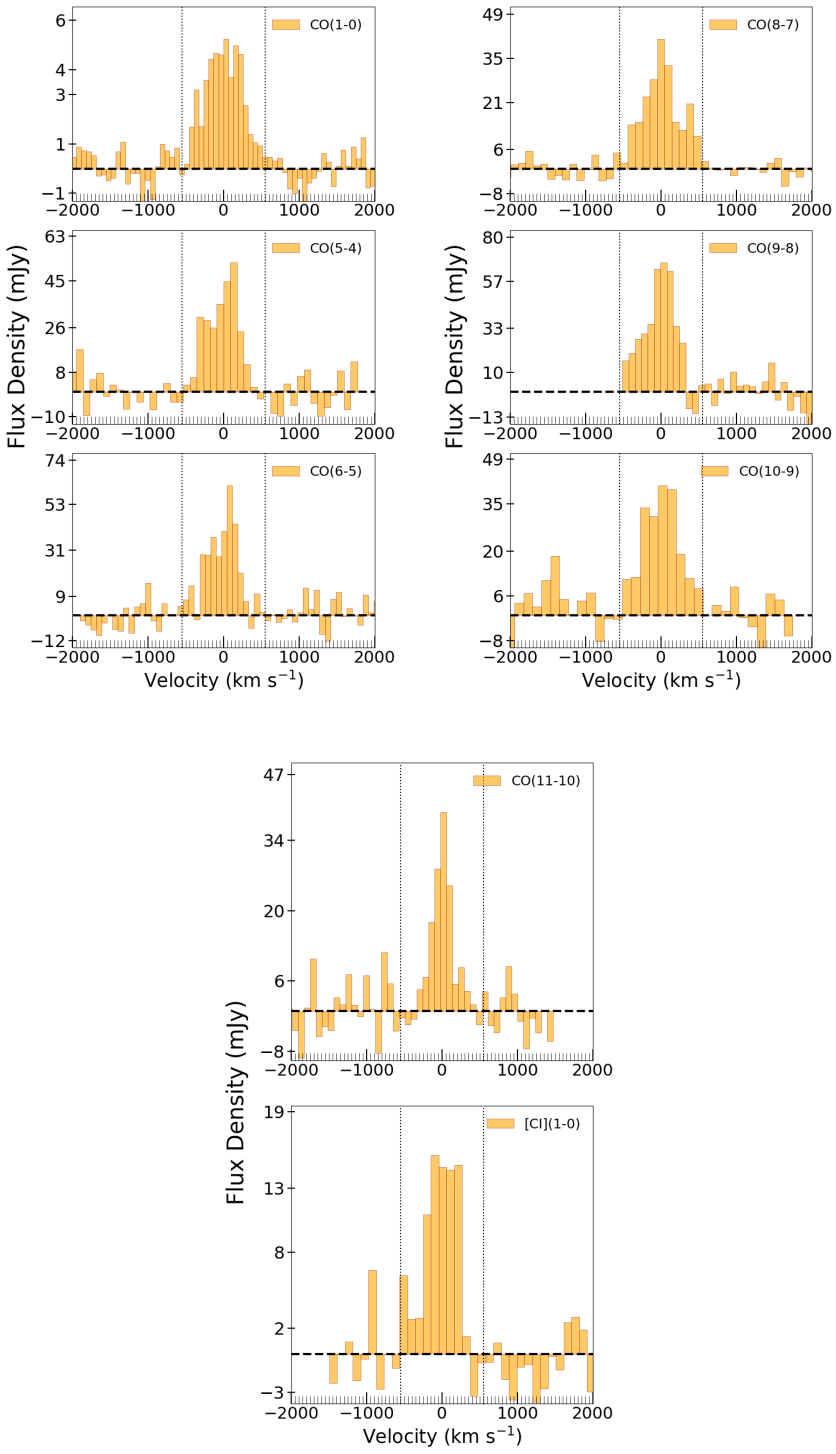

Figure A.20: LPsJ1336. We also model the CO(3-2) and CO(4-3) line measurements presented in Berman et al. (in prep.).

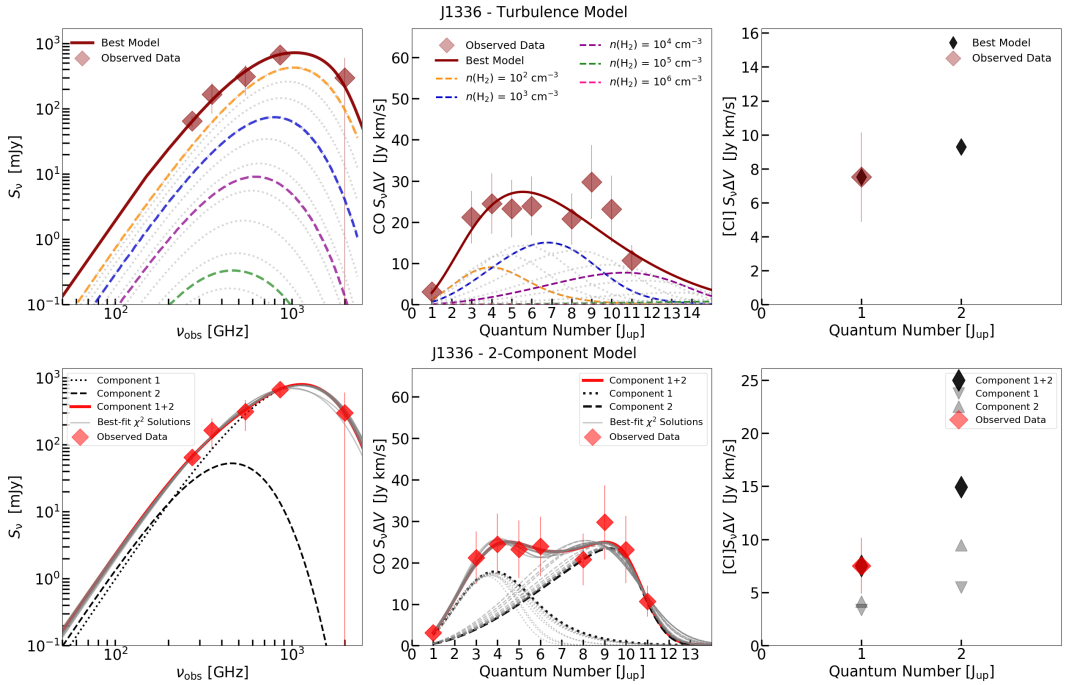

Figure A.21: LPsJ1336 continued.

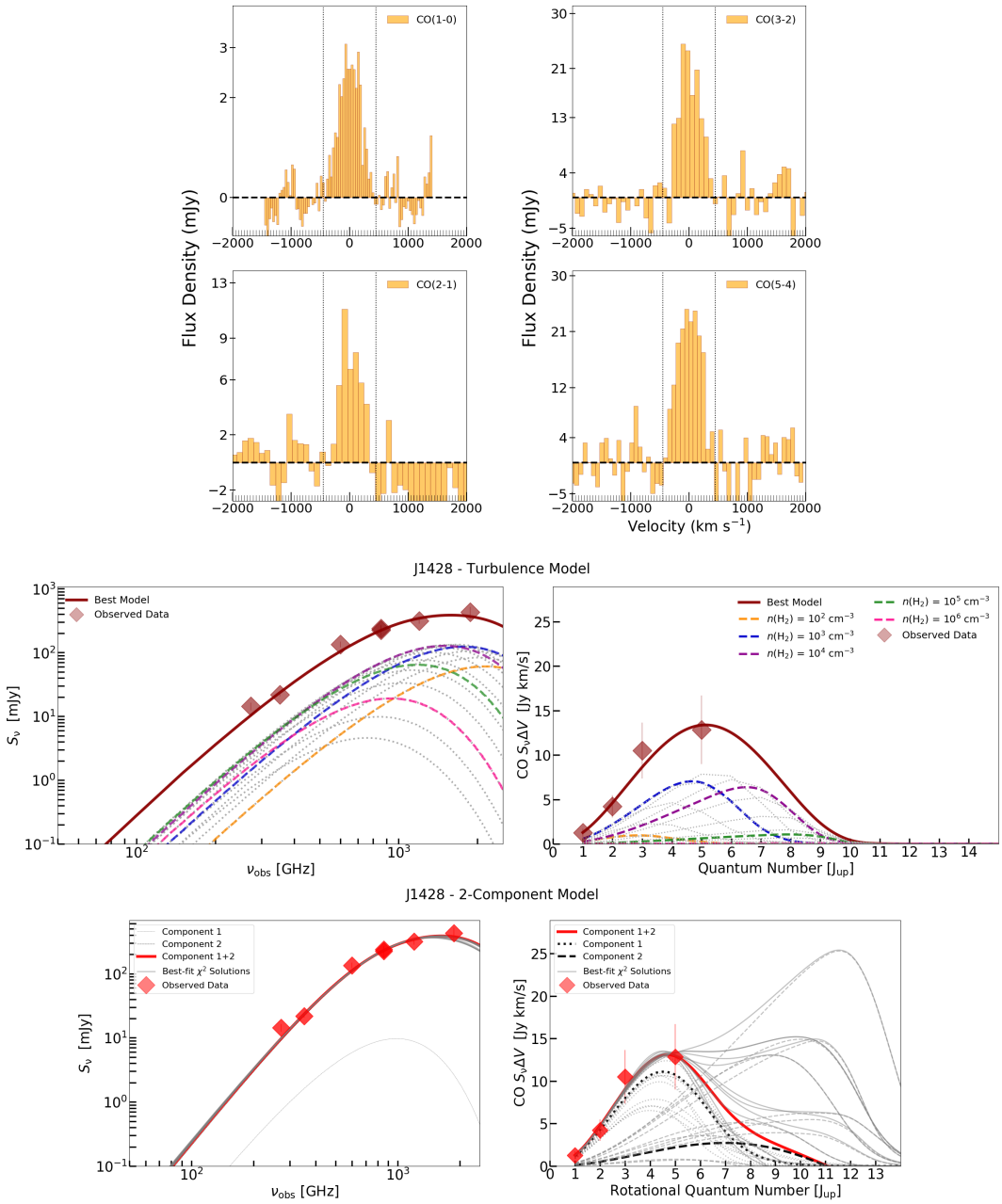

Figure A.22: LPsJ1428. The CO(1-0) and CO(2-1) spectra are also presented in Harrington et al. (2018, 2016).

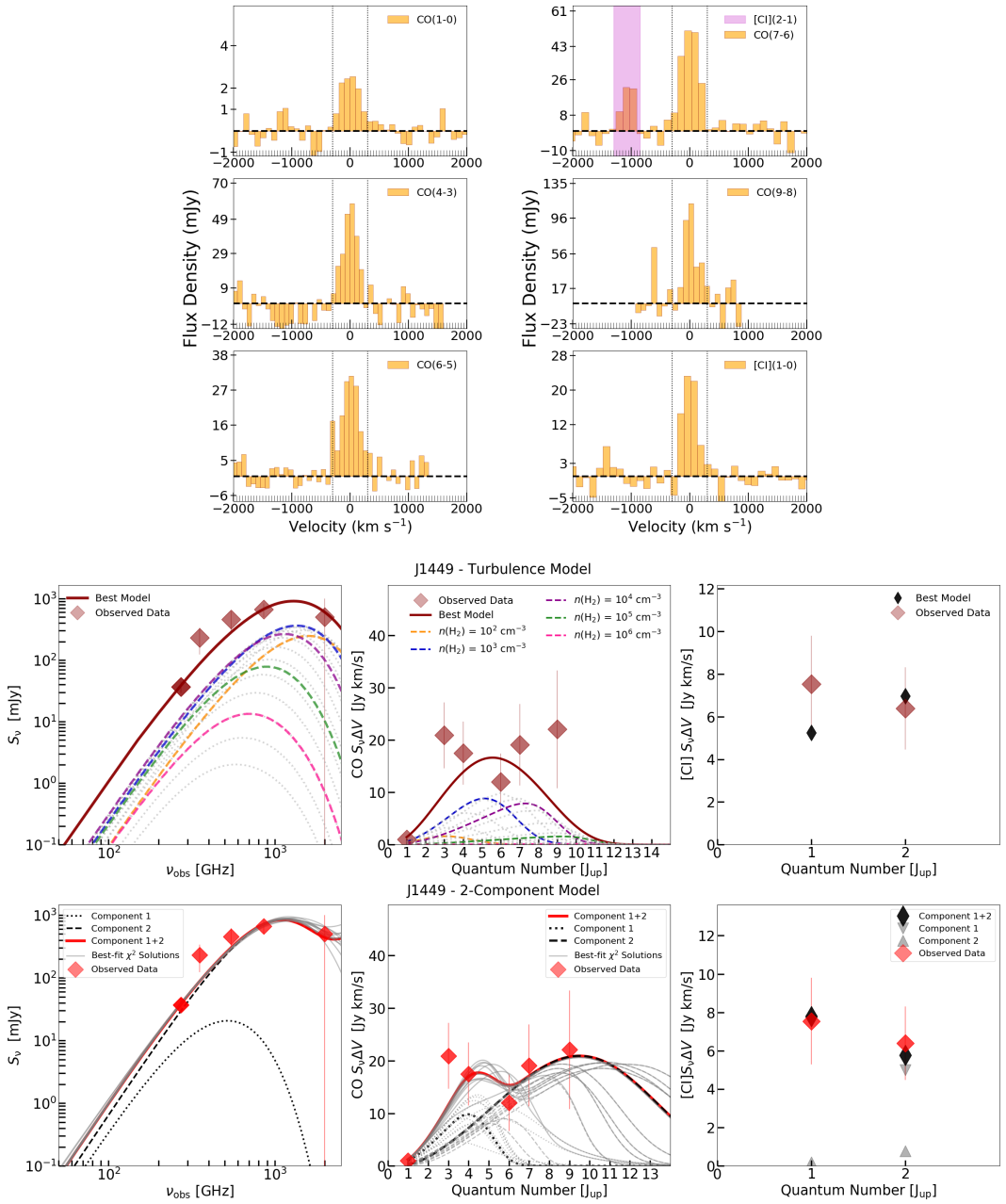

Figure A.23: LPsJ1449. We also model the CO(3-2) line measurement presented in Berman et al. (in prep.).

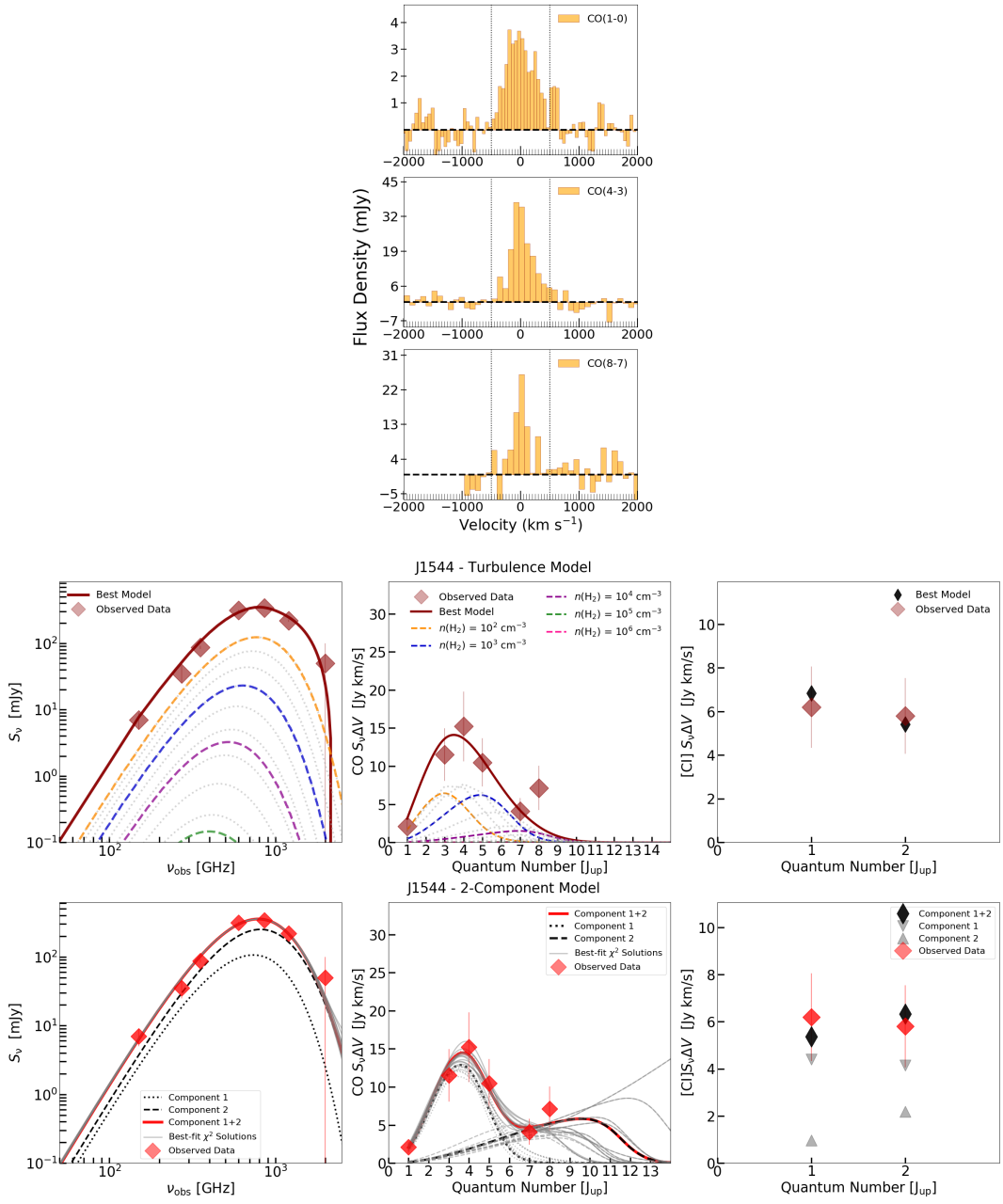

Figure A.24: LPsJ1544. We also model the CO(3-2) line measurement presented in Berman et al. (in prep.), in addition to the CO(5-4) and CO(7-6) line measurements from Cañameras et al. (2018b), and the [CI](1-0) and [CI](2-1) line measurements from Nesvadba et al. (2019).

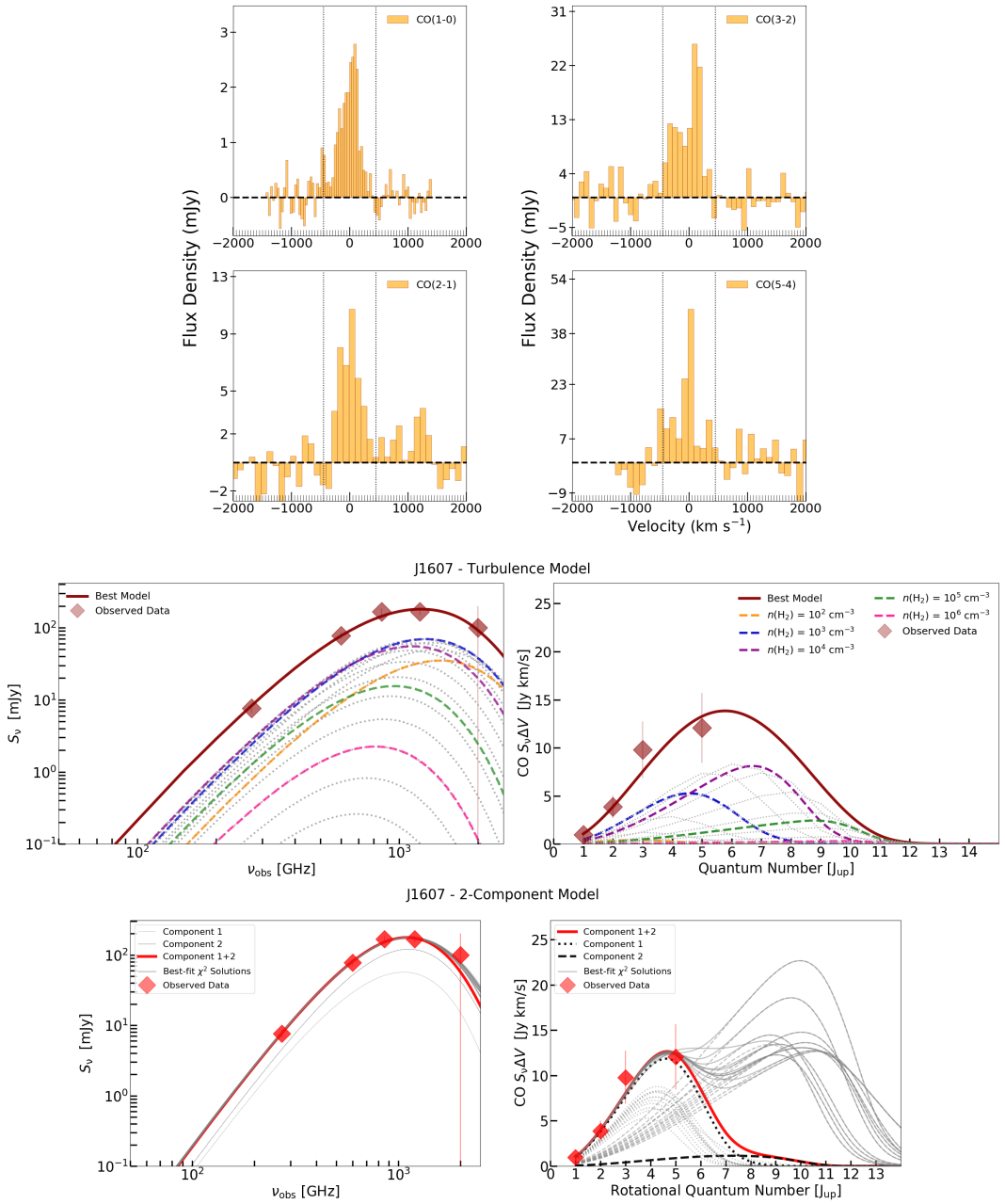

Figure A.25: LPsJ1607. The CO(1-0) and CO(2-1) spectra are also presented in Harrington et al. (2018, 2016).

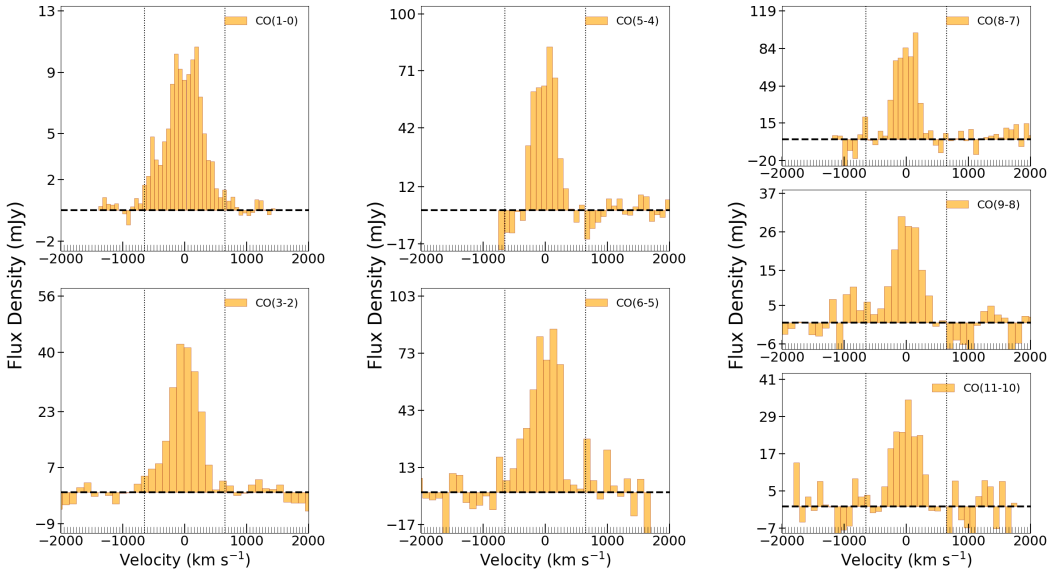

Figure A.26: LPsJ1609. The CO(1-0) and CO(2-1) spectra are also presented in Harrington et al. (2018, 2016). We also model the CO(4-3) and CO(10-9) line measurements reported by Cañameras et al. (2018b) and [CI](1-0) from Nesvadba et al. (2019).

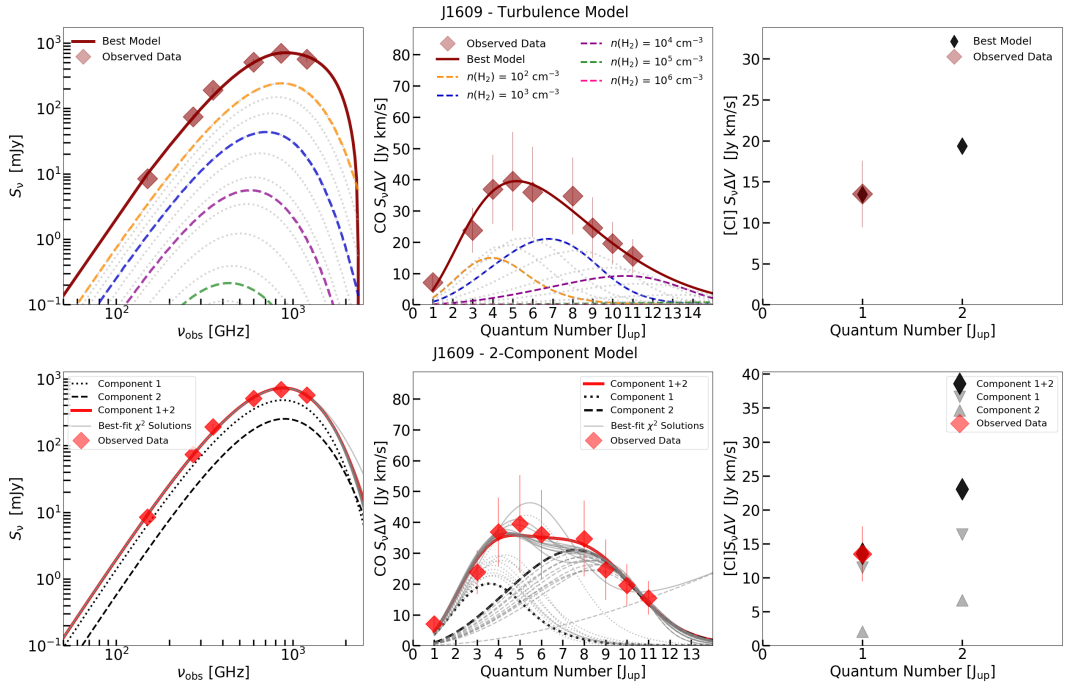

Figure A.27: LPsJ1609 continued.

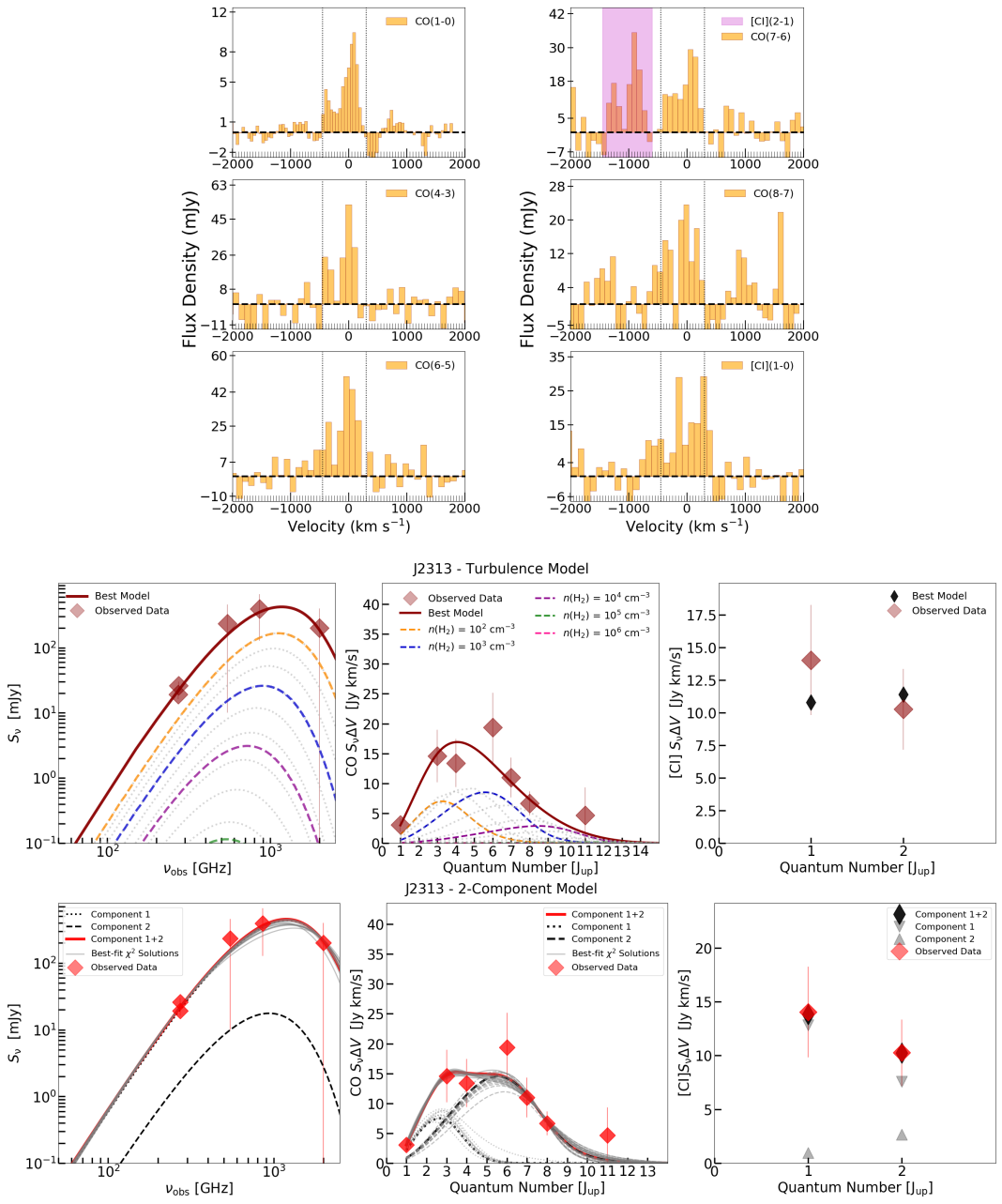

Figure A.28: LPsJ2313. We also model the CO(3-2) line measurement presented in Berman et al. (in prep.).

APPENDIX B

Bibliography

Aannestad P. A., Purcell E. M., 1973, ARA&A, 11, 309

Abdo A. A., et al., 2010, ApJS, 188, 405

Acciari V. A., et al., 2009, Science, 325, 444

Accurso G., et al., 2017, MNRAS, 470, 4750

Alaghband-Zadeh S., et al., 2013, MNRAS, 435, 1493

Allen C. W., 1973, Astrophysical quantities

Amodeo S., et al., 2018, ApJ, 853, 36

Amorín R., Muñoz-Tuñón C., Aguerri J. A. L., Planesas P., 2016, A&A, 588, A23

Anders E., Grevesse N., 1989, GCA, 53, 197

Andreani P., Retana-Montenegro E., Zhang Z.-Y., Papadopoulos P., Yang C., Vegetti S., 2018, A&A, 615, A142

Andrews B. H., Thompson T. A., 2011, ApJ, 727, 97

Apostolovski Y., et al., 2019, A&A, 628, A23

Aravena M., et al., 2013, MNRAS, 433, 498

Aravena M., et al., 2014, MNRAS, 442, 558

Aravena M., et al., 2016, ApJ, 833, 68

Aravena M., et al., 2020, arXiv e-prints, p. arXiv:2006.04284

Archibald E. N., Dunlop J. S., Hughes D. H., Rawlings S., Eales S. A., Ivison R. J., 2001, MNRAS, 323, 417

Aretxaga I., et al., 2011, MNRAS, 415, 3831

Astropy Collaboration et al., 2018, AJ, 156, 123

Austermann J. E., et al., 2010, MNRAS, 401, 160

Bakx T. J. L. C., et al., 2018, MNRAS, 473, 1751

Bakx T. J. L. C., et al., 2020, MNRAS, 496, 2372

Baldwin J. A., Phillips M. M., Terlevich R., 1981, PASP, 93, 5

Ballesteros-Paredes J., Hartmann L., Vázquez-Semadeni E., 1999, ApJ, 527, 285

Bardeen J. M., Bond J. R., Kaiser N., Szalay A. S., 1986, ApJ, 304, 15

Barger A. J., Cowie L. L., Sanders D. B., Fulton E., Taniguchi Y., Sato Y., Kawara K., Okuda H., 1998, Nature, 394, 248

Barger A. J., Cowie L. L., Sanders D. B., 1999, ApJL, 518, L5

Baron D., et al., 2018, MNRAS, 480, 3993

Barro G., et al., 2016, ApJL, 827, L32

Barvainis R., Maloney P., Antonucci R., Alloin D., 1997, ApJ, 484, 695

Bastian N., Covey K. R., Meyer M. R., 2010, ARA&A, 48, 339

Baugh C. M., Lacey C. G., Frenk C. S., Granato G. L., Silva L., Bressan A., Benson A. J., Cole S., 2005a, MNRAS, 356, 1191

Baugh C. M., Lacey C. G., Frenk C. S., Granato G. L., Silva L., Bressan A., Benson A. J., Cole S., 2005b, MNRAS, 356, 1191

Bennett C. L., et al., 1994, ApJ, 434, 587

Bennett C. L., et al., 2003, ApJS, 148, 1

Bennett C. L., Larson D., Weiland J. L., Hinshaw G., 2014, ApJ, 794, 135

Berta S., et al., 2011, A&A, 532, A49

Bertoldi F., et al., 2000, A&A, 360, 92

Béthermin M., Dole H., Beelen A., Aussel H., 2010a, A&A, 512, A78

Béthermin M., Dole H., Beelen A., Aussel H., 2010b, A&A, 512, A78

Béthermin M., et al., 2012, ApJL, 757, L23

Béthermin M., et al., 2016, A&A, 586, L7

Bigiel F., Leroy A., Walter F., Brinks E., de Blok W. J. G., Madore B., Thornley M. D., 2008, AJ, 136, 2846

Bisbas T. G., Papadopoulos P. P., Viti S., 2015, ApJ, 803, 37

Blain A. W., 1996, MNRAS, 283, 1340

Blain A. W., 1998, MNRAS, 297, 511

Blain A. W., 1999, MNRAS, 304, 669

Blain A. W., Longair M. S., 1993, MNRAS, 264, 509

Blain A. W., Smail I., Ivison R. J., Kneib J. P., Frayer D. T., 2002, Physics Reports, 369, 111

Blain A. W., Barnard V. E., Chapman S. C., 2003, MNRAS, 338, 733

Blake G. A., Sutton E. C., Masson C. R., Phillips T. G., 1987, ApJ, 315, 621

Blumenthal G. R., Faber S. M., Primack J. R., Rees M. J., 1984, Nature, 311, 517

Boggess N. W., et al., 1992, ApJ, 397, 420

Bolatto A. D., Wolfire M., Leroy A. K., 2013, ARA&A, 51, 207

Borys C., Chapman S. C., Halpern M., Scott D., 2002, MNRAS, 330, L63

Borys C., et al., 2006, ApJ, 636, 134

Bosma A., 1978, PhD thesis, -

Bothwell M. S., et al., 2013, MNRAS, 429, 3047

Bothwell M. S., Maiolino R., Cicone C., Peng Y., Wagg J., 2016, A&A, 595, A48

Bothwell M. S., et al., 2017, MNRAS, 466, 2825

Bouché N., et al., 2007, ApJ, 671, 303

Bournaud F., Elmegreen B. G., Teyssier R., Block D. L., Puerari I., 2010, MNRAS, 409, 1088

Bouwens R. J., et al., 2012, ApJ, 754, 83

Boyle B. J., Terlevich R. J., 1998, MNRAS, 293, L49

Bradley L. D., et al., 2014, ApJ, 792, 76

Brinchmann J., Charlot S., White S. D. M., Tremonti C., Kauffmann G., Heckman T., Brinkmann J., 2004, MNRAS, 351, 1151

Bronfman L., Cohen R. S., Alvarez H., May J., Thaddeus P., 1988, ApJ, 324, 248

Brott I., et al., 2011, A&A, 530, A115

Brown R. L., Vanden Bout P. A., 1992, ApJL, 397, L19

Brucy N., Hennebelle P., Bournaud F., Colling C., 2020, ApJL, 896, L34

Burgarella D., Buat V., Iglesias-Páramo J., 2005, MNRAS, 360, 1413

Bussmann R. S., et al., 2013, ApJ, 779, 25

Bussmann R. S., et al., 2015, ApJ, 812, 43

Cañameras R., et al., 2015, A&A, 581, A105

Cañameras R., et al., 2017a, A&A, 600, L3

Cañameras R., et al., 2017b, A&A, 604, A117

Cañameras R., et al., 2018a, A&A, 620, A60

Cañameras R., et al., 2018b, A&A, 620, A61

Calzetti D., Kinney A. L., Storchi-Bergmann T., 1994, ApJ, 429, 582

Calzetti D., Armus L., Bohlin R. C., Kinney A. L., Koornneef J., Storchi-Bergmann T., 2000, ApJ, 533, 682

Calzetti D., et al., 2007, ApJ, 666, 870

Carilli C. L., Walter F., 2013, ARA&A, 51, 105

Carilli C. L., et al., 2002, AJ, 123, 1838

Carilli C. L., Hodge J., Walter F., Riechers D., Daddi E., Dannerbauer H., Morrison G. E., 2011, ApJL, 739, L33

Carlstrom J. E., et al., 2011, PASP, 123, 568

Carter M., et al., 2012, A&A, 538, A89

Casey C. M., et al., 2012, ApJ, 761, 140

Casey C. M., et al., 2013, MNRAS, 436, 1919

Casey C. M., Narayanan D., Cooray A., 2014, Physics Reports, 541, 45

Casey C. M., et al., 2018, ApJ, 862, 77

Cen R., Ostriker J. P., 1999, ApJL, 519, L109

Chandrasekhar S., 1951, Proceedings of the Royal Society of London Series A, 210, 26

Chapman S. C., Scott D., Borys C., Fahlman G. G., 2002, MNRAS, 330, 92

Chapman S. C., Blain A. W., Smail I., Ivison R. J., 2005, ApJ, 622, 772

Chary R., Elbaz D., 2001, ApJ, 556, 562

Chomiuk L., Povich M. S., 2011, AJ, 142, 197

Chu Y. H., 2005, in Braun R., ed., Astronomical Society of the Pacific Conference Series Vol. 331, Extra-Planar Gas. p. 297

Chu J. K., et al., 2017, ApJS, 229, 25

Cicone C., et al., 2014, A&A, 562, A21

Cicone C., et al., 2015, A&A, 574, A14

Cicone C., Brusa M., Ramos Almeida C., Cresci G., Husemann B., Mainieri V., 2018, Nature Astronomy, 2, 176

Clements D. L., et al., 2010, A&A, 518, L8

Coe D., et al., 2013, ApJ, 762, 32

Coe D., et al., 2019, ApJ, 884, 85

Colgan S. W. J., Haas M. R., Erickson E. F., Rubin R. H., Simpson J. P., Russell R. W., 1993, ApJ, 413, 237

Colling C., Hennebelle P., Geen S., Iffrig O., Bournaud F., 2018, A&A, 620, A21

Combes F., Leon S., Meylan G., 1999, A&A, 352, 149

Combes F., et al., 2012, A&A, 538, L4

Conley A., et al., 2011, ApJS, 192, 1

Coogan R. T., et al., 2019, MNRAS, 485, 2092

Cormier D., et al., 2015, A&A, 578, A53

Cortzen I., et al., 2020, A&A, 634, L14

Cowie L. L., Barger A. J., Kneib J. P., 2002, AJ, 123, 2197

Cox D. P., 1981, ApJ, 245, 534

Cresci G., et al., 2015, ApJ, 799, 82

Crocker A. F., et al., 2019, ApJ, 887, 105

Crowther P. A., 2007, Annual Review of Astronomy and Astrophysics, 45, 177

D'Agostino J. J., Poetrodjojo H., Ho I. T., Groves B., Kewley L., Madore B. F., Rich J., Seibert M., 2018, MNRAS, 479, 4907

Daddi E., et al., 2009, ApJ, 694, 1517

Daddi E., et al., 2010, ApJ, 713, 686

Daddi E., et al., 2015, A&A, 577, A46

Dale D. A., Helou G., Contursi A., Silbermann N. A., Kolhatkar S., 2001, ApJ, 549, 215

Dale D. A., et al., 2012, ApJ, 745, 95

Dalla Vecchia C., Schaye J., 2008, MNRAS, 387, 1431

Dame T. M., Thaddeus P., 2011, ApJL, 734, L24

Dame T. M., Elmegreen B. G., Cohen R. S., Thaddeus P., 1986, ApJ, 305, 892

Dannerbauer H., Lehnert M. D., Lutz D., Tacconi L., Bertoldi F., Carilli C., Genzel R., Menten K., 2002, ApJ, 573, 473

Dannerbauer H., Harrington K., Díaz-Sánchez A., Iglesias-Groth S., Rebolo R., Genova-Santos R. T., Krips M., 2019, AJ, 158, 34

De Breuck C., et al., 2019, A&A, 631, A167

Decarli R., et al., 2012, ApJ, 752, 2

Decarli R., et al., 2014, ApJ, 782, 78

Decarli R., et al., 2016, ApJ, 833, 69

Díaz-Sánchez A., Iglesias-Groth S., Rebolo R., Dannerbauer H., 2017, ApJL, 843, L22

Díaz-Santos T., et al., 2013, ApJ, 774, 68

Díaz-Santos T., et al., 2016, ApJL, 816, L6

Díaz-Santos T., et al., 2017, ApJ, 846, 32

Dickman R. L., 1975, ApJ, 202, 50

Dickman R. L., 1978, ApJS, 37, 407

Dickman R. L., Snell R. L., Schloerb F. P., 1986, ApJ, 309, 326

Diehl R., 2018, arXiv e-prints, p. arXiv:1811.10604

Dietrich J., et al., 2018, MNRAS, 480, 3562

Dobbs C. L., Pringle J. E., 2013, MNRAS, 432, 653

Dole H., et al., 2004, ApJS, 154, 87

Dong C., et al., 2019, ApJ, 873, 50

Dopita M. A., Mathewson D. S., Ford V. L., 1985, ApJ, 297, 599

Downes D., Eckart A., 2007, A&A, 468, L57

Downes D., Solomon P. M., 1998, ApJ, 507, 615

Downes D., Solomon P. M., Radford S. J. E., 1993, ApJL, 414, L13

Draine B. T., 2011, Physics of the Interstellar and Intergalactic Medium

Draine B. T., Li A., 2007, ApJ, 657, 810

Draine B. T., McKee C. F., 1993, ARA&A, 31, 373

Draine B. T., et al., 2007, ApJ, 663, 866

Dye S., et al., 2014, MNRAS, 440, 2013

Eales S., Lilly S., Gear W., Dunne L., Bond J. R., Hammer F., Le Fèvre O., Crampton D., 1999, ApJ, 515, 518

Eales S., et al., 2010, PASP, 122, 499

Eales S., et al., 2012, ApJ, 761, 168

Efstathiou A., Rowan-Robinson M., Siebenmorgen R., 2000, MNRAS, 313, 734

Ekström S., et al., 2012, A&A, 537, A146

Elbaz D., et al., 2007, A&A, 468, 33

Elbaz D., et al., 2011, A&A, 533, A119

Elbaz D., et al., 2018a, A&A, 616, A110

Elbaz D., et al., 2018b, A&A, 616, A110

Elmegreen B. G., 1991, ApJ, 378, 139

Elmegreen B. G., Scalo J., 2004, ARA&A, 42, 211

Emerson J. P., Jennings R. E., Moorwood A. F. M., 1973, ApJ, 184, 401

Emonts B. H. C., et al., 2014, MNRAS, 438, 2898

Falgarone E., et al., 2017, Nature, 548, 430

Fan X., et al., 2006, AJ, 132, 117

Fanaroff B. L., Riley J. M., 1974, MNRAS, 167, 31P

Fardal M. A., Katz N., Weinberg D. H., Davé R., 2007, MNRAS, 379, 985

Farrah D., et al., 2013, ApJ, 776, 38

Faucher-Giguère C.-A., Quataert E., Hopkins P. F., 2013, MNRAS, 433, 1970

Feltre A., Hatziminaoglou E., Fritz J., Franceschini A., 2012, MNRAS, 426, 120

Ferkinhoff C., Hailey-Dunsheath S., Nikola T., Parshley S. C., Stacey G. J., Benford D. J., Staguhn J. G., 2010, ApJL, 714, L147

Ferkinhoff C., et al., 2011, ApJL, 740, L29

Ferkinhoff C., Brisbin D., Nikola T., Stacey G. J., Sheth K., Hailey-Dunsheath S., Falgarone E., 2015, ApJ, 806, 260

Fernández-Ontiveros J. A., Spinoglio L., Pereira-Santaella M., Malkan M. A., Andreani P., Dasyra K. M., 2016, ApJS, 226, 19

Field G. B., 1965, ApJ, 142, 531

Finkelstein S. L., et al., 2012, ApJ, 756, 164

Finkelstein S. L., et al., 2015, ApJ, 810, 71

Finlator K., Davé R., Papovich C., Hernquist L., 2006, ApJ, 639, 672

Fischer J., et al., 2010, A&A, 518, L41

Fixsen D. J., Bennett C. L., Mather J. C., 1999, ApJ, 526, 207

Fleck R. C. J., 1981, ApJL, 246, L151

Flower D. R., Launay J. M., 1985, MNRAS, 214, 271

Flower D. R., Pineau des Forêts G., 2001, MNRAS, 323, 672

Flower D. R., Pineau des Forêts G., 2003, MNRAS, 343, 390

Fox M. J., et al., 2002, MNRAS, 331, 839

Frayer D. T., et al., 2011, ApJL, 726, L22

Frayer D. T., Maddalena R. J., Ivison R. J., Smail I., Blain A. W., Vanden Bout P., 2018a, ApJ, 860, 87

Frayer D. T., Maddalena R. J., Ivison R. J., Smail I., Blain A. W., Vanden Bout P., 2018b, ApJ, 860, 87

Frerking M. A., Keene J., Blake G. A., Phillips T. G., 1989, ApJ, 344, 311

Friedmann A., 1922, Zeitschrift fur Physik, 10, 377

Frye B. L., et al., 2019, ApJ, 871, 51

Fu H., et al., 2012, ApJ, 753, 134

Fu H., et al., 2013, Nature, 498, 338

Fujimoto S., Ouchi M., Shibuya T., Nagai H., 2017, ApJ, 850, 83

Fukugita M., Peebles P. J. E., 2004, ApJ, 616, 643

García P., Bronfman L., Nyman L.-Å., Dame T. M., Luna A., 2014, ApJS, 212, 2

Gaspari M., Brighenti F., Temi P., 2012, MNRAS, 424, 190

Gawiser E., Silk J., 2000, Physics Reports, 333, 245

Geach J. E., Smail I., Moran S. M., MacArthur L. A., Lagos C. d. P., Edge A. C., 2011, ApJL, 730, L19

Geach J. E., et al., 2013, MNRAS, 432, 53

Geach J. E., et al., 2015, MNRAS, 452, 502

Geach J. E., Ivison R. J., Dye S., Oteo I., 2018, ApJL, 866, L12

Genzel R., et al., 2010, MNRAS, 407, 2091

Genzel R., et al., 2012, ApJ, 746, 69

Genzel R., et al., 2013, ApJ, 773, 68

Genzel R., et al., 2015a, ApJ, 800, 20

Genzel R., et al., 2015b, ApJ, 800, 20

Gerin M., Phillips T. G., 2000, ApJ, 537, 644

Ginsburg A., Federrath C., Darling J., 2013, ApJ, 779, 50

Ginsburg A., et al., 2018, ApJ, 853, 171

Glikman E., Simmons B., Mailly M., Schawinski K., Urry C. M., Lacy M., 2015, ApJ, 806, 218

Glover S. C. O., Clark P. C., 2012, MNRAS, 421, 9

Glover S. C. O., Clark P. C., 2014, MNRAS, 437, 9

Glover S. C. O., Mac Low M. M., 2011, MNRAS, 412, 337

Glover S. C. O., Clark P. C., Micic M., Molina F., 2015, MNRAS, 448, 1607

Goldbaum N. J., Krumholz M. R., Forbes J. C., 2016, ApJ, 827, 28

Goldreich P., Kwan J., 1974, ApJ, 189, 441

Goldsmith P. F., 2001, ApJ, 557, 736

Goldsmith P. F., Langer W. D., Pineda J. L., Velusamy T., 2012, ApJS, 203, 13

Goldsmith P. F., Yıldız U. A., Langer W. D., Pineda J. L., 2015, ApJ, 814, 133

Goto T., et al., 2011, MNRAS, 410, 573

Governato F., et al., 2010, Nature, 463, 203

Gowardhan A., Riechers D. A., Daddi E., Pavesi R., Dannerbauer H., Carilli C., 2017, ApJ, 838, 136

Graciá-Carpio J., et al., 2011, ApJ, 728, L7

Greene J. E., Zakamska N. L., Ho L. C., Barth A. J., 2011, ApJ, 732, 9

Greve T. R., Ivison R. J., Papadopoulos P. P., 2003, ApJ, 599, 839

Greve T. R., et al., 2005, MNRAS, 359, 1165

Greve T. R., Papadopoulos P. P., Gao Y., Radford S. J. E., 2009, ApJ, 692, 1432

Greve T. R., et al., 2012, ApJ, 756, 101

Greve T. R., et al., 2014, ApJ, 794, 142

Guedes J., Callegari S., Madau P., Mayer L., 2011, ApJ, 742, 76

Güsten R., Nyman L. Å., Schilke P., Menten K., Cesarsky C., Booth R., 2006, A&A, 454, L13

Güver T., Özel F., 2009, MNRAS, 400, 2050

Haid S., Walch S., Seifried D., Wünsch R., Dinnbier F., Naab T., 2018, MNRAS, 478, 4799

Haid S., Walch S., Seifried D., Wünsch R., Dinnbier F., Naab T., 2019, MNRAS, 482, 4062

Hailey-Dunsheath S., Nikola T., Stacey G. J., Oberst T. E., Parshley S. C., Bradford C. M., Ade P. A. R., Tucker C. E., 2008, ApJ, 689, L109

Hailey-Dunsheath S., et al., 2012, ApJ, 755, 57

Hainline L. J., Blain A. W., Greve T. R., Chapman S. C., Smail I., Ivison R. J., 2006, ApJ, 650, 614

Harrington K. C., et al., 2016, MNRAS, 458, 4383

Harrington K. C., et al., 2018, MNRAS, 474, 3866

Harrington K. C., et al., 2019, MNRAS, 488, 1489

Harris G. L. H., Harris W. E., 2011, MNRAS, 410, 2347

Harris A. I., et al., 2012, ApJ, 752, 152

Hatsukade B., et al., 2011, MNRAS, 411, 102

Hayward C. C., Kereš D., Jonsson P., Narayanan D., Cox T. J., Hernquist L., 2011, ApJ, 743, 159

Hayward C. C., Jonsson P., Kereš D., Magnelli B., Hernquist L., Cox T. J., 2012, MNRAS, 424, 951

Hayward C. C., Narayanan D., Kereš D., Jonsson P., Hopkins P. F., Cox T. J., Hernquist L., 2013, MNRAS, 428, 2529

Heger A., Fryer C. L., Woosley S. E., Langer N., Hartmann D. H., 2003, ApJ, 591, 288

Heiles C., 1967, ApJ, 148, 299

Heintz K. E., Watson D., 2020, ApJL, 889, L7

Helou G., Soifer B. T., Rowan-Robinson M., 1985, ApJL, 298, L7

Herrera-Camus R., et al., 2016a, ApJ, 826, 175

Herrera-Camus R., et al., 2016b, ApJ, 826, 175

Heyminck S., Kasemann C., Güsten R., de Lange G., Graf U. U., 2006a, A&A, 454, L21

Heyminck S., Kasemann C., Güsten R., de Lange G., Graf U. U., 2006b, A&A, 454, L21

Hezaveh Y. D., Marrone D. P., Holder G. P., 2012, ApJ, 761, 20

Hezaveh Y. D., et al., 2013, ApJ, 767, 132

Hickox R. C., Alexander D. M., 2018, ARA&A, 56, 625

Hildebrand R. H., 1983, QJRAS, 24, 267

Hildebrand R. H., Whitcomb S. E., Winston R., Stiening R. F., Harper D. A., Moseley S. H., 1977, ApJ, 216, 698

Hinshaw G., et al., 2009, ApJS, 180, 225

Hodge J. A., 2010, PhD thesis, University of California, Davis

Hodge J. A., da Cunha E., 2020, arXiv e-prints, p. arXiv:2004.00934

Hodge J. A., Carilli C. L., Walter F., de Blok W. J. G., Riechers D., Daddi E., Lentati L., 2012, ApJ, 760, 11

Hodge J. A., et al., 2016, ApJ, 833, 103

Holland W. S., et al., 1999, MNRAS, 303, 659

Hollenbach D., 1985, ICARUS, 61, 36

Hollenbach D. J., Tielens A. G. G. M., 1997, ARA&A, 35, 179

Hollenbach D. J., Tielens A. G. G. M., 1999, Reviews of Modern Physics, 71, 173

Hopkins P. F., Quataert E., 2010, MNRAS, 407, 1529

Hopkins P. F., Hernquist L., Cox T. J., Kereš D., 2008, ApJS, 175, 356

Hopkins P. F., Quataert E., Murray N., 2011, MNRAS, 417, 950

Hopkins P. F., Quataert E., Murray N., 2012, MNRAS, 421, 3522

Hopkins P. F., Cox T. J., Hernquist L., Narayanan D., Hayward C. C., Murray N., 2013, MNRAS, 430, 1901

Hu W., Dodelson S., 2002, ARA&A, 40, 171

Huang J. S., et al., 2014, ApJ, 784, 52

Hubble E. P., 1926, ApJ, 64, 321

Hubble E., 1929, Proceedings of the National Academy of Science, 15, 168

Hughes D. H., et al., 1998, Nature, 394, 241

Hughes T. M., et al., 2017, MNRAS, 468, L103

Hunt L. K., et al., 2015, A&A, 583, A114

Huynh M. T., et al., 2017, MNRAS, 467, 1222

Iffrig O., Hennebelle P., 2015, A&A, 576, A95

Iglesias-Groth S., Díaz-Sánchez A., Rebolo R., Dannerbauer H., 2017, MNRAS, 467, 330

Indriolo N., Bergin E. A., Falgarone E., Godard B., Zwaan M. A., Neufeld D. A., Wolfire M. G., 2018, ApJ, 865, 127

Iono D., et al., 2009, ApJ, 695, 1537

Irwin M. J., Ibata R. A., Lewis G. F., Totten E. J., 1998, ApJ, 505, 529

Israel F. P., 2005, Ap&SS, 295, 171

Israel F. P., 2020, A&A, 635, A131

Israel F. P., Baas F., 2002, A&A, 383, 82

Israel F. P., Baas F., 2003, A&A, 404, 495

Israel F. P., Rosenberg M. J. F., van der Werf P., 2015, A&A, 578, A95

Ivison R. J., et al., 2010, A&A, 518, L31

Ivison R. J., Papadopoulos P. P., Smail I., Greve T. R., Thomson A. P., Xilouris E. M., Chapman S. C., 2011, MNRAS, 412, 1913

Ivison R. J., et al., 2013, ApJ, 772, 137

Jacquet E., Balbus S., Latter H., 2011, MNRAS, 415, 3591

Jansky K. G., 1933, Nature, 132, 66

Jiang Y.-F., Stone J. M., Davis S. W., 2019, ApJ, 880, 67

Jiménez-Andrade E. F., et al., 2019a, A&A, 625, A114

Jiménez-Andrade E. F., et al., 2019b, A&A, 625, A114

Jiménez-Andrade E. F., et al., 2020, ApJ, 890, 171

Jin S., et al., 2019, ApJ, 887, 144

Johnson S. P., et al., 2013, MNRAS, 431, 662

Johnson H. L., et al., 2018, MNRAS, 474, 5076

Jones T. W., Ryu D., Engel A., 1999, ApJ, 512, 105

Joung M. R., Mac Low M.-M., Bryan G. L., 2009, ApJ, 704, 137

Kaasinen M., et al., 2019, ApJ, 880, 15

Kamenetzky J., Rangwala N., Glenn J., Maloney P. R., Conley A., 2014, ApJ, 795, 174

Kamenetzky J., Rangwala N., Glenn J., Maloney P. R., Conley A., 2016, ApJ, 829, 93

Kassin S. A., et al., 2012, ApJ, 758, 106

Kawara K., et al., 2004, A&A, 413, 843

Keene J., Lis D. C., Phillips T. G., Schilke P., 1997, in van Dishoeck E. F., ed., IAU Symposium Vol. 178, IAU Symposium. pp 129–139

Keller B. W., Kruijssen J. M. D., Wadsley J. W., 2020, MNRAS, 493, 2149

Kennicutt Robert C. J., 1998, ARA&A, 36, 189

Kennicutt R. C., Evans N. J., 2012, ARA&A, 50, 531

Kereš D., Katz N., Weinberg D. H., Davé R., 2005, MNRAS, 363, 2

Kevlahan N., Pudritz R. E., 2009, ApJ, 702, 39

Kewley L. J., Nicholls D. C., Sutherland R. S., 2019, ARA&A, 57, 511

Khatri R., Gaspari M., 2016, MNRAS, 463, 655

Kim J., Park C., Gott J. Richard I., Dubinski J., 2009, ApJ, 701, 1547

Kirkpatrick A., et al., 2013, ApJ, 763, 123

Kirkpatrick A., Pope A., Sajina A., Roebuck E., Yan L., Armus L., Díaz-Santos T., Stierwalt S., 2015, ApJ, 814, 9

Kirkpatrick A., et al., 2017a, ApJ, 849, 111

Kirkpatrick A., et al., 2017b, ApJ, 849, 111

Kirkpatrick A., Sharon C., Keller E., Pope A., 2019, ApJ, 879, 41

Klein B., Philipp S. D., Krämer I., Kasemann C., Güsten R., Menten K. M., 2006, A&A, 454, L29

Klessen R. S., 2000, ApJ, 535, 869

Kochanek C. S., et al., 2000, ApJ, 543, 131

Kolmogorov A., 1941, Akademiia Nauk SSSR Doklady, 30, 301

Kowal G., Lazarian A., Beresnyak A., 2007, ApJ, 658, 423

Kreysa E., et al., 1998, in Phillips T. G., ed., Society of Photo-Optical Instrumentation Engineers (SPIE) Conference Series Vol. 3357, Proc. SPIE. pp 319–325, doi:10.1117/12.317367

Kristensen L. E., Ravkilde T. L., Pineau Des Forêts G., Cabrit S., Field D., Gustafsson M., Diana S., Lemaire J. L., 2008, A&A, 477, 203

Kronberg P. P., Biermann P., Schwab F. R., 1981, ApJ, 246, 751

Kroupa P., 2002, Science, 295, 82

Kroupa P., Weidner C., Pflamm-Altenburg J., Thies I., Dabringhausen J., Marks M., Maschberger T., 2013, The Stellar and Sub-Stellar Initial Mass Function of Simple and Composite Populations. p. 115, doi:10.1007/978-94-007-5612-0_4

Kruegel E., Siebenmorgen R., 1994a, A&A, 288, 929

Kruegel E., Siebenmorgen R., 1994b, A&A, 288, 929

Kruijssen J. M. D., Longmore S. N., 2013, MNRAS, 435, 2598

Krumholz M. R., 2014, Physics Reports, 539, 49

Krumholz M. R., Burkhart B., 2016, MNRAS, 458, 1671

Krumholz M. R., McKee C. F., 2005, ApJ, 630, 250

Krumholz M. R., Matzner C. D., McKee C. F., 2006, ApJ, 653, 361

Krumholz M. R., Klein R. I., McKee C. F., 2007, ApJ, 656, 959

Krumholz M. R., Klein R. I., McKee C. F., Offner S. S. R., Cunningham A. J., 2009a, Science, 323, 754

Krumholz M. R., McKee C. F., Tumlinson J., 2009b, ApJ, 699, 850

Krumholz M. R., Leroy A. K., McKee C. F., 2011, ApJ, 731, 25

Krumholz M. R., Dekel A., McKee C. F., 2012, ApJ, 745, 69

Krumholz M. R., Burkhart B., Forbes J. C., Crocker R. M., 2018, MNRAS, 477, 2716

Kwan J., Thuan T. X., 1974, ApJ, 194, 293

Lada C. J., Lombardi M., Alves J. F., 2010, ApJ, 724, 687

Lamarche C., et al., 2017, ApJ, 836, 123

Larson R. B., 1987, in Thuan T. X., Montmerle T., Tran Thanh van J., eds, Starbursts and Galaxy Evolution. pp 467–482

Leitherer C., Heckman T. M., 1995, ApJS, 96, 9

Leitherer C., et al., 1999, ApJS, 123, 3

Lemke D., et al., 1996, A&A, 315, L64

Lenkić L., et al., 2020, AJ, 159, 190

Lentati L., et al., 2015, ApJ, 800, 67

Leroy A., Bolatto A., Stanimirovic S., Mizuno N., Israel F., Bot C., 2007, ApJ, 658, 1027

Leroy A. K., et al., 2011, ApJ, 737, 12

Leroy A. K., et al., 2013, AJ, 146, 19

Lestrade J.-F., Carilli C. L., Thanjavur K., Kneib J.-P., Riechers D. A., Bertoldi F., Walter F., Omont A., 2011, ApJL, 739, L30

Leung T. K. D., Riechers D. A., Pavesi R., 2017, ApJ, 836, 180

Leung T. K. D., et al., 2019a, ApJ, 871, 85

Leung T. K. D., et al., 2019b, ApJ, 871, 85

Leung T. K. D., Pallottini A., Ferrara A., Mac Low M.-M., 2020, ApJ, 895, 24

Liang L., Feldmann R., Faucher-Giguère C.-A., Kereš D., Hopkins P. F., Hayward C. C., Quataert E., Scoville N. Z., 2018, MNRAS, 478, L83

Liang L., et al., 2019, MNRAS, 489, 1397

Lilley A. E., 1955, ApJ, 121, 559

Lilly S. J., Le Fevre O., Hammer F., Crampton D., 1996, ApJL, 460, L1

Lilly S. J., Eales S. A., Gear W. K. P., Hammer F., Le Fèvre O., Crampton D., Bond J. R., Dunne L., 1999, ApJ, 518, 641

Liu D., Gao Y., Isaak K., Daddi E., Yang C., Lu N., van der Werf P., 2015, ApJL, 810, L14

Liu L., et al., 2017, ApJ, 846, 5

Liu D., et al., 2019, ApJ, 887, 235

Livermore R. C., Finkelstein S. L., Lotz J. M., 2017, ApJ, 835, 113

Lonsdale C. J., Hacking P. B., 1987, in Bergeron J., Kunth D., Rocca-Volmerange B., Tran Thanh Van J., eds, High Redshift and Primeval Galaxies. pp 141–145

Lu R.-S., Broderick A. E., Baron F., Monnier J. D., Fish V. L., Doeleman S. S., Pankratius V., 2014, ApJ, 788, 120

Lu N., et al., 2017, ApJS, 230, 1

Lu N., et al., 2018, ApJ, 864, 38

Lucy L. B., 1971, ApJ, 163, 95

Lutz D., et al., 2016, A&A, 591, A136

Madau P., Dickinson M., 2014, ARA&A, 52, 415

Madau P., Ferguson H. C., Dickinson M. E., Giavalisco M., Steidel C. C., Fruchter A., 1996, MNRAS, 283, 1388

Maeder A., Meynet G., 2000, A&A, 361, 159

Magdis G. E., et al., 2011, ApJL, 740, L15

Magdis G. E., et al., 2012, ApJ, 760, 6

Magdis G. E., et al., 2016, MNRAS, 456, 4533

Magnelli B., Elbaz D., Chary R. R., Dickinson M., Le Borgne D., Frayer D. T., Willmer C. N. A., 2011, A&A, 528, A35

Magnelli B., et al., 2012, A&A, 548, A22

Magnelli B., et al., 2013, A&A, 553, A132

Magnelli B., et al., 2014, A&A, 561, A86

Maiolino R., et al., 2005, A&A, 440, L51

Maiolino R., Caselli P., Nagao T., Walmsley M., De Breuck C., Meneghetti M., 2009, A&A, 500, L1

Malhotra S., et al., 2001, ApJ, 561, 766

Maloney P., Black J. H., 1988, ApJ, 325, 389

Marchesini D., van Dokkum P. G., Förster Schreiber N. M., Franx M., Labbé I., Wuyts S., 2009, ApJ, 701, 1765

Marganian P., Garwood R. W., Braatz J. A., Radziwill N. M., Maddalena R. J., 2013, GBTIDL: Reduction and Analysis of GBT Spectral Line Data (ascl:1303.019)

Marrone D. P., et al., 2018a, Nature, 553, 51

Marrone D. P., et al., 2018b, Nature, 553, 51

Marshall P. J., et al., 2016, MNRAS, 455, 1171

Martizzi D., Fielding D., Faucher-Giguère C.-A., Quataert E., 2016, MNRAS, 459, 2311

Mashian N., et al., 2015, ApJ, 802, 81

Mauersberger R., Henkel C., Walsh W., Schulz A., 1999, A&A, 341, 256

McKee C. F., 1989, ApJ, 345, 782

McKee C. F., Ostriker E. C., 2007, ARA&A, 45, 565

McKee C. F., Williams J. P., 1997, ApJ, 476, 144

McLure R. J., et al., 2015, VizieR Online Data Catalog, p. J/MNRAS/432/2696

McNamara B. R., et al., 2014, ApJ, 785, 44

McNamara B. R., Russell H. R., Nulsen P. E. J., Hogan M. T., Fabian A. C., Pulido F., Edge A. C., 2016, ApJ, 830, 79

Meijerink R., Spaans M., Israel F. P., 2006, ApJL, 650, L103

Meijerink R., Spaans M., Israel F. P., 2007, A&A, 461, 793

Meijerink R., Spaans M., Loenen A. F., van der Werf P. P., 2011, A&A, 525, A119

Melchiorri F., Ceccarelli C., Pietranera L., Melchiorri B. O., 1981, ApJL, 250, L1

Mentuch Cooper E., et al., 2012, ApJ, 755, 165

Mineo S., Gilfanov M., Lehmer B. D., Morrison G. E., Sunyaev R., 2014, MNRAS, 437, 1698

Molina F. Z., Glover S. C. O., Federrath C., Klessen R. S., 2012, MNRAS, 423, 2680

Moser L., et al., 2017, A&A, 603, A68

Mullaney J. R., Alexander D. M., Goulding A. D., Hickox R. C., 2011, MNRAS, 414, 1082

Mullaney J. R., et al., 2012, MNRAS, 419, 95

Münch G., Wilson O. C., 1962, ZAp, 56, 127

Murphy E. J., et al., 2011, ApJ, 737, 67

Nagao T., Maiolino R., De Breuck C., Caselli P., Hatsukade B., Saigo K., 2012, A&A, 542, L34

Nakamura F., Li Z.-Y., 2007, ApJ, 662, 395

Narayanan D., Davé R., 2013, MNRAS, 436, 2892

Narayanan D., Krumholz M. R., 2014, MNRAS, 442, 1411

Narayanan D., et al., 2008a, ApJS, 176, 331

Narayanan D., Cox T. J., Shirley Y., Davé R., Hernquist L., Walker C. K., 2008b, ApJ, 684, 996

Narayanan D., Cox T. J., Hayward C. C., Younger J. D., Hernquist L., 2009, MNRAS, 400, 1919

Narayanan D., Krumholz M. R., Ostriker E. C., Hernquist L., 2012, MNRAS, 421, 3127

Narayanan D., et al., 2015, Nature, 525, 496

Navarro J. F., Steinmetz M., 2000, ApJ, 528, 607

Nayyeri H., et al., 2016, ApJ, 823, 17

Negrello M., Perrotta F., González-Nuevo J., Silva L., de Zotti G., Granato G. L., Baccigalupi C., Danese L., 2007, MNRAS, 377, 1557

Negrello M., et al., 2010, Science, 330, 800

Negrello M., et al., 2013, MNRAS, 429, 1309

Negrello M., et al., 2017a, MNRAS, 465, 3558

Negrello M., et al., 2017b, MNRAS, 465, 3558

Neri R., et al., 2020, A&A, 635, A7

Nesvadba N. P. H., Cañameras R., Kneissl R., Koenig S., Yang C., Le Floc'h E., Omont A., Scott D., 2019, A&A, 624, A23

Nikola T., Stacey G. J., Brisbin D., Ferkinhoff C., Hailey-Dunsheath S., Parshley S., Tucker C., 2011a, ApJ, 742, 88

Nikola T., Stacey G. J., Brisbin D., Ferkinhoff C., Hailey-Dunsheath S., Parshley S., Tucker C., 2011b, ApJ, 742, 88

Noeske K. G., et al., 2007, ApJL, 660, L43

Noll S., Burgarella D., Giovannoli E., Buat V., Marcillac D., Muñoz-Mateos J. C., 2009, A&A, 507, 1793

Norman C., Silk J., 1980, ApJ, 238, 158

Oberst T. E., et al., 2006, ApJL, 652, L125

Oberst T. E., Parshley S. C., Nikola T., Stacey G. J., Löhr A., Lane A. P., Stark A. A., Kamenetzky J., 2011, ApJ, 739, 100

Obreschkow D., Croton D., De Lucia G., Khochfar S., Rawlings S., 2009, ApJ, 698, 1467

Offner S. S. R., Clark P. C., Hennebelle P., Bastian N., Bate M. R., Hopkins P. F., Moraux E., Whitworth A. P., 2014, in Beuther H., Klessen R. S., Dullemond C. P., Henning T., eds, Protostars and Planets VI. p. 53 (arXiv:1312.5326), doi:10.2458/azu_uapress_9780816531240-ch003

Ojha R., et al., 2001, ApJ, 548, 253

Oliver S. J., et al., 2012, MNRAS, 424, 1614

Omont A., 2007, Reports on Progress in Physics, 70, 1099

Ostriker E. C., 1998, in Holt S. S., Kallman T. R., eds, American Institute of Physics Conference Series Vol. 431, American Institute of Physics Conference Series. pp 484–494 (arXiv:astro-ph/9712337), doi:10.1063/1.55937

Ostriker E. C., Shetty R., 2011, ApJ, 731, 41

Ostriker E. C., McKee C. F., Leroy A. K., 2010, ApJ, 721, 975

Oteo I., Zwaan M. A., Ivison R. J., Smail I., Biggs A. D., 2016, ApJ, 822, 36

Oteo I., Zwaan M. A., Ivison R. J., Smail I., Biggs A. D., 2017, ApJ, 837, 182

Padoan P., Jones B. J. T., Nordlund Å. P., 1997, ApJ, 474, 730

Panuzzo P., et al., 2010, A&A, 518, L37

Papadopoulos P. P., Greve T. R., 2004, ApJL, 615, L29

Papadopoulos P. P., Thi W.-F., Miniati F., Viti S., 2011, MNRAS, 414, 1705

Papadopoulos P. P., van der Werf P. P., Xilouris E. M., Isaak K. G., Gao Y., Mühle S., 2012a, MNRAS, 426, 2601

Papadopoulos P. P., van der Werf P., Xilouris E., Isaak K. G., Gao Y., 2012b, ApJ, 751, 10

Papadopoulos P. P., et al., 2014, ApJ, 788, 153

Parkin T. J., et al., 2013, ApJ, 776, 65

Pavesi R., et al., 2016, ApJ, 832, 151

Pavesi R., Riechers D. A., Faisst A. L., Stacey G. J., Capak P. L., 2019, ApJ, 882, 168

Peacock J. A., Wall J. V., 1982, MNRAS, 198, 843

Peebles P. J. E., 1982, ApJL, 263, L1

Pei Y. C., 1993, ApJ, 403, 7

Penzias A. A., Wilson R. W., 1965, ApJ, 142, 419

Perna M., et al., 2018, A&A, 619, A90

Petuchowski S. J., Bennett C. L., Haas M. R., Erickson E. F., Lord S. D., Rubin R. H., Colgan S. W. J., Hollenbach D. J., 1994, ApJ, 427, L17

Pety J., 2005, in Casoli F., Contini T., Hameury J. M., Pagani L., eds, SF2A-2005: Semaine de l'Astrophysique Francaise. p. 721

Pham D. T., Castellani M., 2009, Proceedings of the Institution of Mechanical Engineers, Part C: Journal of Mechanical Engineering Science, 223, 2919

Planck Collaboration XXVII 2015, A&A, 582, A30

Planck Collaboration et al., 2011a, A&A, 536, A7

Planck Collaboration et al., 2011b, A&A, 536, A21

Planck Collaboration et al., 2014, A&A, 571, A28

Planck Collaboration et al., 2015, A&A, 576, A107

Poggianti B. M., et al., 2017, ApJ, 844, 48

Pope A., et al., 2006, MNRAS, 370, 1185

Pope A., et al., 2013, ApJ, 772, 92

Popesso P., et al., 2012, A&A, 537, A58

Puls J., Vink J. S., Najarro F., 2008, A&A Rev., 16, 209

Punsly B., Hill G. J., Marziani P., Kharb P., Berton M., Crepaldi L., Indahl B. L., Zeimann G., 2020, ApJ, 898, 169

Puschnig J., et al., 2020, arXiv e-prints, p. arXiv:2004.09142

Quirk W. J., Tinsley B. M., 1973, ApJ, 179, 69

Ramachandran V., et al., 2019, A&A, 625, A104

Rangwala N., et al., 2011, ApJ, 743, 94

Rawle T. D., et al., 2014, ApJ, 783, 59

Reddy N. A., Steidel C. C., Pettini M., Adelberger K. L., Shapley A. E., Erb D. K., Dickinson M., 2008, ApJS, 175, 48

Renaud F., Kraljic K., Bournaud F., 2012, ApJL, 760, L16

Riechers D. A., et al., 2006, ApJ, 650, 604

Riechers D. A., Hodge J., Walter F., Carilli C. L., Bertoldi F., 2011, ApJL, 739, L31

Riechers D. A., et al., 2013, Nature, 496, 329

Riechers D. A., et al., 2014, ApJ, 796, 84

Riechers D. A., et al., 2019, ApJ, 872, 7

Riechers D. A., et al., 2020, ApJL, 896, L21

Rieke G. H., Alonso-Herrero A., Weiner B. J., Pérez-González P. G., Blaylock M., Donley J. L., Marcillac D., 2009, ApJ, 692, 556

Riess A. G., et al., 1998, AJ, 116, 1009

Riess A. G., et al., 2011, ApJ, 730, 119

Rivera J., et al., 2019, ApJ, 879, 95

Robertson H. P., 1929, Proceedings of the National Academy of Science, 15, 822

Robitaille T. P., Whitney B. A., 2010, ApJL, 710, L11

Rodighiero G., et al., 2011, ApJL, 739, L40

Romano D., Matteucci F., Zhang Z. Y., Papadopoulos P. P., Ivison R. J., 2017, MNRAS, 470, 401

Rosdahl J., Schaye J., Dubois Y., Kimm T., Teyssier R., 2017, MNRAS, 466, 11

Rosenberg M. J. F., Kazandjian M. V., van der Werf P. P., Israel F. P., Meijerink R., Weiß A., Requena-Torres M. A., Güsten R., 2014, A&A, 564, A126

Rosenberg M. J. F., et al., 2015, ApJ, 801, 72

Roussel H., et al., 2007, ApJ, 669, 959

Rowan-Robinson M., et al., 1991, Nature, 351, 719

Różańska A., Czerny B., Kunneriath D., Adhikari T. P., Karas V., Mościbrodzka M., 2014, MNRAS, 445, 4385

Różańska A., Kunneriath D., Czerny B., Adhikari T. P., Karas V., 2017, MNRAS, 464, 2090

Rubin V. C., Ford W. K. J., Thonnard N., 1980, ApJ, 238, 471

Rujopakarn W., et al., 2010, ApJ, 718, 1171

Rujopakarn W., et al., 2016a, ApJ, 833, 12

Rujopakarn W., et al., 2016b, ApJ, 833, 12

Russell H. R., et al., 2016, MNRAS, 458, 3134

Saintonge A., et al., 2013, ApJ, 778, 2

Saintonge A., et al., 2016a, MNRAS, 462, 1749

Saintonge A., et al., 2016b, MNRAS, 462, 1749

Salmon B., et al., 2015, ApJ, 799, 183

Salomé P., Guélin M., Downes D., Cox P., Guilloteau S., Omont A., Gavazzi R., Neri R., 2012, A&A, 545, A57

Salpeter E. E., 1955, ApJ, 121, 161

Sandage A., 1970, ApJ, 162, 841

Sanders D. B., Mirabel I. F., 1996, ARA&A, 34, 749

Sanders D. B., Soifer B. T., Elias J. H., Madore B. F., Matthews K., Neugebauer G., Scoville N. Z., 1988, ApJ, 325, 74

Sanders D. B., Phinney E. S., Neugebauer G., Soifer B. T., Matthews K., 1989, ApJ, 347, 29

Sanders D. B., Scoville N. Z., Soifer B. T., 1991, ApJ, 370, 158

Sandstrom K. M., et al., 2013, ApJ, 777, 5

Sargent M. T., Béthermin M., Daddi E., Elbaz D., 2012, ApJL, 747, L31

Sargent M. T., et al., 2014, ApJ, 793, 19

Savage B. D., Code A. D., 1970, in Muller R., Houziaux L., Butler H. E., eds, IAU Symposium Vol. 36, Ultraviolet Stellar Spectra and Related Ground-Based Observations. p. 302

Savage B. D., Sembach K. R., 1996, ApJ, 470, 893

Scalo J., Elmegreen B. G., 2004, ARA&A, 42, 275

Scannapieco C., et al., 2012, MNRAS, 423, 1726

Schinnerer E., et al., 2016, ApJ, 833, 112

Schmidt M., 1959, ApJ, 129, 243

Schmidt W., Federrath C., Hupp M., Kern S., Niemeyer J. C., 2009, A&A, 494, 127

Schmidt W., Engels J. F., Niemeyer J. C., Almgren A. S., 2016, MNRAS, 459, 701

Schneider N., Simon R., Kramer C., Kraemer K., Stutzki J., Mookerjea B., 2003a, A&A, 406, 915

Schneider R., Ferrara A., Salvaterra R., Omukai K., Bromm V., 2003b, Nature, 422, 869

Schruba A., et al., 2012, AJ, 143, 138

Schulz B., et al., 2017, arXiv e-prints, p. arXiv:1706.00448

Scott K. S., et al., 2010, MNRAS, 405, 2260

Scott K. S., et al., 2011, ApJ, 733, 29

Scott K. S., et al., 2012a, MNRAS, 423, 575

Scott K. S., et al., 2012b, MNRAS, 423, 575

Scoville N. Z., Solomon P. M., 1974, ApJL, 187, L67

Scoville N., Young J. S., 1983, ApJ, 265, 148

Scoville N. Z., Yun M. S., Clemens D. P., Sand ers D. B., Waller W. H., 1987, ApJS, 63, 821

Scoville N. Z., Sargent A. I., Sanders D. B., Soifer B. T., 1991, ApJL, 366, L5

Scoville N., Lee N., LeFloch E., Sanders D., 2012, in American Astronomical Society Meeting Abstracts #220. p. 517.05

Scoville N., et al., 2014, ApJ, 783, 84

Scoville N., et al., 2016a, ApJ, 820, 83

Scoville N., et al., 2016b, ApJ, 824, 63

Scoville N., et al., 2017, ApJ, 837, 150

Seifried D., et al., 2017, MNRAS, 472, 4797

Serjeant S., 2012, MNRAS, 424, 2429

Shapley A. E., 2011, ARA&A, 49, 525

Sharma M., Nath B. B., 2012, ApJ, 750, 55

Sharon C. E., Riechers D. A., Hodge J., Carilli C. L., Walter F., Weiß A., Knudsen K. K., Wagg J., 2016, ApJ, 827, 18

Shetty R., Glover S. C., Dullemond C. P., Klessen R. S., 2011a, MNRAS, 412, 1686

Shetty R., Glover S. C., Dullemond C. P., Ostriker E. C., Harris A. I., Klessen R. S., 2011b, MNRAS, 415, 3253

Shu F. H., Adams F. C., Lizano S., 1987, ARA&A, 25, 23

Siebenmorgen R., Krügel E., Spoon H. W. W., 2004, A&A, 414, 123

Siebenmorgen R., Heymann F., Efstathiou A., 2015, A&A, 583, A120

Silk J., 1997, ApJ, 481, 703

Silk J., Mamon G. A., 2012, Research in Astronomy and Astrophysics, 12, 917

Silverman J. D., et al., 2008, ApJ, 679, 118

Simpson J. M., et al., 2014, ApJ, 788, 125

Simpson J. M., et al., 2015, ApJ, 799, 81

Simpson J. M., et al., 2017, ApJ, 839, 58

Smail I., Ivison R. J., Blain A. W., 1997, ApJL, 490, L5

Smail I., Ivison R. J., Blain A. W., Kneib J. P., 2002, MNRAS, 331, 495

Smith N., 2014, ARA&A, 52, 487

Solomon P. M., Sage L. J., 1988, ApJ, 334, 613

Solomon P. M., Vanden Bout P. A., 2005, ARA&A, 43, 677

Solomon P. M., Rivolo A. R., Barrett J., Yahil A., 1987, ApJ, 319, 730

Solomon P. M., Downes D., Radford S. J. E., 1992, ApJL, 387, L55

Solomon P. M., Downes D., Radford S. J. E., Barrett J. W., 1997, ApJ, 478, 144

Spergel D. N., et al., 2007, ApJS, 170, 377

Spilker J. S., et al., 2016, ApJ, 826, 112

Spilker J., Bezanson R., Marrone D. P., Weiner B. J., Whitaker K. E., Williams C. C., 2017, in American Astronomical Society Meeting Abstracts #229. p. 229.05

Spingola C., et al., 2020, MNRAS, 495, 2387

Spinoglio L., et al., 2012, ApJ, 758, 108

Spinoglio L., Pereira-Santaella M., Dasyra K. M., Calzoletti L., Malkan M. A., Tommasin S., Busquet G., 2015, ApJ, 799, 21

Spitzer L., 1978, Physical processes in the interstellar medium, doi:10.1002/9783527617722.

Stacey G. J., Geis N., Genzel R., Lugten J. B., Poglitsch A., Sternberg A., Townes C. H., 1991, ApJ, 373, 423

Stacey G. J., Hailey-Dunsheath S., Ferkinhoff C., Nikola T., Parshley S. C., Benford D. J., Staguhn J. G., Fiolet N., 2010, ApJ, 724, 957

Stacey H. R., et al., 2018, MNRAS, 476, 5075

Stanway E. R., Eldridge J. J., 2018, preprint, (arXiv:1811.03856)

Stark D. P., 2016, ARA&A, 54, 761

Strandet M. L., et al., 2016, ApJ, 822, 80

Strandet M. L., et al., 2017, ApJL, 842, L15

Sturm E., et al., 2010, A&A, 518, L36

Stutzki J., et al., 1997, ApJL, 477, L33

Su T., et al., 2017, MNRAS, 464, 968

Swinbank A. M., et al., 2008, MNRAS, 391, 420

Swinbank A. M., et al., 2011, ApJ, 742, 11

Swinbank A. M., et al., 2015, ApJL, 806, L17

Tacconi L. J., Genzel R., Tecza M., Gallimore J. F., Downes D., Scoville N. Z., 1999, ApJ, 524, 732

Tacconi L. J., et al., 2006, ApJ, 640, 228

Tacconi L. J., et al., 2008, ApJ, 680, 246

Tacconi L. J., et al., 2010, Nature, 463, 781

Tacconi L. J., et al., 2018, ApJ, 853, 179

Tacconi L. J., Genzel R., Sternberg A., 2020, arXiv e-prints, p. arXiv:2003.06245

Tadaki K.-i., et al., 2020, ApJ, 889, 141

Talia M., et al., 2018, MNRAS, 476, 3956

Tamura Y., Oguri M., Iono D., Hatsukade B., Matsuda Y., Hayashi M., 2015, PASJ, 67, 72

Tayal S. S., 2011, The Astrophysical Journal Supplement Series, 195, 12

Tenorio-Tagle G., Silich S., Martínez-González S., Muñoz-Tuñón C., Palouš J., Wünsch R., 2013, ApJ, 778, 159

Teyssier R., Chapon D., Bournaud F., 2010, ApJL, 720, L149

Thompson T. A., Quataert E., Murray N., 2005, ApJ, 630, 167

Thompson T. A., Quataert E., Waxman E., Murray N., Martin C. L., 2006, ApJ, 645, 186

Thomson A. P., et al., 2012, MNRAS, 425, 2203

Thomson A. P., Ivison R. J., Owen F. N., Danielson A. L. R., Swinbank A. M., Smail I., 2015, MNRAS, 448, 1874

Tielens A. G. G. M., Hollenbach D., 1985, ApJ, 291, 722

Tomassetti M., Porciani C., Romano-Diaz E., Ludlow A. D., Papadopoulos P. P., 2014, MNRAS, 445, L124

Townes C. H., Schawlow A. L., 1975, Microwave spectroscopy.

Tsai C.-W., et al., 2015, ApJ, 805, 90

Tunnard R., Greve T. R., 2017, ApJ, 849, 37

Übler H., et al., 2019, ApJ, 880, 48

Valentino F., et al., 2018, ApJ, 869, 27

Valentino F., et al., 2020, ApJ, 890, 24

Van Loo S., Butler M. J., Tan J. C., 2013, ApJ, 764, 36

Vazquez-Semadeni E., 1994, ApJ, 423, 681

Vazquez-Semadeni E., Passot T., Pouquet A., 1996, ApJ, 473, 881

Veilleux S., Kim D. C., Sanders D. B., 2002, ApJS, 143, 315

Veilleux S., Rupke D. S. N., Swaters R., 2009, ApJL, 700, L149

Veilleux S., Maiolino R., Bolatto A. D., Aalto S., 2020, A&A Rev., 28, 2

Venemans B. P., Neeleman M., Walter F., Novak M., Decarli R., Hennawi J. F., Rix H.-W., 2019, ApJL, 874, L30

Vieira J. D., et al., 2010, ApJ, 719, 763

Vieira J. D., et al., 2013, Nature, 495, 344

Viero M. P., et al., 2014, ApJS, 210, 22

Vishwas A., et al., 2018, ApJ, 856, 174

Wada K., Norman C. A., 2001, ApJ, 547, 172

Walsh D., Carswell R. F., Weymann R. J., 1979, Nature, 279, 381

Walter F., Kerp J., Duric N., Brinks E., Klein U., 1998, ApJL, 502, L143

Walter F., Riechers D., Cox P., Neri R., Carilli C., Bertoldi F., Weiss A., Maiolino R., 2009, Nature, 457, 699

Walter F., Weiß A., Downes D., Decarli R., Henkel C., 2011, ApJ, 730, 18

Walter F., et al., 2014, ApJ, 782, 79

Walter F., et al., 2016, ApJ, 833, 67

Wardlow J. L., et al., 2013, ApJ, 762, 59

Webb T. M. A., 2002, PhD thesis, Department of Astronomy and Astrophysics, University of Toronto

Weiß A., Walter F., Neininger N., Klein U., 1999, A&A, 345, L23

Weiß A., Neininger N., Hüttemeister S., Klein U., 2001, A&A, 365, 571

Weiß A., Henkel C., Downes D., Walter F., 2003, A&A, 409, L41

Weiß A., Downes D., Henkel C., Walter F., 2005a, A&A, 429, L25

Weiß A., Walter F., Scoville N. Z., 2005b, A&A, 438, 533

Weiß A., Downes D., Neri R., Walter F., Henkel C., Wilner D. J., Wagg J., Wiklind T., 2007a, A&A, 467, 955

Weiß A., Downes D., Neri R., Walter F., Henkel C., Wilner D. J., Wagg J., Wiklind T., 2007b, A&A, 467, 955

Weiß A., Kovács A., Güsten R., Menten K. M., Schuller F., Siringo G., Kreysa E., 2008, A&A, 490, 77

Weiß A., et al., 2013, ApJ, 767, 88

Whitaker K. E., van Dokkum P. G., Brammer G., Franx M., 2012, ApJL, 754, L29

Whitaker K. E., et al., 2014, ApJ, 795, 104

Whitaker K. E., Pope A., Cybulski R., Casey C. M., Popping G., Yun M. S., 2017, ApJ, 850, 208

White S. D. M., Rees M. J., 1978, MNRAS, 183, 341

Wilson O. C., Minich G., Flather E., Coffeen M. F., 1959, ApJS, 4, 199

Wilson T. L., Serabyn E., Henkel C., Walmsley C. M., 1986, A&A, 158, L1

Wisnioski E., et al., 2015, ApJ, 799, 209

Wolfire M. G., Hollenbach D., McKee C. F., 2010, ApJ, 716, 1191

Xie T., Allen M., Langer W. D., 1995, ApJ, 440, 674

Yang C., et al., 2017, A&A, 608, A144

Yang G., Brandt W. N., Darvish B., Chen C. T. J., Vito F., Alexander D. M., Bauer F. E., Trump J. R., 2018, MNRAS, 480, 1022

Yang J., et al., 2019a, AJ, 157, 236

Yang C., et al., 2019b, A&A, 624, A138

Yao L., Seaquist E. R., Kuno N., Dunne L., 2003, ApJ, 588, 771

Young J. S., Scoville N. Z., 1991, ARA&A, 29, 581

Young J. S., Schloerb F. P., Kenney J. D., Lord S. D., 1986, ApJ, 304, 443

Young J. S., et al., 1995, ApJS, 98, 219

Young J. S., Allen L., Kenney J. D. P., Lesser A., Rownd B., 1996, AJ, 112, 1903

Yun M. S., Carilli C. L., 2002, ApJ, 568, 88

Yun M. S., et al., 2008, MNRAS, 389, 333

Zanella A., et al., 2018, MNRAS, 481, 1976

Zavala J. A., et al., 2018, Nature Astronomy, 2, 56

Zhang Z.-Y., et al., 2018a, MNRAS, 481, 59

Zhang Z.-Y., Romano D., Ivison R. J., Papadopoulos P. P., Matteucci F., 2018b, Nature, 558, 260

Zhao Y., et al., 2013, ApJL, 765, L13

Zhao Y., et al., 2016, ApJ, 819, 69

Zuckerman B., Evans N. J. I., 1974, ApJL, 192, L149

Zuckerman B., Palmer P., 1975, ApJL, 199, L35

Zweibel E. G., 2013, Physics of Plasmas, 20, 055501

Zwicky F., 1933, Helvetica Physica Acta, 6, 110

da Cunha E., et al., 2013, ApJ, 766, 13

de Jong T., Clegg P. E., Soifer B. T., Rowan-Robinson M., Habing H. J., Houck J. R., Aumann H. H., Raimond E., 1984, ApJL, 278, L67

van der Tak F. F. S., Black J. H., Schöier F. L., Jansen D. J., van Dishoeck E. F., 2007, A&A, 468, 627

van der Werf P. P., et al., 2010, A&A, 518, L42

von Hoerner S., 1951, ZAp, 30, 17

von Weizsäcker C. F., 1951, ApJ, 114, 165

List of Figures

List of Tables

Acknowledgements

I would like to take this moment to truly thank everyone who has supported me from the very beginning of my time in Bonn. Initially it was Alex Karim who personally gave me the offer to join Frank Bertoldi's sub-mm galaxy evolution group, after an enjoyable interview with both Alex and Frank. I am eternally grateful for being given this opportunity. I will always remember going from Boston to Frankfurt airport, and then taking a train to Bonn Hbf for the first time – carrying a backpack full of books, a suitcase with clothes and a cajon inside, two djembes with clothes inside, another couple of duffle bags, a couple of talking drums and my laptop. Frank happened to be available to pick me up, and he brought me to the guest house of the MPIfR – he even carried one of my djembes! I will always thank Frank for being frank and detailed, and for enabling me to jump into my PhD work with a high level of autonomy. I feel as if he treated me as a colleague, rather than only a student. With the expert eyes and ears of my day-to-day supervisor, Benjamin Magnelli, I learned how to truly write scientific papers and conduct high quality research. I have been blessed with a high level of training and insight into the various aspects of being an observer and researcher, most notably from Axel Weiß. I am grateful to Axel for many things, and for setting an example for me to look up to.

I would also like to thank Eric Faustino Jimenez-Andrade for his careful proofreading of various draft versions of this thesis. I want to thank all of my officemates – Ana Paola Mikler Celis, Eric, and Jens Erler for the sense of family and friendship over the years. My PhD would not have felt complete without the friendships made along the way with others in Frank's research group, including Toma Badescu, Eleni Vardoulaki, Emilio Romano Diaz and Christos Karoumpis. I'll smile when I think back to our shared times at conferences and meetings.

As it can be difficult to transition to a new country and also to pursue a PhD, I am thankful to all of my friends in Bonn who made life that much easier amidst the ups and downs of this rollercoaster. In fact, I have certainly experienced losing my sense of Self many times and it is quite unsettling – mentally, emotionally and physically. I hope that my many friendships here in Bonn are long-lasting, and we can continue to reflect back during our times spent here along the river Rhein. I am always going to appreciate what Luca Grassitelli, Rusu, Ana, Nathan Grin, Hans Nguyen, Mary Cruces, Ziad Modak, Rovina Pinto, Flavia Amaral and others did for me when I broke my ankle and had to have three separate surgeries between June 2018 and September 2019. I want to acknowledge the fun times at the IMPRS retreats each year since 2016, and I hope to stay in contact with as many people as possible. Thank you as well to all of the student representatives, particularly Mary Cruces, Felix Poetzl and Tasha Gautam for making the 3 years as IMPRS student representative enjoyable and constructive. This was largely due to the on-going support from IMPRS coordinator, Rainer Mauersberger.

I would like to pay particular attention to the wholehearted support and patience of Li, Barbara

and Simone, from the MPIfR, for providing the logistical foundation upon arriving. I am forever in a debt of gratitude to our now retired secretary, Christina Stein-Schmitz, for her thoughtfulness, gracefulness and patience when taking care of the logistics surrounding my work and many travels. She was always there to answer questions and provide reassurance, and since she has left I have been fortunate enough to have also had a strong level of support from the new secretary Sabine Derdau for the final documents needed to complete my thesis and time here in Bonn.

With the combined financial support of the International Max Planck Research School for Astronomy and Astrophysics in Bonn (IMPRS), the Bonn and Cologne Graduate School program (BCGS) and the Deutsche Forschungsgemeinschaft (DFG), through the SFB 956 program, I have had the fortune of traveling to various conferences across the world. I have also had the unique opportunity to observe with many of the world's best radio telescopes and to develop a strong international collaboration. I am determined to come back to Bonn and to continually develop the work I've done here.